

The Flow around a Fish-inspired Heaving and Pitching Hydrofoil

by

Timothy Lau

Supervised by

Assoc. Prof. Richard M. Kelso

Dr. Peter V. Lanspeary

School of Mechanical Engineering,
Faculty of Engineering, Computer and Mathematical Sciences,
The University of Adelaide,
South Australia 5005,
Australia

*A thesis submitted in fulfillment of the requirements for the degree Doctor of Philosophy in
Mechanical Engineering on the 20th of December 2010*

This page is intentionally blank.

Contents

Contents	i
List of Figures	vii
List of Tables	xiv
List of Symbols	xvi
Statement of Originality	xxvi
Permission to Copy	xxvii
Abstract	xxviii
Acknowledgments	xxx
Chapter 1. Introduction and Literature Review	1
1.1 Introduction	1
1.2 Background	2
1.2.1 The Q-S model applied to hovering insects	7
1.2.2 Unsteady flow control in carangiform propulsion	10
1.2.3 Unsteady foil wake patterns	14
1.2.4 Observed fish kinematics in the literature	16
1.2.5 Formation number	19
1.3 Aims	20
1.4 Thesis outline	21

Chapter 2. Experimental Setup and Apparatus	23
2.1 Introduction	23
2.2 General description of experiments	23
2.2.1 Description of flow facility	23
2.2.2 Foil properties	24
2.2.3 Foil motion mechanism	26
2.3 Foil properties and kinematics	26
2.3.1 Pitching	26
2.3.2 Heaving	32
2.3.3 Derived kinematic parameters	32
2.3.3.1 Trailing edge motion	32
2.3.3.2 Strouhal number	33
2.3.3.3 Angle of attack	33
2.3.3.4 Heave dominance parameter, χ	34
2.3.3.5 $St_{h,0}$ and St_0	34
2.3.4 Chosen foil kinematic parameters	35
2.4 Implementation of digital Particle Image Velocimetry (PIV)	35
2.4.1 Light sheet generating optics	36
2.4.2 Imaging system	37
2.4.3 Particle seeding	37
2.4.3.1 Particle image size	39
2.4.4 Laser timing and synchronisation	40
2.4.5 PIV processing parameters	43
2.4.5.1 Image pre-processing	44
2.4.5.2 Image processing parameters	44
2.4.5.3 Outlier detection (Phase 1)	45
2.5 Post - processing of PIV data	45
2.5.1 Outlier detection (Phase 2)	45

2.5.2	Phase averaging	46
2.5.3	The estimation of the random errors in PIV velocity measurements . . .	46
2.5.3.1	Based on a sample set of phase-locked velocity fields	46
2.5.3.2	Based on theoretical error estimation	47
2.5.3.3	Random errors in the phased-averaged data	48
2.5.4	Smoothing of velocity vectors	53
2.5.5	Estimation of vorticity and circulation	53
2.5.5.1	Estimation of vorticity	54
2.5.5.2	Errors in the vorticity field	54
2.5.5.3	Estimation of circulation	56
2.5.5.4	Errors in circulation	56
2.6	Implementation of strain gauge measurements	57
2.7	Flow visualisation	60
2.8	Chapter summary	62
 Chapter 3. The Theoretical Quasi-Steady (Q-S) Model		64
3.1	Introduction	64
3.2	Forces due to the foil lift	65
3.2.1	Suitable values of k_{theory}	66
3.3	Forces due to the foil drag	69
3.4	Forces due to added mass of the entrained fluid	71
3.5	Total lift and drag coefficients	72
3.6	Time averaged forces	72
3.7	Froude efficiency, η_F	73
3.8	Productivity	74
3.9	Behaviour of foil kinematics at high St_h	74
3.10	Vorticity distribution behind the foil	76
3.10.1	Vorticity shed due to the foil bound vortex	76

Contents

3.10.2	Vorticity shed due to the no-slip boundary condition	78
3.10.3	Total vorticity shed into the wake	78
3.10.4	Theoretical wake widths	80
3.10.5	First moment of circulation, M_Γ	82
3.11	Numerical results	82
3.11.1	Foil dynamics	83
3.11.2	Wake dynamics	87
3.12	A note on the limitations of the Q-S model	91
3.13	Chapter summary	92
Chapter 4. Experimental Force and Efficiency Measurements		94
4.1	Introduction	94
4.2	Group I : Pure heave (sets 1-3)	95
4.3	Group II : Heave dominant (sets 4-6)	95
4.4	Group III : Moderate pitch & heave (sets 7-9)	100
4.5	Group IV : Pitch dominant (sets 10-12)	105
4.6	Discussion	105
4.7	Conclusion	118
Chapter 5. Wake Patterns of an Unsteady Foil		120
5.1	Introduction	120
5.2	Dye visualisation	120
5.3	Three-dimensional hydrogen bubble visualisation	125
5.3.1	Spanwise view	126
5.3.1.1	Group III, set 8 : $\chi = 0.87, \frac{h_0}{c} = 0.5, \theta_0 = 30^\circ$	126
5.3.1.2	Group I, set 2 : $\chi = \infty, \frac{h_0}{c} = 0.5, \theta_0 = 0^\circ$	128
5.3.2	Planform view	133
5.4	PIV-derived vorticity fields	143
5.4.1	Wake patterns for group III, set 8: $\chi = 0.87, \frac{h_0}{c} = 0.5, \theta_0 = 30^\circ$	143

5.4.2	Wake patterns for group I, set 2 : $\chi = \infty$, $\frac{h_0}{c} = 0.5$, $\theta_0 = 0^\circ$	148
5.4.3	The interaction of leading edge and trailing edge vorticity	149
5.5	Interpretation of unsteady foil wake structure	152
5.6	Conclusions	158
Chapter 6. Quantitative Wake Measurements		163
6.1	Introduction	163
6.2	The generation of optimal vortical wake structures	163
6.3	Quasi-steady model (II) of wake dynamics	166
6.3.1	Q-S-II results	172
6.4	Experimental measurement of M_Γ , $\Gamma_{total,c}$ and A_c	174
6.5	Experimental and numerical results	179
6.6	Conclusions	190
Chapter 7. Concluding Remarks		192
7.1	Discussion and summary	192
7.2	Implications of research findings	199
7.3	Conclusion	205
7.4	Recommendations for future work	205
Bibliography		207
Appendix A. Summary of foil parameters, flow conditions, and results		217
Appendix B. Experimental Measurement of Forces		231
B.1	Introduction	231
B.2	Method I : Force estimates derived from 2D velocity fields	231
B.2.1	Linear momentum balance	231
B.2.1.1	Mass balance	232
B.2.1.2	Momentum balance	233

Contents

B.2.1.3	Estimation of the V_r term	235
B.2.2	Further simplification	236
B.2.3	The “momentum” equation	237
B.2.3.1	Simplification of the “momentum equation”	239
B.2.4	Vortex added mass method	240
B.2.5	Test cases	241
B.3	Force measurements from strain gauges	246
B.4	Errors in experimental force and efficiency data	247
B.5	Chapter summary	248
Appendix C. Estimating Circulation based on Discrete Velocity Data		250
C.1	Introduction	250
C.2	Estimation of circulation	250
C.3	Vorticity estimation schemes	251
C.3.1	Definition of vorticity	251
C.3.2	Finite difference techniques	253
C.3.3	Iterative techniques	253
C.3.4	Circulation-method	254
C.4	Performance of vorticity calculation schemes	255
C.4.1	Analytic values of random error transmission	256
C.5	Description of numerical experiment	257
C.6	Vorticity bias error	259
C.7	Errors in circulation	261
C.8	Conclusions and recommendations	267

List of Figures

1.1	Schematic profile of a carangiform swimmer	3
1.2	Reverse Karman street behind a swimming carangiform	14
2.1	Schematic of flow facility	25
2.2	Effect of Cam Thickness on Pitching Profile ($\theta_0 = 45^\circ$)	27
2.3	Experimental setup	28
2.4	Foil mechanism	29
2.5	Geometry of cam - follower interface	30
2.6	Definitions of foil kinematic parameters	31
2.7	Experimental optical arrangement	38
2.8	Block diagram of synchronisation system	41
2.9	Synchronisation circuit	42
2.10	Timing diagram	43
2.11	Example of a typical phase-averaged flapping foil velocity field (continued on next page)	49
2.11	Example of a typical phase-averaged flapping foil velocity field (continued) . .	50
2.12	Example of a typical flapping foil vorticity field, derived from phase-averaged velocity data. Vorticity contour colorbars are in units of $\frac{1}{s}$ (continued on next page)	51
2.12	Example of a typical flapping foil vorticity field, derived from phase-averaged velocity data. Vorticity contour colorbars are in units of $\frac{1}{s}$ (continued)	52
2.13	The circ-5 vorticity estimation scheme	55
2.14	Force measurement system	57

List of Figures

2.15	Example of filtered and unfiltered strain gauge measurement (normal to the foil chord) of a flapping foil	58
2.16	Hydrogen bubble imaging locations	61
3.1	Steady-state lift coefficients vs α obtained a) numerically for a NACA 0025 foil at $Re = 8 \times 10^5$ (Sheldahl and Klimas, 1981), and b) experimentally for a NACA 0026 foil at $Re \approx 6,500$, performed at the University of Adelaide. c) is the linear curve fit of data from b)	67
3.2	Steady-state drag coefficients vs α obtained a) numerically for a NACA 0025 foil at $Re = 1 \times 10^4$ (Sheldahl and Klimas, 1981), b) experimentally, for a NACA 0015 foil at $Re = 3.6 \times 10^5$ (Sheldahl and Klimas, 1981), c) computationally, for a flat plate at $Re \approx 1,800$ (Wu and Sun, 2004), and d) experimentally for a NACA 0026 foil at $Re \approx 6,500$, performed at the University of Adelaide. e) is the order-3 polynomial fit of data from a)	70
3.3	“Virtual mass” of fluid entrained by the foil	73
3.4	Vorticity shed into the wake of an unsteady foil due to the change in bound circulation	77
3.5	The vorticity shed at the trailing edge of the foil, due to the Kutta condition	79
3.6	Definition of wake width, A_c	81
3.7	Relationship between α_{max} and St_h	83
3.8	Predicted foil kinematic parameters as a function of St_h based on the Q-S model (continued on following page)	84
3.8	Predicted foil kinematic parameters as a function of St_h based on the Q-S model (continued)	85
3.9	Wake dynamics predicted by the Q-S model, for sets 1, 4, 7 and 10	89
3.10	Wake dynamics predicted by the Q-S model for sets 2, 5, 8 and 11	90
4.1	Thrust and side force coefficients, C_t and C_s , for set 1 : $\frac{h_0}{c} = 0.75$, $\theta_0 = 0^\circ$	96
4.2	Thrust and side force coefficients, C_t and C_s , for set 2 : $\frac{h_0}{c} = 0.5$, $\theta_0 = 0^\circ$	97
4.3	Thrust and side force coefficients, C_t and C_s , for set 3 : $\frac{h_0}{c} = 0.25$, $\theta_0 = 0^\circ$	98
4.4	Productivity, η and Froude efficiency, η_F for set 2 : $\frac{h_0}{c} = 0.5$, $\theta_0 = 0^\circ$	99
4.5	Thrust and side force coefficients, C_t and C_s , for set 4 : $\frac{h_0}{c} = 0.75$, $\theta_0 = 15^\circ$	101

4.6	Thrust and side force coefficients, C_t and C_s , for set 5 : $\frac{h_0}{c} = 0.5$, $\theta_0 = 15^\circ$. . .	102
4.7	Thrust and side force coefficients, C_t and C_s , for set 6 : $\frac{h_0}{c} = 0.25$, $\theta_0 = 15^\circ$. . .	103
4.8	Productivity, η and Froude efficiency, η_F for set 4 : $\frac{h_0}{c} = 0.75$, $\theta_0 = 15^\circ$	104
4.9	Thrust and side force coefficients, C_t and C_s , for set 7 : $\frac{h_0}{c} = 0.75$, $\theta_0 = 30^\circ$. . .	106
4.10	Thrust and side force coefficients, C_t and C_s , for set 8 : $\frac{h_0}{c} = 0.5$, $\theta_0 = 30^\circ$. . .	107
4.11	Thrust and side force coefficients, C_t and C_s , for set 9 : $\frac{h_0}{c} = 0.25$, $\theta_0 = 30^\circ$. . .	108
4.12	Productivity, η and Froude efficiency, η_F for set 7 : $\frac{h_0}{c} = 0.75$, $\theta_0 = 30^\circ$	109
4.13	Thrust and side force coefficients, C_t and C_s , for set 10 : $\frac{h_0}{c} = 0.75$, $\theta_0 = 45^\circ$. . .	110
4.14	Thrust and side force coefficients, C_t and C_s , for set 11 : $\frac{h_0}{c} = 0.5$, $\theta_0 = 45^\circ$. . .	111
4.15	Thrust and side force coefficients, C_t and C_s , for set 12 : $\frac{h_0}{c} = 0.25$, $\theta_0 = 45^\circ$. . .	112
4.16	Productivity, η and Froude efficiency, η_F for set 11 : $\frac{h_0}{c} = 0.5$, $\theta_0 = 45^\circ$	113
4.17	Comparison of current experimental results with results from Anderson <i>et al.</i> (1998), for $\theta_0 = 15^\circ$	114
4.18	Comparison of current experimental results with results from Anderson <i>et al.</i> (1998), for $\theta_0 = 30^\circ$	114
4.19	Time-averaged thrust coefficient based on an average of the PIV and strain gauge measurements, $C_{t,ave}$ vs St_h for all flow cases. For a definition of set numbers, please refer to Table 2.1 or Table 4.1	116
5.1	Dye flow visualisation for $St < St_0$, $\frac{h_0}{c} = 0.5$, $\theta_0 = 45^\circ$, $St = 0.14$, $St_{0,exp} = 0.5$, $Re = 3,500$	122
5.2	Dye flow visualisation for $St \approx St_0$	123
5.3	Dye flow visualisation for $St > St_0$	124
5.3	Dye flow visualisation for $St > St_0$ (continued)	125
5.4	Definition of top dead centre (TDC) and bottom dead centre (BDC)	126
5.5	Hydrogen bubble image sequence, spanwise view, for group III, set 8 : $\frac{h_0}{c} = 0.5$, $\theta_0 = 30^\circ$, $St = 0.13$, $St_{0,exp} = 0.26$, $Re = 2,800$	127
5.6	Hydrogen bubble image sequence, spanwise view, for group III, set 8 : $\frac{h_0}{c} = 0.5$, $\theta_0 = 30^\circ$, $St = 0.29$, $St_{0,exp} = 0.26$, $Re = 2,500$ (continued on following page)	129
5.6	Hydrogen bubble image sequence, spanwise view, for group III, set 8 : $\frac{h_0}{c} = 0.5$, $\theta_0 = 30^\circ$, $St = 0.29$, $St_{0,exp} = 0.26$, $Re = 2,500$ (continued)	130

List of Figures

5.7	Hydrogen bubble image sequence, spanwise view, for group III, set 8 : $\frac{h_0}{c} = 0.5$, $\theta_0 = 30^\circ$, $St = 0.44$, $St_{0,exp} = 0.26$, $Re = 1,500$ (continued on following page)	131
5.7	Hydrogen bubble image sequence, spanwise view, for group III, set 8 : $\frac{h_0}{c} = 0.5$, $\theta_0 = 30^\circ$, $St = 0.44$, $St_{0,exp} = 0.26$, $Re = 1,500$ (continued)	132
5.8	Hydrogen bubble image sequence, spanwise view, for group I, set 2 : $\frac{h_0}{c} = 0.5$, $\theta_0 = 0^\circ$, $St = 0.14$, $St_{0,exp} = 0.20$, $Re = 2,000$	134
5.9	Hydrogen bubble image sequence, spanwise view, for group I, set 2 : $\frac{h_0}{c} = 0.5$, $\theta_0 = 0^\circ$, $St = 0.24$, $St_{0,exp} = 0.20$, $Re = 1,200$ (continued on following page)	135
5.9	Hydrogen bubble image sequence, spanwise view, for group I, set 2 : $\frac{h_0}{c} = 0.5$, $\theta_0 = 0^\circ$, $St = 0.24$, $St_{0,exp} = 0.20$, $Re = 1,200$ (continued)	136
5.10	Hydrogen bubble image sequence, spanwise view, for group I, set 2 : $\frac{h_0}{c} = 0.5$, $\theta_0 = 0^\circ$, $St = 0.36$, $St_{0,exp} = 0.20$, $Re = 1,500$	137
5.11	Hydrogen bubble image sequence, planform view, group III, set 8: $\frac{h_0}{c} = 0.5$, $\theta_0 = 30^\circ$, $St = 0.29$, $St_{0,exp} = 0.26$, $Re = 2,500$ (continued on following page)	139
5.11	Hydrogen bubble image sequence, planform view, group III, set 8: $\frac{h_0}{c} = 0.5$, $\theta_0 = 30^\circ$, $St = 0.29$, $St_{0,exp} = 0.26$, $Re = 2,500$ (continued)	140
5.12	Hydrogen bubble image sequence, planform view, group I, set 2: $\frac{h_0}{c} = 0.5$, $\theta_0 = 0^\circ$, $St = 0.36$, $St_{0,exp} = 0.20$, $Re = 1,500$ (continued on following page)	141
5.12	Hydrogen bubble image sequence, planform view, group I, set 2: $\frac{h_0}{c} = 0.5$, $\theta_0 = 0^\circ$, $St = 0.36$, $St_{0,exp} = 0.20$, $Re = 1,500$ (continued)	142
5.13	Vorticity contours for group III, set 8 : $\frac{h_0}{c} = 0.5$, $\theta_0 = 30^\circ$, $St = 0.13$, $St_{0,exp} = 0.26$, $Re = 12,000$	145
5.14	Vorticity contours for group III, set 8 : $\frac{h_0}{c} = 0.5$, $\theta_0 = 30^\circ$, $St = 0.18$, $St_{0,exp} = 0.26$, $Re = 9,000$	145
5.15	Vorticity contours for group III, set 8 : $\frac{h_0}{c} = 0.5$, $\theta_0 = 30^\circ$, $St = 0.22$, $St_{0,exp} = 0.26$, $Re = 7,000$	146
5.16	Vorticity contours for group III, set 8 : $\frac{h_0}{c} = 0.5$, $\theta_0 = 30^\circ$, $St = 0.29$, $St_{0,exp} = 0.26$, $Re = 10,500$	146
5.17	Vorticity contours for group III, set 8 : $\frac{h_0}{c} = 0.5$, $\theta_0 = 30^\circ$, $St = 0.35$, $St_{0,exp} = 0.26$, $Re = 8,750$	147
5.18	Vorticity contours for group III, set 8 : $\frac{h_0}{c} = 0.5$, $\theta_0 = 30^\circ$, $St = 0.44$, $St_{0,exp} = 0.26$, $Re = 7,000$	147

5.19	Vorticity contours for group III, set 8 : $\frac{h_0}{c} = 0.5$, $\theta_0 = 30^\circ$, $St = 0.59$, $St_{0,exp} = 0.26$, $Re = 5,000$	148
5.20	Vorticity contours for group I, set 2 : $\frac{h_0}{c} = 0.5$, $\theta_0 = 0^\circ$, $St = 0.14$, $St_0 = 0.2$, $Re = 8,750$	150
5.21	Vorticity contours for group I, set 2 : $\frac{h_0}{c} = 0.5$, $\theta_0 = 0^\circ$, $St = 0.18$, $St_0 = 0.2$, $Re = 7,000$	150
5.22	Vorticity contours for group I, set 2 : $\frac{h_0}{c} = 0.5$, $\theta_0 = 0^\circ$, $St = 0.24$, $St_0 = 0.2$, $Re = 5,000$	151
5.23	Vorticity contours for group I, set 2 : $\frac{h_0}{c} = 0.5$, $\theta_0 = 0^\circ$, $St = 0.36$, $St_0 = 0.2$, $Re = 3,500$	151
5.24	Vorticity contours for group I, set 2 : $\frac{h_0}{c} = 0.5$, $\theta_0 = 0^\circ$, $St = 0.48$, $St_0 = 0.2$, $Re = 5,000$	152
5.25	The interaction of leading edge and trailing edge vorticity. Foil parameters : $\frac{h_0}{c} = 0.5$, $\theta_0 = 0^\circ$ and $St = 0.36$, $St_0 = 0.2$, $Re = 3,500$ (continued on following page)	153
5.25	The interaction of leading edge and trailing edge vorticity (continued). Foil parameters : $\frac{h_0}{c} = 0.5$, $\theta_0 = 0^\circ$ and $St = 0.36$, $St_0 = 0.2$, $Re = 3,500$	154
5.26	Schematic of wake patterns behind the unsteady hydrofoil	156
5.27	Proposed vortex skeleton of the 3D unsteady foil wake	157
5.28	Observed vortex patterns in the wake of an unsteady hydrofoil. For a brief description of these wake patterns, please refer to Table 5.1.	162
6.1	Formation of optimal vortical structures	165
6.2	Schematic of possible simulated wake patterns with $N_{vortices} = 2$ (continued on following page)	168
6.2	Schematic of possible simulated wake patterns with $N_{vortices} = 2$ (continued)	169
6.3	Example of vorticity fields produced in the Q-S-II simulations. Vorticity contours have units $\frac{1}{s}$	171
6.4	Results of Q-S-II wake simulations, part 1 (continued on following page)	173
6.4	Results of Q-S-II wake simulations, part 1 (continued)	174
6.5	Results of Q-S-II wake simulations, part 2 (continued on following page)	175

List of Figures

6.5	Results of Q-S-II wake simulations, part 2 (continued)	176
6.6	Evaluation of circulation of shed vortical structures behind the foil. Flow is from left to right. Foil kinematic parameters: $\frac{h_0}{c} = 0.25$, $\theta_0 = 15^\circ$, and $St = 0.44$ (continued on following page)	177
6.6	Evaluation of circulation of shed vortical structures behind the foil. Flow is from left to right. Foil kinematic parameters: $\frac{h_0}{c} = 0.25$, $\theta_0 = 15^\circ$, and $St = 0.44$ (continued)	178
6.7	Wake dynamics for set 2 : $\frac{h_0}{c} = 0.5$, $\theta_0 = 0^\circ$ (Group I)	180
6.8	Wake dynamics for set 5 : $\frac{h_0}{c} = 0.5$, $\theta_0 = 15^\circ$ (Group II)	181
6.9	Wake dynamics for set 8 : $\frac{h_0}{c} = 0.5$, $\theta_0 = 30^\circ$ (Group III)	182
6.10	Wake dynamics for set 11 : $\frac{h_0}{c} = 0.5$, $\theta_0 = 45^\circ$ (Group IV)	183
6.11	Summary of wake measurements for all flow cases. Set numbers refer to foil kinematic parameters defined in Table 2.1 (continued on following page) . . .	185
6.11	Summary of wake measurements for all flow cases. Set numbers refer to foil kinematic parameters defined in Table 2.1 (continued)	186
6.12	Relationship between the foil time-averaged thrust coefficient, C_t and the non-dimensional first moment of circulation, \tilde{M}_Γ . Set numbers refer to foil kinematic parameters defined in Table 2.1	188
7.1	Summary of experimentally measured time-averaged foil thrust coefficients, $C_{t,ave}$ vs the heave-based Strouhal number, St_h . Set numbers refer to foil kinematic parameters defined in table 7.2	195
7.2	Schematic representation of possible wake profiles behind an unsteady foil . .	198
7.3	Summary of experimentally measured time-averaged foil thrust coefficients, $C_{t,ave}$ vs the non-dimensional moment of circulation, \tilde{M}_Γ . Set numbers refer to foil kinematic parameters defined in table 7.2	199
B.1	Control volume around a hydrofoil	232
B.2	A hydrofoil in a control volume $V(t)$	237
B.3	Time averaged velocity fields relative to the foil at various St , for selected test cases where $\frac{h_0}{c} = 0.5$ and $\theta_0 = 30^\circ$. Flow is from left to right. Note that the vectors in the shadow of the foil are disabled	242

B.4	Velocity profiles along the control volume of the foil for selected test cases in figure B.3. For definitions of V_1 , V_2 , V_3 and V_4 , see figure B.1	243
B.5	Time averaged thrust coefficient, C_t calculated using various methods vs Strouhal number, St , for selected test cases.	244
B.6	Time averaged thrust coefficient, C_t calculated using the " V_r equation" and the "flat plate" equation	245
B.7	Comparison of $C_{t,piv}$ and $C_{t,sg}$ at $\frac{h_0}{c} = 0.5$ and $\theta_0 = 30^\circ$	247
C.1	Example of region of integration for the flapping foil experiments. Flow is from left to right. Vorticity contours are in units $\frac{1}{s}$	252
C.2	Velocity field of an analytic Oseen vortex for $\frac{\Delta}{L} = 0.46154$	259
C.3	Effect of $\frac{\Delta}{L}$ and ϵ_u on the circulation bias error for the centre-difference scheme	262
C.4	Effect of $\frac{\Delta}{L}$ and ϵ_u on the random error in circulation for the centre-difference scheme	263
C.5	Effect of vorticity estimation schemes and ϵ_u on the circulation bias error at a fixed $\frac{\Delta}{L} = 0.29$	264
C.6	Effect of vorticity estimation schemes and ϵ_u on the random error in circulation at a fixed $\frac{\Delta}{L} = 0.29$	265
C.7	Total errors in the circulation estimate for all tested schemes at $\epsilon_u = 0.05$ and $\frac{\Delta}{L} = 0.29$. For list of scheme designations, please refer to table C.5	266

List of Tables

1.1	Examples of mathematical models applied to carangiform propulsion	6
1.2	Summary of observed Strouhal numbers of swimming and flying creatures . .	18
2.1	Summary of foil kinematics, organised into individual sets and groups	36
3.1	Summary of values of k_{theory} obtained from literature and current experiments .	68
3.2	Results for St_0 based on the quasi-steady model	87
3.3	Foil wake width \tilde{A}_c and moment of circulation \tilde{M}_Γ when $St_h = St_{h,0,qs}$	91
4.1	Summary of experimentally measured values of St_0	117
5.1	Summary of observed wake patterns behind the unsteady foil. For a schematic representation of these wake patterns, refer to Figure 5.28.	159
7.1	Summary of observed wake patterns behind the unsteady foil. For a schematic representation of these wake patterns, refer to figure 7.2.	197
7.2	Summary of foil kinematic parameters	200
7.3	Summary of significant experimental observations as a function of St . For definitions of wake pattern abbreviations (LK-H, P+Xs, etc), refer to 7.1)	201
7.4	Summary of significant experimental observations as a function of foil kinematic parameters	202
A.1	Summary of foil kinematic parameters	218
A.2	Experimental results for set 1	219
A.3	Experimental results for set 2	220
A.4	Experimental results for set 3	221

A.5	Experimental results for set 4	222
A.6	Experimental results for set 5	223
A.7	Experimental results for set 6	224
A.8	Experimental results for set 7	225
A.9	Experimental results for set 8	226
A.10	Experimental results for set 9	227
A.11	Experimental results for set 10	228
A.12	Experimental results for set 11	229
A.13	Experimental results for set 12	230
C.1	Commonly used finite difference techniques (Raffel <i>et al.</i> , 1998)	253
C.2	Coefficients for compact schemes	253
C.3	Random noise transmission coefficients (Etebari and Vlachos, 2005)	257
C.4	Summary of normalised bias errors at Oseen vortex core, $\widetilde{\omega}_{bias}$ for various vorticity schemes	260
C.5	Summary of the performance of each vorticity estimation scheme	267

List of Symbols

Note: In many instances the tail of a swimming carangiform fish and the unsteady foil are used interchangeably.

A	Reference amplitude for determining Strouhal number. In this thesis, typically $A = A_{te}$ unless otherwise specified
A_c	Wake width estimated from the centroid of shed vorticity in the wake
\tilde{A}_c	A_c normalised to the chord length of the foil
A_{cam}	Distance between centre to the pivot point of the cam
$A_{foil,max}$	Maximum thickness of the unsteady foil
A_p	Reference area for determining the thrust coefficient. For an unsteady foil, this area is the planform area, $A_p = c \cdot s$
A_{te}	Peak-to-peak trailing edge amplitude of the unsteady foil
A_w	Wake width
c	Foil chord length
C_D	Drag coefficient of the unsteady foil
C_{Df}	Drag coefficient due to form drag and skin friction
C_{Df}^*	Drag coefficient of the unsteady foil at large St_h
C_{Di}	Drag coefficient due to induced drag
\bar{c}_{ii}	Two-dimensional approximation to the added mass coefficient of the vortices in the wake

$c_{projected}$	Projected chord of the foil
C_L	Time-averaged lift coefficient of the unsteady foil
C_s	Time-averaged side force coefficient of the unsteady foil
C_t	Time-averaged thrust coefficient of the unsteady foil. Subscripts “piv” and “sg” refer to the value of C_t measured from particle image velocimetry and strain gauges respectively. Subscript “ave” refers to the average value of $C_{t,piv}$ and $C_{t,sg}$
D	Diameter of jet orifice
d_e	Effective seeding particle image size
d_p	Diameter of seeding particles
d_s	Diffraction limited image size of seeding particle
f	Frequency of foil oscillation, in Hz
\vec{F}	Total force vector acting on the foil
$F_C(t)$	Instantaneous chordwise component of the force developed by the unsteady foil
$\frac{f}{D}$	f-number of the camera lens
$F_D(t)$	Instantaneous drag developed by the unsteady foil
$F_{Df}(t)$	Instantaneous drag developed by the unsteady foil due to pressure drag and skin friction
$F_{Di}(t)$	Instantaneous drag developed by the unsteady foil due to induced drag
$F_L(t)$	Instantaneous lift force developed by the unsteady foil
$F_N(t)$	Instantaneous force developed normal to the unsteady foil chord
$FN(t)$	Formation number, defined as $FN(t) = \frac{U_j t}{D}$
$F_S(t)$	Instantaneous side force developed by the unsteady foil
$F_{SD}(t)$	Side force component of $F_D(t)$

List of Symbols

$F_{SL}(t)$	Side force component of $F_L(t)$
$F_{SV}(t)$	Side force due to “virtual” or “added” mass of entrained fluid
$f_{shedding}$	Frequency of the “free” vortex shedding behind the undriven foil
$F_T(t)$	Instantaneous thrust force developed by the unsteady foil
$\overline{F_T(t)}$	Time-averaged thrust force developed by the unsteady foil
$F_{TD}(t)$	Thrust component of $F_D(t)$
$F_{TL}(t)$	Thrust component of $F_L(t)$
$h(t)$	Unsteady foil instantaneous heave
$h_{cen,n}$	Location of centroid (along y axis) of negative vorticity. Subscripts “shed,bound” and “kutta” refer to the centroids of vorticity shed due to the change in bound circulation around the foil, and the no-slip boundary condition at the foil trailing edge, respectively
$h_{cen,p}$	Location of centroid (along y axis) of positive vorticity. Subscripts “shed,bound” and “kutta” refer to the centroids of vorticity shed due to the change in bound circulation around the foil, and the no-slip boundary condition at the foil trailing edge, respectively
h_0	Unsteady foil heave amplitude
\hat{i}	Unit vector in the x-direction
\vec{I}	Unit tensor
\hat{j}	Unit vector in the y-direction
k	Reduced frequency, $k = \frac{\pi f c}{U_\infty} \equiv \pi St_c$
\hat{k}	Unit vector in the z-direction
k_i	Correction factor for induced drag
k_{theory}	Constant relating C_L to $\sin \alpha$
K_{scheme}	Random noise transmission coefficient of the vorticity estimation scheme
$k_{\Gamma,sim}$	Constant relating C_t to \widetilde{M}_Γ , as determined using simulations

L	Reference length scale. When used to determine the Reynolds number, typically $L = c$. When used to describe the Oseen vortex, L is the characteristic radius
L_f	Follower arm length
L_{flow}	Characteristic length scale in the flow
\dot{m}	Mass flux
M	Magnification of optical arrangement
$M_\theta(t)$	Instantaneous pitching moment developed by the unsteady foil
M_Γ	Moment of circulation, defined as $M_\Gamma = \Gamma_{total} \cdot A_c$
\widetilde{M}_Γ	Normalised moment of circulation, defined as $\widetilde{M}_\Gamma = \widetilde{\Gamma}_{total,c} \cdot \widetilde{A}_c$
\hat{n}	Unit vector, $\hat{n} = (\hat{i}, \hat{j}, \hat{k})$
N_p	Average number of particles in each PIV interrogation window
$N_{valid,i}$	Number of valid vectors used, at any point i in the measured flow field, to obtain phase-averaged flow field
$N_{vortices,s}$	Number of discrete vortical structures shed of any particular sign s , where $s = p$ for positive and $s = n$ for negative
p	Pressure
P_{in}	Power required to produce the unsteady foil motion over one oscillation cycle
r	Radial distance from the core of the analytically defined Oseen vortex
r_{cam}	Radius of cam
R_{ct}	Half-thickness of cam
Re	Reynolds number
Re_c	Reynolds number based on the chord length of the foil
r_m	Median of the residuals of the eight velocity vectors surrounding any given point in the discretised velocity field

List of Symbols

r'_0	Normalised residual at any given point in the discretised velocity field
s	Span of the foil
St	Strouhal number, typically based on A_{te} , unless otherwise specified
St_0	Strouhal number at which the time-averaged thrust developed by the unsteady foil is zero. Subscripts “exp”, “qs” and “simp” refer to the value of St_0 based on experimental measurements, quasi-steady model estimates, and simplified analytical equations respectively
St_c	Strouhal number based on the chord length of the foil
St_h	Strouhal number based on the heave amplitude of the unsteady foil
$St_{h,0}$	Heave-based Strouhal number at which the time-averaged thrust developed by the unsteady foil is zero (See also St_0)
St_{shed}	Strouhal number of the “free” vortex shedding behind the undriven foil
St_{te}	Strouhal number based on A_{te}
Stk	Stokes number
t	Time
T	Period of unsteady foil oscillation
\vec{T}	Viscous stress tensor
u	x -component of velocity
U	Flow speed
U_j	Velocity of expelled fluid at the jet exit
U_m	Median of the eight velocity vectors surrounding any given point in the discretised velocity field
$u_{oseen}(r)$	Tangential velocity component of the analytically defined Oseen vortex
U_∞	Free-stream speed, or fish swimming speed
v	y -component of velocity

\vec{V}	Velocity vector, $\vec{V} = (V_x, V_y, V_z)$
\vec{V}_b	Surface velocity of foil
$V_{eff}(t)$	Effective velocity of the unsteady foil, relative to the surrounding fluid)
$V_{eff,te}(t)$	Effective velocity of the trailing edge of the unsteady foil, relative to the surrounding fluid
$V_{f,te}(t)$	Fluid velocity at trailing edge of the foil
V_{max}	Maximum velocity magnitude in the velocity field
V_r	Representative velocity term introduced to simplify the three-dimensional momentum balance equations derived in Appendix B. V_r can be thought of as the x-component of the velocity of a packet of fluid leaving the x-y plane of the control volume. Subscript “est” stands for the experimentally derived estimate
V_s	Settling velocity of seeding particles
\vec{V}_{vw}	Velocity vector of the wake vortices
$\vec{V}_{\frac{T}{2}}$	Velocity vector field time-averaged between $0 \leq t \leq \frac{T}{2}$
$v_{\phi,i,C}$	Velocity at any given phase ϕ , point i and oscillation cycle C in the discretised velocity field
$\overline{v_{\phi,i}}$	Phase-averaged velocity at any given phase ϕ and point i in the discretised velocity field
w	Depth of control volume
x	Spatial co-ordinate, orthogonal to y
\vec{x}	Spatial vector, $\vec{x} = (x, y, z)$
x_{cv}	Location of the control volume boundary relative to the origin
y	Spatial co-ordinate, orthogonal to x
$y_{shed}(t)$	Location along the y axis where the vorticity is shed into the unsteady foil wake

List of Symbols

$y_{te}(t)$	Trailing edge displacement (in the y-direction) of the unsteady foil
$z(t)$	Variable introduced for simplification, where $z(t) = \pi S t_h \cos \phi(t)$
$\alpha(t)$	Instantaneous angle of attack of the foil
α_{max}	Maximum angle of attack achieved by the unsteady foil during an entire oscillating cycle
$\alpha_{static-stall}$	Stall angle of the foil under steady conditions
χ	Heave dominance parameter, defined as $\chi = \frac{h_0}{c \cdot \tan \theta_0}$
ϵ_b	Error in the PIV cross correlation due to background noise in the PIV images
ϵ_d	Error in the PIV cross correlation due to particle image density
ϵ_g	Error in the PIV cross correlation due to velocity gradients
ϵ_l	Error in the PIV cross correlation due to particle image displacement
ϵ_p	Error in the PIV cross correlation due to particle image size
ϵ_s	Error associated with the accurate determination of the magnification of the optical setup
ϵ_t	Error in the determination of the actual value of Δt
$\epsilon_{threshold}$	Threshold level of residuals for determining outliers in the measured velocity field
ϵ_u	Estimated random error in the measured velocity field
$\epsilon_{u,i}$	Estimated random error in the measured velocity field at any point i , normalised to the free-stream velocity
$\epsilon_{u,max}$	Maximum estimated random error in the velocity field
$\epsilon_{u,pa}$	Estimated random error in the phase-averaged velocity field
ϵ_ω	Estimated error in vorticity, relative to the peak vorticity
Δ	Grid spacing of discretised velocity field
Δ_{f-q}	Flashlamp to Q-switch time delay

Δt	Time delay between laser pulses
ϕ	Unsteady foil phase angle, defined as $\phi = 2\pi f$
$\vec{\phi}$	Velocity potential vector
γ	Angle between the foil centreline and the lift-component of force
Γ	Circulation
$\Gamma_{bound}(t)$	Circulation of the bound vortex around the unsteady foil
$\Gamma_{i,j}$	Circulation around point i and j in the discretised velocity field
$\Gamma_{kutta}(t)$	Circulation of the vorticity shed into the wake due to the no-slip boundary condition
$\Gamma_{primary}$	Circulation of primary vorticity
$\Gamma_{s,i}$	Circulation of discrete vortical structure i of particular sign s ($s = p$ for positive and $s = n$ for negative)
$\Gamma_{secondary}$	Circulation of secondary vorticity
$\Gamma_{shed,bound}(t)$	Circulation of the vorticity shed behind the unsteady foil due to a change in strength of the bound vortex
Γ_{total}	Circulation of the total vorticity (of any given sign) that is shed into the wake. Subscripts p and n denote positive and negative vorticity respectively
$\tilde{\Gamma}_{total,c}$	Normalised value of Γ_{total}
Γ_{vel}	Circulation, computed using a velocity integral
Γ_{vor}	Circulation, computed using a vorticity integral
η	Productivity, defined as $\eta = \frac{C_t}{C_s}$
η_F	Propulsive (Froude) efficiency of the unsteady foil
λ	Wavelength of illuminating light
λ_0	Random error transmission ratio
Λ	Aspect ratio of the unsteady foil

List of Symbols

μ	Dynamic viscosity of working fluid (water, unless otherwise specified)
$\theta(t)$	Unsteady foil instantaneous pitch angle. Subscripts “ideal”, “thin” and “thick” refer to the pitching motion developed by an “ideal” mechanical system, a mechanical system with an infinitesimally thin cam, and the current mechanical system with a cam of finite thickness
θ_0	Unsteady foil pitch amplitude
ρ	Density of working fluid (water, unless otherwise specified)
ρ_p	Density of seeding particles
σ_j	Jitter in the imaging triggering system
σ_u	Random noise in the velocity field
σ_{vel}	Random error component in the estimation of circulation (velocity integral)
σ_{vor}	Random error component in the estimation of circulation (vorticity integral)
σ_ω	Random noise in the vorticity field
σ_Γ	Random error component in the estimation of circulation
$\sigma_{\Gamma,total}$	Total error in the estimation of circulation
τ	Relaxation time of the seeding particles
ω	Out-of-plane vorticity
$\vec{\omega}$	Vorticity vector, $\vec{\omega} = (\omega_x, \omega_y, \omega_z)$
ω_{bias}	Bias error in vorticity
ω_{kutta}	Vorticity shed into the wake due to the no-slip boundary condition at the foil trailing edge
ω_{max}	Maximum value in the vorticity field
ω_n	Negative component of ω
$\omega_{oseen}(r)$	Out-of-plane vorticity distribution of the analytically defined Oseen vortex
$\omega_{shed,bound}$	Vorticity shed into the wake due to the change in bound circulation around the unsteady foil

ω_t	Minimum vorticity threshold for determining path of integration for computing circulation
$\omega_{\frac{T}{2}}$	Vorticity time-averaged between the range $0 \leq t \leq \frac{T}{2}$
Ψ	Phase difference between heave and pitch
$\nabla_{virtual}$	Volume of “virtual” fluid entrained by the unsteady foil

Statement of Originality

I hereby declare that this work contains no material which has been accepted for the award of any other degree or diploma in any university or institution and, to the best of my knowledge and belief, contains no material previously published or written by another person except where due reference has been made in the text.

Signed

Date

Permission to Copy

I give consent to this copy of my thesis, when deposited in the University Library, being made available for loan and photocopying, subject to the provisions of the Copyright Act 1968.

Signed

Date

Abstract

An extensive investigation into the flow around a fish-inspired heaving and pitching hydrofoil was performed using a combination of two dimensional digital particle image velocimetry (PIV), direct strain gauge force & moment measurements, dye visualisation and three dimensional hydrogen bubble visualisation. The intention of this investigation was to study the effect of the foil dynamics on the foil wake structure and hydrodynamic forces, with the ultimate goal of determining if the oscillating foil, and by implication, fish, employ unsteady flow mechanisms to generate optimal thrust.

The experiments were performed by systematically varying the foil non-dimensional heave-amplitude-to-chord ratio, $\frac{h_0}{c} = 0.25 - 0.75$, the foil pitch amplitude, $\theta_0 = 0^\circ - 45^\circ$, and the free-stream velocity, U_∞ . The phase difference between the pitching and heaving motion is $\Psi = 90^\circ$ (heave lagging pitch). Experiments consisted of 113 different flow cases for dye visualisation, 38 flow cases for hydrogen bubble visualisation, and 108 flow cases for simultaneous PIV and force measurements. The resultant Strouhal numbers, based on the heave amplitude, fall into the range $0.1 \lesssim St_h \lesssim 1$, while the Reynolds numbers, based on the foil chord length, were approximately $500 \lesssim Re \lesssim 12,500$.

The experimentally measured time-averaged thrust coefficient, C_t , obtained independently using PIV and direct strain gauge measurements, shows excellent agreement, and indicates that very large values of $C_t > 10$ can be generated by the foil, particularly when non-dimensional heave amplitude is large relative to the pitch amplitude, and St_h is large. The results also indicate that in all investigated cases, there is no sign of a sudden loss in lift that is associated with the “stall” phenomenon usually seen in steady foils, even when the unsteady foil achieves very large instantaneous angles of attack ($\alpha_{max} > 60^\circ$).

To obtain a context for comparison, a quasi-steady model (Q-S model) of the oscillating hydrofoil was developed, based on the assumption that the flow around the unsteady foil at any given instant is equivalent to the flow around an identical steady foil with the same angle of attack. For most foil dynamic parameters and flow conditions, the value of C_t predicted by the Q-S model shows excellent agreement with the results obtained experimentally. However, when $\frac{h_0}{c}$

is large compared to θ_0 , the experimentally measured values of C_t far exceed the theoretical predictions. This suggests that the oscillating foil employs unsteady flow mechanisms to augment thrust production when $\frac{h_0}{c}$ is large relative to θ_0 .

Flow visualisation of the foil wake indicates that different wake patterns are produced, depending on the flow conditions. The observed wake patterns are interpreted as a combination of “primary” vorticity, which is associated with the production of lift (and hence thrust) by the foil, and “secondary” vorticity, which is associated with the drag produced by the foil. During each foil half-cycle, secondary vorticity manifests itself as multiple vortical roll-ups (“S” vortices), whereas the primary vorticity sheds as a single, typically large vortex, which combines with adjacent “S” vortices to form one “P” vortex. When $\frac{h_0}{c}$ is large compared to θ_0 , these “P” vortices are observed as very large leading edge vortices with strong spanwise flow (towards the foil centreline). These leading edge vortical structures are further evidence that the foil employs unsteady flow mechanisms to generate large thrust coefficients.

Based on the positions of these “P” and “S” vortices in the wake, we define three distinct wake regimes, a) “Drag regime”, occurring at $St_h \lesssim 0.15$, b) “Transitional regime”, occurring at $0.15 \lesssim St_h \lesssim 0.3$ and c) “Thrust regime”, occurring at $St_h \gtrsim 0.3$, whereby each regime produces subtly different wake patterns.

The wake behind the foil is also analysed quantitatively by measuring the first moment of circulation of the foil wake, $\tilde{M}_\Gamma = \tilde{\Gamma}_{total,c} \times \tilde{A}_c$, where $\tilde{\Gamma}_{total,c}$ is total circulation generated by the foil (of any given sign) per cycle, and \tilde{A}_c is the wake width based on the centroids of the shed vorticity. In an important finding, it is shown that the data for C_t vs \tilde{M}_Γ collapse onto a single curve, regardless of flow conditions and foil dynamic parameters. For most ($\approx 95\%$) of the cases measured, it is shown that C_t is approximately linearly proportional to \tilde{M}_Γ , indicating that the thrust produced by the foil can be increased by generating large vortical structures and increasing the wake width.

Based on these results, we therefore conclude that the foil employs unsteady flow mechanisms only when $\frac{h_0}{c}$ is large relative to θ_0 . Under these conditions, large C_t are generated by the foil due to the generation of leading edge vortical structures with large circulation, which are positioned far away from the foil time-averaged centreline.

Acknowledgments

It has often been said that the production of a Ph.D. thesis is a lonely endeavor. If that is true, then this thesis is an exception, for it has been borne with the aid of a large number of people, whos help I gladly acknowledge.

First and foremost, I would like to thank my principal supervisor, Associate Professor Richard Kelso, who, among many things, has made himself available on countless occasions to do the highly under-rated job of advising me on fluid mechanics. His enthusiasm for the study of fluid mechanics is highly contagious, and his faith in his students, although in some cases unwarranted, provides a strong measure of support and motivation.

I would also like to thank my co-supervisor, Dr. Peter Lanspeary, for providing me ample technical assistance, particularly with post-processing of my experimental data.

To my colleague and friend Eyad Hassan, who, in many instances, kept my mind off work with his light-hearted discussions on trajectories of vortex rings, Gaussian distributed laser light intensities, the importance of BNC T-connectors, and the accuracies of circulation estimation schemes.

I would like to extend my appreciation to the support network of the Adelaide University Mechanical Engineering department, including the computing, workshop and instrumentation staff. In particular, I would like to thank George Osborne, who single-handedly constructed the strain gauge measurement system, and assembled the hydrogen bubble visualisation apparatus.

Lastly, I would like to thank my friends and family, for your constant reminders that there is more to life than integral equations and Matlab.

Chapter 1

Introduction and Literature Review

1.1 Introduction

Biomimetics, which is the process of reverse engineering natural systems for utilisation in man-made applications, is a particularly fruitful genre of study due to the potential benefits it may provide. This is due to the fact that the evolutionary process, which automatically weeds out bad designs from the good, has allowed nature to develop creatures with remarkable capabilities. Sub-optimal designs simply do not survive this strenuous process. As this evolutionary process has been running for a relatively long time, intuitively it can be safely assumed that most creatures have converged, or are close to converging, upon their ideal design. This ideal design would give the creature certain capabilities to ensure it has a good chance of surviving in its environment. This “ideal” design, of course, would naturally differ from creature to creature, and is strongly dependent on its surroundings. This is fortunate as it allows the mimicry of appropriate characteristics of particular creatures to suit specific applications.

It then follows that there is strong motivation to mimic various aspects of nature, fish swimming not an exception. Although the question of how fish swim may sound trivial, it has emerged that fish swimming could play a major part in revolutionizing the design of water craft. More specifically, biomimetic fish propulsion is seen as a major influence in the design of autonomous underwater vehicles (Sfakiotakis *et al.*, 1999).

The potential for biomimetic aquatic propulsion is immense. Aquatic creatures come in a large range of shapes and sizes, from tiny zooplankton to enormous whales, adopt various swimming gaits, from steady swimming to “burst and coast” swimming, and employ different methods of locomotion. Aquatic creatures may generate locomotion via whole-body undulations (such

1.2 Background

as the eel), tail oscillations (such as the dolphin), oscillations and undulations of fins and appendages (such as the seahorse) or via jet-like propulsion mechanisms (such as the jellyfish). The motion and dynamics of these undulations, oscillations, and body contortions may also vary between species. The study of fish locomotion, therefore, may provide inspiration for the design of highly efficient, maneuverable and stealthy submerged vehicles (Bandyopadhyay, 2002).

However, to narrow the scope for study, we concentrate on steadily swimming aquatic animals that predominantly use the motion of their caudal tails to generate the forces and moments on its body. We define this class of aquatic swimmers as “carangiform” swimmers, consistent with the classification of Breder (1926). The inspiration for limiting the study to carangiform swimmers is the fact that carangiform fish are ubiquitous in nature, and they are usually associated with high-powered propulsion (Lighthill, 1975; Webb, 1984; Triantafyllou and Triantafyllou, 1995).

We indirectly study carangiform swimming by employing a fully submerged fish-inspired unsteady hydrofoil. This unsteady hydrofoil undergoes controlled simultaneous heaving and pitching motions which approximates the kinematics of carangiform caudal tails. The unsteady foil is used as a model of carangiform tails both a) as a matter of convenience, since controlled experiments with live fish have been shown to be difficult (Stamhuis *et al.*, 2002), and b) for the simultaneous study of the potential of an unsteady foil as a practical propulsion mechanism for underwater vehicles.

1.2 Background

Traditionally, the propulsion of carangiform swimmers has been explained in terms of the forces generated by the motion of the carangiform caudal tails. These caudal tails can be modelled as wing-like structures undergoing simultaneous heaving and pitching motions (Anderson *et al.*, 1998; Blake, 1983a; Dickinson, 1996; Lighthill, 1969; Sfakiotakis *et al.*, 1999; Triantafyllou *et al.*, 2000; Videler, 1993; Vogel, 1996; Yates, 1983), as shown in Figure 1.1. The heaving and pitching motions are usually described mathematically as

$$h(t) = h_0 \cos(2\pi ft - \psi) \quad (1.1)$$

$$\theta(t) = \theta_0 \cos(2\pi ft) \quad (1.2)$$

respectively, where h_0 is the heave amplitude, θ_0 is the pitch amplitude, f is the oscillating frequency (in Hz), ψ is the phase difference between the heave and pitch, and t is time. The

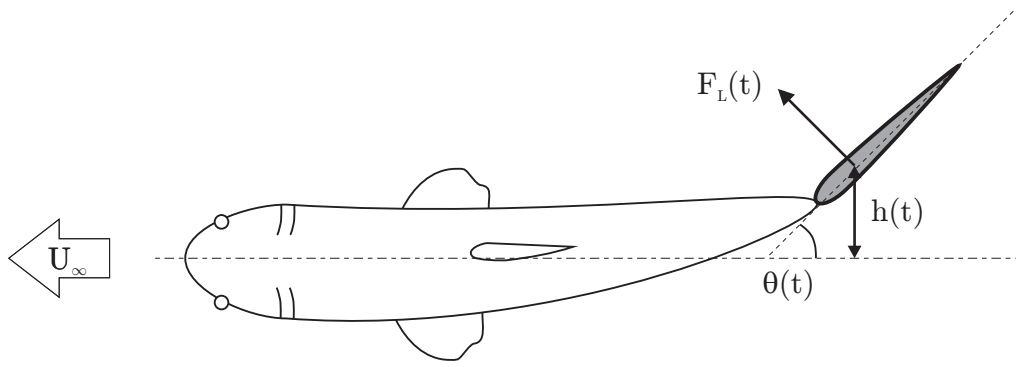


Figure 1.1: Schematic profile of a carangiform swimmer

heave amplitude is typically normalised to the chord of the foil, resulting in a non-dimensional heave amplitude $\frac{h_0}{c}$. In many instances, it is also convenient to describe the foil-like carangiform tails using the maximum instantaneous angle of attack achieved during an entire oscillating cycle, α_{max} , and the non-dimensional Strouhal number, which is defined as

$$St = \frac{fA}{U_\infty} \quad (1.3)$$

where U_∞ is the free-stream velocity (in the case of a swimming fish, this is also equal to the swimming speed; see Figure 1.1), A is an appropriate amplitude, usually taken as the amplitude of the tail motion (measured from peak to trough), A_{te} , unless otherwise stated. Of additional interest is the Reynolds number of the flow, defined as

$$Re = \frac{\rho U_\infty L}{\mu} \quad (1.4)$$

where ρ and μ are the density and viscosity of the fluid respectively, and L is an appropriate length scale. For studies on live fish swimming, L is usually the length of the fish, while in studies of insects and unsteady foils, L usually refers to the wing/foil chord length, c .

If the angles of attack are favorable, then intuitively, the carangiform caudal tails act like hydrofoils in a free-stream, generating unsteady lift forces that are similar to steady state lift forces at each instantaneous angle of attack. Across an entire tail oscillation period, the upstream-facing component of this lift may produce nett thrust to propel the actively swimming fish.

Various mathematical models have been employed to describe the flow around, and consequently, the forces generated by, the tails of swimming fish (e.g. Cheng and Murillo, 1984; Chopra, 1974; Lighthill, 1969, 1970; Wu, 1961; Triantafyllou *et al.*, 2000; Yates, 1983). These mathematical models will not be discussed in detail, however, the keen reader may refer to a recent review by Wu (2001).

1.2 Background

Typically each of these models has inherent simplifying assumptions, and in general all models attempt to estimate the propulsive capabilities of aquatic propulsion based on two values, namely, the time-averaged thrust coefficient, C_t , and the propulsive (Froude) efficiency, η_F . These are respectively defined as

$$C_t = \frac{F_T}{\frac{1}{2}\rho U_\infty^2 A_p} \quad (1.5)$$

$$\eta_F = \frac{F_T \cdot U_\infty}{P_{in}} \quad (1.6)$$

where F_T is the thrust force, A_p is an appropriate reference area, and P_{in} is the input power required to produce the flapping motion of the tail/foil.

Intuitively, for carangiform fish undergoing steady propulsion, it is assumed that the fish optimise propulsion to maximise efficiency. Historically, these mathematical models have been used to show that carangiform fish can achieve very high propulsive efficiencies when swimming steadily.

As an example, Chopra (1976) used a two-dimensional reactive force theory to mathematically model the large amplitude motions of carangiform lunate tails. Chopra assumed that even though the carangiform tail amplitudes were large, the instantaneous angles of attack of the tail relative to the incoming flow, α , were always small, and thus the vorticity generated by the tail is weak. The large amplitude lunate tail model provided a strong link between the tail kinematics (in particular the trailing edge amplitude, A_{te} and the reduced frequency, $k = \frac{\pi f c}{U_\infty} \equiv \pi St_c$), and the tail dynamics (in particular the time-averaged thrust coefficient C_t and the propulsive efficiency, η_F). The results indicate that C_t increases as either St_c , A_{te} or α_{max} increases. Propulsive efficiencies display a broad peak at moderate-to-large values of A_{te} , regardless of St_c or α_{max} , and maximum propulsive efficiencies are on order of $\eta_F \gtrsim 80\%$.

Yates (1983) provides further examples of the application of mathematical theory to aquatic propulsion. Based on the observed kinematics of steadily swimming trout by Webb (1971), Yates used an inviscid slender body theory to estimate the propulsive efficiency of trout as $\eta_F = 89\%$. Additionally, Yates applied an unsteady lifting line theory to the observed kinematics of porpoises by Lang and Daybell (1963) and obtained an estimated propulsive efficiency of $\eta_F = 92\%$.

Webb (1988) observed and recorded two carangiform species, the tiger musky and the rainbow trout, swimming steadily in a water channel. Based on the swimming kinematics of these fish, Webb used the large amplitude slender body theory, developed by Lighthill (1971), to determine that these carangiform fish can achieve propulsive efficiencies in excess of $\eta_F \approx 85\%$.

Bose and Lien (1989) used a small amplitude unsteady theory to predict the propulsive efficiency of a whale based on the measured caudal tail geometry. They report that the whale can achieve a peak propulsive efficiency of $\eta_F = 87\%$, occurring at pitch amplitudes of $\theta_0 = 30^\circ$.

Liu and Bose (1993) applied a quasi-vortex-lattice method to predict the propulsive efficiencies of various cetaceans, based on their fin geometries. Peak propulsive efficiencies of $\eta_F \approx 90\%$ were found to occur when the heave-based Strouhal number was $St_h \approx 0.25$, for all examined cetaceans.

Blickhan and Cheng (1994) merged a model of an oscillating mechanical elastic system together with unsteady flow theory applied to a rigid fin to estimate the propulsive efficiencies of a number of cetacean species. Based on kinematic data of swimming cetaceans from (Lang and Daybell, 1963) and (Videler and Kamermans, 1985), it was estimated that the cetaceans could achieve a maximum propulsive efficiency of $\eta_F \approx 78 - 98\%$.

Muller *et al.* (1997) used particle image velocimetry (PIV) to quantitatively study the wake of a steadily swimming mullet, at $Re \approx 20,000$. Based on a method proposed by Spedding *et al.* (1984), the PIV-derived vorticity fields of the wake were used to calculate the energy content of the shed vortices behind the swimming mullet, which were subsequently used to estimate the propulsive efficiency. Muller *et al.* report propulsive efficiencies of the steadily swimming mullet as $\eta_F \approx 97\%$. In similar experiments, Nauen and Lauder (2002) used stereoscopic particle image velocimetry (PIV) to obtain three-dimensional planar velocity components of the wake of a swimming rainbow trout. Based on the experimental velocity measurements, Nauen and Lauder used a simplified analysis of carangiform dynamics by Blake (1983a) to estimate that the propulsive (Froude) efficiency of trout, swimming at Reynolds numbers of $Re \approx 20,000$, was approximately $\eta_F \approx 74\%$.

Fish (1993) filmed the steady swimming kinematics of 5 trained bottlenose dolphins within the range of $3 \times 10^6 \lesssim Re \lesssim 1.5 \times 10^7$. Fish used a mathematical model, based on three dimensional unsteady lifting line theory (Chopra and Kambe, 1977), to estimate the propulsive efficiency, propulsive power, and drag coefficient of these swimming dolphins. Fish discovered that the propulsive efficiencies were approximately $\eta_F \approx 81\%$, while the drag coefficient was $C_D \approx 0.2$, which was approximately 7 times the drag coefficient of an equivalent rigid model of the dolphin. The propulsive power generated by the dolphins was consistent with published data on muscular power outputs of swimming mammals.

In similar studies, Fish (1998) and Rohr and Fish (2004) applied Chopra and Kambe's three dimensional unsteady lifting line theory to the observed dynamics of various species of cetaceans trained to swim in a large pool of water. Peak propulsive efficiencies reported were in the range of $\eta_F \approx 80 - 90\%$, depending on the species and the dynamics of the cetacean swimming.

1.2 Background

Description of Mathematical Model	Creature	Estimated Propulsive Efficiency, η_F	Reference
Two dimensional reactive force theory	-	$\approx 80\%$	Chopra (1976)
Inviscid slender body theory	Trout, Porpoise	$\approx 89 - 92\%$	Yates (1983)
Large amplitude slender body theory	Tiger Musky, Rainbow Trout	$\approx 85\%$	Webb (1988)
Small amplitude unsteady theory	Whale	$\approx 87\%$	Bose and Lien (1989)
Wake energy method	Mullet	$\approx 97\%$	Muller <i>et al.</i> (1997)
Inviscid resistive model	Rainbow Trout	$\approx 74\%$	Nauen and Lauder (2002)
Three dimensional unsteady lifting line theory	Bottlenose Dolphin	$\approx 81\%$	Fish (1993)
Three dimensional unsteady lifting line theory	Various Cetaceans	$\approx 80 - 90\%$	Fish (1998); Rohr and Fish (2004)
Quasi vortex lattice method	Various Cetaceans	$\approx 90\%$	Liu and Bose (1993)
Mechanical elastic model coupled with unsteady wing theory	Various Cetaceans	$\approx 78 - 98\%$	Blickhan and Cheng (1994)

Table 1.1: Examples of mathematical models applied to carangiform propulsion

Of all the mathematical models, the most applicable to this thesis is the “Quasi-Steady” (Q-S) model (McCroskey, 1982). The Q-S model facilitates the comparison of observed fish swimming dynamics with the estimated tail dynamics based on existing classical hydrodynamic knowledge. If the Q-S model fails to explain carangiform swimming dynamics, then one may argue that fish employ “unsteady” flow mechanisms during locomotion (Blake, 1983a).

The Q-S model is relatively simple to implement. The underlying assumption of the Q-S model is that the flow around the oscillating tail/hydrofoil at any given instant in time t is equivalent to the flow around a steady foil with the same kinematic foil and flow conditions (in particular, the same angle of attack, α and free-stream velocity, U_∞). If this assumption holds, then classical “steady” hydrodynamic theory can be used to predict the forces generated by the tails of carangiform fish. For example, based on the Q-S model, the lift generated by the oscillating, or unsteady foil can be predicted from the instantaneous angle of attack profile, $\alpha(t)$, since according to classical aerodynamic theory, the lift force produced by a lifting surface is proportional to $\sin \alpha$. A more detailed discussion on the quasi-steady model, applied to unsteady foils, is provided in Chapter 3, however, for a general description of the quasi-steady theory the keen reader may refer to McCroskey (1982).

1.2.1 The Q-S model applied to hovering insects

Historically, in the realm of biological propulsion, the quasi-steady model has been used extensively in the study of the flight of hovering insects at low Reynolds numbers. In these studies, the Q-S model has played a major role in providing evidence that hovering insects use unsteady flow mechanisms to generate larger-than-expected lift forces.

In an early study, Weis-Fogh (1972) applied the Q-S model to the observed flight kinematics of hovering hummingbirds and fruit flies at $Re \approx 100 - 10,000$. Based on the quasi-steady model, Weis-Fogh calculated the lift coefficients of hummingbirds and fruit flies to be $C_L = 1.8$ and $C_L = 0.8$ respectively, which was sufficient to lift the weight of these creatures. Weis-Fogh therefore concluded that the Q-S model is sufficient to explain the flight of these creatures.

In a later study, Weis-Fogh (1973) applied the Q-S model to a larger range of hovering animals. Weis-Fogh discovered that for the majority of investigated animal species, the forces predicted using the Q-S model is sufficient to explain the flight behaviour of these animals. However, for the case of a wasp actively flying at very low Reynolds numbers of $Re \approx 10 - 20$, the lift force predicted using the Q-S model is less than the weight of the wasp, leading to suggestions that the wasp uses unsteady flow mechanisms to generate larger-than-predicted lift forces during free-flight.

1.2 Background

In a comprehensive study of hovering insects, Ellington (1984b) rejected the applicability of the quasi-steady theory on modelling hovering insect flight. Using kinematic observations of Hoverflies in particular, Ellington estimated that the forces developed by the Hoverfly wings, based on the quasi-steady model, is insufficient to generate the required lift forces to balance the weight of the fly. Instead, Ellington advocates that the wings of flying insects augment force production using unsteady flow mechanisms. Without providing substantial evidence, Ellington suggests that these unsteady mechanism may consist of the generation and control of strong vortical structures during wing rotation, and the development of large vortices on the leading edge of the wing during the translation. Ellington proposes that the flow around the leading edge vortex reattaches close to the trailing edge of the wing, resulting in a separation bubble close to the surface of the wing which possibly increases the effective camber of the wing. Furthermore, Ellington draws parallels between the leading edge vortices developed by insect wings, and the “dynamic stall” or “delayed stall” mechanism observed in airfoils, whereby an airfoil at large angles of attack can generate large, short-duration forces prior to stalling (McCroskey, 1982).

Although Ellington’s experiments provide some evidence of both the invalidity of the Q-S model when applied to hovering insects, and the possible use of unsteady flow mechanisms by hovering insects, Ellington does not provide direct force measurements. Dickinson and Gotz (1993) attempted to address this lack of force measurements by directly measuring transient forces produced by a fully submerged thin flat plate which was impulsively started from rest at a fixed angle of attack at low $Re \approx 100 - 400$. These experiments were further extended by Dickinson (1994) to include periodic stopping and rotating of the flat plate, which approximates the flapping motion of hovering insect wings. These experiments indicated that the transient forces developed by the flat plate has complex time histories, which are not consistent with the classical quasi-steady model. In particular, it was discovered that the flat plate can generate large instantaneous forces during the beginning of its stroke, exceeding quasi-steady estimates, and in particular, the Wagner effect. These large lift forces coincide with the development of strong leading edge vortices by the wing, providing more evidence that insects use unsteady flow mechanisms to augment force production.

In similar experiments, Sane and Dickinson (2001) measured the forces on an unsteady flapping wing at low $Re \lesssim 1,000$, and compared their results to Q-S model estimates. Sane and Dickinson reported that the experimentally-measured time-averaged lift and drag coefficients are both larger than Q-S estimates. Furthermore, based on the force measurements, they also concluded that the Q-S model significantly overestimates the aerodynamic efficiency of the unsteady wings.

Usherwood and Ellington (2002a) measured the instantaneous forces on an impulsively started two-bladed propeller at $Re \approx 8,000$. The blades of the propeller were modelled on the plan-form shape of hawkmoths. They discovered that the vertical force (which can be interpreted as “thrust”) coefficients developed by the propeller could be relatively high, in excess of $C_t \gtrsim 1.5$, particularly when the angles of attack were large ($\alpha \gtrsim 40^\circ$). They also discovered that the vertical force coefficient was larger during the start of the propeller rotation, at which time leading edge vortices were observed. This further reinforces the link between the generation of leading edge vortices, and the augmentation of propulsive forces.

Leading edge vortices were also observed in experiments by Birch and Dickinson (2003), who performed simultaneous particle image velocimetry and strain gauge force measurements on an insect-inspired unsteady wing at low $Re \approx 160$. Birch and Dickinson observe a peak in instantaneous force measurements during the beginning of the translation of the wing, which coincided with the onset of generation and growth of a large leading edge vortex by the wing.

Wu and Sun (2004) used computational fluid dynamics to investigate the flow around a model of a flapping fruit fly wing at low Reynolds numbers ($Re \approx 20 - 1,800$). They numerically solved the 3D Navier-Stokes equations, and obtained estimates for the transient lift and drag coefficients produced by the model. Their results show good agreement when compared to force measurements of insect-inspired wings published by Usherwood and Ellington (2002b), and show that the time-averaged lift coefficients can be relatively large, $C_L \approx 1.9$, when the angles of attack were large ($\alpha \gtrsim 45^\circ$). These large time-averaged lift coefficients, which are typically 2-3 times larger than Q-S estimates, are due to the large instantaneous lift forces generated during the middle portion of the half-stroke cycle. During this phase of the wing stroke, Wu and Sun observe a large vortical structure which remains attached to the leading edge of the wing.

Pullin and Wang (2004) studied the time-dependent forces on an impulsively started, accelerating wing numerically and analytically by modelling the wing as a 2-D flat plate in an inviscid flow. Their results indicate that the transient forces generated by the wing are dependent on the time-histories of the wing dynamics, and hence the quasi-steady assumption is wholly invalid. Furthermore, they obtain non-zero forces just after the wing is impulsively started, where $U_\infty \approx 0$, leading to very large thrust coefficients at the beginning of the wing acceleration. Pullin and Wang suggest that this could be linked to the large thrust coefficients generated by unsteady wings at the beginning and end of the flapping half cycle, as observed in Dickinson (1994).

Okamoto and Azuma (2005) measured the instantaneous forces and moments acting on an unsteady flat plate of various profiles at $Re < 10,000$. They conclude that the time-averaged lift forces generated by the flat plate are very large when the heave amplitude is large. They relate

1.2 Background

these large forces to the leading edge flow separation which occurs when the heave amplitude, and hence, the angle of attack is large. Furthermore, Okamoto and Azuma also report that the strength of the leading edge vortex, and the lift coefficient developed by the unsteady flat plate, increases when the leading edge of the flat plate is sharpened.

Based on the mounting evidence, it is then clear that at low Reynolds numbers, hovering insects use unsteady flow mechanisms to generate forces. This is highlighted by the fact that the Q-S model has been shown to be insufficient to explain the observed dynamics of various flying insects (Ellington, 1984b; Maxworthy, 1981) and the measured transient forces on wing-like apparatus (e.g. Dickinson, 1994; Wu and Sun, 2004). The evidence suggests that the larger-than-expected forces developed by hovering insects are due to the exploitation of unsteady flow mechanisms, including the generation and development of large leading edge vortices (Dickinson *et al.*, 1999; Sane, 2003; Wang, 2005). It has further been suggested that without the growth of the leading edge vortex, the Q-S theory may be sufficiently accurate to effectively model insect propulsion (Sane and Dickinson, 2002; Birch and Dickinson, 2003).

However, the use of unsteady flow control has only been demonstrated for hovering insects at low Reynolds numbers. Although there has been suggestions that these unsteady flow mechanisms may be valid at larger Reynolds numbers (Usherwood and Ellington, 2002b), it remains unclear if swimming carangiform fish, whose tails have different kinematic motions than the wings of hovering insects, employ unsteady flow mechanisms to generate efficient propulsion.

1.2.2 Unsteady flow control in carangiform propulsion

In the study of hovering insects, there is ample evidence indicating that hovering insects can use unsteady flow mechanisms to augment thrust. However, in the study of carangiform locomotion, the current literature is not as abundant. Nonetheless, there has been some evidence of the use of unsteady flow control by steadily swimming carangiform fish.

In a landmark paper, Gray (1936) estimated the power output of observed steadily swimming dolphins by assuming that the drag on an actively swimming dolphin is equal to the drag produced by an equivalent rigid model of a dolphin towed at the same speed, under turbulent flow conditions. Gray discovered, based on this power output estimate, that the muscles of the observed steadily swimming dolphins would have to produce more than seven times the power (per unit muscle mass) of other mammals, leading to the proposition that dolphins may use unsteady flow mechanisms to reduce drag. Kramer (1960) suggested that this discrepancy is due to the compliant outer skin of dolphins, which may act as a “damper of turbulence energy”, and thus may be capable of relaminarising the boundary layer of an actively swimming dolphin.

Many decades later, this relaminarisation mechanism was also observed in experiments by Techet (2001). Techet studied the near-boundary flow around a mechanical robotic tuna (Robo-Tuna) and around a waving plate at high Reynolds numbers and found that the undulatory motion of the robotic tuna and the waving plate can relaminarise the boundary layer and reduce the turbulence when the ratios of the wavespeed of the undulations to the flow speed is approximately 1.1 - 1.4.

In an altogether different experiment, Webb (1971) measured the body geometry and recorded the swimming kinematics of trout. The drag on the swimming trout was estimated by adding loads (in the form of appendages) with known drag coefficients to the swimming trout and subsequently recording the resultant tail kinematics. The no-load drag was then obtained by extrapolation from these results. The drag on the swimming fish was then used to estimate the power output of the swimming trout. This experimentally estimated power output was compared with theoretical predictions using the quasi-steady model, which was developed by Taylor (1952), and an inviscid model, developed by Lighthill (1970). Webb reports that experimentally estimated power outputs were not comparable with the Q-S model, while Lighthill's inviscid model over-estimated trout power output by up to 50%.

Videler and Kamermans (1985) recorded the tail kinematics of swimming dolphins, and subsequently used the quasi-steady model to estimate the forces generated by the tails of these dolphins. It was found that the forces estimated using the Q-S model are as little as 20% of the thrust forces required to generate the measured acceleration of the dolphin, implying that the quasi-steady assumption is invalid.

Tuncer and Kaya (2005) numerically solved the Navier-Stokes equations for the 2D flow around an unsteady NACA 0012 foil at $Re = 10,000$. Their results demonstrate that large time-averaged thrust coefficients can be generated by the unsteady foil at large heave amplitudes, where large leading edge vortices are observed. On the other hand, propulsive efficiencies can be increased by reducing the heave amplitude and maximum angle of attack, α_{max} , which in turn reduces the strength of the leading edge vortices.

In an important experiment, Triantafyllou *et al.* (1993) performed a linear stability analysis on the wake of a heaving and pitching hydrofoil. They showed that the wake of the unsteady foil is convectively unstable, and is strongly governed by the Strouhal number, St (see Equation 1.3). In particular, they found that the “maximum spatial amplification of vortical structures” in the wake occurs when $0.25 < St < 0.35$. Interestingly, based on a survey of published data on carangiform swimmers, they found that the majority of the carangiform swimmers tended to swim within this St range as well. This leads to the hypothesis that an unsteady foil develops thrust most efficiently within $0.25 < St < 0.35$, and furthermore, that carangiform swimmers

1.2 Background

tend to optimise propulsion for efficiency. Triantafyllou *et al.* (1993) further reinforced the importance of St on the kinematics of the unsteady foil by plotting the thrust coefficient measurements, based on their experiments as well as the experiments by Isshiki and Murakami (1984) and Koochesfahani (1989), which all show similar trends with respect to St . Triantafyllou *et al.* (1993) also measured the transient forces generated by the unsteady foil, and showed that propulsive efficiencies were generally low, peaking at $\eta \approx 20\%$. This peak was shown to roughly coincide with the range $0.25 < St < 0.35$.

The importance of the Strouhal number was also observed in similar experiments by Anderson *et al.* (1998). Anderson *et al.* performed PIV and force measurements on a NACA 0012 flapping hydrofoil at $Re \approx 40,000$ and discovered that the unsteady foil can produce thrust at high propulsive efficiencies, $\eta_F \approx 85\%$. This optimal development of thrust occurs in the range of $0.25 < St < 0.4$, and at relatively large angles of attack, $\alpha_{max} \approx 15 - 25^\circ$, where flow visualisation indicates that the foil generates large leading edge vortical structures. The results of Anderson *et al.* also indicate that the thrust coefficient increases as St increases, and compares well to linear and nonlinear inviscid theory for $St < 0.3$. These results are further corroborated in very similar experiments on heaving and pitching hydrofoils by Read *et al.* (2003), who obtained peak propulsive efficiencies of $\eta_F \approx 72\%$. This peak was shown to occur at $St \approx 0.16$ and $\alpha_{max} \approx 15^\circ$.

Wang (2000) used a finite difference scheme to solve the two-dimensional incompressible Navier-Stokes equations for a purely heaving wing of elliptical cross-section at $Re = 100 - 10,000$. Wang presented time-averaged thrust coefficients and propulsive efficiencies of the unsteady wing in terms of the trailing edge Strouhal number, St and chord-based Strouhal number, St_c . The results indicate that C_t and η_F peak at $St_c \approx 0.7$, regardless of St_h , contradicting results by (Anderson *et al.*, 1998; Read *et al.*, 2003). Wang's results also indicate that propulsive efficiencies are typically low, below $\eta_F \lesssim 10\%$ in the range of $0.15 < St < 0.25$.

Barrett *et al.* (1999) studied the forces on a fish-like robot with an oscillating tail (the RoboTuna) at large $Re \approx 1,000,000$ with an artificially tripped turbulent boundary layer, and found that the undulating fish-like robot can reduce its drag up to 70% when compared to the same body towed rigid. This drag reduction occurs when $0.12 < St < 0.35$, and when the wavespeed of the undulating body exceeds the speed of the body. Also, Barrett *et al.* found that maximum drag reduction occurs when $14^\circ \lesssim \alpha_{max} \lesssim 25^\circ$, and when the trailing edge amplitude, A_{te} is large. The drag reduction is explained in terms of relaminarisation of the boundary layer and the control of body-shed vortices by the caudal tail to create a reverse Karman vortex street (the reverse Karman vortex street is discussed in Section 1.2.3).

This notion of vorticity control by unsteady fish-inspired foils, and by extension, carangiform propulsion, has recently emerged as the dominant theory behind the failure of the Q-S model, and the performance of aquatic propulsion (Anderson *et al.*, 1998; Dickinson, 1996; Fish and Lauder, 2006; Triantafyllou *et al.*, 2000, 2002, 2004; Zhu *et al.*, 2002). This follows studies by Tokumaru and Dimotakis (1991), who showed that the drag on a rotating cylinder can be reduced by controlling the vortex shedding behind the cylinder at particular non-dimensional frequencies.

Furthermore, evidence of the capability of an unsteady foil to extract energy by the control of vortices was shown in experiments by Gopalkrishnan *et al.* (1994). Based on visualisation of the flow around an oscillating foil behind a D-section cylinder at low $Re = 550$, Gopalkrishnan *et al.* show that the flapping foil can control and reposition the incoming vortices resulting in three distinct wake modes. In mode 1, dubbed the “expanding wake”, the wake consists of vortices shed by both the cylinder and the flapping foil, which do not combine. In mode 2, named “destruction interaction”, the incoming vortices shed by the cylinder combine destructively with vortices of opposite rotational sign shed by the oscillating foil. The resultant wake behind the foil then consists of vortices of very small strengths. In mode 3, called “constructive interaction”, the vortices generated by the cylinder combines with vortices of similar rotational sign shed by the flapping foil, resulting in a wake containing vortical structures of large circulation. Gopalkrishnan *et al.* also performed force measurements of the flapping foil behind the D-section cylinder at larger $Re = 20,000$, which indicates that peaks in flapping foil propulsive efficiency occurs at approximately the same conditions that result in mode 2. Using an inviscid numerical model of Gopalkrishnan *et al.*’s experiment, Streitlien *et al.* (1996) estimate that the flapping foil behind a D-cylinder can achieve propulsive efficiencies greater than 100%. Using a similar setup as Gopalkrishnan *et al.*, Beal *et al.* (2006) showed that a flapping foil in the wake of a bluff body can generate forces at negative power, that is, the foil is capable of extracting energy from the shed vortices in the bluff body wake.

Wolfgang *et al.* (1999) performed flow visualisation on a swimming giant danio using planar particle image velocimetry. They also compared the experimental results with the results from a numerical model of the swimming danio. Based on the experimental and numerical wake vorticity patterns, Wolfgang *et al.* concluded that the generation of efficient thrust by the swimming giant danio is inextricably linked to the control and shedding of wake vortices. Their results also indicate that the fish tend to swim within the range $0.25 \lesssim St \lesssim 0.4$, providing further evidence linking this critical Strouhal number range, the use of vorticity control, and the generation of efficient thrust in aquatic propulsion.

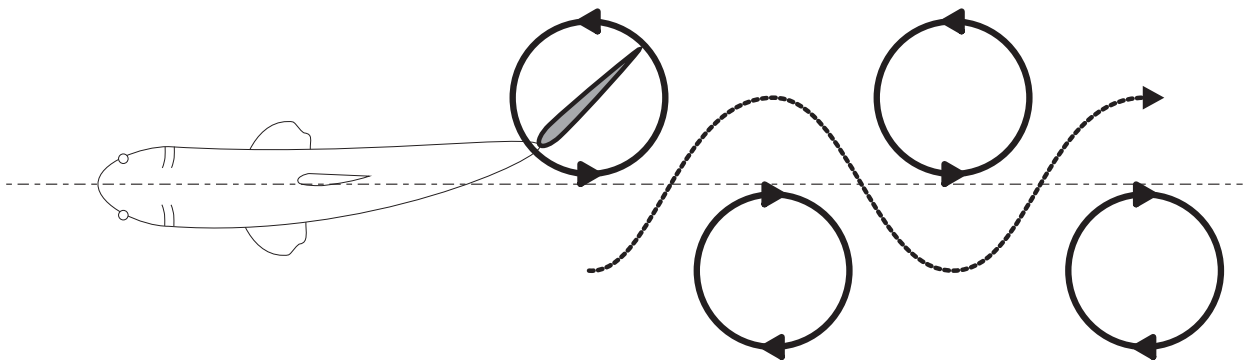


Figure 1.2: Reverse Karman street behind a swimming carangiform

1.2.3 Unsteady foil wake patterns

Thus far, we have focused our discussion on the dynamics of unsteady foils, and the possible use of unsteady flow mechanisms by steadily swimming carangiform fish. However, we have neglected to take into account the wake dynamics of the unsteady foil. An investigation of the foil wake dynamics can be useful on two fronts. Firstly, an investigation of the unsteady foil wake dynamics can provide indirect information on the forces generated by the oscillating foil. Secondly, the wake patterns behind the foil may also provide evidence that an oscillating foil is capable of unsteady flow control. This is due to the fact that the postulated vorticity control by unsteady foils will eventually have an affect on the vorticity distribution in the wake of the foil.

In the various flow visualisation studies on carangiform locomotion, it has largely emerged that the wake of an actively swimming carangiform fish consists of an alternating row of counter-rotating vortices, arranged in a zig-zag pattern (Aleyev, 1977; Videler, 1993). This is called a reverse Karman vortex street, and is illustrated in Figure 1.2. The rotational directions of these shed vortices implies that there is a wavy jet in the wake, and hence there is a nett momentum excess in the wake leading to the development of positive thrust forces by the unsteady foil. In flow visualisation experiments (using particle image velocimetry) on a steadily swimming mullet, Muller *et al.* (1997) observe that these wake patterns are induced by the motions of the carangiform caudal tail, or more explicitly, the vortices shed into the wake are shed corresponding to the location of the tail trailing edge. These vortices are then assumed to be generated by the motion of the carangiform tail, and are interpreted as a combination of “starting” and “stopping” vortices, shed once per half-cycle, consistent with classical aerodynamic theory (Dickinson, 1996; Lighthill, 1969; Videler, 1993; Vogel, 1996).

In recent studies of unsteady foils and carangiform locomotion, the reverse Karman street wake pattern has been associated with the development of thrust optimised for efficiency (Triantafyllou *et al.*, 2002). In numerical studies on flapping foils, Streitlien *et al.* (1996) reports that the

size of the wake, or the size of the wavy jet in between the wake vortices, can play a major part in the dynamics of the foil. When the width of the wake is large, the unsteady foil tends to generate large time-averaged thrust coefficients, however when the width of the wake is small, the unsteady foil generates low thrust at high propulsive efficiency. In the study of the flow patterns of a swimming giant danio by Wolfgang *et al.* (1999), it was suggested that the actively swimming fish generates optimal thrust by the appropriate selection of the frequency and spacing of these wake vortices.

Anderson *et al.* (1998) performed flow visualisation on a NACA 0012 flapping foil at $Re \approx 1,100$ and correlated the optimal thrust production of a heaving and pitching foil with the development of foil leading edge vortices, which flow downstream and combine with the vortices generated by the trailing edge of the foil to produce a wake in the shape of a reverse von Karman vortex street. Anderson *et al.* thus conclude that the reverse Karman street wake pattern is associated with high propulsive efficiencies. In similar experiments consisting of flow visualisation and force measurements of oscillating foils by Read *et al.* (2003), it was found that the propulsive efficiency of the unsteady foil is strongly related to the wake structure behind the foil, although they do not explicitly clarify the nature of this relationship.

There is also some indication that the wake patterns behind an unsteady foil are not limited to the reverse Karman vortex street. In flow visualisation experiments on simultaneously translating and pitching foils at $Re = 1500 - 10,000$, Ohmi *et al.* (1990) and Ohmi *et al.* (1991) observe that a number of qualitatively different flow patterns are possible. They classify the wake patterns into four different regimes, and report that the two main governing parameters which determine the foil wake pattern are the pitch amplitude, θ_0 and the chord-based Strouhal number, St_c . In separate flow visualisation experiments on unsteady foils, Anderson *et al.* (1998) classified the various wake patterns of the foil into six different regimes, which were found to be strongly correlated with the St (based on the peak-to-peak trailing edge amplitude of the foil) and the maximum instantaneous angle of attack of the foil, α_{max} .

Meanwhile, in similar experiments on oscillating foils by Hover *et al.* (2004), it was found that the wake patterns are related to the profile of the instantaneous angle of attack, $\alpha(t)$. For any given Strouhal number, Hover *et al.* discovered that the resultant wake pattern is subtly different for different angle of attack profiles, which also corresponded to different measurements of unsteady foil thrust and propulsive efficiency.

In three dimensional dye flow visualisation of a heaving and pitching hydrofoil at $Re \approx 160$, von Ellenrieder *et al.* (2003) reveal that the 3D wake pattern behind the foil is highly complex, and is a function of St , θ_0 and in particular, the phase between the heaving and pitching motions, ψ . In numerical simulations of von Ellenrieder *et al.*'s experiments, Blondeaux *et al.* (2005)

1.2 Background

interpret the 3D wake patterns behind the oscillating foil as a combination of vortex-ring-like structures consisting of leading edge vortices which connect with trailing edge vortical structures of opposite rotational direction. Using dye flow visualisation, Buchholz and Smits (2006) observed the flow around a purely pitching rigid flat plate with a span-to-chord ratio of 0.54 and a Strouhal number of $St \approx 0.23$ in a constant free-stream. The Reynolds numbers for these experiments were $Re_c = 640$. Buchholz and Smits interpret the three-dimensional flow in the wake as consisting of a series of horse-shoe vortices of alternating sign, shed twice per flapping cycle. The discrete horse-shoe vortices shed per half flapping cycle are observed to evolve and interact with the vortical structures downstream of the wake, whereby vorticity of like-sign are observed to merge. Buchholz and Smits observe that this wake model is robust with respect to variations in the Reynolds number, aspect ratio, and pitching amplitude, although the ranges of these parameters were not explicitly defined.

Young and Lai (2004) studied the flow around a purely heaving foil by numerically solving the 2-D Navier-Stokes equations. Based on the positions and rotational directions of the vortices shed from the leading and trailing edges of the oscillating foil, they classify the wake into three patterns, namely, a “drag” wake, a “neutral” wake and a “thrust” wake. They discovered that although the structure of the wake and the corresponding forces developed by the foil are strongly governed by St , it is not the single parameter controlling the flow. Furthermore, Young and Lai also note that the generation of forces by the foil is strongly governed by the flow around the leading edge of the foil.

These differing observations of wake patterns behind unsteady foils are compounded by the findings of Videler *et al.* (1999), who report that in some cases the wakes of swimming fish need not consist of a reverse Karman street, but may also consist of two vortices of opposing sign shed per tail half cycle. At present, it remains unclear why fish may generate different wake patterns, and if the reverse Karman street is truly linked with the optimal propulsion of aquatic locomotion. It also remains unclear if the reverse Karman vortex street is evidence of unsteady flow control by aquatic swimmers, and if there is a clear link between the tail/foil kinematics and the wake patterns generated.

1.2.4 Observed fish kinematics in the literature

At this stage it would be prudent to obtain kinematic data on actual carangiform swimmers, rather than dispense conjecture on the appropriate tail kinematics for optimal locomotion. To achieve this, we perform a review of existing published literature on the kinematics of observed steadily swimming carangiform fish.

A number of decades ago, Webb (1971) recorded the swimming kinematics of steadily swimming trout in a water channel and report that the kinematic tail parameter $f \times A_{te}$ varied linearly with the steady swimming speed. Based on these trends, it is estimated that the resultant Strouhal number is approximately $St \approx 0.3 - 0.45$. In similar experiments using two different carangiform fish species, the tiger musky and rainbow trout, Webb (1988) discovered that in both species of fish, steady swimming coincided with Strouhal numbers in the range of $0.2 \lesssim St \lesssim 0.4$.

Fish (1993) recorded the steady swimming kinematics of trained bottlenose dolphins swimming in a large tank. The results of the recordings indicate that the dolphins tended to swim with a large range of maximum instantaneous angles of attack, $\alpha_{max} \approx 5^\circ - 30^\circ$. Furthermore, Fish's results also indicate that the dolphins had an approximately fixed trailing edge amplitude, while the flapping frequency was approximately linearly proportional to the swimming velocity. From these results, it is estimated that the dolphins typically swam at $0.23 \lesssim St \lesssim 0.44$. On the other hand, in a study by Videler and Kamermans (1985) on dolphins, they report that the steadily swimming dolphins swam with a pitch amplitude of $\theta_0 \approx 20 - 30^\circ$ and at low maximum instantaneous angles of attack $\alpha_{max} \approx 0 - 8^\circ$, regardless of swimming velocity. These results are consistent with the observations in a similar experiment by Fish (1998), who recorded the swimming kinematics of a range of steadily swimming cetaceans. Fish observed that the cetaceans consistently swam with tail pitch amplitudes in the range $\theta_0 \approx 20 - 40^\circ$, at Strouhal numbers of $St \approx 0.19 - 0.33$. Based on these values, it is estimated that the maximum angle of attack is low, $\alpha_{max} \lesssim 10^\circ$. Observations on swimming cetaceans were greatly expanded by Rohr and Fish (2004), who also found a similar trend, where most of the swimming cetaceans tended to swim within the range of $0.2 < St < 0.35$, regardless of species, size, and swimming speed.

Lowe (1996) used a video camera to record the tail kinematics of juvenile hammerhead sharks steadily swimming in a recirculating water channel at $Re \approx 3.2 \times 10^5$. Lowe discovered that the shark tail-beat frequency, f , is an approximately linear function with the swimming speed, while the tail-beat amplitude, A_{te} , is relatively constant within the range of investigated swimming speeds. This results in a constant value of $St \approx 0.27$, regardless of the shark swimming speed. Muller *et al.* (1997) used particle image velocimetry to quantitatively study the wake of a steadily swimming mullet, at $Re \approx 20,000$. The results of Muller *et al.* indicate that the mullet swam at a Strouhal number of $St \approx 0.34$. Dowis *et al.* (2003) recorded the steady swimming kinematics of Pacific bonito, and discovered that the fish tail flapping frequency was approximately linearly proportional to the swimming speed, while the tail amplitude was relatively constant. From their results, it is estimated that the bonito swam within the range $St \approx 0.23 - 0.26$.

1.2 Background

Creature	Observed Wing/Tail Strouhal Number, St_{te}	Reference
Trout	$\approx 0.3 - 0.45$	Webb (1971)
Sockeye Salmon	$\approx 0.27 - 0.45$	Webb (1973a)
Tiger Musky and Rainbow Trout	$\approx 0.2 - 0.4$	Webb (1988)
Bottlenose Dolphins	$\approx 0.23 - 0.44$	Fish (1993)
Juvenile Hammerhead Sharks	≈ 0.27	Lowe (1996)
Mullet	≈ 0.34	Muller <i>et al.</i> (1997)
Cetaceans	$\approx 0.19 - 0.33$	Fish (1998)
Pacific Bonito	$\approx 0.23 - 0.26$	Dowis <i>et al.</i> (2003)
Various Birds, Bats and Insects	$\approx 0.2 - 0.4$	Taylor <i>et al.</i> (2003)
Cetaceans	$\approx 0.2 - 0.35$	Rohr and Fish (2004)

Table 1.2: Summary of observed Strouhal numbers of swimming and flying creatures

In a study of the effect of caudal fin amputation on the steady swimming kinematics of sockeye salmon, Webb (1973a) reports that for the majority of tested cases (approximately 90%), the salmon chose to swim in the range $0.27 \lesssim St \lesssim 0.45$. Reynolds numbers were in the range of $2.7 \times 10^4 \lesssim Re \lesssim 1.34 \times 10^5$.

The ubiquitous usage of tail kinematics within the range $St \approx 0.2 - 0.4$ is not limited to aquatic propulsion. Taylor *et al.* (2003) performed a survey of existing literature on 42 species of flying creatures, consisting of birds, bats and insects that were observed to fly at steady speed. They found out that approximately 75% of the species flew steadily in the range of $0.19 < St < 0.41$, regardless of cruising velocity or wing size.

Based on this evidence, it is then clear that most carangiform fish tend to swim at the Strouhal number range roughly corresponding to $St \approx 0.2 - 0.4$. However, it remains uncertain why carangiform fish choose to swim within this critical range. Possibly, this Strouhal number range may be linked with the observations of the “free” (that is, unforced) shedding of vortices behind bodies such as a sphere (Williamson and Roshko, 1988; Nakamura, 1996), or an airfoil (Breuer and Jovicic, 2001), whereby the vortices shed into the wake have a spacing and frequency that

results in $St \approx 0.2$. Alternatively, another possible explanation of the fact that aquatic animals tend to swim at $St \approx 0.2 - 0.4$ may lie in the concept of the “optimal development of vortical structures” - a concept which is further explained in the following section.

1.2.5 Formation number

In a fundamental study of the nature of vortex ring formation, Gharib *et al.* (1998) pushed a column of water of length L through a circular orifice of diameter D into a tank of still water and discovered that the vortex ring generated reaches a maximum circulation at a particular dimensionless number called the “formation number” or the “formation time”, FN . In the case of their experiment, it was discovered that this formation number is solely defined by the geometry of the apparatus, such that $FN = \frac{L}{D}$, whereby the vortex ring reaches a maximum circulation at the range $FN \approx 3.6 - 4.5$. Beyond this non-dimensional formation number, the leading vortex ring “pinches off”, and any remaining vorticity generated by the jet is fed into a trailing shear layer-like structure. As the leading vortex ring does not receive any more vorticity, it reaches its maximum circulation at $FN \approx 4$.

This concept of “formation time” was shown to be applicable to the flow around bluff bodies in experiments by Jeon and Gharib (2004). Jeon and Gharib performed an experiment consisting of a cylinder of diameter D impulsively started from rest in a still body of fluid. The vorticity generation process behind the cylinder was observed to occur symmetrically during the early stages of the cylinder translation. However, at a non-dimensional formation number of $FN = \frac{L}{D} \approx 4$, where L is the distance traveled by the cylinder, it was found that the vortex generation process shows signs of asymmetry. During this onset of asymmetry, the vortical structures behind the cylinder achieve maximum circulation, and any further vorticity generated at the boundary of the cylinder is fed into separate vortical structures.

In further studies on the premise of “formation time”, Milano and Gharib (2005) performed an experiment using a translating and rotating flat plate in a body of motionless fluid. Milano and Gharib automated the experiment, varying the kinematic properties of the plate to maximise the measured lift component. They discovered that for most of the cases where the flat plate generated high lift values, these occurred when the formation number of the flat plate, defined as the ratio of the horizontal distance traveled by the plate leading edge and the projected chord length, was between $FN \approx 3.6 - 4.6$. At this formation number range, it was also observed that the leading edge vortices generated by the flat plate reached their maximum circulation before shedding off the plate into the wake.

1.3 Aims

These initial experiments suggest that, depending on how the fluid flow is manipulated, vortical structures of maximal circulation can be generated. In the case of an unsteady flat plate, this optimal generation of vortical structures has been shown to be linked with the development of large lift forces. Thus, it has been suggested that efficient thrust in aquatic locomotion may be developed if fish generate vortical structures of maximal circulation (Linden and Turner, 2001, 2004; Dabiri *et al.*, 2006). If so, it is also possible that there is an inherent connection between the critical Strouhal number range of $St \approx 0.2 - 0.4$ shown by carangiform swimmers, and the formation number range of $FN \approx 3.6 - 4.5$.

1.3 Aims

Based on the available literature, it is clear that there is mounting evidence to suggest that unsteady foils, and by extension, carangiform swimmers, may employ unsteady flow mechanisms (Dickinson, 1996; Fish and Lauder, 2006; Linden and Turner, 2004; Rayner, 1995; Triantafyllou *et al.*, 2000, 2004). In studies of unsteady foils, it is slowly emerging that optimal thrust is generated at $St \approx 0.2 - 0.4$, and at moderately large angles of attack, $\alpha_{max} \approx 15 - 25^\circ$ (Anderson *et al.*, 1998; Read *et al.*, 2003). In a survey of steadily swimming carangiform locomotion, it was discovered that the majority of fish swam within this critical Strouhal number range, although it was also observed that fish tended to swim with their caudal tails spanning much lower angles of attack, within the range $\alpha_{max} \lesssim 10^\circ$.

Even if carangiform fish do employ unsteady flow mechanisms, it is uncertain how, and under what flow conditions, this unsteady mechanism is achieved. In studies of hovering insects at low Reynolds numbers, the augmentation of lift forces by insect wings is associated with the generation of large, attached, leading edge vortices (Birch and Dickinson, 2001; Ellington, 1984b; Sane and Dickinson, 2001; Sane, 2003; Wang, 2005). As leading edge vorticity has also been observed in the studies of oscillating foils at larger Reynolds numbers, there is a possibility that carangiform swimmers employ unsteady flow mechanisms via the generation of large leading edge vortical structures. A second, not mutually exclusive, unsteady flow mechanism may be linked with the concept of the “optimal formation of vortical structures”, whereby carangiform fish may generate efficient locomotion by generating and shedding vortices of maximum possible circulation.

Nevertheless, at this stage, there is a lack of evidence to make any conclusive statements regarding the mechanism of unsteady flow control. It remains uncertain if and how unsteady flow control is employed by steadily swimming carangiform fish, and whether this unsteady flow control is strongly linked to the tail kinematics. This is further compounded by the fact that

there remains insufficient research linking the forces and propulsive efficiencies developed by an unsteady foil to the kinematics of the foil motion. Furthermore, there is a paucity of literature linking the kinematics of the flapping foil with the subsequent wake patterns produced by the foil.

Therefore, following the discussion above, the aims of this project are to investigate steady carangiform propulsion via a study of a fully immersed unsteady heaving and pitching hydrofoil in a steady flow. We also attempt to address a lack of studies on the applicability of the Q-S model on unsteady foils, which may provide conclusive evidence that oscillating foils do employ unsteady flow mechanisms to augment thrust production. Therefore, in explicit terms, the aims of this thesis are to:

1. Determine the relationship between the hydrodynamic forces and the kinematics of an unsteady foil, if any;
2. Determine the relationship between the unsteady foil wake patterns, and the kinematics of the foil;
3. Ascertain whether a pitching and heaving hydrofoil can employ unsteady flow mechanisms to augment force production;
4. Investigate the mechanics of the unsteady flow control, if it exists;
5. Determine whether the concept of “formation time” is applicable to the flow behind an unsteady foil;
6. Investigate the ubiquitous use of carangiform tail kinematics which result in the the range $St \approx 0.2 - 0.4$;
7. Classify the observed wake structures produced by the flapping foil into a generalised “wake map”.

1.4 Thesis outline

To achieve these goals we perform an extensive investigation of the flow around a simultaneously heaving and pitching hydrofoil using a combination of dye and three-dimensional hydrogen bubble visualisation, particle image velocimetry, and direct force measurements via strain gauges. The details of the foil kinematics, experimental setup, and subsequent post-processing methodology are explained in Chapter 2.

1.4 Thesis outline

In Chapter 3, we develop a quasi-steady model of a heaving and pitching hydrofoil specifically for use with this current study. The foil properties within the Q-S model were chosen to match the properties of the physical experimental hydrofoil. In Chapter 4, we report the experimentally measured foil dynamics, including the thrust coefficient and the propulsive efficiency as a function of the foil kinematics. These results are also compared to the results predicted using the Q-S model. In Chapter 5, we perform a survey of the possible wake patterns generated by the unsteady foil. We also provide a general explanation of the mechanism of generation of these patterns, and classify these wake patterns into different groups, and flow regimes. In Chapter 6, the wake of the unsteady foil is studied quantitatively using the experimentally measured PIV vorticity fields. The circulations and positions of the shed vortices are measured, and are reported as a function of the foil kinematics. We also provide a link between the foil wake patterns, and the thrust coefficients generated by the foil. The conclusions and implications of this current study, and future work, are discussed in Chapter 7.

Chapter 2

Experimental Setup and Apparatus

2.1 Introduction

This chapter outlines the equipment and techniques used to perform the experiments on the unsteady hydrofoil. This includes a discussion on the flow facility and the foil kinematic parameters used in the current experiments. We also discuss the implementation of the three experimental techniques used in the current experiments, namely, two-dimensional planar digital particle image velocimetry (PIV), direct force measurements via strain gauges, and flow visualisation using dye and hydrogen bubbles.

2.2 General description of experiments

2.2.1 Description of flow facility

All experiments were performed in a flow facility located in the Holden Laboratory in the School of Mechanical Engineering, at the University of Adelaide. The flow facility consists of a recirculating closed circuit water channel, as shown in Figure 2.1. The working section has a length of 2000 mm, and a cross section of 500×500 mm. The three sides of the working section are made of polymethyl methacrylate, or more commonly known as acrylic glass. This allows the working section to be viewed from three different directions.

The water channel is driven by a frequency-controlled centrifugal pump, which provides a uniform flow through the working section with a range of approximately 5-300 mm/s when the water channel is completely filled. However, for all experiments described in this thesis,

2.2 General description of experiments

the flow was varied between $U_{\infty} = 10 - 250 \frac{mm}{s}$, leading to $Re = 500 - 12,500$. Hydrogen bubble visualisation, as well as simultaneous force measurements and PIV were performed at $Re = 1,250 - 12,500$, while dye visualisation was performed at $Re = 500 - 3,500$.

Before the flow issues into the working section, the fluid passes through a series of flow conditioners which consists of two perforated plates, a honeycomb flow straightener and three nylon mesh screens (with a open area of 58%). Finally, the flow passes through a 4:1 two-dimensional contraction before it enters the working section.

The turbulence intensity within the working section of the water channel was measured to be 2.1% at a free-stream flow rate of 200 mm/s (Hassan, 2005).

2.2.2 Foil properties

The foil was designed based on a NACA 0026 cross section profile, with a rectangular planform of chord length, $c = 50$ mm and span, $s = 200$ mm, leading to an aspect ratio of 4. The reason for choosing this particular chord length was to balance the conflicting requirements of the PIV system, and the force measurement system. A smaller chord length allows for higher PIV spatial resolution (since a smaller sampling area can be used), however, a larger chord length allows for larger hydrodynamic forces and hence a better signal to noise ratio in the strain gauge measurements.

The aspect ratio of the investigated foil may be considered low, resulting in a flow that has significant three-dimensional effects. However, the use of devices such as end-plates to reduce these three-dimensional effects was not considered, due to the fact that the experiment was designed to mimic the flow around a fish tail, which is expected to be inherently three-dimensional as well.

The foil was placed in the water tunnel such that the distance from its mid-span centreline to the floor of the water tunnel and the free surface was always maintained at approximately 3 chord lengths. This was to ensure that the free surface and boundaries were sufficiently far away from the foil to maintain an undisturbed flow.

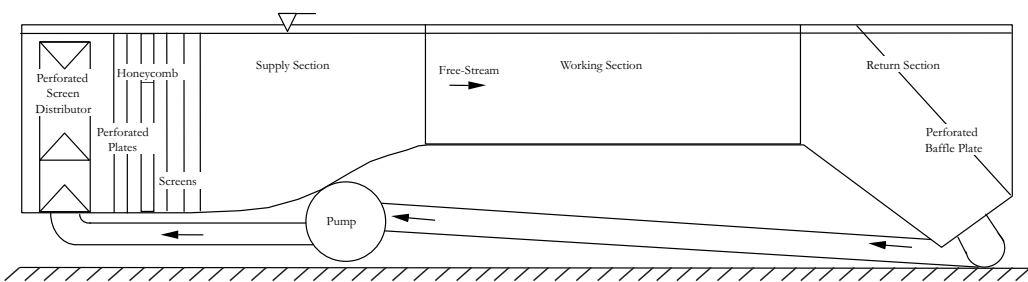


Figure 2.1: Schematic of flow facility

2.3 Foil properties and kinematics

2.2.3 Foil motion mechanism

To accomplish the required motion, the unsteady foil is driven into independent heaving and pitching using two separate stepper motors. The stepper motors are controlled using an in-house stepper motor controller, which is driven by a signal generator. The heave motor produces a side-to-side heave motion on a platform using a scotch yoke mechanism, whereas the pitch motor, which is mounted on the heave platform, rotates the foil via a simple cam-follower mechanism (see Figure 2.3).

The kinematic properties of the foil due to the pitching and heaving are discussed in more detail below.

2.3 Foil properties and kinematics

The intention of using an unsteady hydrofoil in these experiments is to mimic the motion of carangiform fish tails during locomotion. Hence, it is important that the motion of the unsteady foil be similar to the motion of the caudal fin/tail of a swimming carangiform fish. Although the exact motions of the tail of a swimming fish is, as yet, unknown, the tail motion can be approximated by a pure harmonic pitching and heaving motion (Triantafyllou *et al.*, 2000).

2.3.1 Pitching

The “ideal” pitching motion, as used in other experiments of flapping foils (e.g. Anderson *et al.*, 1998; von Ellenrieder *et al.*, 2003) is described by a pure sinusoidal motion,

$$\theta_{ideal}(t) = \theta_0 \cdot \cos \phi(t) \quad (2.1)$$

where θ_0 is the pitch amplitude and $\phi(t)$ is the flapping phase angle (in radians), which we define as

$$\phi(t) = 2\pi f t \quad (2.2)$$

where $f = \frac{1}{T}$ is the flapping frequency (in Hz), and t is time.

However, our experimental setup cannot provide us with a pure sinusoidal pitching motion. The pitching motion is created by a cam connected to a stepper motor (see Figure 2.5). The cam profile is a circle offset by a constant value A_{cam} . The follower motion is thus

$$h_{cam} = A_{cam} \cdot \cos \phi(t) \quad (2.3)$$

Following this, the amplitude of pitch oscillation, for a follower arm length of L_f is

$$\theta_0 = \arctan\left(\frac{A_{cam}}{L_f}\right) \quad (2.4)$$

Therefore, assuming the cam is infinitesimally thin, the pitching motion of the foil would be

$$\theta_{thin}(t) = \arctan\left[\frac{A_{cam} \cdot \cos \phi(t)}{L_f}\right] \quad (2.5)$$

$$= \arctan[\tan \theta_0 \cdot \cos \phi(t)] \quad (2.6)$$

However, in reality, the cam has a thickness of $2R_{ct}$, and with some mathematical manipulation it can be shown that

$$\theta_{thick}(t) = \arcsin\left[\frac{R_{ct}}{\sqrt{L_f^2 + (A_{cam} \cdot \cos \phi(t) - R_{ct})^2}}\right] + \arctan\left[\frac{A_{cam} \cdot \cos \phi(t) - R_{ct}}{L_f}\right] \quad (2.7)$$

where $\theta_{thick}(t)$ is the actual pitching motion of the foil. Note that for small R_{ct} , $\theta_{thick} \approx \theta_{thin}$. For the current experiments, the ratio of $\frac{R_{ct}}{L_f} \approx 25$. Thus, for this value, the effect of the cam thickness of the pitching profile is illustrated in 2.2 below for the case when $\theta_0 = 45^\circ$. The difference between θ_{thick} and θ_{ideal} at $\phi = 180^\circ$ is approximately 1%.

Unless otherwise specified, throughout this thesis we use $\theta(t) = \theta_{thick}(t)$.

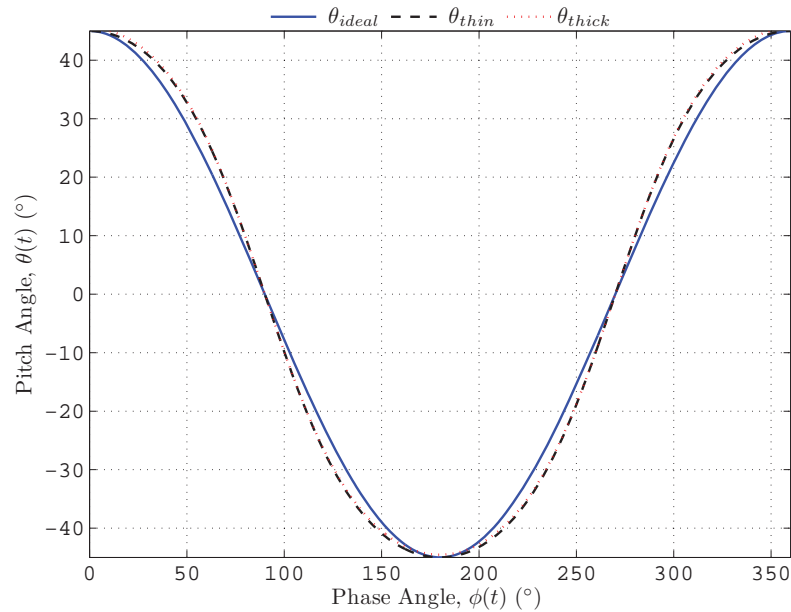


Figure 2.2: Effect of Cam Thickness on Pitching Profile ($\theta_0 = 45^\circ$)

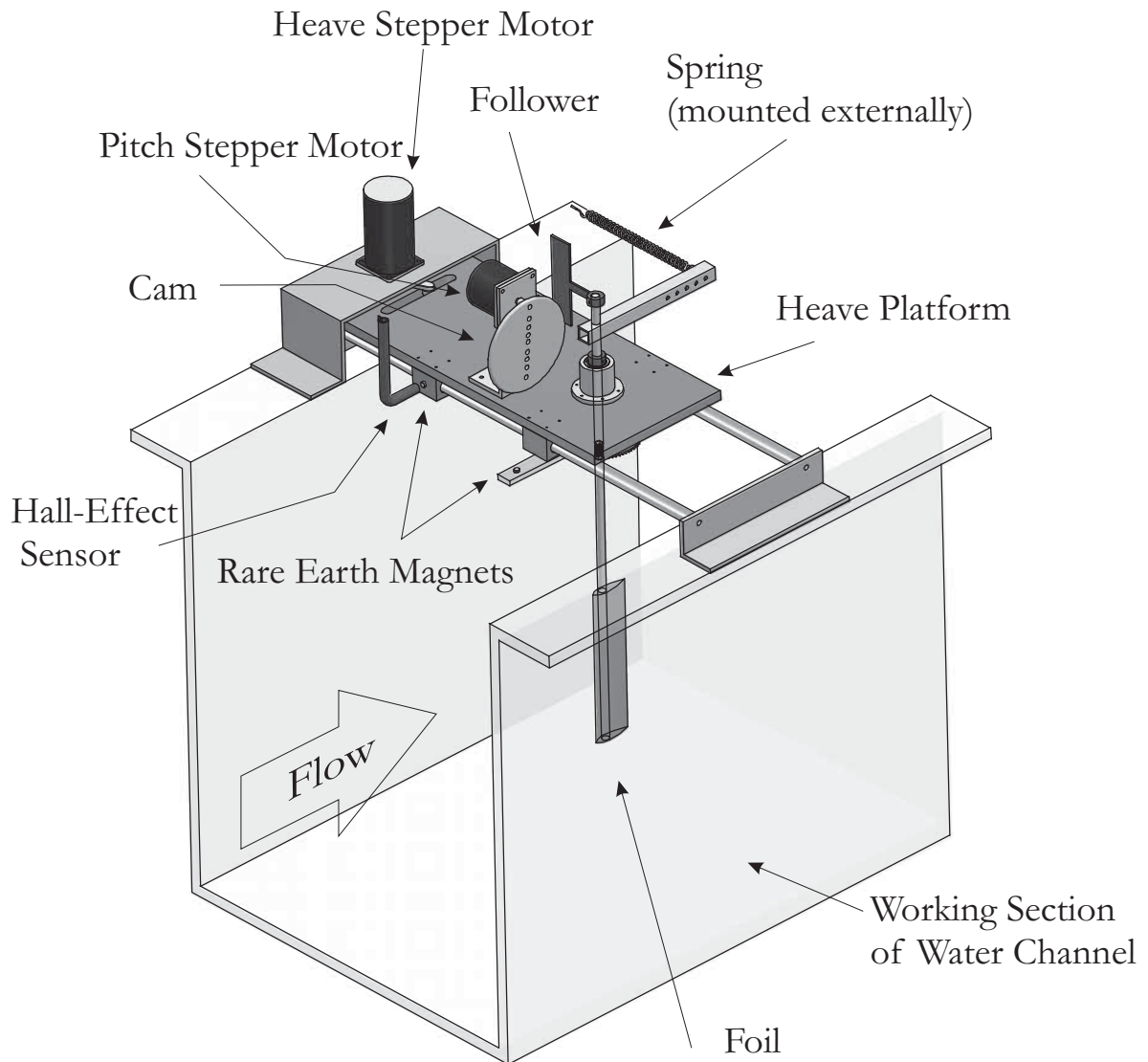


Figure 2.3: Experimental setup

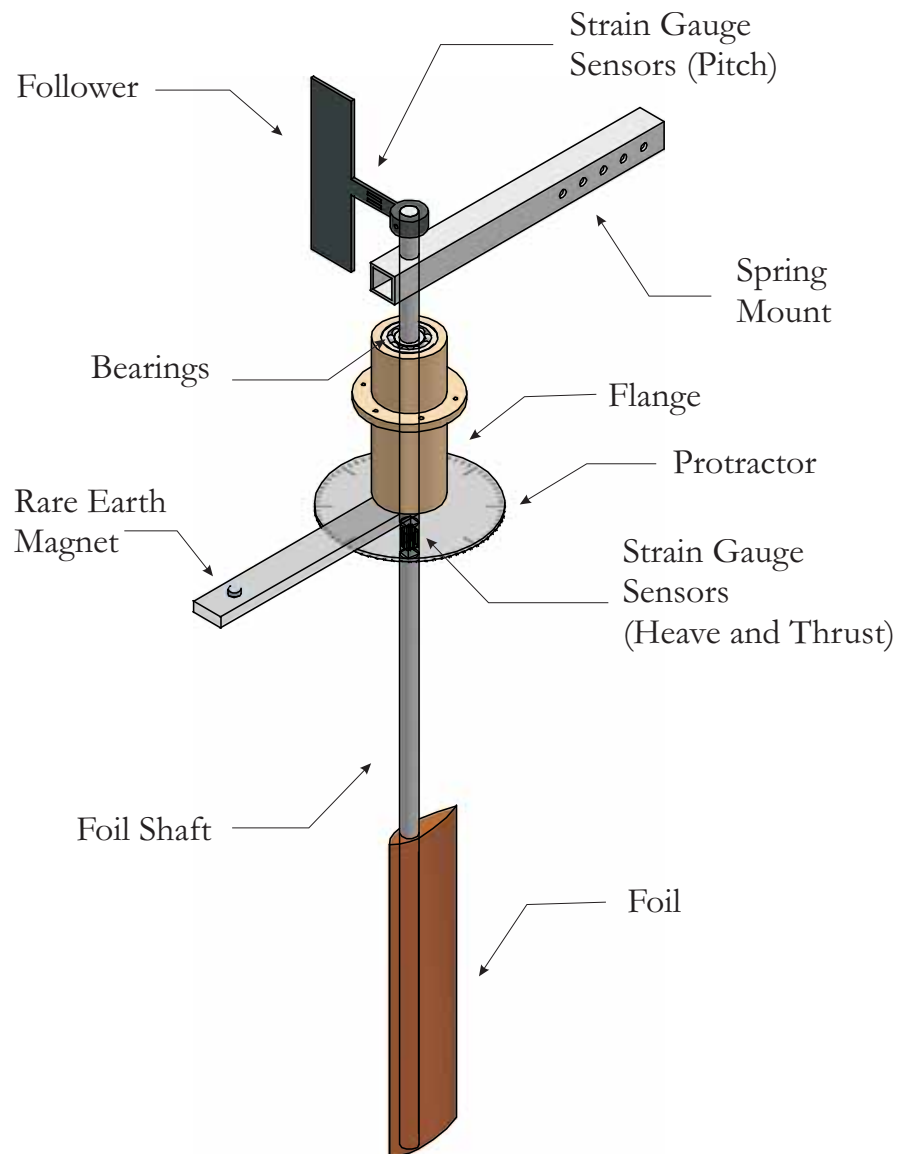


Figure 2.4: Foil mechanism

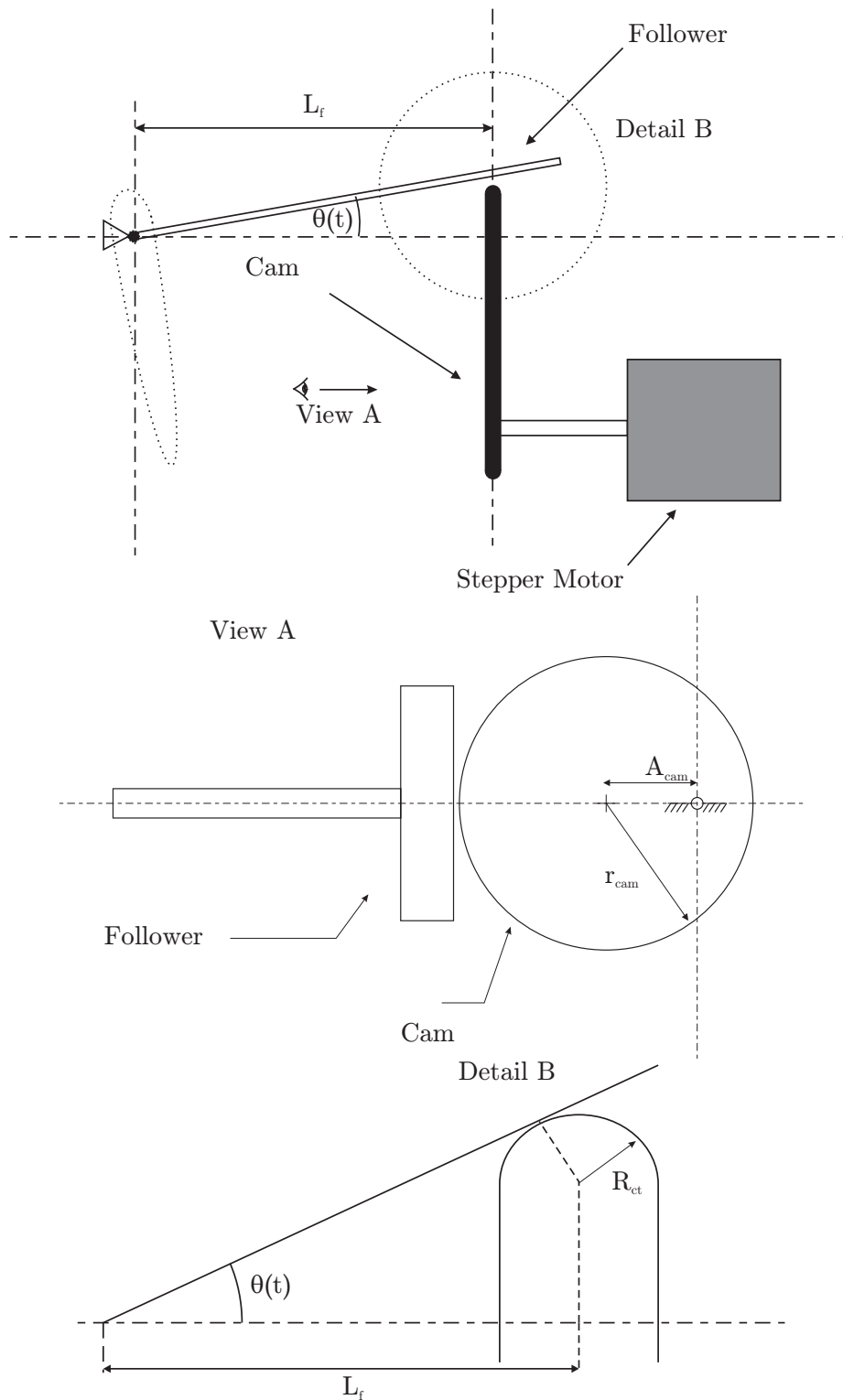


Figure 2.5: Geometry of cam - follower interface

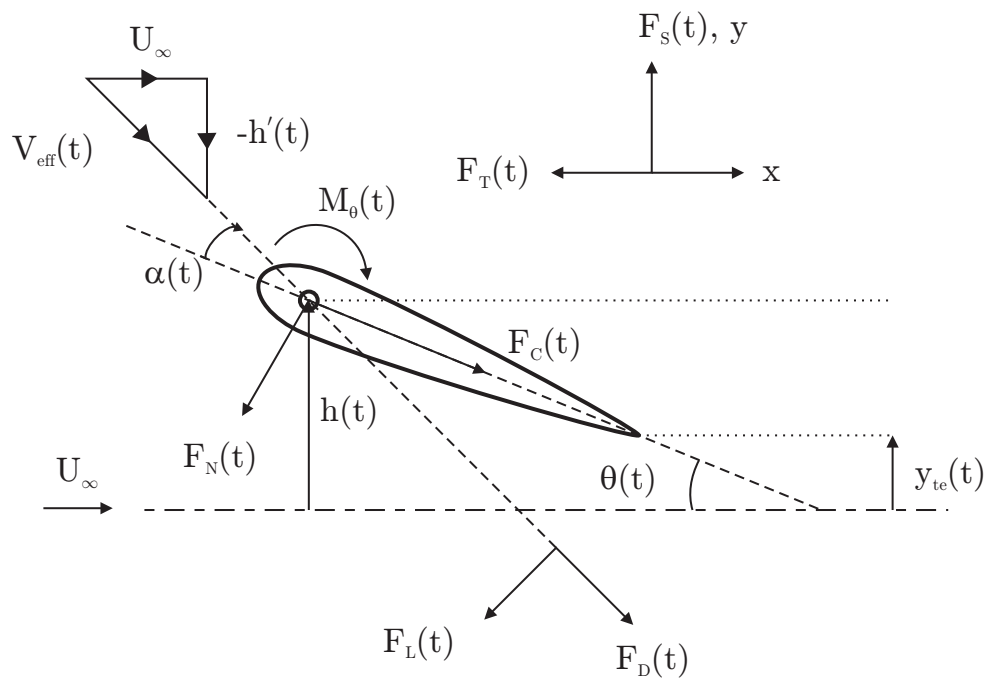


Figure 2.6: Definitions of foil kinematic parameters

2.3 Foil properties and kinematics

2.3.2 Heaving

The heaving motion, $h(t)$ is produced by a scotch yoke mechanism, which provides a pure harmonic motion,

$$h(t) = h_0 \cdot \cos(\phi(t) - \psi) \quad (2.8)$$

$$= h_0 \cdot \sin \phi(t) \quad (2.9)$$

where h_0 is the heave amplitude and ψ is the phase difference between heave and pitch. In all experiments, the phase difference was fixed at $\psi = 90^\circ$, due to the fact that it is the most commonly investigated case in unsteady flows (for example, see Anderson *et al.* 1998; Gopalkrishnan *et al.* 1994; von Ellenrieder *et al.* 2003), and has been shown to produce thrust at higher Strouhal numbers than in cases where $\Psi \neq 90^\circ$ (Read *et al.*, 2003).

The heave velocity can then be expressed as

$$h'(t) = -2\pi f h_0 \cdot \cos \phi(t). \quad (2.10)$$

2.3.3 Derived kinematic parameters

2.3.3.1 Trailing edge motion

From geometry (see Figure 2.6), the displacement of the trailing edge of the foil from the centreline is:

$$y_{te}(t) = h(t) - 0.7c \cdot \sin \theta(t) \quad (2.11)$$

where c is the chord length of the foil. Note that the position of the centre of rotation of the foil is located at $0.3c$ from the leading edge of the foil.

The total excursion of the trailing edge of the foil is then

$$A_{te} = y_{te,max} - y_{te,min} \quad (2.12)$$

where $y_{te,max}$ and $y_{te,min}$ are the maximum and minimum values of equation 2.11 respectively, within the range $0 \leq t \leq T$. Equation 2.12 is solved numerically due to the difficulty in obtaining an analytic solution.

2.3.3.2 Strouhal number

We now define three Strouhal numbers used throughout this thesis. These Strouhal numbers are defined based on the trailing edge excursion, the foil heave amplitude, and the foil chord length, respectively:

$$St_{te} = \frac{f \cdot A_{te}}{U_{\infty}} \quad (2.13)$$

$$St_h = \frac{2f \cdot h_0}{U_{\infty}} \quad (2.14)$$

$$St_c = \frac{f \cdot c}{U_{\infty}} \quad (2.15)$$

Throughout this thesis, the term “Strouhal” number or St will generally refer to St_{te} unless otherwise stated.

2.3.3.3 Angle of attack

If we define the angle of attack $\alpha(t)$ as positive in the orientation as shown in Figure 2.6, then it can be determined that

$$\alpha(t) = -\theta(t) + \arctan \left[\frac{h'(t)}{U_{\infty}} \right] \quad (2.16)$$

$$= \arctan [\pi \cdot St_h \cdot \cos \phi(t)] - \theta(t) \quad (2.17)$$

If we use the simplification $\theta(t) \approx \theta_{thin}(t)$, then using equations 2.5 and 2.17, we can show that

$$\tan \alpha(t) = \frac{\cos \phi(t) \cdot (\pi St_h - \tan \theta_0)}{\pi St_h \cos^2 \phi(t) \cdot \tan \theta_0 + 1} \quad (2.18)$$

With mathematical manipulation, it can be shown that the term $\tan \alpha(t)$ reaches a maximum and minimum respectively at

$$\phi(t) = 0 \quad \text{for} \quad St_h \leq \frac{1}{\pi \tan \theta_0} \quad (2.19)$$

$$\phi(t) = \arccos \sqrt{\frac{1}{\pi St_h \tan \theta_0}} \quad \text{for} \quad St_h \geq \frac{1}{\pi \tan \theta_0} \quad (2.20)$$

2.3 Foil properties and kinematics

Thus, the maximum instantaneous angle of attack achieved within an entire oscillating cycle, α_{max} , can be expressed analytically as

$$\alpha_{max} = \pm [\arctan(\pi St_h) - \theta_0] \quad \text{for} \quad St_h \leq \frac{1}{\pi \tan \theta_0} \quad (2.21)$$

$$\alpha_{max} = \pm \arctan \left[\frac{\tan \theta_0 - \pi St_h}{2\sqrt{\pi St_h \tan \theta_0}} \right] \quad \text{for} \quad St_h \geq \frac{1}{\pi \tan \theta_0} \quad (2.22)$$

Since, for most foil kinematic parameters and flow conditions tested in the current experiments, $St_h \leq \frac{1}{\pi \tan \theta_0}$, the relationship between the magnitude of the maximum angle of attack, and the heave-based Strouhal number is

$$St_h = \frac{\tan(\theta_0 + \alpha_{max})}{\pi} \quad (2.23)$$

2.3.3.4 Heave dominance parameter, χ

In many instances, it is important to distinguish between cases where the non-dimensional heave amplitude, $\frac{h_0}{c}$, is large compared to the pitch amplitude, θ_0 , and vice versa. Thus, for convenience, we define the parameter χ as

$$\chi = \frac{h_0}{c \tan \theta_0} \quad (2.24)$$

which is roughly the ratio of the contribution of the heaving motion and the pitching motion to the foil trailing edge amplitude y_{te} . When χ is large ($\chi \gtrsim 1.5$), the motion of the foil is dominated by heaving motions, while when χ is small ($\chi \lesssim 0.5$), the motion of the foil is dominated by pitching motions.

2.3.3.5 $St_{h,0}$ and St_0

We define the special Strouhal numbers $St_{h,0}$ and St_0 as the Strouhal numbers at which the time-averaged thrust on the foil is expected to be equal to zero. For the highly simplified case where the foil is assumed to produce negligible drag, this occurs when the maximum angle of attack, $\alpha_{max} = 0$, thus

$$St_{h,0,simp} = \frac{\tan \theta_0}{\pi} \quad (2.25)$$

$$St_{0,simp} = \frac{A_{te}}{2\pi c \chi} \quad (2.26)$$

In this simplified case, at $St > St_0$, $\alpha_{max} > 0$, and hence thrust in the time-average sense is expected to be developed. Hence, the ratio of $\frac{St}{St_0} \equiv \frac{St_h}{St_{h,0}}$ is a convenient term to use to predict when the foil is expected to produce nett thrust, whereby nett thrust is expected to be developed by the foil when $\frac{St}{St_0} \equiv \frac{St_h}{St_{h,0}} > 1$. It can be shown with some manipulation that

$$\frac{St}{St_0} \equiv \frac{St_h}{St_{h,0}} = 2\pi St_c \chi = 2 \cdot k \cdot \chi \quad (2.27)$$

where $k = \frac{\pi \cdot f \cdot c}{U_\infty}$ is the feathering parameter, which is a non-dimensional parameter sometimes used to describe the unsteadiness of oscillating foils (Dickinson, 1996; Ellington, 1995; Lighthill, 1975; Chopra, 1974; Bose and Lien, 1989; Triantafyllou *et al.*, 2000). Therefore, in a time-averaged sense, the unsteady foil is expected to produce thrust when $2 \cdot k \cdot \chi > 1$ and drag when $2 \cdot k \cdot \chi < 1$.

2.3.4 Chosen foil kinematic parameters

The foil kinematic settings, in particular the non-dimensional heave amplitude, $\frac{h_0}{c}$, and the pitch amplitude, θ_0 , are arranged into groups corresponding to constant values of θ_0 , and in order of increasing St_0 . The individual foil kinematic sets and groups are summarised in Table 2.1. This results in a parametric matrix whereby the experimental sets are organised in increasing order of pitch-dominance (decreasing χ).

2.4 Implementation of digital Particle Image Velocimetry (PIV)

Particle image velocimetry is a common technique employed to measure the velocity field in a plane of a particular flow. Usually, only the in-plane velocity components can be determined. PIV usually consists of a light-sheet generating system, which illuminates the flow in the plane of interest. The flow is seeded with reflective particles, which are in turn imaged by a camera and stored onto a computer. The flow is illuminated in very quick bursts, at a fixed time interval, Δt , and these images can be cross-correlated to obtain the velocity field. The main advantage of PIV is that it enables the velocity to be measured within a whole field, rather than at a particular point. This is particularly useful for wake measurements as the velocity field of the entire wake can be measured almost instantaneously. The main limitation of the current setup of PIV is that it only allows measurement of the in-plane velocity components, and has a low sampling rate, which is fixed at 10Hz.

2.4 Implementation of digital Particle Image Velocimetry (PIV)

Group	Set	$\frac{h_0}{c}$	$\theta_0(^{\circ})$	χ	$\frac{St}{St_h}$	$St_{0,simp}$	$St_{h,0,simp}$
I	1	0.75	0	∞	1.00	0	0
	2	0.50			1.00	0	
	3	0.25			1.00	0	
II	4	0.75	15	2.80	1.03	0.09	0.09
	5	0.50		1.87	1.07	0.09	
	6	0.25		0.93	1.25	0.11	
III	7	0.75	30	1.30	1.13	0.21	0.18
	8	0.5		0.87	1.26	0.23	
	9	0.25		0.43	1.78	0.33	
IV	10	0.75	45	0.75	1.29	0.41	0.32
	11	0.50		0.50	1.52	0.49	
	12	0.25		0.35	2.35	0.75	

Table 2.1: Summary of foil kinematics, organised into individual sets and groups

This section discusses the implementation of the PIV technique specifically on the flapping foil experiment. For a more general discussion on the PIV technique, the reader may refer to Smits and Lim (2000) and Raffel *et al.* (1998).

The current PIV experiments consisted of 106 different flow conditions and foil kinematic parameters, leading to a Reynolds number range of $Re \approx 1,250 - 12,500$.

2.4.1 Light sheet generating optics

A pulsed light source was generated using a double-cavity Quantel Brilliant B Twins Nd:YAG laser, which has a fixed flashlamp pulse frequency of 10Hz. The output from the laser head was a collimated coherent monochromatic beam with a wavelength of 532nm and an approximate beam diameter of 9mm. The maximum energy per laser burst is rated at 380mJ, although the energy can be controlled by changing the flashlamp-to-Q-switch time delay, Δ_{f-q} . Typical values for Δ_{f-q} varied between 290 μ s and 320 μ s, which corresponded to an energy per laser

pulse of approximately 190-220mJ. The duration of each laser pulse was approximately 6ns (as quoted by the manufacturer).

To create a sheet of light, the laser beam was guided through an arrangement of optical elements, as shown in Figure 2.7. The first optic, M1, is a high energy mirror, specifically designed to turn the laser beam 90 degrees. After the beam was turned to the required direction, the beam then passed through three cylindrical lenses, L1, L2 and L3, each with focal lengths 100mm, -50mm and -12.7mm respectively. The first two lenses were used to control the thickness of the beam by varying the distance between lens L1 and L2. The distance between L1 and L2 was nominally set to approximately 50mm, and was varied by approximately ± 0.2 mm. The final lens, L3, was used to spread the beam into a light sheet. The resulting light sheet thickness was approximately 0.8-1.0mm.

Across almost all experimental realisations, the light sheet was maintained such that it impinged on the span-wise centreline of the foil. Checks were also made at three locations along the water channel (marked C1, C2 and C3 in Figure 2.7) to ensure that the light sheet thickness remained constant throughout the working section.

2.4.2 Imaging system

Images of the field-of-view (FOV) of interest were captured using a Kodak Megaplug ES 1.0 10-bit CCD camera. The camera has a sensor resolution of 1008×1018 pixels, and a sensor size of 9×9 mm. The camera was run in the “triggered double exposed” mode, and therefore the camera captured image pairs at the same rate as the laser flashlamp frequency (i.e. 10Hz).

Two different lenses were used in tandem with the camera - a Nikkor AF 50mm f/1.4D lens and a Nikkor AF 70-300mm f/4-5.6D lens. The latter lens was used when a smaller field-of-view was required due to its higher focal length. However, where possible, the former lens was used due to its larger aperture (lower f-number) which allowed more light into the camera.

The camera was placed on a two-degree-of-freedom traverse such that it viewed the flapping foil and the region of interest from the bottom of the water channel (as shown in Figure 2.7).

2.4.3 Particle seeding

The water channel was seeded with hollow glass spheres with a mean diameter of $d_p = 20\mu\text{m}$ and a density of $\rho_p = 1030\text{kg}/\text{m}^3$. The density of the seeding particles is very close to that of the density of water, resulting in seeding particle settling times that are very high relative to the time scales in the flow of interest (see calculations to follow).

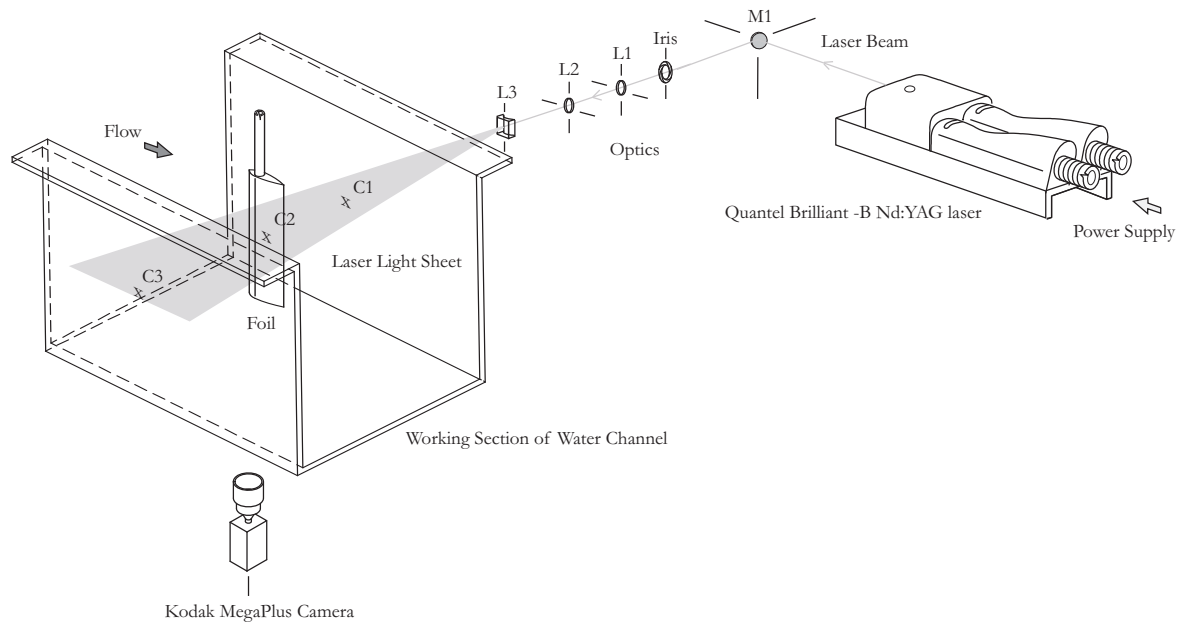


Figure 2.7: Experimental optical arrangement

The value of $d_p \approx 20\mu\text{m}$ is generally considered an acceptable seeding particle size, balancing the conflicting requirements that seeding particles follow the flow faithfully while still reflecting sufficient light (Melling, 1997; Adrian, 1991; Raffel *et al.*, 1998). A good estimate of how well any given particle follows the flow is the Stokes number for a spherical particle, Stk , where $Stk \ll 1$ indicates that the particles follow the flow faithfully over a characteristic length. The Stokes number is defined as

$$Stk = \frac{\tau U}{L_{flow}} = \frac{\rho_p U d_p^2}{18\mu L_{flow}} \quad (2.28)$$

where U is a characteristic velocity of the system, L_{flow} is a characteristic length (say, the size of a vortical structure or an eddy), and τ is the relaxation time. For the flapping foil experiments, it is estimated that the upper limit to the value of U would be approximately 250mm/s, and a lower limit to the characteristic length scale of a vortical structure to be approximately 2mm (which is 4% of the foil chord length). Therefore, the corresponding Stokes number, $Stk \approx 2.55 \times 10^{-3} \ll 1$, which suggests that the particles faithfully follow the flow for most of the experimental realisations down to vortical structures as small as 2mm.

With some manipulation, from equation 2.28, we can also determine the settling velocity, V_s to be

$$\begin{aligned} V_s &= \frac{g \cdot d_p^2 \cdot (\rho_p - \rho)}{18\mu} \\ &\approx 7 \times 10^{-12} \frac{m}{s} \end{aligned} \quad (2.29)$$

Therefore, it takes the particles approximately 7.1×10^9 seconds to settle 50mm (the chord length of the foil).

The seeding particles were added into the water channel as follows: the particles were added in small amounts to a small bottle, which in turn was then filled with water from the water channel. The water-particle mixture in the bottle was then added slowly at various locations in the water channel while the channel was running at its maximum rated speed. The water channel was then left to run for approximately one hour before each experimental run to ensure a uniform seeding particle density throughout the water channel.

2.4.3.1 Particle image size

The particle image size plays an important role in determining the accuracy of the entire PIV system; a large seeding particle image size produces large random errors in the velocity measurements, while small seeding particle image sizes tend to increase the bias error in the velocity

2.4 Implementation of digital Particle Image Velocimetry (PIV)

measurements, which manifests itself as “peak-locking” (Raffel *et al.*, 1998). Raffel *et al.* suggest a good compromise is for the particle image size to be approximately twice the recording camera pixel size.

The effective particle image size that falls onto the camera sensor, d_e , is combination of the size of the particle size, d_p , the magnification of the lenses and optical arrangement, M , and the diffraction limited image size of the particle, d_s , as given by the equation

$$d_e = \sqrt{M^2 d_p^2 + d_s^2} \quad (2.30)$$

where

$$d_s = 2.44 (1 + M) \frac{f}{D} \lambda \quad (2.31)$$

and $\frac{f}{D}$ is the f-number of the camera lens. λ is the wavelength of the illuminating light, in this case, $\lambda = 532\text{nm}$ (Prasad, 2000). The magnification used in the flapping foil experiments was $M \approx 0.07 - 0.09$, and the f-numbers used were $\frac{f}{D} = 1.4 - 5.6$. Using a mean particle diameter of $d_p \approx 20\mu\text{m}$, this gives an approximate effective particle image size of $d_e \approx 2.4 - 8.2\mu\text{m}$. The size of the sensor pixels is approximately $9\mu\text{m}$ square, and therefore, as it stood, d_e remained smaller than the suggested value of d_e of twice the pixel size. Thus, to increase d_e , a trial-and-error method was employed whereby the camera lens was de-focused slightly until an acceptable value of d_e was obtained (Kalt, 2005).

2.4.4 Laser timing and synchronisation

One of the benefits of having a periodic flow is that the random error in the measured velocity field can be reduced by phase averaging the data across a large number of image pairs. However, to accomplish this, the flapping foil has to be synchronised with the laser flashlamps such that image pairs are produced at exactly the same point on each cycle of the flapping foil. This was achieved using a synchronisation system as shown in Figure 2.8.

Rare earth magnets were mounted on the heave platform, and on an arm-extension which was mounted to the foil shaft (see Figures 2.3 and 2.4). When the magnets reached a particular position corresponding to the foil phase-of-interest, it triggered a set of hall effect sensors which were mounted externally to the water channel and experimental apparatus. In all experiments, the sensors were placed at the far extremities of the pitch and heave amplitudes respectively, where the frequency of the signal from the sensor was simply the flapping foil frequency, f . The outputs from the sensors have a square wave form, with a typical pulse width on order of 1ms. Maximum jitter was approximately $100\text{-}200\mu\text{s}$.

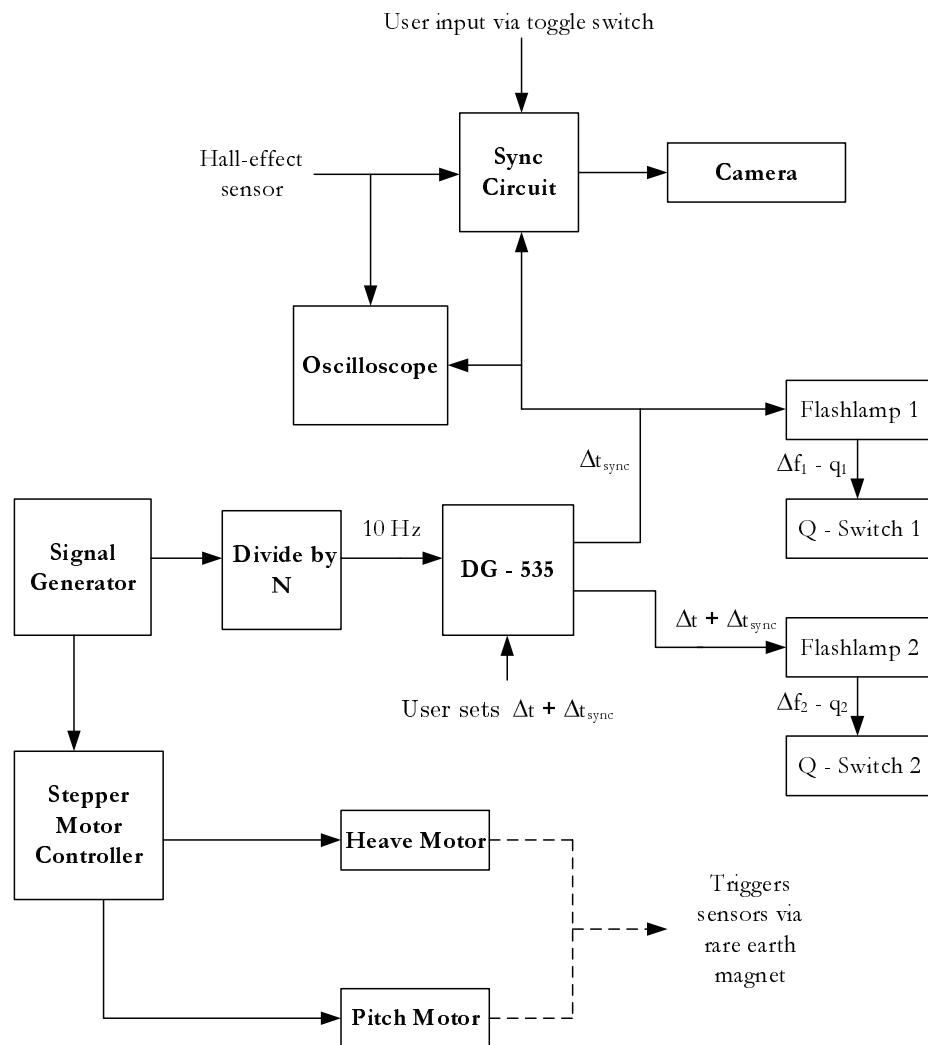


Figure 2.8: Block diagram of synchronisation system

2.4 Implementation of digital Particle Image Velocimetry (PIV)

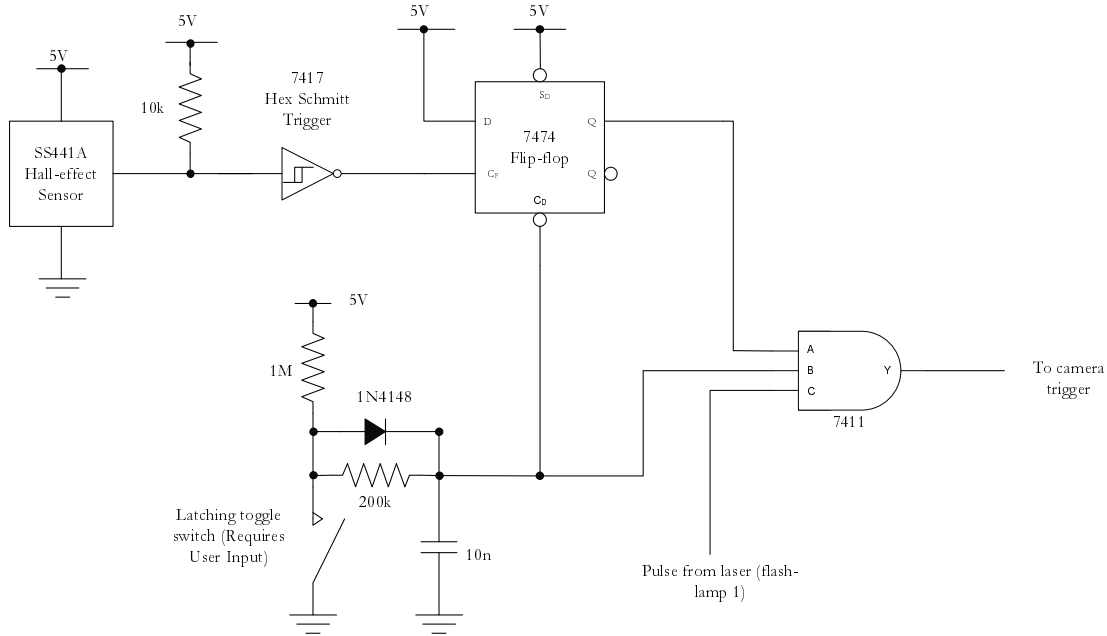


Figure 2.9: Synchronisation circuit

As the laser pulsing frequency was fixed at 10Hz, the period of the flapping foil was set to values that are integer multiples of 0.1s. Typically, the flapping frequency was set to $f = 1\text{Hz}$, and therefore the phase averaged velocity fields were obtained at 10 different foil oscillating phases.

To minimise the phase drift between the laser and the flapping foil, the whole system was driven by a low jitter signal generator, therefore ensuring that the whole system was phase-locked. The signal generator controls the frequency of the flapping foil by driving the stepper motors, which were run in a half-step mode.

The output from the signal generator was run through a frequency divider to ensure that the signal going into the laser was always maintained at 10Hz. This signal was then connected into a Stanford DG-535 pulse delay generator, which was used to generate two signals delayed by Δt and Δt_{sync} with respect to the original input signal, respectively. The time delay Δt was used as a time delay between the pulsing of two independent flashlamps of the laser, and therefore Δt was used to set the time separation between two successive PIV images that formed an image pair. Then, Δt_{sync} was used to synchronise the signal from the hall effect sensor, and the signal from the first flashlamp, that is, Δt_{sync} was varied until the rising edge of the signal from flashlamp

1 was aligned with the approximate pulse-centre of the signal from the hall effect sensors (see Figure 2.10)..

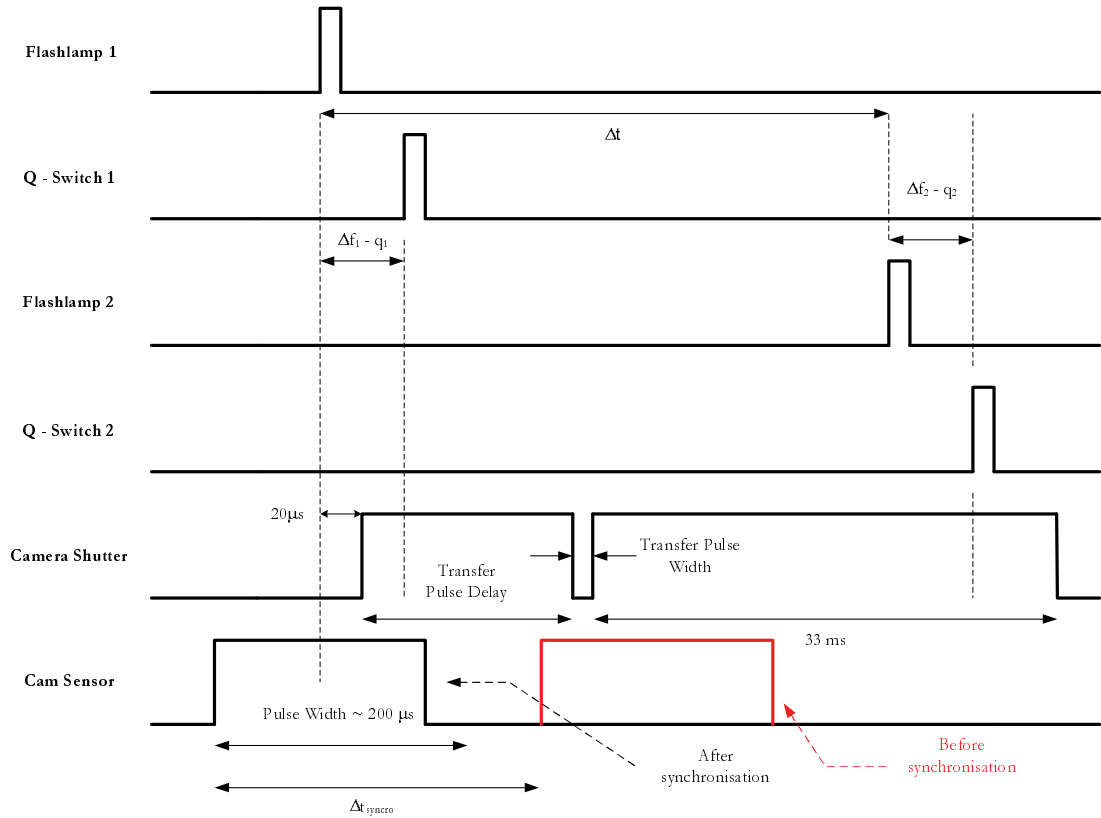


Figure 2.10: Timing diagram

Finally, the output from flashlamp 1 also triggered the camera via a synchronisation circuit, designed to allow the user an external “begin” trigger. The synchronisation circuit is shown in Figure 2.9. When the latching toggle switch was closed by the user, the circuit waited until it received a signal from the hall effect sensors, at which point it allowed the camera to be triggered by flashlamp 1. In this way, the first image recorded of every experimental realisation remained at a fixed foil oscillating phase.

2.4.5 PIV processing parameters

All PIV image pairs were processed using the command line interface of PIV-View 1.75. The interface allows the user to select between a range of options for image pre-processing, image processing parameters and outlier detection.

2.4 Implementation of digital Particle Image Velocimetry (PIV)

2.4.5.1 Image pre-processing

Prior to cross-correlating the image pairs, the images were pre-processed to allow more accurate data processing. This consisted of applying a “dynamic threshold” to each image, where the image intensity values were cropped below a certain floor value, and above a particular ceiling value. In these experiments, these values were set to 5% and 99% of the peak intensity value respectively.

Furthermore, all PIV images were passed through a 2×2 anti-aliasing filter, which “smears” the image intensity values slightly and essentially acts as a low pass filter. Due to the fact that the particle image sizes in the flapping foil experiments are slightly small (see Section 2.4.3.1), the anti-aliasing filter had the added effect of producing slightly larger particle image sizes due to this “smearing” effect.

2.4.5.2 Image processing parameters

Images were processed using an interrogation window size of 16×16 pixels, with 50% overlap. Images were processed using a 2-pass Hart cross correlation. The 2-pass correlation, which is also called the “adaptive local window shifting correlation”, works in the following way: an estimate of the displacement vector is obtained for each interrogation window by first passing the image pairs through a regular correlation algorithm. Once this is complete, each interrogation window is shifted by the same value as the estimated displacement vector, and the correlation is computed again with the shifted interrogation window. This increases the accuracy of the correlation by reducing the amount of in-plane particles that are lost outside of the interrogation window.

The Hart-correlation, introduced by Hart (2000), is a method which attempts to reduce the noise in the correlation plane by multiplying the correlation data of a particular interrogation window with the correlation data of a closely adjacent interrogation window. This is based on the assumption that two slightly spatially separated correlation planes should have approximately the same value of particle-shift (or displacement vector), but different random noise values. Therefore, by multiplying the two correlation planes, the correlation peak can be increased relative to the random noise. This method, however, only works for vector fields which do not have large velocity gradients.

The locations of the correlation peaks to within sub-pixel values were estimated by fitting a 3-point Gaussian profile to the correlation data values. A Gaussian profile was chosen because, theoretically, the profile of the particle image intensity is Gaussian, and therefore the correlation profile should be Gaussian as well (Raffel *et al.*, 1998).

2.4.5.3 Outlier detection (Phase 1)

Outlying or spurious vectors were detected using a maximum displacement difference criterion, whereby a vector was marked as an outlier if the displacement difference between itself and 4 or more neighbouring vectors exceeds a particular threshold value. This threshold value varied between particular experimental realisations, however, the most commonly used value in the flapping foil experiments was a value of 5 pixels¹. Outliers were then replaced with the value of the secondary correlation peak, or, if the secondary correlation peak was also an outlier, the outlier was replaced with the third correlation peak. If the third correlation peak was also an outlier, the vector was disabled.

2.5 Post - processing of PIV data

Once the data were processed using Piv-view, the data (in .txt form) was loaded into MatlabTM for further post - processing. This includes further outlier detection (see below), followed by a phase-averaging process, smoothing of the velocity vectors, and finally, vorticity and circulation computation.

2.5.1 Outlier detection (Phase 2)

A second, more rigorous, outlier detection phase was implemented using a method suggested by Westerweel and Scarano (2005). This method uses the residuals of the vectors as a basis for determining whether a vector is an outlier. The normalised residual at any point O in the vector field is defined as

$$r'_0 = \frac{|U_0 - U_m|}{r_m + \epsilon_r} \quad (2.32)$$

where U_0 is the velocity at point O and U_m is the median of the velocity of the 8 surrounding neighbours of U_0 . The median of the residuals of the 8 surrounding neighbours around U_0 is given by r_m , where the residuals are calculated using $r_i = |U_i - U_m|$ at every point $i = 1, 2, 3 \dots 8$. The term ϵ_r is simply a small value used to ensure that the denominator of the normalised residual does not approach zero, which may occur in some flows with very small velocity fluctuations (a uniform flow stream, for example). For all experiments presented in this thesis, ϵ_r was set to 0.1 pixels.

A particular vector is deemed an outlier if $r'_0 > \epsilon_{threshold}$, where $\epsilon_{threshold}$ is a threshold level. Westerweel and Scarano suggests using a value of $\epsilon_{threshold} = 2.0$, however, we used a more

¹Note: Compare this value to the interrogation window size, which is 16 pixels.

2.5 Post - processing of PIV data

stringent value of $\epsilon_{threshold} = 1.7$ due to the fact that it was preferred to disable all spurious data at the expense of some valid data, due to the nature of the phase averaging process, since spurious data may artificially bias the valid data.

2.5.2 Phase averaging

A minimum of 400 image pairs were obtained for each phase of each experimental case. This provided a minimum of 400 vector fields for each phase of each experimental case, which were then averaged to obtain one phase-averaged velocity field for each phase. Only valid data were averaged - outliers were disabled and were not used in any computation. Data in the phase-averaged velocity field were then validated by checking the number of vectors used in the averaging process at any given point. If a particular vector in the phase averaged velocity field was computed using less than 95% of the maximum possible number of vectors (i.e., 380 vectors out of a possible 400 vectors usually), that particular vector in the phase-averaged velocity field was disabled.

2.5.3 The estimation of the random errors in PIV velocity measurements

Here, we employ two methods to estimate the uncertainty in the instantaneous PIV velocity measurements. In the first method, we simply use a statistical analysis based on a sample set consisting of instantaneous velocity fields at any given phase. Since, in theory, at any given phase the true instantaneous velocity field should be identical, the variation between velocity samples should provide a measure of the uncertainty in the velocity measurements. In the second method, we estimate the uncertainty in the instantaneous velocity fields based on the estimated error contributions of the experimental apparatus. These methods are discussed individually below.

2.5.3.1 Based on a sample set of phase-locked velocity fields

The phase averaging of velocity vectors allows the estimation of the magnitude of the random errors in the velocity field due to the inaccuracy of the experimental system. This is done by estimating the standard deviation in the samples of the instantaneous velocity field. If, at any given phase ϕ , the magnitude of a velocity component at any point i and any cycle C in the instantaneous velocity field is $v_{\phi,i,C}$, and the phase averaged velocity component is $\overline{v_{\phi,i}}$, then the magnitude of the random velocity error in the velocity field normalised to the free-stream

velocity is

$$\epsilon_{u,i} = 2 \frac{\sqrt{\frac{1}{N_{valid,i}} \cdot \sum_{t=C}^{N_{valid,i}} (v_{\phi,i,C} - \overline{v_{\phi,i}})^2}}{U_{\infty}} \quad (2.33)$$

where $N_{valid,i}$ is the number of valid velocity samples used to obtain $v_{\phi,i}$.

This process is repeated for both x and y components of velocity, at every point i in the field. Maximum random errors in the velocity field, $\epsilon_{u,max}$, generally occur at the centre of the vortex cores, where velocity gradients are high. Typical values of maximum random velocity errors in individual flow cases is $\epsilon_{u,max} \approx 7\%$, whereas the maximum random error recorded for all experimental cases was $\epsilon_{u,max} \approx 10.1\%$, which occurred at $\frac{h_0}{c} = 0.75$, $\theta_0 = 0^\circ$ and $St = 0.71$ (which incidentally is the highest foil heave amplitude and the highest recorded St value). Typical mean values of $\epsilon_{u,i}$ across the whole velocity field is approximately 2-3%.

2.5.3.2 Based on theoretical error estimation

The random errors in the instantaneous PIV velocity field can also be estimated by adding the individual contribution of various sources of experimental error. The major sources of errors identified include, but are not strictly limited to:

1. $\epsilon_t = \frac{\sigma_j}{\Delta t}$, the error in the determination of the laser pulse delay separation, Δt , due to jitter in the triggering mechanism, σ_j ;
2. ϵ_s , the error associated with the accurate determination of the magnification of the optical setup;
3. ϵ_p , the error in the cross correlation due to the particle image size;
4. ϵ_d , the error in the cross correlation due to the particle image density;
5. ϵ_l , the error in the cross correlation due to the particle image displacement;
6. ϵ_g , the error in the cross correlation due to velocity gradients in the velocity field;
7. ϵ_b , the error in the cross correlation due to background noise (in terms of light intensity) in each measured PIV image.

For a typical flapping foil PIV experiment discussed in this thesis, it is estimated that the jitter, σ_j , in the laser triggering mechanism was approximately $0.5 \mu s$ (obtained from manufacturers specifications), and a typical value of Δt was approximately $3000 \mu s$. Therefore, $\epsilon_t \approx 1.67 \times$

2.5 Post - processing of PIV data

10^{-4} . The calibration of the magnification of the optical setup was accomplished by measuring the size, in pixels, of a “target” image with a known grid spacing. The measurement was usually taken across a distance of approximately 900 pixels, and the error in the estimation of the beginning and the end of the measurement line was 0.5 pixels each. Therefore, $\epsilon_s \approx 1.12 \times 10^{-3}$.

The errors listed in 3-7 above are estimated based on the Monte Carlo simulations performed by Raffel *et al.* (1998). For a typical PIV image pair obtained from the flapping foil experiments, it is estimated that the particle image size $d_p \approx 2$ pixels, the particle image density $N_p \approx 7 - 8$ particles per 16×16 pixel interrogation window and the typical particle image displacement, ΔD , were approximately 4-5 pixels. The background noise in the camera was estimated to be approximately 10%. A “typical” value of velocity gradient is difficult to estimate, because the velocity gradients vary greatly within a single velocity field, let alone across all experimental realisations. However, for flow conditions and foil kinematic parameters where moderate to large velocity gradients develop, it is estimated that the largest velocity gradients in the field are on order of ≈ 0.09 pixels per pixel. Based on these PIV values and the results published by Raffel *et al.*, we obtain $\epsilon_p \approx 0.06$ pixels, $\epsilon_d \approx 0.035$ pixels, $\epsilon_l \approx 0.05$ pixels, $\epsilon_g \approx 0.2$ pixels and $\epsilon_b \approx 0.025$ pixels. Therefore, the random noise in the instantaneous velocity field, normalised to the free-stream velocity is

$$\begin{aligned} \epsilon_{u,i} &\approx \sqrt{\epsilon_t^2 + \epsilon_s^2 + \frac{\epsilon_p^2 + \epsilon_d^2 + \epsilon_l^2 + \epsilon_g^2 + \epsilon_b^2}{\Delta D^2}} \\ &\approx 4.9\% \end{aligned} \quad (2.34)$$

Note that at areas where the velocity gradients were small, that is, if $\epsilon_g \rightarrow 0$, then using equation 2.34, the random noise in the velocity field reduces to $\epsilon_u \approx 2\%$, which is very close to the values obtained experimentally in Section 2.5.3.1 above.

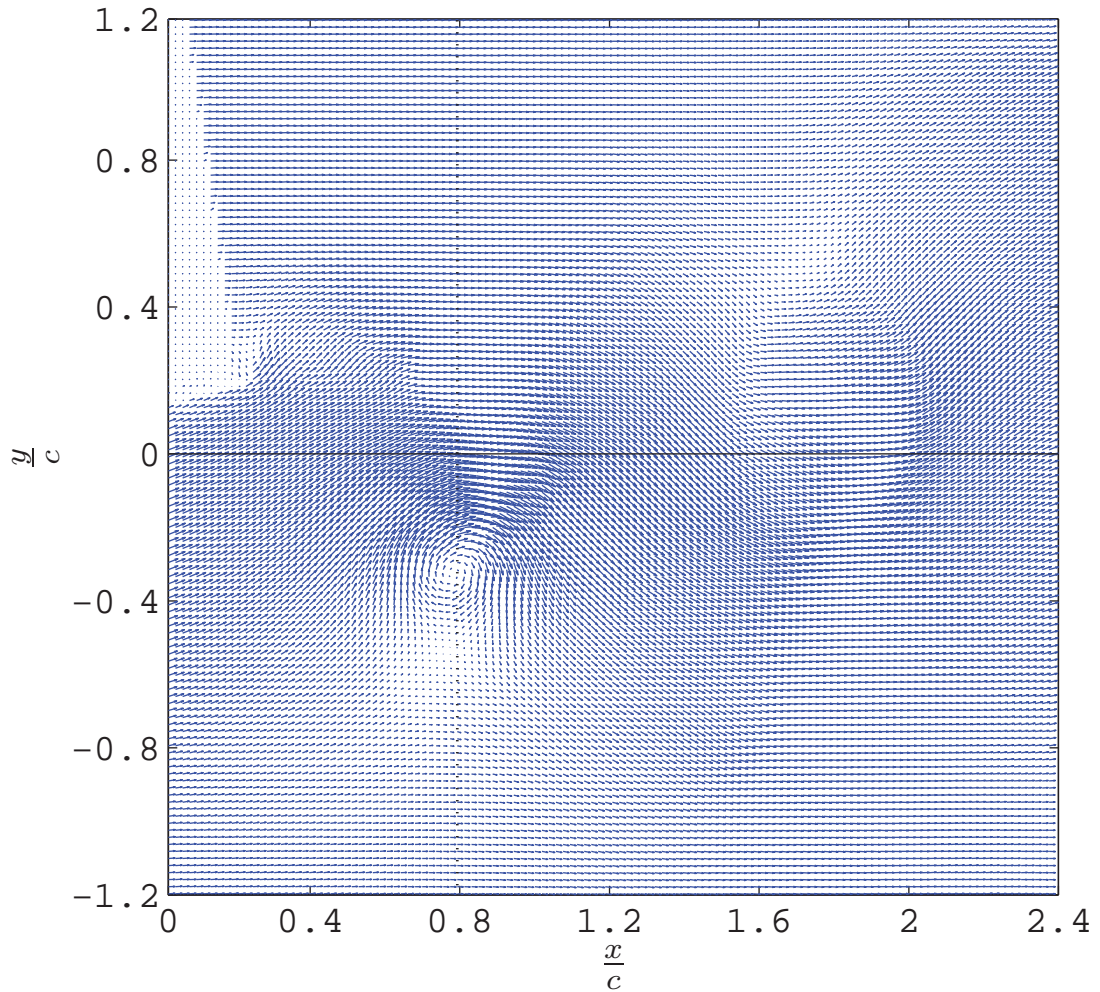
2.5.3.3 Random errors in the phased-averaged data

The errors discussed above are the random errors in the instantaneous velocity field, however, in most cases, the phase-averaged velocity field is used. If the distribution of random errors in the velocity field is assumed to be Gaussian, then the random error in the phase-averaged velocity field is

$$\epsilon_{u,pa} = \frac{\epsilon_{u,i}}{\sqrt{N_{valid}}} \quad (2.35)$$

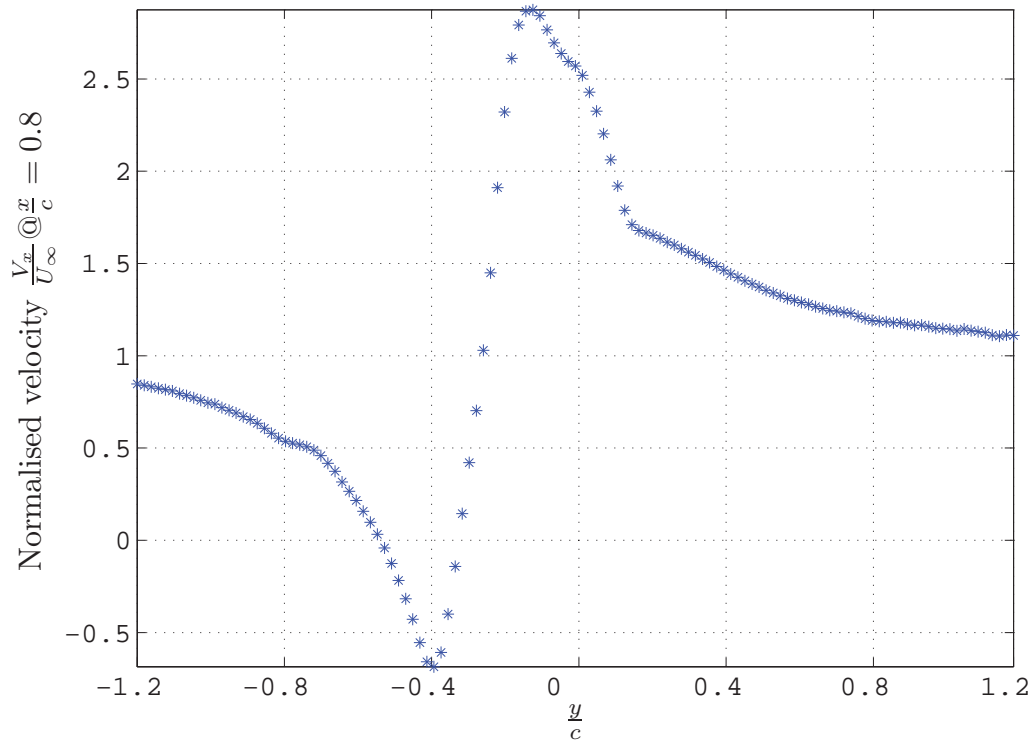
For a flow condition which has a particularly noisy instantaneous velocity field, we may use $\epsilon_{u,i} \approx 7\%$, and for a typical value of $N_{valid} \approx 380$, we obtain $\epsilon_{u,pa} \approx 0.35\%$.

This value of $\epsilon_{u,pa}$ can be directly compared to the noise values in the experimentally obtained PIV velocity field. An example of a velocity field behind a flapping foil is shown in Figure 2.11a. The velocity distribution, along an arbitrary axis, at say $\frac{x}{c} = 0.8$, is shown in Figures 2.11b and 2.11c, where Figure 2.11c is magnified view of Figure 2.11b, limited to the range of $\frac{y}{c} \approx 0.85 - 1.2$. From Figure 2.11c, it can be determined that the error in the velocity (relative to the free-stream velocity U_∞) is less than 0.5%.

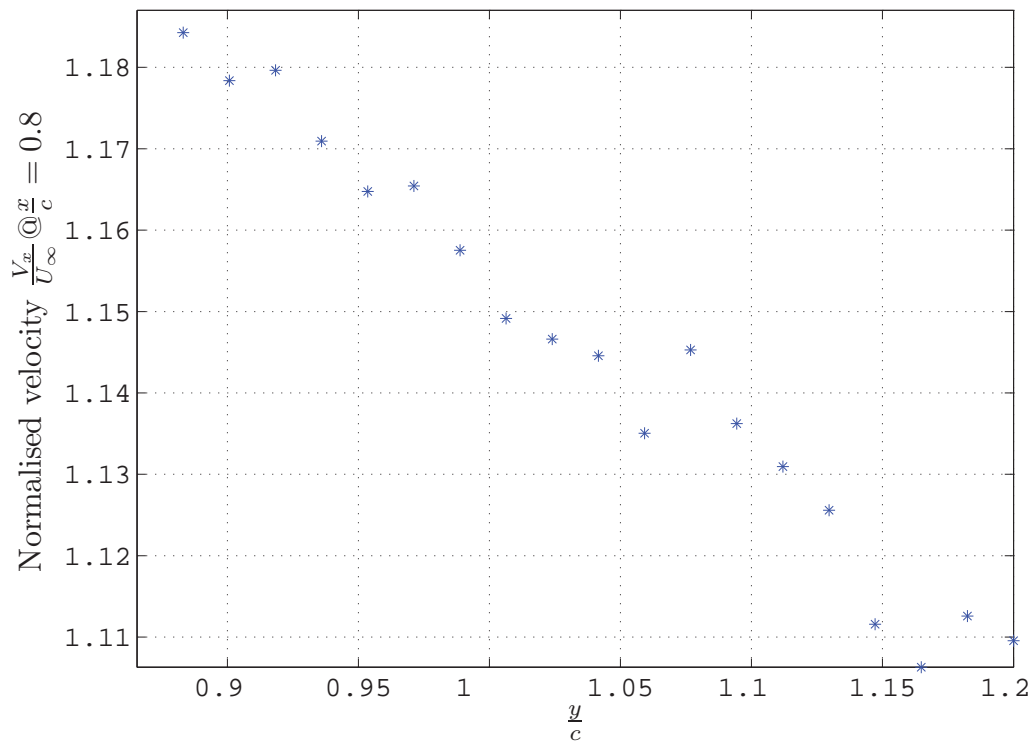


(a) Example of phase-averaged PIV velocity field. Note that the lack of vectors in the upper left hand corner is due to the shadow of the foil

Figure 2.11: Example of a typical phase-averaged flapping foil velocity field (continued on next page)

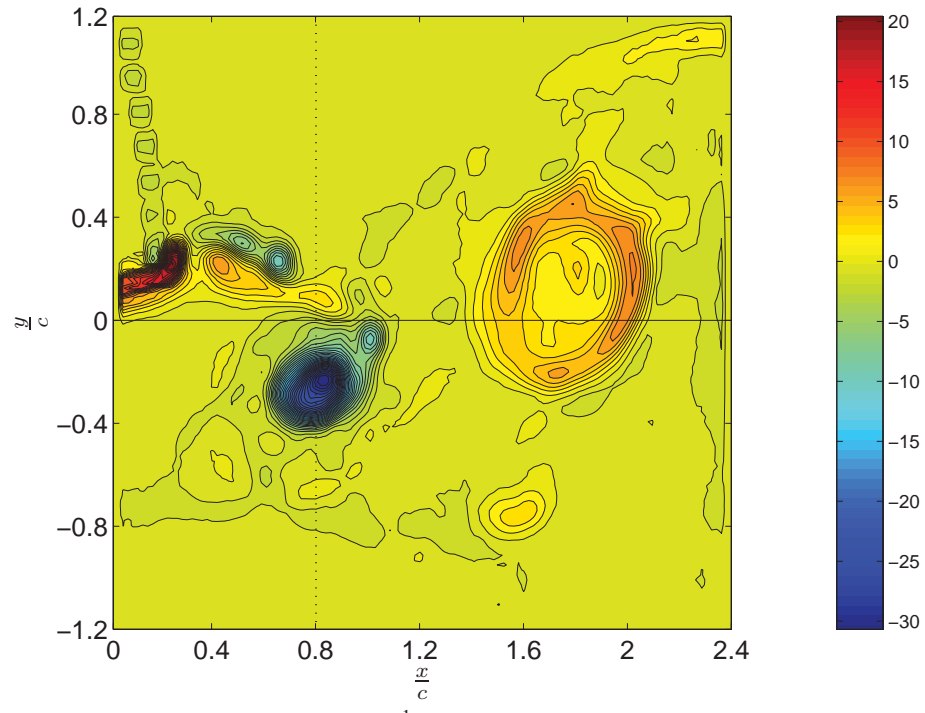


(b) Velocity profile along $x/c = 0.8$

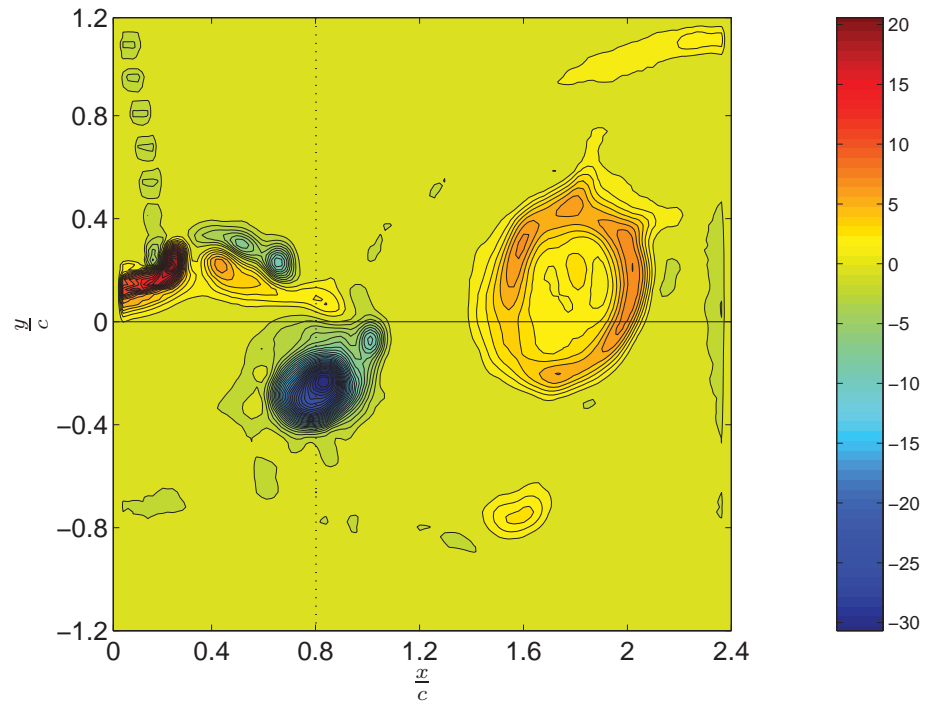


(c) Velocity profile along $x/c = 0.8$, in the range of $y/c \approx 0.85 - 1.2$

Figure 2.11: Example of a typical phase-averaged flapping foil velocity field (continued)

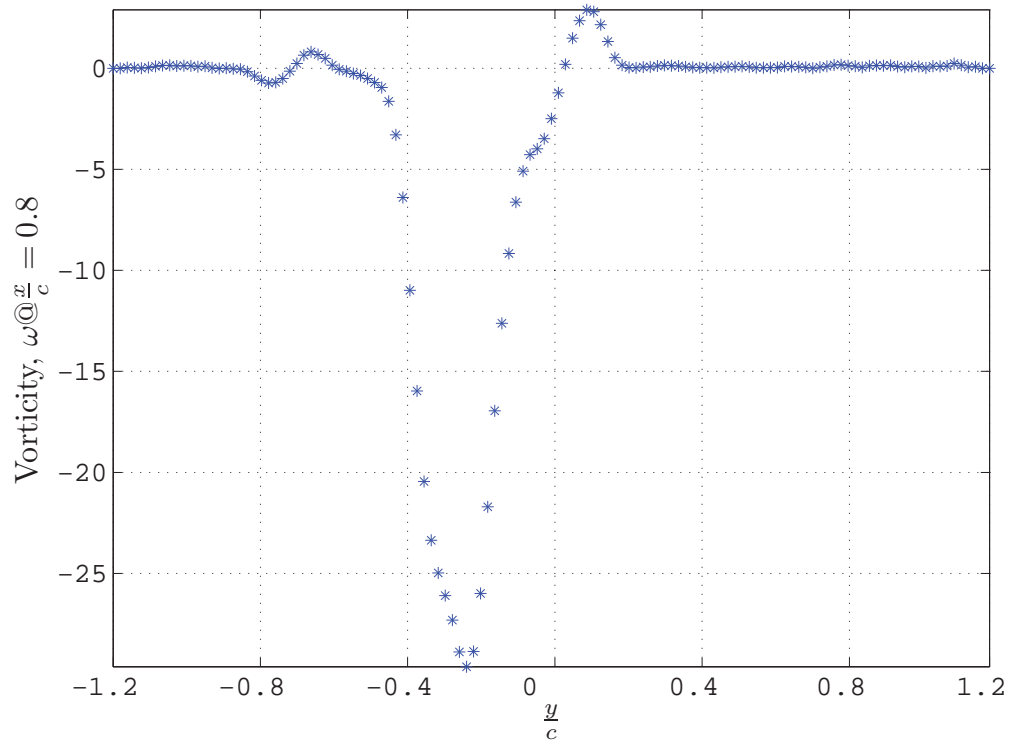


(a) Vorticity contours with $\omega_t = 0.2 \frac{1}{s}$. Note that the vorticity in the upper left hand corner of the image is artificial, due to the shadow of the foil

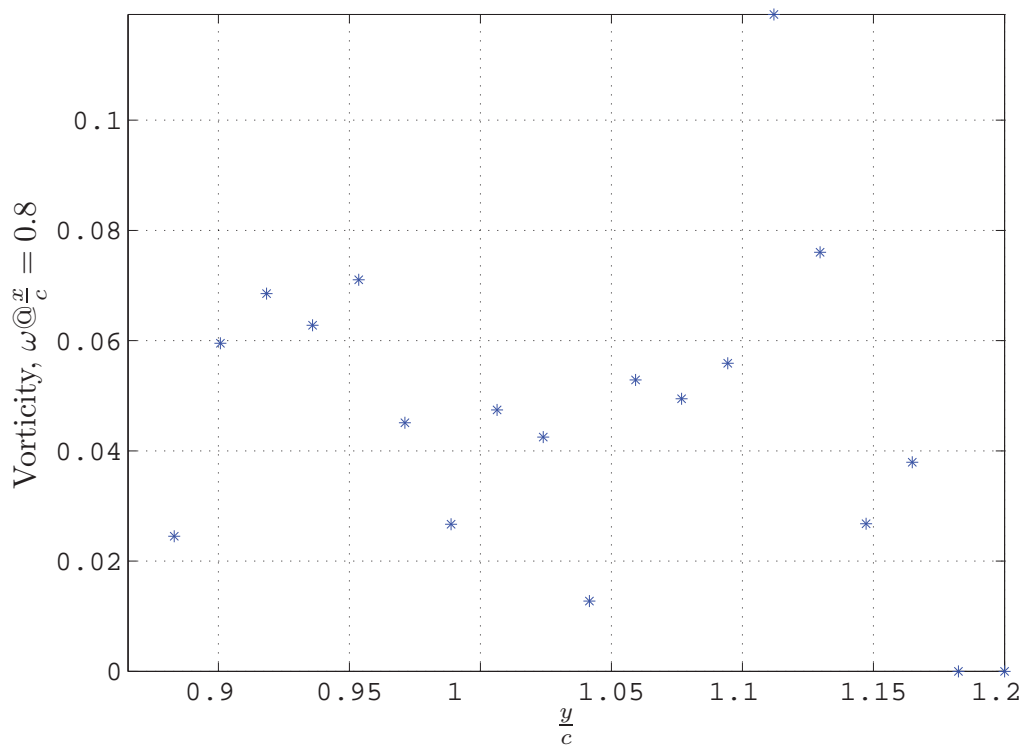


(b) Vorticity contours with $\omega_t = 0.4 \frac{1}{s}$. Note that the vorticity in the upper left hand corner of the image is artificial, due to the shadow of the foil

Figure 2.12: Example of a typical flapping foil vorticity field, derived from phase-averaged velocity data. Vorticity contour colorbars are in units of $\frac{1}{s}$ (continued on next page)



(c) Vorticity profile along $\frac{x}{c} = 0.8$



(d) Vorticity profile along $\frac{x}{c} = 0.8$, in the range of $\frac{y}{c} = 0.85 - 1.2$

Figure 2.12: Example of a typical flapping foil vorticity field, derived from phase-averaged velocity data. Vorticity contour colorbars are in units of $\frac{1}{s}$ (continued)

2.5.4 Smoothing of velocity vectors

In light of the low value of random errors in the phase averaged velocity field described above, no smoothing was performed on either the instantaneous or the phase averaged velocity field.

2.5.5 Estimation of vorticity and circulation

One of the key steps in the post-processing of the data is the estimation of the vorticity field, due to the fact that in many instances, the vorticity field can provide a wealth of information. The vorticity field can only be obtained by differentiating the velocity field; for discrete data, nine different methods of numerically differentiating the velocity field were considered, namely the a) centre difference scheme, b) poly-4 scheme, c) least squares scheme, d) Richardson-6 scheme, e) circulation-3 method, f) circulation-5 method, g) compact-4 scheme, h) compact-6 scheme, and i) the hybrid-CR4 scheme (Etebari and Vlachos, 2005; Raffel *et al.*, 1998; Hassan *et al.*, 2007). Due to the importance of this post-processing step, each of these methods are defined, compared and discussed in Appendix C. This is done by discretising the velocity field of an analytical Oseen vortex into a square grid with a particular resolution. Random noise is added into the discretised velocity data, and the noisy velocity data are processed using these vorticity estimation schemes. The vorticity estimates produced by each scheme are then compared to the analytic vorticity values of the Oseen vortex. Each vorticity estimation scheme is judged based on a number of criteria; a) its random noise transmission, b) the bias error in vorticity, and c) its ability to accurately and consistently estimate circulation.

Based on this analysis, the following conclusions can be made:

1. Each vorticity estimation scheme introduces a vorticity bias error and transmits the random error in the velocity field into the vorticity field;
2. The transmission of random errors from the velocity field into the vorticity field can be quantified analytically;
3. In most cases, the random error transmission and bias errors show opposite trends; it is difficult to reduce both the random and bias errors simultaneously;
4. Of all vorticity estimation schemes investigated, the scheme with the lowest random noise transmission ratio is the circ-5 scheme, whereas the scheme with the highest random noise transmission ratio is the Richardson-6 scheme;

2.5 Post - processing of PIV data

5. When evaluating circulation, the velocity integral is less sensitive to random noise in velocity than the vorticity integral;
6. The bias and random errors in the estimation of circulation are more sensitive to random noise than the bias error in the vorticity field, and therefore, to compute the circulation accurately, a circulation estimation scheme with a low random noise transmission ratio should be chosen, or the velocity field should be smoothed prior to the evaluation of circulation;
7. The best scheme for the purposes of estimating circulation is the circ-5 scheme.

2.5.5.1 Estimation of vorticity

Based on the conclusions above, the circ-5 scheme is used to estimate vorticity (which will eventually be used in the process of estimating circulation). The circ-5 method estimates the vorticity at any given point i, j by computing the circulation around a 5x5 velocity kernel around the point i, j , and dividing the circulation by the area of the kernel (see Figure 2.13), that is

$$\omega_{i,j} \approx \frac{\Gamma_{i,j}}{16\Delta^2} \quad (2.36)$$

where

$$\begin{aligned} \Gamma_{i,j} = & \frac{1}{2}\Delta(u_{i-2,j-2} + 2u_{i-1,j-2} + 2u_{i,j-2} + 2u_{i+1,j-2} + u_{i+2,j-2}) \\ & + \frac{1}{2}\Delta(v_{i+2,j-2} + 2v_{i+2,j-1} + 2v_{i+2,j} + 2v_{i+2,j+1} + u_{i+2,j+2}) \\ & - \frac{1}{2}\Delta(u_{i+2,j+2} + 2u_{i+1,j+2} + 2u_{i,j+2} + 2u_{i-1,j+2} + u_{i-2,j+2}) \\ & - \frac{1}{2}\Delta(v_{i-2,j+2} + 2v_{i-2,j+1} + 2v_{i-2,j} + 2v_{i-2,j-1} + u_{i-2,j-2}) \end{aligned}$$

and u and v are the x and y components the velocity, respectively, while Δ is the velocity grid spacing.

2.5.5.2 Errors in the vorticity field

The errors in the vorticity field can be estimated using the equation (see appendix C)

$$K_{scheme} = \frac{\sigma_{\omega}}{\sigma_u} \cdot \Delta \quad (2.37)$$

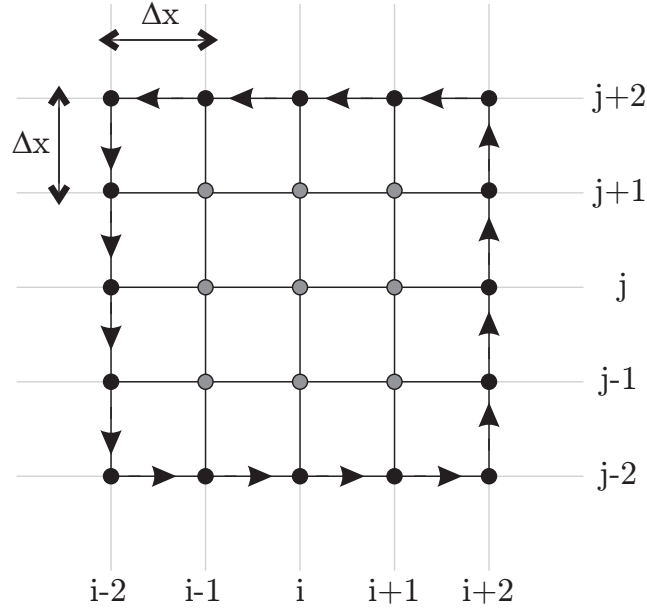


Figure 2.13: The circ-5 vorticity estimation scheme

where K_{scheme} is the random noise transmission coefficient of the vorticity estimation scheme used, σ_ω is a measure of the random noise in the vorticity field, and $\sigma_u = \epsilon_u \cdot U_\infty$ is a measure of the random noise in the velocity field. For the circ-5 scheme, $K_{scheme} = 0.2339$. For a typical experimental value of $\Delta \approx 1.2$ mm/pixel, $U_\infty \approx 100$ mm/s, and a random error in the phase-averaged velocity of $\epsilon_{u,pa} = 0.0035$ (see Section 2.5.3.3), the random error in the phase-averaged vorticity field is

$$\begin{aligned} \sigma_\omega &\approx \frac{K_{circ-5}}{\Delta} \cdot \epsilon_u \cdot U_\infty \\ &\approx 0.1 \frac{1}{s} \end{aligned}$$

This value of σ_ω can also be verified by looking at a vorticity profile taken from a PIV vorticity field, as shown in Figures 2.12c and 2.12d, which is taken along the axis $\frac{x}{c} = 0.8$ of the vorticity field shown in Figure 2.12b (dashed black line). The errors in vorticity, estimated directly from the experimental vorticity field, are also on order of $\sigma_\omega \approx 0.1 \frac{1}{s}$.

Since typical peak vorticity values in the field are approximately $\omega_{max} \approx 30 - 60 \frac{1}{s}$, the error in the vorticity, relative to the peak vorticity is in the range of

$$\epsilon_\omega \approx 0.15 - 0.35\%$$

2.5.5.3 Estimation of circulation

To compute the circulation, we use the velocity integral

$$\Gamma_{vel} = \oint_l \vec{V} \cdot d\vec{l} \quad (2.38)$$

where l is the path of integration, and \vec{V} is the velocity vector.

Circulation is computed by first defining a path of integration, l . The evaluation of the path of integration l is done by defining a starting location, which could be entered manually by the user or alternatively, a generic property of the vorticity field could be specified (the peak value of vorticity, for example). Generally however, the user manually inputs the location of a point that is visibly enclosed by an iso-vortical contour of a particular vortical structure of interest. From this starting point, the path of integration then expands out towards the boundaries until it reaches a maximum radius, or a vorticity threshold limit, ω_t , both which are set by the user. The resulting closed path is then the path l . This process is repeated for all vortical structures of interest. Note that this process is also described in Appendix C.

For all flow cases, the vorticity threshold limit was set to $\omega_t = 0.4 \frac{1}{s}$, which was sufficiently large to ensure that most of the noise in the vorticity field was not included while sufficiently small to ensure that most of the true vorticity was included in the estimation of circulation. The effect of the threshold limit is evident in Figures 2.12a ($\omega_t = 0.2 \frac{1}{s}$) and 2.12b ($\omega_t = 0.4 \frac{1}{s}$), which show typical vorticity field data.

2.5.5.4 Errors in circulation

The only viable method to estimate the errors in the evaluation of circulation is to use results from the numerical simulations described in Appendix C. To properly estimate the errors in circulation, we must firstly estimate the resolution of the PIV data, relative to the vortical structures of interest, $\frac{\Delta}{L}$, where $2L$ is the radius of vortical structure of interest, roughly measured as the radius which contains approximately 95% of the vorticity within that structure. The value of $\frac{\Delta}{L}$ varies between and within experimental sets, however, based on a number of typical flapping foil experiments (see Figures 2.11 and 2.12), it is estimated that $\frac{\Delta}{L} \approx 0.29$ (that is, approximately 15 vectors across a vortical structure). The random noise in the velocity has already been estimated as $\epsilon_u = 0.0035$ (see Section 2.5.3.3). For the circ-5 scheme, with no smoothing, it is estimated that the total error in the circulation is less than 2%.

2.6 Implementation of strain gauge measurements

One of the main aims of the flapping foil experiments is to determine the forces developed by the flapping foil, and furthermore, the efficiency of the flapping foil at various foil kinematic parameters. To accomplish this, strain gauges were employed to measure a) the deflections of the foil shaft in the chordwise, C and normal, N directions, and b) the deflections of the follower (pitch moment). These three independent deflections were measured using 4 strain gauges each, set up in a Wheatstone-bridge arrangement. This allows consistent measurements of strain, independent of the room temperature. All strain gauge measurements were run simultaneously with PIV to ensure that results from the strain gauge measurements and the PIV can be directly compared.

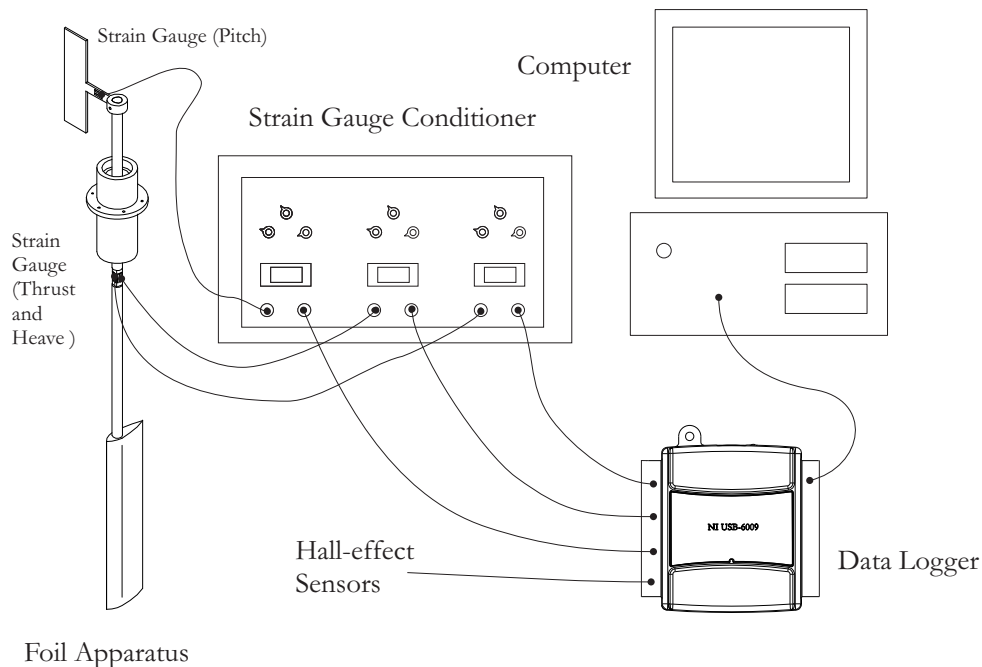
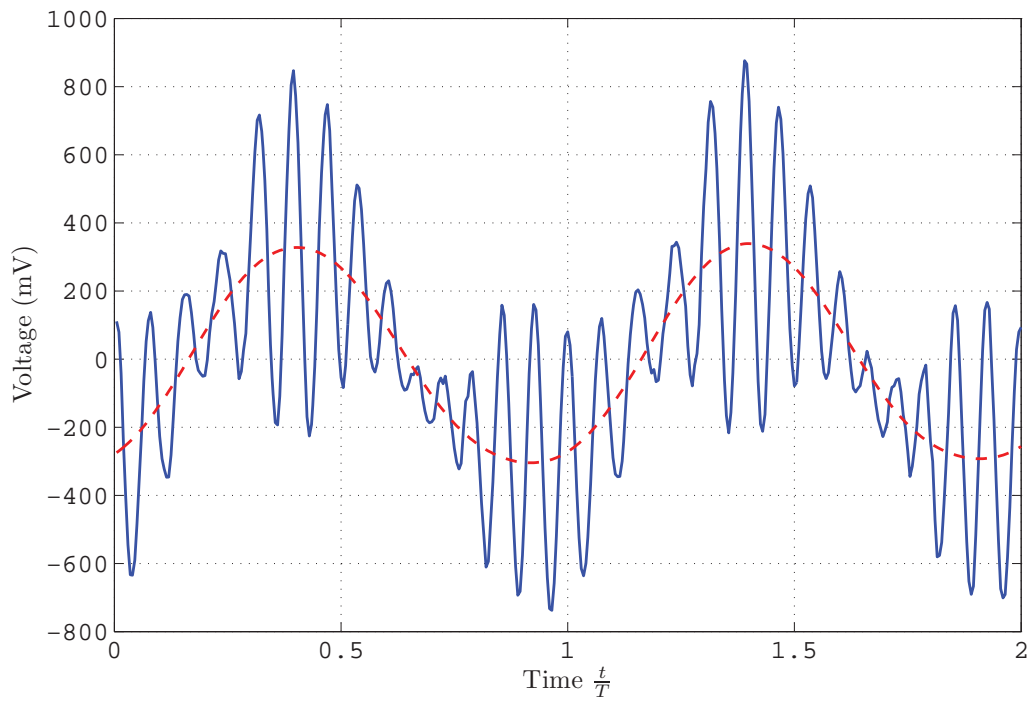


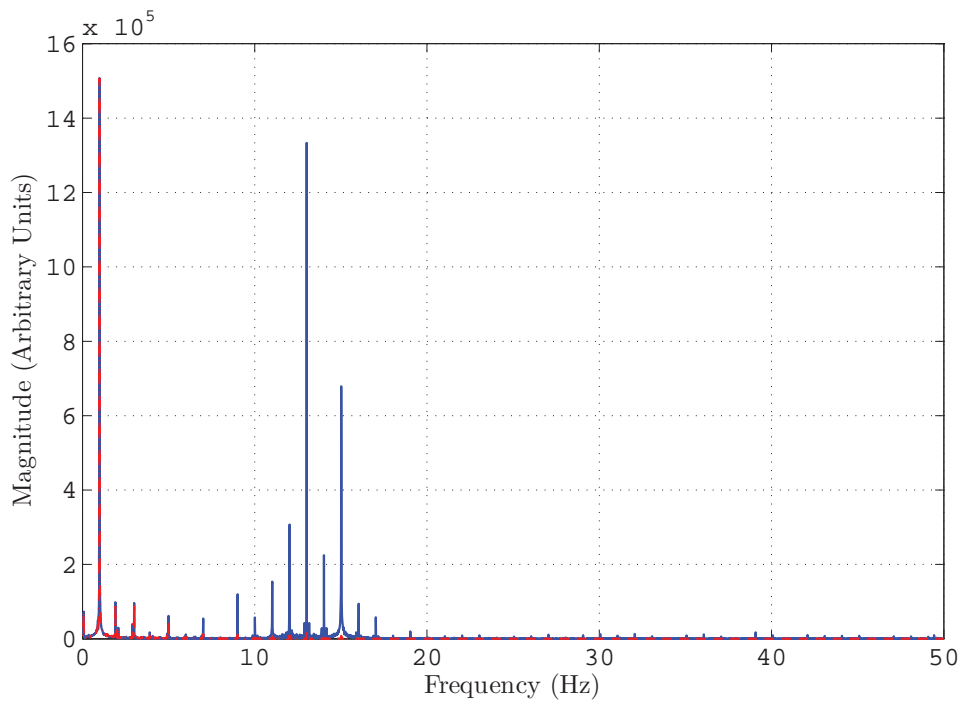
Figure 2.14: Force measurement system

The strain gauges were connected to a variable-gain, 3-input strain gauge conditioning circuit. The voltage output from the strain gauge conditioning circuit was then connected to the differential input of a 14-bit NI-USB 6009 data logger, which in turn was connected to a computer via a USB port (see Figure 2.14). The outputs from the hall-effect sensors were also connected to the data logger, allowing the voltage measurements to be synchronised with the motion of the foil. The gain in the strain gauge conditioning circuit was varied in each experimental case to utilise the entire voltage range of the data logger, hence minimising digital truncation errors produced by the data logger.

2.6 Implementation of strain gauge measurements



(a) Voltage measurement from strain gauge normal to the foil chord



(b) Frequency response of strain gauge measurement normal to the foil chord

Figure 2.15: Example of filtered and unfiltered strain gauge measurement (normal to the foil chord) of a flapping foil

The measurements were recorded using Labview 7.1. The sampling rate was set to 200Hz across all experimental cases, and typical recording time for each case was approximately 10 minutes, therefore giving approximately 120,000 data points per experimental case.

At the beginning of each day, before the water channel was activated and before the flapping foil mechanism was turned on, the strain gauge readings were all reset to zero. At the end of each day, the strain gauge readings were again repeated when the water channel and flapping foil mechanism were turned off, to measure the drift in the voltage readings over the day. Furthermore, at the end of each experimental case, the water channel was completely drained and the strain gauge measurements were repeated to measure the forces on the foil due to its own inertia. It should be noted that even with the water channel completely drained of water, there would be a small aerodynamic force on the foil, however, this is expected to be very small, on order of 0.1% of the hydrodynamic force.

A power spectrum of the voltage values was obtained using a discrete fast-fourier-transform (FFT), computed using Matlab. The power spectra of all three voltage components display peaks at the same locations, and in particular, a strong peak corresponding to the flapping foil frequency, as expected. However, one other significant peak is also noticeable, at 13.6 Hz. This peak was observed even when the foil was not in motion (i.e., the stepper motors were turned off). Therefore, it is postulated that the source of this unwanted noise is due to the unavoidable vibrations triggering resonance frequencies in the physical experimental setup, in spite of the application of vibration isolators at various junctions within the experimental setup.

To reduce the noise in the voltage signal, the signal was processed using an order-4 Butterworth filter with a cutoff frequency of 5 Hz. An example of a voltage signal along with its frequency response, obtained from the heave strain gauge, is shown in Figure 2.15. Once the filtered sample was obtained, a phase-averaged voltage sample was then evaluated by averaging all the voltage values across the entire sample which occur at the same foil phase (where the phase is determined with reference to the hall-effect sensor).

The phase averaged voltage sample contains both inertial and hydrodynamic forces on the foil. To isolate the voltage signal due to hydrodynamic forces alone, the voltage signal due to the inertia of the foil, which was also filtered and phase-averaged, was subtracted from the original voltage sample.

The strain gauges were calibrated by hanging known masses at various locations along the foil. Weights hung normal to the planform area provide calibration for the normal component of force, $F_N(t)$, while weights hung parallel to the chord of the foil provide calibration for the chordwise component of force, $F_C(t)$. To obtain the moments produced by the foil, $M_\theta(t)$, calibration was performed by hanging weights at different locations perpendicular to the follower's

2.7 Flow visualisation

surface. This results in three force/moment components, $F_C(t)$, $F_N(t)$ and $M_\theta(t)$ (see Figure 2.6). Finally, these force measurements were converted into global co-ordinate system force components, using the formula

$$F_{T,sg}(t) = -F_C(t) \cdot \cos \theta(t) + F_N(t) \cdot \sin \theta(t) \quad (2.39)$$

$$F_{S,sg}(t) = -F_C(t) \cdot \sin \theta(t) - F_N(t) \cdot \cos \theta(t) \quad (2.40)$$

$$M_{\theta,sg}(t) = M_\theta(t) \quad (2.41)$$

where $F_{T,sg}$, $F_{S,sg}$ and $M_{\theta,sg}$ are the thrust force, side force, and moment on the foil, due to hydrodynamic forces only, as measured using strain gauges.

2.7 Flow visualisation

Two different flow visualisation techniques were employed to study the flow around the heaving and pitching hydrofoil. In initial experiments, dye, which was ejected from the leading edge of the foil, was used to visualise the flow around the mid-span of the foil. These initial experiments have already been described in Lau *et al.* (2004), and consisted of 113 different flow cases.

Further flow visualisation was performed on the unsteady foil at foil kinematic conditions specifically chosen to match, wherever possible, the conditions of the PIV and strain gauge experiments. Using a hydrogen bubble wire which spans the entire length of the foil from wingtip to wingtip, this flow visualisation experiment was performed with the intention of studying the three-dimensional flow patterns around the unsteady foil.

The hydrogen bubble technique works on the principle that when a negatively charged electrode is placed in water, positively charged hydrogen bubbles will form on the wire. These bubbles, which are clearly visible when illuminated, have a size on order of the diameter of the wire. Therefore, by using a thin wire, the size of the bubbles will be small enough to enable them to follow the flow faithfully. For a more detailed explanation of the hydrogen bubble method, the reader is referred to Chapter 2 of Smits and Lim (2000).

In the flapping foil experiments, the negatively charged electrode used was a $50\mu\text{m}$ diameter tungsten wire, which was wrapped around the entire span of the foil, on both sides, at approximately the line of maximum thickness of the foil. The position of the wire was adjustable, such that the distance from the wire to the surface of the foil could be varied. Ideally, the wire should be placed on the surface of the foil to ensure proper seeding of the foil boundary layer, however, in reality this was not practical as the hydrogen bubbles became attached to the surface of the

foil, therefore compromising the quality of the visualisation process. Thus, as a compromise, the hydrogen bubble was fixed at approximately 0.7mm away from the surface of the foil.

Images of the flow were captured at various locations along the water channel, most notably at locations A (side view), B (angled side view) and C (bottom view) as shown in Figure 2.16. Images were captured using a Canon EOS 20D digital still camera with a Canon EF 50mm f/1.4 USM lens and a Sony DCR-TRV900E 3CCD digital video camera. The Canon digital still camera was controlled using an in-house timing circuit, which triggered off the sensors mounted on the flapping foil mechanism. The digital camera timing circuit divided the flapping period by a preset amount, which was set to 50, and subsequently sent a pulse to the camera once every cycle but with a pre-calculated phase lag (which takes into account the pulse and shutter time delay), essentially allowing the camera to capture images at 50 equally-spaced phases of the flapping cycle.

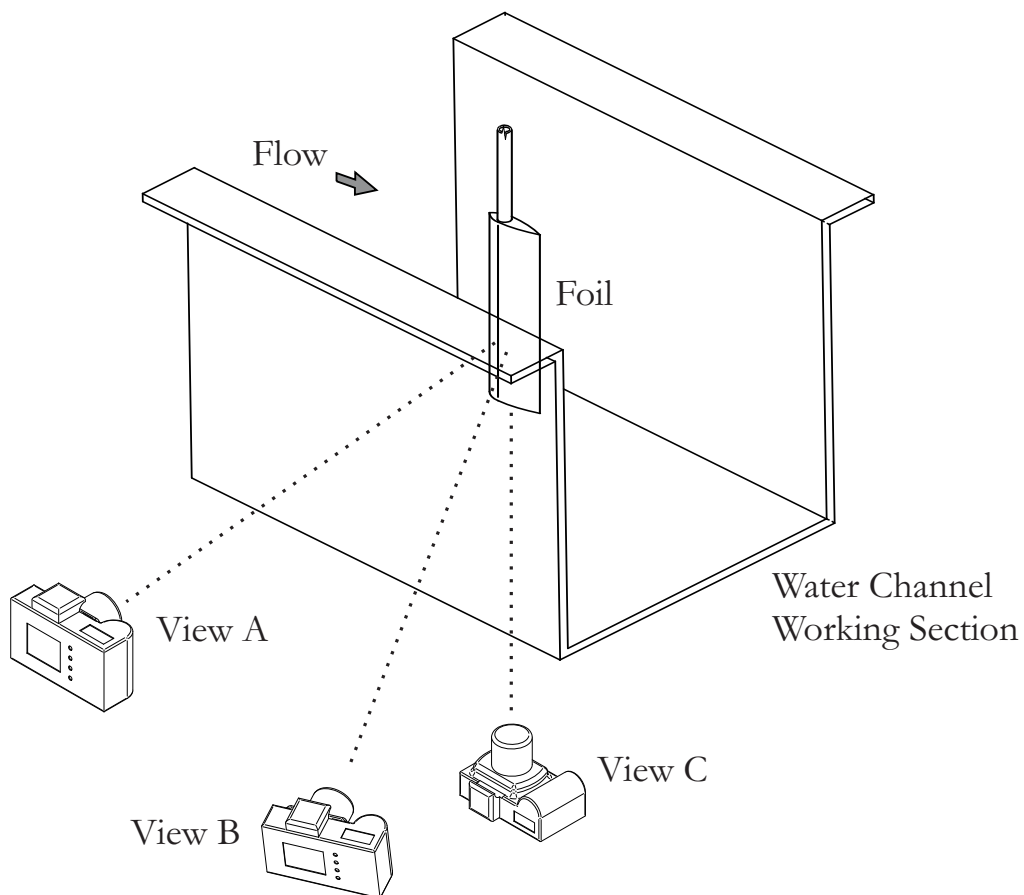


Figure 2.16: Hydrogen bubble imaging locations

2.8 Chapter summary

The hydrogen bubble experiments consisted of 38 flow cases which were chosen from the 106 flow cases performed in the PIV experiments. These 38 flow cases were repeated for two different Reynolds numbers. In the first instance, hydrogen bubble visualisation was performed at Reynolds numbers corresponding to the Reynolds number of the PIV experiment ($Re \approx 1,250 - 12,500$). These experiments were then repeated at lower Reynolds number ($Re \approx 500 - 3,500$). The lower Reynolds number experiments provide clearer flow visualisation at the expense that they may not be directly comparable to the PIV data.

2.8 Chapter summary

Simultaneous digital particle image velocimetry and force measurements were performed on a heaving and pitching hydrofoil in a water channel at $Re = 1,250 - 12,500$. The foil heaving motion was produced with a scotch yoke mechanism, while the pitching motion was produced using a cam-follower device. The foil heave and pitch amplitudes, as well as the flow rate and foil flapping frequency, were varied to produce 106 different flow cases.

Strain gauges located on the foil shaft and on the shoulder of the follower allowed force measurements to be obtained along three components of the foil, namely the foil chordwise force, normal force and pitching moment. The strain gauges were connected to a strain gauge conditioning system, which produced a voltage output for each of these force components. The voltages were then processed to remove noise using a 4-pole Butterworth filter with a 5 Hz cut-off frequency. Hydrodynamic forces were then obtained by subtracting the measured voltage due to the inertia of the foil system.

At the same time the force measurements were taken, PIV was simultaneously performed on the flapping foil. The images captured at each experimental case were first pre-processed by setting a dynamic threshold floor and ceiling value, and by using an anti-aliasing filter, before the images were cross-correlated to obtain a velocity field at each phase of the flapping foil. Typically for each experimental run, a minimum of 400 images were obtained for each phase. The vector fields at each phase were then phase averaged to obtain one velocity field per phase. Vorticity and circulation values were then extracted from this velocity field for further analysis using the circ-5 vorticity estimation scheme.

Quantitative planar flow visualisation via PIV is further supported with qualitative dye and hydrogen bubble flow visualisation of the flapping foil. The images of the flow were captured using a combination of a digital still camera and video camera, which were placed at various

locations around the water channel. Hydrogen bubble visualisation was performed for 38 different flow conditions, which were selected from the possible 106 flow conditions investigated using simultaneous PIV and force measurements.

Chapter 3

The Theoretical Quasi-Steady (Q-S) Model

3.1 Introduction

In this chapter, we attempt to predict the hydrodynamic forces on the unsteady foil based on the foil dynamics and classical steady-state aerodynamics. This is also known as the quasi-steady (Q-S) model. Fundamentally, the Q-S model is based on the argument that the forces on an unsteady foil at any given time are the same as the forces developed by a similar steady foil with the same geometric and dynamic foil parameters at that time. In essence, the Q-S model takes an instantaneous “snapshot” of the unsteady foil and applies steady-state hydrodynamic theory to that snapshot. Even though the Q-S model is flawed in many ways, it still may prove useful as a basis for comparison with experimental force measurements obtained experimentally.

In this thesis, the Q-S model is employed mainly to estimate the foil dynamics, in particular the time-averaged thrust coefficient, C_t , the time-averaged side force coefficient, C_s and the propulsive efficiency, η_F . This is done by predicting the instantaneous lift and drag forces produced by the foil using the quasi-steady concept. The framework of the quasi-steady concept applied to an airfoil can be traced back to Theodorsen (1935), however, the Q-S model discussed in this thesis was implemented specifically for the NACA0026 foil that was used in the physical experiments, and hence was implemented independently of existing literature.

3.2 Forces due to the foil lift

The lift coefficient of a static foil in a steady free-stream, based on the Q-S model and potential flow, is

$$C_L = k_{theory} \cdot \sin \alpha \quad (3.1)$$

where k_{theory} is some constant, which is dependent on the Reynolds number, as well as the geometry of the foil (for example, the foil aspect ratio and maximum thickness-to-chord ratio), and α is the angle of attack of the foil (Prandtl and Tietjens, 1934; Jones, 1940; Vallentine, 1967).

Equation 3.1 is usually invoked for low angles of attack, below the static stall angle of the foil, $\alpha_{static-stall}$. However, for the oscillating foil in these experiments, we shall assume that equation 3.1 holds for $0 \leq \alpha \leq \pi/2$ radians, that is, we shall assume that the foil never stalls.

At this stage it would be prudent to define the non-dimensional lift coefficient as

$$C_L = \frac{F_L}{\frac{1}{2}\rho U^2 \cdot c \cdot s} \quad (3.2)$$

where F_L is the lift force, ρ is the density of the fluid, U is an appropriate flow speed, c is the chord length of the foil, and s is the span of the foil. Thus, we can convert equation 3.1 into the instantaneous lift force,

$$F_L(t) = \frac{1}{2} \cdot \rho \cdot c \cdot s \cdot k_{theory} V_{eff}^2(t) \sin(\alpha(t)) \quad (3.3)$$

where $V_{eff}(t)$ is the effective velocity of the flow around foil (see Figure 2.6), defined as

$$V_{eff}(t) = \sqrt{U_\infty^2 + (h'(t))^2} \quad (3.4)$$

Furthermore, if we define the term $\gamma(t)$ as the angle between the foil centreline and the lift-component of force on the foil,

$$\gamma(t) = \frac{\pi}{2} - \arctan\left(\frac{h'(t)}{U_\infty}\right) \quad (3.5)$$

then equation 3.3 can then be divided into two components, the useful thrust force due to the lift, $F_{TL}(t)$, and the side force due to the lift, $F_{SL}(t)$

$$F_{TL}(t) = -\frac{1}{2} \cdot \rho \cdot c \cdot s \cdot k_{theory} \sin(\alpha(t)) (U_\infty^2 + h'(t)^2) \cdot \cos \gamma(t) \quad (3.6)$$

3.2 Forces due to the foil lift

$$F_{SL}(t) = \frac{1}{2} \cdot \rho \cdot c \cdot s \cdot k_{theory} \sin(\alpha(t)) (U_{\infty}^2 + h'(t)^2) \cdot \sin \gamma(t) \quad (3.7)$$

Equations 3.6 and 3.7 can be further reduced by making the simplification $z(t) = \pi St_h \cos \phi(t)$ where St_h is heave-based Strouhal, $St_h = \frac{2fh_0}{U_{\infty}}$,

$$\begin{aligned} F_{TL}(t) &= -1/2 \cdot \rho \cdot c \cdot s \cdot U_{\infty}^2 \cdot k_{theory} \sin \alpha(t) (z^2(t) + 1) \cdot \sin(\arctan(z(t))) \\ &= -1/2 \cdot \rho \cdot c \cdot s \cdot U_{\infty}^2 \cdot k_{theory} \sin \alpha(t) (z^2(t) + 1)^{\frac{1}{2}} \cdot z(t) \end{aligned} \quad (3.8)$$

$$\begin{aligned} F_{SL}(t) &= 1/2 \cdot \rho \cdot c \cdot s \cdot U_{\infty}^2 \cdot k_{theory} \sin \alpha(t) (z^2(t) + 1) \cdot \cos(\arctan(z(t))) \\ &= 1/2 \cdot \rho \cdot c \cdot s \cdot U_{\infty}^2 \cdot k_{theory} \sin \alpha(t) (z^2(t) + 1)^{\frac{1}{2}} \end{aligned} \quad (3.9)$$

3.2.1 Suitable values of k_{theory}

For a real symmetrical wing in a steady flow, equation 3.1 has been shown experimentally and computationally to be accurate up to the stall angle (Abbott and von Doenhoff, 1959; Jacobs, 1932; Loftin Jr. and Smith, 1949; Sheldahl and Klimas, 1981). However, the exact value of k_{theory} is dependent on the shape of the foil and the flow conditions, in particular the Reynolds number. For example, Prandtl and Tietjens (1934) analytically obtained the lift coefficients of a generic rectangular wing with an aspect ratio, $\Lambda = 5$, and obtained a value of $k_{theory} \approx 3.8$. This value is somewhat different to the commonly known analytical value of $k_{theory} = 2\pi$ for a infinitely long (two-dimensional) flat plate in a potential flow.

Experimentally, at large Reynolds numbers, Jacobs (1932) measured the lift and drag coefficients of a NACA 0012 foil with endplates at various angles of attack at $Re = 3.1 \times 10^6$. Jacobs obtained a value of $k_{theory} \approx 5.8$. Abbott and von Doenhoff (1959) published lift and drag coefficient curves for various wing sections at various Re . Based on these curves, for a NACA 0012 foil at $Re = 3 \times 10^6$, it can be estimated that $k_{theory} \approx 6.1$. Loftin Jr. and Smith (1949) measured the lift and drag on 15 different NACA foils, including a NACA 0012 foil. They obtained a value of $k_{theory} \approx 5.1$ for a two-dimensional flow over a NACA 0012 foil at $Re = 7 \times 10^5$. Sheldahl and Klimas (1981) experimentally measured the lift and drag values of various NACA 00-series foils for angles of attack within the range $0^\circ \leq \alpha \leq 180^\circ$ at $Re > 3.5 \times 10^5$. The results obtained are then extrapolated to lower Re with the aid of computational software. Based on Sheldahl and Klimas's results, it is estimated that $k_{theory} \approx 4$ for a NACA 0012 foil at $Re = 1 \times 10^4$ and $k_{theory} \approx 2.8$ for a NACA 0025 foil at $Re = 8 \times 10^4$. More recently, Akbari and Price (2003) computationally simulated the 2-D laminar flow over a NACA 0012 foil using a vortex method. They obtain a value of $k_{theory} \approx 2.6$ at $Re = 1 \times 10^4$.

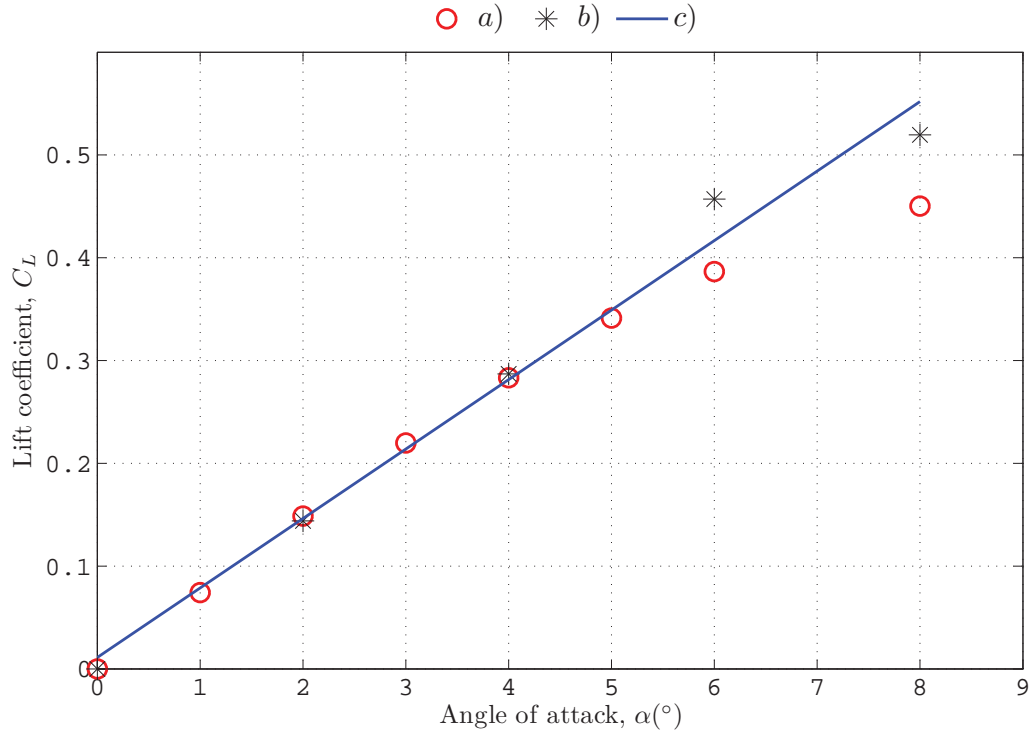


Figure 3.1: Steady-state lift coefficients vs α obtained a) numerically for a NACA 0025 foil at $Re = 8 \times 10^5$ (Sheldahl and Klimas, 1981), and b) experimentally for a NACA 0026 foil at $Re \approx 6,500$, performed at the University of Adelaide. c) is the linear curve fit of data from b)

At lower Reynolds numbers, Wu and Sun (2004) computationally studied the flow around a 3D flat plate of $\Lambda \approx 3$ with rounded leading and trailing edges at fixed angles of attack. For $Re > 100$, Wu and Sun obtain a value of $k_{theory} \approx 3$, which is consistent with the similar experimental results obtained by Usherwood and Ellington (2002b) and Dickinson *et al.* (1999).

To obtain a good estimation of the value of k_{theory} for the actual NACA 0026 foil (with $\Lambda = 4$) used in the current flapping foil experiments, the forces on the NACA 0026 foil were measured in a steady flow at $Re = 6,500$ at 10 different discrete angles of attack (at 2 degree increments) using the strain gauge setup as discussed in Section 4.

The results are shown in Figure 3.1 along with selected data from the findings of Sheldahl and Klimas (1981). Note that Figure 3.1 is only plotted to $\alpha = 8^\circ$ due to the fact that the foil was observed to stall at approximately $\alpha_{static-stall} \approx 8^\circ$. From a linear curve-fit of the strain gauge measurements, it is estimated that for the current NACA 0026 foil, the value of $k_{theory} \approx 3.9$, which will be the value used throughout this thesis. This result is consistent with the values provided in the literature for similar Reynolds numbers and aspect ratios, which are summarised in Table 3.1.

Wing shape	k_{theory}	Re	Source / Publication
NACA 0012, $\Lambda = \infty$	≈ 5.8	3.1×10^6	Jacobs (1932)
Rectangular Wing, $\Lambda = 5$	≈ 3.8	N/A	Prandtl and Tietjens (1934)
NACA 0012, $\Lambda = \infty$	≈ 5.1	7×10^5	Loftin Jr. and Smith (1949)
NACA 0012, $\Lambda = \infty$	≈ 6.1	3×10^6	Abbott and von Doenhoff (1959)
NACA 0012, $\Lambda = \infty$	≈ 4.0	1×10^4	Sheldahl and Klimas (1981)
NACA 0025, $\Lambda = \infty$	≈ 3.8	8×10^4	Sheldahl and Klimas (1981)
Flat plate, rounded L.E and T.E, $\Lambda \approx 3$	≈ 3.0	≈ 100	Dickinson <i>et al.</i> (1999)
Flat plate, rounded L.E and T.E, $\Lambda \approx 4.5 - 16$	$\approx 2.8 - 3.5$	$3 \times 10^3 - 1.1 \times 10^4$	Usherwood and Ellington (2002b)
Flat plate, rounded L.E and T.E, $\Lambda \approx 3$	≈ 3.0	≈ 100	Wu and Sun (2004)
NACA 0012, $\Gamma = \infty$	≈ 2.6	1×10^4	Akbari and Price (2003)
NACA 0026, $\Lambda = 4$	≈ 3.9	$500 - 1.25 \times 10^4$	Current Experiments

Table 3.1: Summary of values of k_{theory} obtained from literature and current experiments

3.3 Forces due to the foil drag

To obtain the forces developed by the unsteady foil due to drag, we start by defining the drag coefficient as

$$C_D = \frac{F_D}{\frac{1}{2}\rho U^2 c s} \quad (3.10)$$

where F_D is the drag force on the foil. The drag on the foil can be divided into two main components,

$$C_D = C_{Df} + C_{Di} \quad (3.11)$$

where C_{Di} is the induced drag of the foil, and C_{Df} is the combination of pressure drag and skin friction of the foil. At any given time, the induced drag of the foil is defined by the equation,

$$C_{Di} = \frac{k_i \cdot C_L^2}{\pi \Lambda} \quad (3.12)$$

where k_i is a correction factor for non-elliptical wings (typically $k_i > 1$), which was set to $k_i = 1.1$ (Clancy, 1975), and Λ is the aspect ratio of the wing. Therefore, the instantaneous drag force on the foil due to induced drag is

$$F_{Di}(t) = \frac{2k_i F_L^2(t)}{\pi \Lambda \rho c s (U_\infty^2 + h'(t)^2)} \quad (3.13)$$

where $F_L(t)$ is defined in equation 3.3.

To obtain C_{Df} , we have to rely on empirical data as there is no analytical equation that describes the value of C_{Df} as a function of the angle of attack of the foil.

To estimate the empirical equation of C_{Df} , we compare published drag values from sources previously listed in Section 3.2.1 above. The comparisons show that the results at high Reynolds numbers of Jacobs (1932), Abbott and von Doenhoff (1959), Loftin Jr. and Smith (1949) and Sheldahl and Klimas (1981) show very similar C_{Df} values across most Re , regardless of the shape of the foil. At low Re , the results of Dickinson *et al.* (1999), Usherwood and Ellington (2002b) and Wu and Sun (2004) are again consistent with each other, and show a similar trend to the drag values obtained at high Re , except that the magnitude of C_{Df} is approximately twice as high (see Figure 3.2).

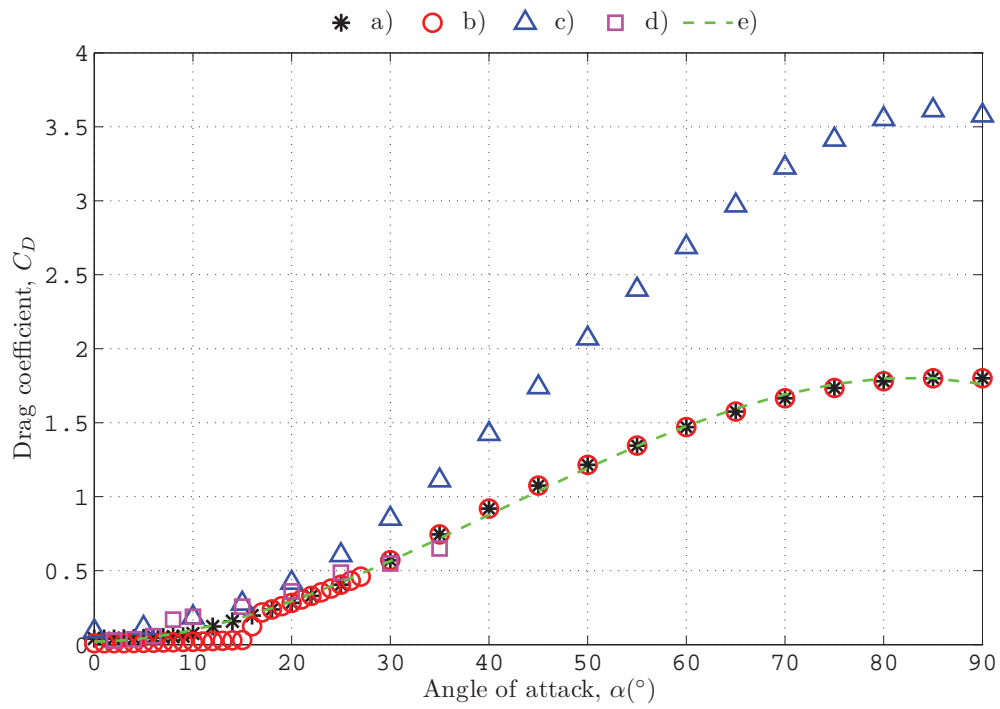


Figure 3.2: Steady-state drag coefficients vs α obtained a) numerically for a NACA 0025 foil at $Re = 1 \times 10^4$ (Sheldahl and Klimas, 1981), b) experimentally, for a NACA 0015 foil at $Re = 3.6 \times 10^5$ (Sheldahl and Klimas, 1981), c) computationally, for a flat plate at $Re \approx 1,800$ (Wu and Sun, 2004), and d) experimentally for a NACA 0026 foil at $Re \approx 6,500$, performed at the University of Adelaide. e) is the order-3 polynomial fit of data from a)

Furthermore, using the strain gauge measurements obtained around a steady NACA 0026 foil at various angles of attack which was performed in the University of Adelaide, we can obtain an estimate of the relationship between the foil drag coefficient C_D , and the angle of attack, α . Results are shown in Figure 3.2, plotted together with selected results from Sheldahl and Klimas (1981) and Wu and Sun (2004). Although our current strain gauge results are not in perfect agreement with results of Wu and Sun and Sheldahl and Klimas, the current results are consistently within the same order of magnitude. Notice the “jump” in the value of the drag measured by the strain gauges at $\alpha \approx 8^\circ$; this is where noticeable flow separation around the foil occurs (i.e. stall), corresponding to a sudden increase in the drag force.

As our results are slightly inconsistent, we chose to use the results of Sheldahl and Klimas to obtain the empirical relationship for C_D with respect to α . Using an order-3 curve fit of Sheldahl and Klimas’s numerical results for a NACA 0025 wing at $Re = 10,000$, we obtain

$$C_{Df}(t) \approx -1.158 |\alpha^3(t)| + 2.492 |\alpha^2(t)| + 0.0518 |\alpha(t)| + 0.02 \quad (3.14)$$

Note the use of the absolute value of the angle of attack, $|\alpha(t)|$, because it is assumed that the pressure drag and skin friction generated by the symmetrical foil are the same for both negative and positive angles of attack.

The instantaneous drag force on the foil due to pressure drag and skin friction is then

$$\begin{aligned} F_{Df}(t) &= 1/2 \rho c (U_\infty^2 + h'(t)^2) C_{Df}(t) \\ &= 1/2 \rho U_\infty^2 c s (z^2(t) + 1) C_{Df}(t) \end{aligned} \quad (3.15)$$

The thrust and side forces due to the total drag on the foil are then

$$\begin{aligned} F_{TD}(t) &= -(F_{Df}(t) + F_{Di}(t)) \cdot \sin \gamma(t) \\ &= -(F_{Df}(t) + F_{Di}(t)) \cdot \frac{1}{(z^2(t) + 1)^{\frac{1}{2}}} \end{aligned} \quad (3.16)$$

$$\begin{aligned} F_{SD}(t) &= (F_{Df}(t) + F_{Di}(t)) \cdot \cos \gamma(t) \\ &= (F_{Df}(t) + F_{Di}(t)) \cdot \frac{z(t)}{(z^2(t) + 1)^{\frac{1}{2}}} \end{aligned} \quad (3.17)$$

3.4 Forces due to added mass of the entrained fluid

As the foil moves through the fluid, it accelerates and displaces surrounding fluid, which causes an additional side force component on the foil, F_{SV} . This force is estimated using the “virtual”

3.5 Total lift and drag coefficients

or “added” mass method, which estimates that the volume of fluid affected by the motion of the foil can be approximated by the volume of a cylinder encompassing a projected chord length of the foil, as shown in Figure 3.3.

The volume of the virtual cylinder is

$$\begin{aligned}\forall_{virtual}(t) &= \pi \frac{c_{projected}^2}{4} \cdot s \\ &= \pi \frac{c^2 s}{4} \sin^2 \alpha(t)\end{aligned}\quad (3.18)$$

where $c_{projected}$ is the projected chord of the foil.

The force due to the added or virtual mass is then

$$F_{SV}(t) = \rho \cdot \forall_{virtual}(t) \cdot V'_{eff}(t) \quad (3.19)$$

Using equations 2.10, 3.4, 3.19, and recalling that $St_h = \frac{2 \cdot f \cdot h_0}{U_\infty}$, $St_c = \frac{f \cdot c}{U_\infty}$ and $z = \pi \cdot St_h \cdot \cos \phi(t)$, we can show that

$$F_{SV}(t) = \frac{1}{2} \rho U_\infty^2 c s \pi^3 \cdot St_h \cdot St_c \cdot \sin \phi(t) \cdot \sin^2 \alpha(t) \cdot z(t) \cdot (z^2(t) + 1)^{-\frac{1}{2}} \quad (3.20)$$

3.5 Total lift and drag coefficients

Finally, the total instantaneous thrust and drag on the foil, predicted using the Q-S model, can be expressed as

$$F_T(t) = F_{TL}(t) + F_{TD}(t) \quad (3.21)$$

$$F_S(t) = F_{SL}(t) + F_{SD}(t) + F_{SV}(t) \quad (3.22)$$

3.6 Time averaged forces

In many instances it is useful to define the time-averaged values of kinematic parameters of the foil. As the motion of the foil is symmetric, the time averaged values across the whole foil period $0 \leq t \leq T$ is the same as the values averaged across $0 \leq \phi \leq \frac{T}{4}$, where $T = \frac{1}{f}$ is the flapping foil period, and f is the flapping foil frequency.

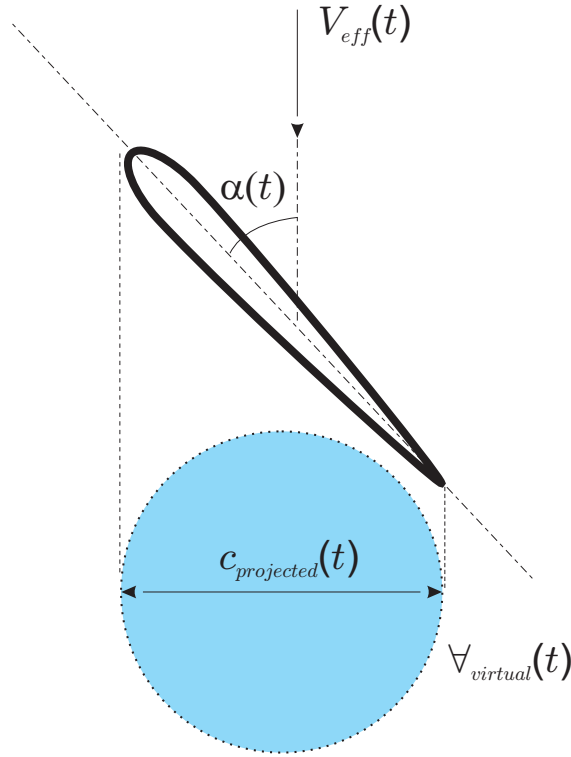


Figure 3.3: “Virtual mass” of fluid entrained by the foil

Thus we can define the time averaged thrust and side force coefficient (using small subscript t and s respectively) of the foil to be

$$C_t = \frac{\frac{4}{T} \int_0^{\frac{T}{4}} F_T(t) dt}{\frac{1}{2} \rho U_\infty^2 c s} \quad (3.23)$$

$$C_s = \frac{\frac{4}{T} \int_0^{\frac{T}{4}} F_S(t) dt}{\frac{1}{2} \rho U_\infty^2 c s} \quad (3.24)$$

3.7 Froude efficiency, η_F

We define the propulsive (Froude) efficiency of the foil to be

$$\begin{aligned} \eta_F &= \frac{\overline{F_T(t)} \cdot U_\infty}{\left| \overline{F_S(t) \cdot h'(t)} \right| + \left| \overline{M_\theta(t) \cdot \theta'(t)} \right|} \times 100\% \\ &= \frac{\int_0^{\frac{T}{4}} F_T(t) dt}{\left| \int_0^{\frac{T}{4}} F_S(t) dt \right| + \left| \int_0^{\frac{T}{4}} M_\theta(t) \cdot \theta'(t) dt \right|} \times 100\% \end{aligned} \quad (3.25)$$

3.8 Productivity

where $M_\theta(t)$ is the pitching moment on the foil, and $\theta'(t)$ is the angular velocity of the foil. For cases where the moments are small, or, where the pitch amplitudes are small or zero, then the Froude efficiency reduces to

$$\begin{aligned}\eta_F &\approx \frac{\overline{F_T(t)} \cdot U_\infty}{\overline{F_S(t) \cdot h'(t)}} \\ &\approx \frac{1}{\pi St_h} \cdot \frac{\int_0^{\frac{T}{4}} F_T(t) dt}{\left| \int_0^{\frac{T}{4}} F_S(t) \cos \phi(t) dt \right|}\end{aligned}\quad (3.26)$$

Note that if the drag on the foil is neglected, it can be shown that equation 3.26 reduces to $\eta_F = 1$ for all foil kinematic parameters and flow conditions.

3.8 Productivity

From equations 3.6 and 3.7, we can define a term analogous to the lift-to-drag ratio that is usually associated with efficiency of lifting surfaces; this term is denoted “productivity”,

$$\eta = \frac{\overline{F_T(t)}}{\overline{F_S(t)}} \times 100\% \quad (3.27)$$

$$= \frac{\int_0^{\frac{T}{4}} F_T(t) dt}{\left| \int_0^{\frac{T}{4}} F_S(t) dt \right|} \times 100\% \quad (3.28)$$

3.9 Behaviour of foil kinematics at high St_h

We can estimate the behaviour of the thrust, side forces, productivities, and propulsive efficiencies of the foil at high St_h based on the Q-S model. This is done by first neglecting the effect of the induced drag term (i.e. by setting $k_i = 0$), and by assuming that the effect of virtual mass of the entrained fluid is small (i.e. $F_{SV} \approx 0$). Then from equations 3.21 and 3.23 we obtain,

$$C_t = \frac{4}{T} \int_0^{\frac{T}{4}} \left[-k_{theory} \sin \alpha(t) (z^2(t) + 1)^{\frac{1}{2}} \cdot z(t) - (z^2(t) + 1)^{\frac{1}{2}} C_{Df}(t) \right] dt$$

At large values of St_h , we can make the approximation $(z^2(t) + 1)^{\frac{1}{2}} \approx z(t)$, therefore

$$C_t \approx \frac{4}{T} \int_0^{\frac{T}{4}} z(t) \cdot [-k_{theory} \sin \alpha(t) \cdot z(t) - C_{Df}(t)] dt$$

and furthermore, since $-k_{theory} \sin \alpha(t) \cdot z(t) - C_{Df}(t) \approx -k_{theory} \sin \alpha(t) \cdot z(t)$ and $\sin \alpha(t) \approx \sin(\theta_0 - \pi/2) \approx -\cos \theta_0$,

$$\begin{aligned} C_t &\approx \frac{4}{T} \int_0^{\frac{T}{4}} z(t) \cdot [k_{theory} \cos \theta_0 \cdot z(t)] dt \\ &\approx \frac{4}{T} k_{theory} \cos \theta_0 \int_0^{\frac{T}{4}} z^2(t) dt \\ &\approx \frac{k_{theory} St_h^2 \pi^2 \cos \theta_0}{2} \\ &\propto St_h^2, \cos \theta_0 \end{aligned}$$

Using similar arguments, and making the approximation $C_{Df} \approx C_{Df}^*(\theta_0) = -1.158(\theta_0 - \frac{\pi}{2})^3 + 2.492(\theta_0 - \frac{\pi}{2})^2 + 0.0518(\theta_0 - \frac{\pi}{2}) + 0.02$ for large St_h ,

$$\begin{aligned} C_{s,theory} &= \frac{4}{T} \int_0^{\frac{T}{4}} [-k_{theory} \sin \alpha(t) (z^2(t) + 1)^{\frac{1}{2}} - (z^2(t) + 1)^{\frac{1}{2}} \cdot z(t) C_{Df}(t)] dt \\ &\approx \frac{4}{T} \int_0^{\frac{T}{4}} z(t) \cdot [-k_{theory} \sin \alpha(t) - C_{Df}^*(\theta_0) \cdot z(t)] dt \\ &\approx \frac{4}{T} \int_0^{\frac{T}{4}} z(t) \cdot [C_{Df}^*(\theta_0) \cdot z(t)] dt \\ &\approx \frac{2C_{Df}^*(\theta_0)}{\pi} \int_0^{\frac{T}{4}} z^2(t) dt \\ &\approx \frac{\pi^2 St_h^2 C_{Df}^*(\theta_0)}{2} \\ &\propto St_h^2, \theta_0^3, \theta_0^2, \theta_0 \end{aligned}$$

The productivity at high St_h is then

$$\begin{aligned} \eta &= \frac{C_t}{C_s} \\ &\approx \frac{k_{theory} \cos \theta_0}{C_{Df}^*(\theta_0)} \end{aligned}$$

3.10 Vorticity distribution behind the foil

The propulsive efficiency is then approximated by

$$\begin{aligned}
 \eta_F &= \frac{1}{\pi St_h} \cdot \frac{\int_0^{\frac{T}{4}} F_T(t) dt}{\int_0^{\frac{T}{4}} F_S(t) \cos(t) dt} \\
 \eta_{F,theory} &\approx \frac{1}{\pi St_h} \cdot \frac{k_{theory} St_h^2 \pi^2 \cos \theta_0}{2} \cdot \frac{\pi}{2 C_{Df}^*(\theta_0) \int_0^{\frac{T}{4}} z^2(t) \cdot \cos(t) dt} \\
 &\approx \frac{3 k_{theory} \cos \theta_0}{8 St_h C_{Df}^*(\theta_0)} \quad (3.29)
 \end{aligned}$$

Note that the term $\frac{\cos \theta_0}{C_{Df}^*(\theta_0)}$ is an elaborate function of θ_0 (and powers of θ_0), however, it portrays an approximately linear function to θ_0 at low values of θ_0 , and approximately a linear function to θ_0^2 at higher values of θ_0 .

From the results above, using the Q-S model, for any given value of θ_0 it is predicted that the time averaged thrust and side force coefficients $C_{t,theory}$ and $C_{s,theory}$, are linearly proportional to St_h^2 at high values of St_h . More interestingly, the productivity η is independent of St_h , whereas the propulsive efficiency $\eta_{F,theory}$ is inversely proportional to St_h . This suggests that an unsteady foil produces optimal thrust at low values of St_h .

3.10 Vorticity distribution behind the foil

With the aid of the quasi-steady model, we can theoretically predict the amount of vorticity (in terms of circulation), of any given sign, that is shed per foil cycle. Furthermore, we can predict the distribution of this vorticity, and therefore, calculate geometric properties of the wake, such as the wake width, based on the quasi-steady model. This is done by considering two different mechanisms of generating vorticity by a “lifting surface”; firstly, the vorticity shed due to the change in the circulation of the bound vortex around the foil, and secondly, the vorticity shed due to the no-slip boundary condition on the foil surface.

3.10.1 Vorticity shed due to the foil bound vortex

If we assume that the Kutta condition holds, then we can obtain a relationship between the magnitude of the instantaneous lift force, $F_L(t)$ that the foil experiences, and the strength of the bound vortex on the foil, $\Gamma_{bound}(t)$ at any particular time t , using the equation

$$F_L(t) = \rho \cdot V_{eff}(t) \cdot \Gamma_{bound}(t) \cdot s \quad (3.30)$$

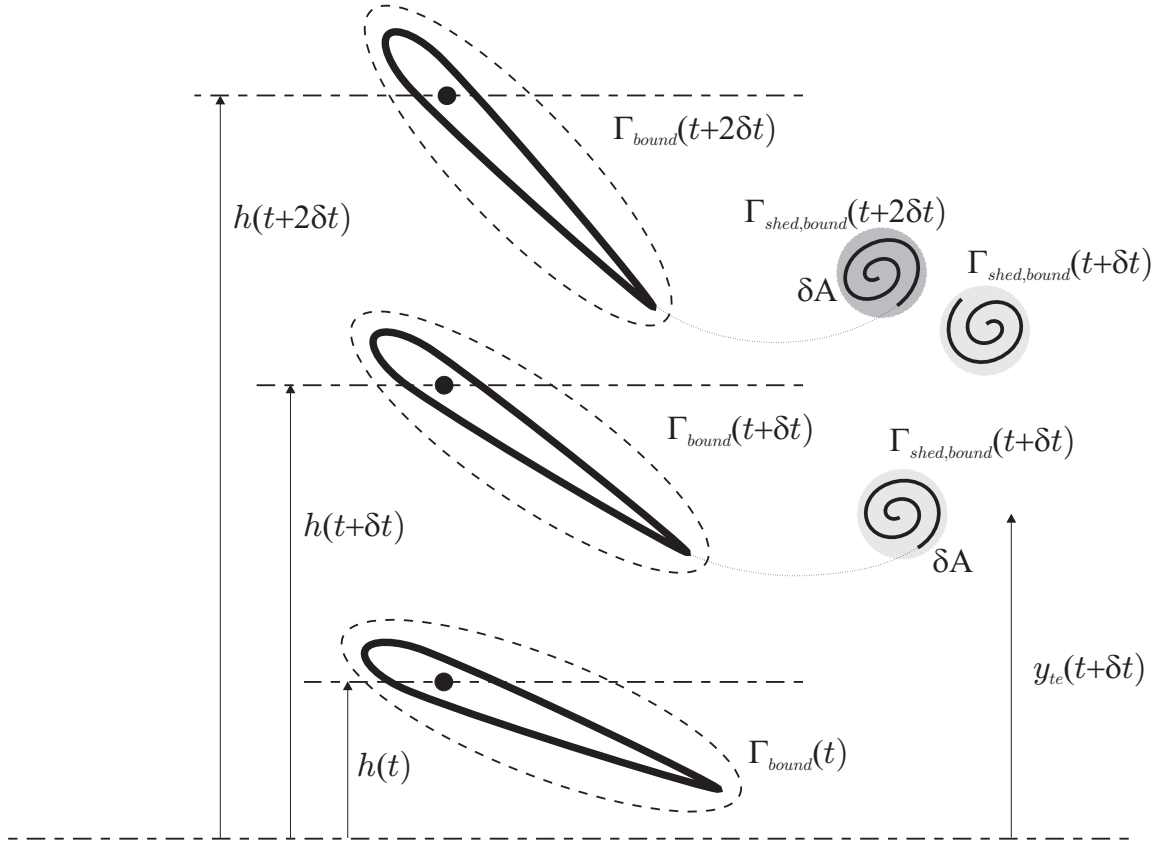


Figure 3.4: Vorticity shed into the wake of an unsteady foil due to the change in bound circulation

Equating 3.30 with the instantaneous lift force described in equation 3.3, we obtain

$$\Gamma_{bound}(t) = 0.5 \cdot V_{eff}(t) \cdot c \cdot k_{theory} \cdot \sin \alpha(t) \quad (3.31)$$

Kelvin's circulation theorem implies that any change in the bound circulation around the wing, $\Gamma_{bound}(t)$, has to be balanced by shed vorticity with circulation $\Gamma_{shed,bound}(t)$ of equal but opposite strength to the change in circulation of the bound vortex. The shed vorticity with circulation $\Gamma_{shed,bound}(t)$ is assumed to propagate into the wake as discrete vortical structures, each with an area δA , at a location $y_{shed}(t)$ (as shown in Figure 3.4). Therefore, at time $t + \delta t$,

$$\Gamma_{shed,bound}(t + \delta t) = \Gamma_{bound}(t + \delta t) - \Gamma_{bound}(t) \quad (3.32)$$

As $\delta t \rightarrow 0$, then

$$\Gamma_{shed,bound}(t) = \frac{d\Gamma_{bound}}{dt}(t) \cdot dt \quad (3.33)$$

3.10.2 Vorticity shed due to the no-slip boundary condition

Invoking the no-slip condition at the foil boundary, and assuming the Kutta condition is satisfied, then the fluid velocity at the trailing edge, $V_{f,te} = 0$, and thus the circulation along the path p_{te} (see Figure 3.5) is

$$\Gamma_{kutta} = \oint_{p_{te}} \vec{V} \cdot d\vec{l} \quad (3.34)$$

$$= \vec{V}_{eff,te} \cdot d\vec{l} - \vec{V}_{f,te} \cdot d\vec{l} \quad (3.35)$$

$$= \vec{V}_{eff,te} \cdot d\vec{l} \quad (3.36)$$

where the effective velocity of the trailing edge is,

$$\vec{V}_{eff,te} = \vec{U}_{\infty} + \vec{h}'(t) + 0.7 \cdot c \cdot \vec{\theta}'(t) \quad (3.37)$$

It should be noted that the term $0.7 \cdot c \cdot \vec{\theta}'(t)$ is the apparent flow velocity seen by the foil trailing edge due to the rotation of the foil. The value $0.7 \cdot c$ is derived from the fact that the foil pitching axis is 0.7 chord lengths away from the foil trailing edge. The path taken by a particle of fluid is $d\vec{l}$, where the particle of fluid is assumed to be moving at an average velocity of $\frac{\vec{V}_{eff,te} + \vec{V}_{f,te}}{2}$ for any given time δt , thus

$$d\vec{l} = \frac{\vec{V}_{eff,te} + \vec{V}_{f,te}}{2} \delta t \quad (3.38)$$

$$= \frac{\vec{V}_{eff,te}}{2} dt \quad (3.39)$$

as $\delta t \rightarrow 0$. Note that since the path p_{te} can be arbitrarily chosen such that $d\vec{l}$ is always parallel to $\vec{V}_{eff,te}$ without loss of generality, only the magnitude of the effective trailing edge velocity needs to be considered. Finally, equation 3.35 can be written as

$$\Gamma_{kutta}(t) = V_{eff,te}(t) \cdot d\vec{l} \quad (3.40)$$

$$= \frac{V_{eff,te}^2(t)}{2} \cdot dt \quad (3.41)$$

3.10.3 Total vorticity shed into the wake

If we assume that, for a very small change in time δt at time t , all vorticity of circulation $\Gamma_{kutta}(t)$ and $\Gamma_{shed,bound}(t)$ are shed into the wake homogeneously in a unit area δA at a location

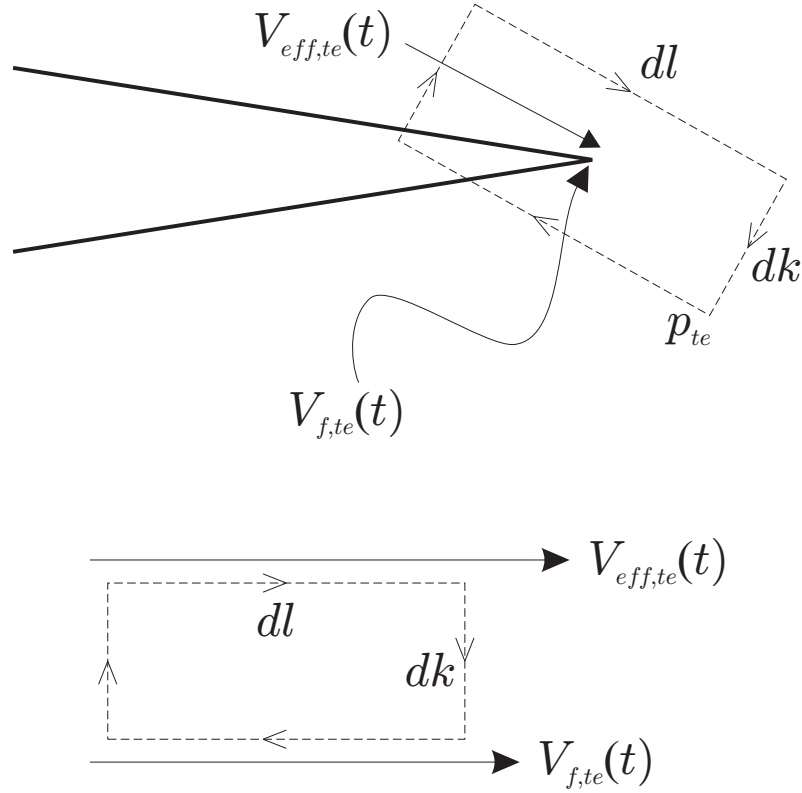


Figure 3.5: The vorticity shed at the trailing edge of the foil, due to the Kutta condition

corresponding to $y_{shed}(t)$ (as shown in Figure 3.4), and that there is no cross annihilation of vorticity of opposing sign, then the vorticity shed by the foil at any given point in time is simply

$$\omega_{kutta}(t) = \frac{1}{\delta A} \cdot \frac{V_{eff,te}^2(t)}{2} \cdot dt \quad (3.42)$$

and the vorticity shed due to the bound vortex on the wing is

$$\omega_{shed,bound}(t) = \frac{1}{\delta A} \cdot \frac{d\Gamma_{bound}}{dt}(t) \cdot dt \quad (3.43)$$

Thus, assuming the motion of the foil is symmetrical, the total amount of vorticity shed per foil cycle, of any given sign, will have a circulation of

$$\Gamma_{total} = 2 \oint_0^{\frac{T}{4}} [\omega_{shed,bound}(t) + \omega_{kutta}(t)] \cdot dt \cdot \delta A \quad (3.44)$$

$$= 2 \oint_0^{\frac{T}{4}} \left[\frac{d\Gamma_{bound}}{dt}(t) + \frac{V_{eff,te}^2(t)}{2} \right] \cdot dt \quad (3.45)$$

3.10 Vorticity distribution behind the foil

For convenience, we define the vorticity shed by the foil due to the transient change in bound circulation around the foil as the “primary” vorticity, while we define the vorticity shed by the foil due to the no-slip foil boundary condition and the Kutta condition as the “secondary” vorticity. Thus, we can define

$$\Gamma_{primary} = \oint_0^{\frac{T}{4}} \frac{d\Gamma_{bound}}{dt}(t) dt \quad (3.46)$$

and

$$\Gamma_{secondary} = \oint_0^{\frac{T}{4}} \frac{V_{eff,te}^2(t)}{2} dt \quad (3.47)$$

Therefore, equation 3.45 can be written as

$$\Gamma_{total} = 2 [\Gamma_{primary} + \Gamma_{secondary}] \quad (3.48)$$

Finally, we can normalise Γ_{total} with the freestream velocity and the chord length to obtain,

$$\tilde{\Gamma}_{total,c} = \frac{\Gamma_{total}}{U_{\infty} \cdot c} \quad (3.49)$$

3.10.4 Theoretical wake widths

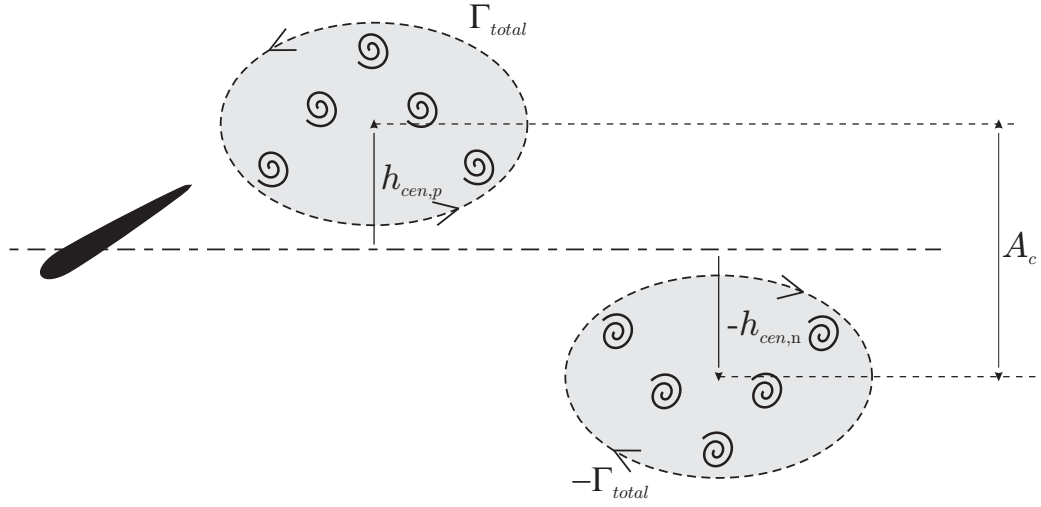
If we define $h_{cen,p}$ and $h_{cen,n}$ as the positions of the centroids of positive and negative vorticity respectively (as shown in Figure 3.6), then we can define a wake width based on the locations of the vorticity centroids,

$$A_c = -h_{cen,n} + h_{cen,p} \quad (3.50)$$

where the wake patterns are expected to be of a regular Karman-street form for $A_c < 0$, and a reverse Karman street form for $A_c > 0$. For $A_c \approx 0$, the wake pattern is defined to be transitional, and is expected to be of an in-line form.

If we assume that the motion of the foil is symmetrical, then

$$A_c = 2h_{cen,p} \equiv -2h_{cen,n} \quad (3.51)$$

Figure 3.6: Definition of wake width, A_c

The value of $h_{cen,p}$ can be obtained by super-imposing the centroid of the vorticity shed due to lift $h_{cen,p,shed,bound}$, and the vorticity shed due to the Kutta condition $h_{cen,p,kutta}$, where

$$h_{cen,p,shed,bound} = \frac{\int_0^{T/4} y_{shed}(t) \cdot \omega_{shed,bound}(t) \cdot dt}{\int_0^{T/4} \omega_{shed,bound}(t) \cdot dt} \quad (3.52)$$

and

$$h_{cen,p,kutta} = 0 \quad (3.53)$$

due to the fact that the vorticity shed at the trailing edge due to the Kutta condition is symmetrically shed along the centreline of the foil motion. Therefore, the centroid of the total positive vorticity shed throughout the foil cycle is

$$h_{cen,p} = \frac{h_{cen,p,shed,bound} \cdot \int_0^{T/4} \omega_{shed,bound}(t) \cdot dt + h_{cen,p,kutta} \cdot \int_0^{T/4} \omega_{kutta} \cdot dt}{\int_0^{T/4} \omega_{shed,bound}(t) \cdot dt + \int_0^{T/4} \omega_{kutta}(t) \cdot dt} \quad (3.54)$$

$$= \frac{h_{cen,p,shed,bound} \cdot \int_0^{T/4} \omega_{shed,bound}(t) \cdot dt}{\int_0^{T/4} \omega_{shed,bound}(t) \cdot dt + \int_0^{T/4} \omega_{kutta}(t) \cdot dt} \quad (3.55)$$

Finally, we normalise the wake width by the foil chord length, to obtain

$$\begin{aligned} \tilde{A}_c &= \frac{A_c}{c} \\ &= \frac{-2h_{cen,p}}{c} \end{aligned} \quad (3.56)$$

3.11 Numerical results

3.10.5 First moment of circulation, M_Γ

Of additional interest is the non-dimensional first moment of circulation of the vorticity shed into the wake of the unsteady foil, defined as

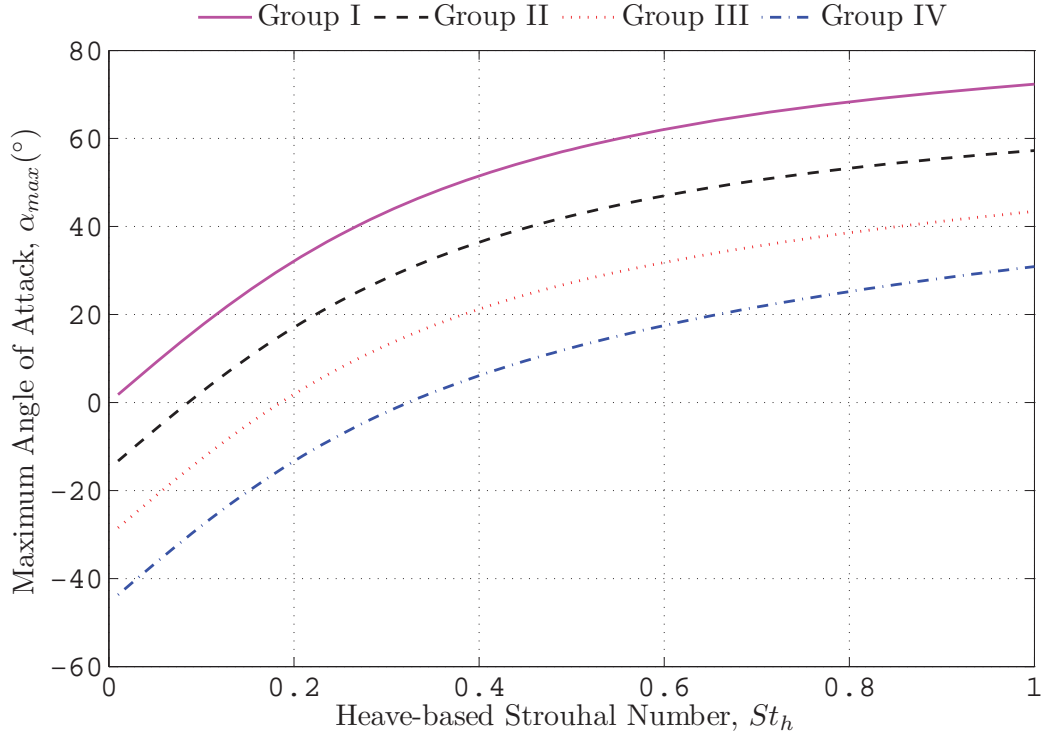
$$\tilde{M}_\Gamma = \tilde{\Gamma}_{total,c} \times \tilde{A}_c \quad (3.57)$$

The motivation for defining this term is based on the intuitive idea that a velocity surplus in the wake in a time-averaged sense can be generated by two means, firstly, by increasing the wake width \tilde{A}_c , and secondly, by increasing the strength of the shed circulation, $\tilde{\Gamma}_{total,c}$.

3.11 Numerical results

The Q-S model equations are solved numerically within the range $0 \leq St_h \leq 1$ for the foil kinematic parameters listed in Table 2.1. Where integrals are involved, the equations are numerically integrated using the trapezoidal method. Results are shown in Figures 3.8 to 3.10. The quasi-steady results for the time averaged thrust coefficient C_t , side force coefficient C_s , productivity η and propulsive efficiency η_F show collapse within each foil kinematic group (where groups are defined in Table 2.1) when plotted against St_h , indicating the importance of the Strouhal number.

However, as the maximum angle of attack achieved during an entire foil cycle, α_{max} is also of importance, we first reiterate the relationship between α_{max} and St_h , first discussed in Chapter 2. We illustrate this relationship, explicitly specified in equation 2.23, in Figure 3.7. Figure 3.7 indicates that α_{max} increases rapidly between $0 \lesssim St_h \lesssim 0.4$, and starts to level off as $St_h \approx 0.6$, although we do note that this is subjective. The maximum angles of attack are generally large, particularly for cases where the non-dimensional heave amplitude is large compared to the pitch amplitude (group I), where maximum angles of attack exceed 60° at $St_h = 1$. At $St_h \approx 0.2$, which is approximately the Strouhal number at which some steadily swimming fish have been observed to swim (see Chapter 1), the angles of attack are significantly lower, with $\alpha_{max} \approx 0 - 15^\circ$ for groups II-III. However, for the purely heaving hydrofoil (group I), the maximum angles of attack remain significantly large, on order of $\alpha_{max} \approx 30^\circ$ even at the moderate Strouhal number of $St_h = 0.2$.

Figure 3.7: Relationship between α_{max} and St_h

3.11.1 Foil dynamics

Figures 3.8a and 3.8b show the time-averaged thrust, C_t and side force coefficients, C_s respectively. The time-averaged thrust and side force coefficients increase non-linearly as St_h increases, and it appears that C_t is approximately proportional to St_h^2 , as predicted in Section 3.9. The time-averaged thrust coefficient C_t increases at a greater relative rate than C_s , as shown by the increasing productivity (η) values, shown in Figure 3.8c. The thrust coefficients approach very large values, particularly for groups I and II, where the non-dimensional heave amplitude is large relative to the pitch amplitude (i.e., χ is large); at $St_h = 1$, all groups except group IV, where χ is small, have $C_t > 10$. However, the generation of large thrust coefficients is also accompanied by the development of large time-averaged side forces, as shown by the low value of productivity at high χ . Furthermore, when χ is large, propulsive efficiencies, η_F , are generally low compared to cases where χ is small (see Figure 3.8d).

It is also interesting to note that even though the productivity, η , increases with St_h , the propulsive efficiencies, η_F decrease, and will eventually asymptote to 0 as $St_h \rightarrow \infty$ (see equation 3.29). Propulsive efficiencies peak at $St_h \approx St_{h,0,simp}$, where the thrust and side force coefficients are generally very small. Efficiencies are generally good for groups III and IV, where $\frac{h_0}{c}$ is small compared to θ_0 , with $\eta_F \approx 65 - 75\%$, although it has to be noted that the Q-S model neglects

3.11 Numerical results

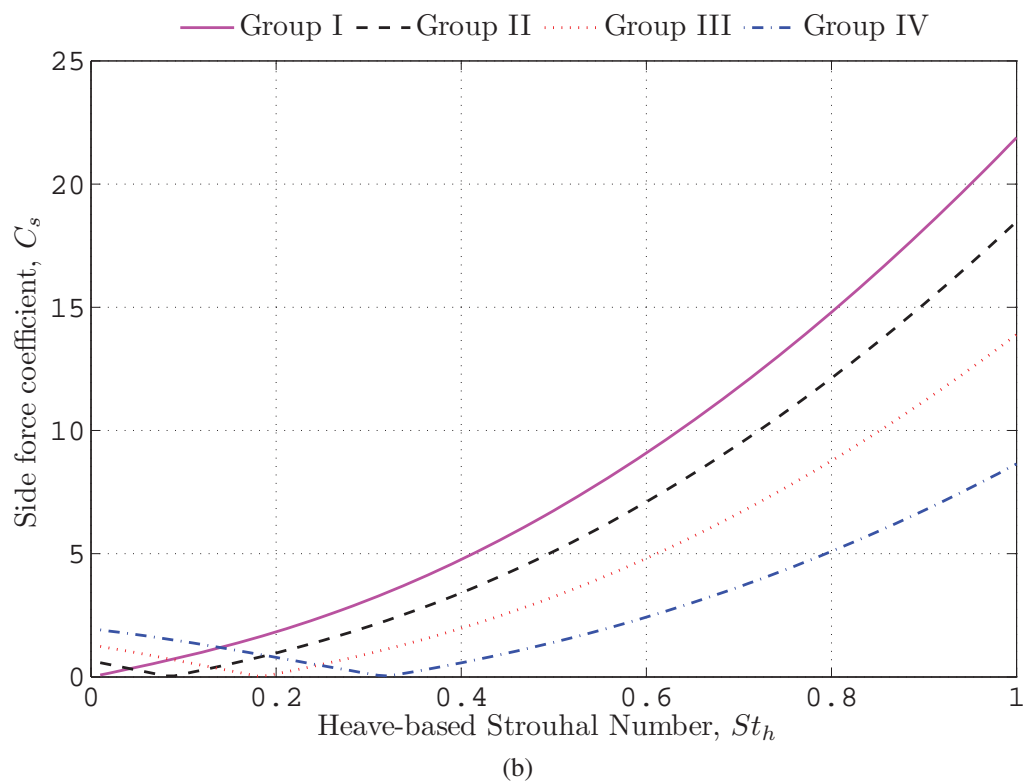
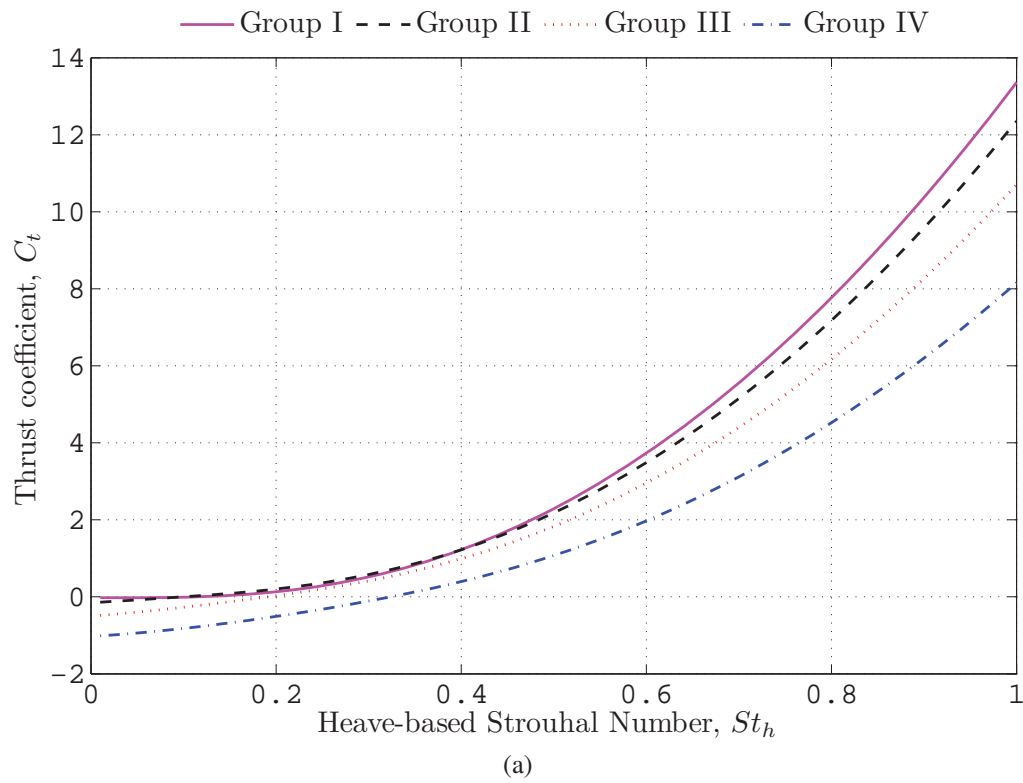


Figure 3.8: Predicted foil kinematic parameters as a function of St_h based on the Q-S model (continued on following page)

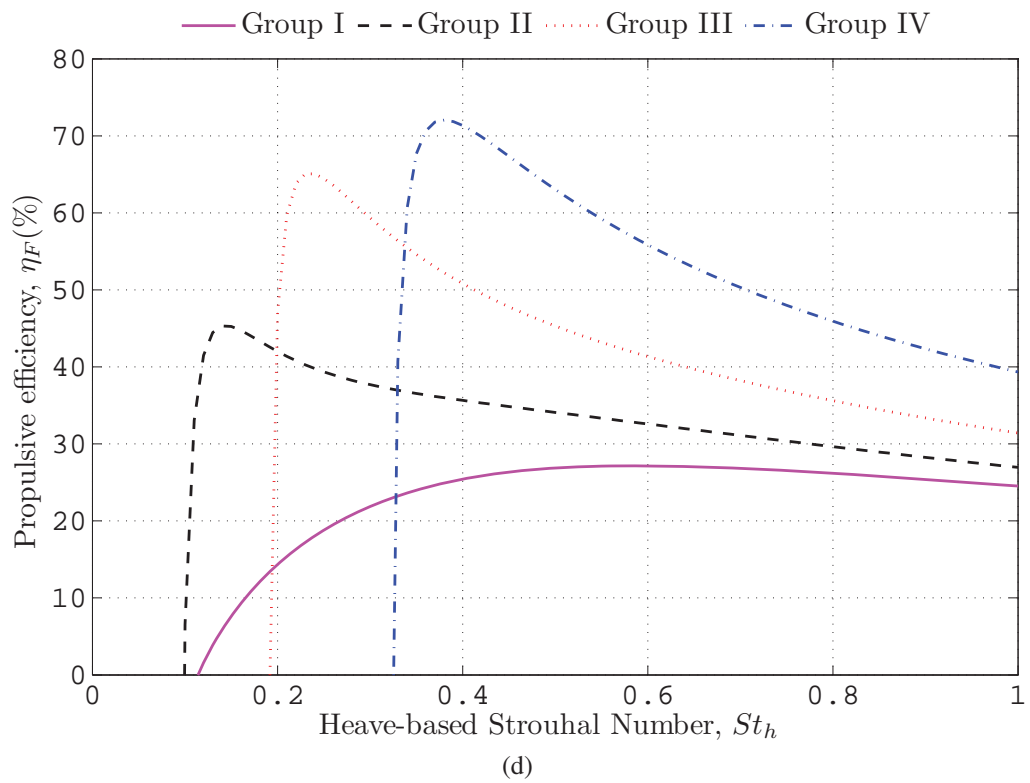
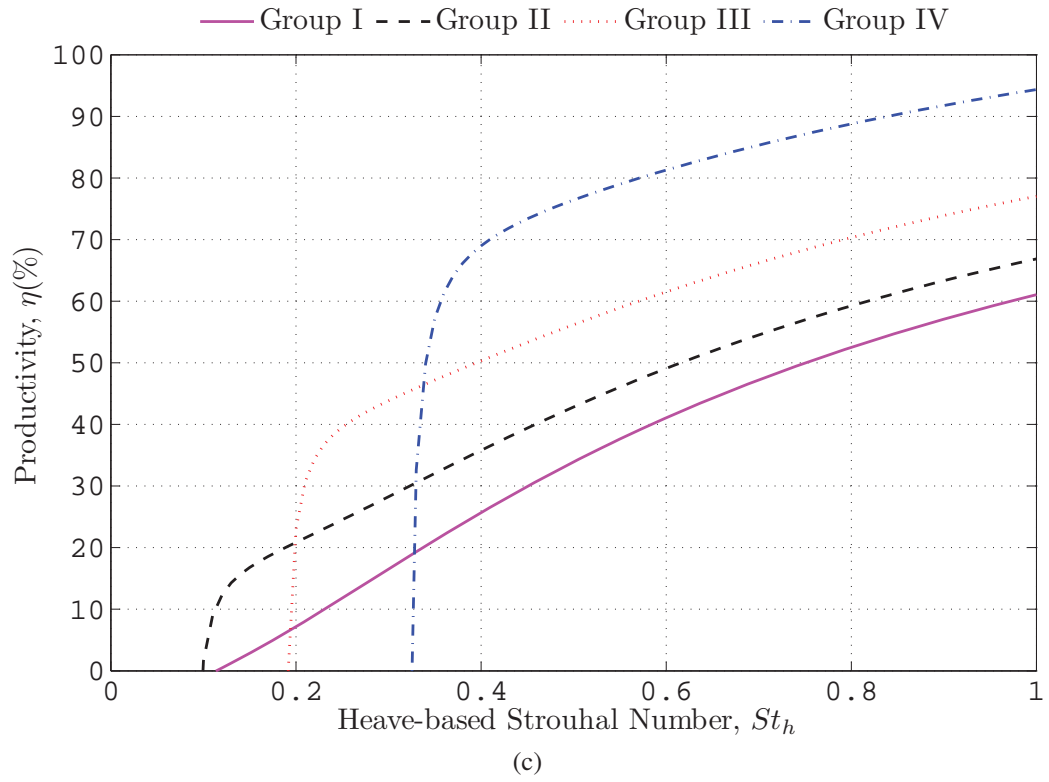


Figure 3.8: Predicted foil kinematic parameters as a function of St_h based on the Q-S model (continued)

3.11 Numerical results

the power required to rotate the foil, and hence the propulsive efficiencies will be overestimated for cases where the pitch amplitudes are significant.

The value of St at which the foil starts generating thrust based on the quasi-steady model, $St_{0,qs}$, can be obtained directly from the C_t data in Figure 3.8a. The values of $St_{0,qs}$ and $St_{0,h,qs}$ are summarised in Table 3.2, along with values of $St_{0,simp}$ and $St_{h,0,simp}$ obtained from the simplified analysis described in Section 2.3.3.5. The difference between $St_{0,simp}$, which is obtained analytically by assuming that the drag on the foil is negligible, and the value $St_{0,qs}$, which does not neglect drag, is fairly small. The only noticeable discrepancy is in the case where the foil is purely heaving (group I), where $St_{0,qs}$ is larger than initially expected, even surpassing the value of $St_{0,qs}$ of group II. Nevertheless, the general trend of St_0 indicates that for cases where the heave amplitude is significant, thrust can be developed at lower Strouhal numbers.

Two major observations can be made based on the Q-S model results presented here. Firstly, as St increases, the unsteady foil can generate very large thrust coefficients, particularly when the non-dimensional heave amplitude is large compared to the pitch amplitude (i.e., χ is large); however, at large St and χ , the efficiencies are generally very small. Secondly, the efficiencies generally peak at $St \approx St_0$, where the thrust coefficients are relatively small (or zero).

From these observations, we suggest two different modes of propulsion :

1. An “acceleration mode”, for use when large thrust coefficients are required at the expense of propulsive efficiency, generated when $\frac{h_0}{c}$ is large compared to θ_0 (groups I or II) and at large Strouhal numbers,
2. A “cruise mode”, for use when a balance of moderate thrust and efficiency is required, generated when $\chi \approx 1$ (group III), and when $St \approx St_0$.

It is interesting to note that for group III, the value of $St_0 \approx 0.2 - 0.3$, which is approximately the same Strouhal number range at which aquatic animals have been observed to swim steadily at (Fish, 1998; Rohr and Fish, 2004; Triantafyllou *et al.*, 1993; Videler and Kamermans, 1985), as previously discussed in Chapter 1. Furthermore, the survey of steadily swimming cetaceans by Fish, as well as Videler and Kamermans, also indicates that most of the studied carangiform fish tended to swim with a pitch amplitude $\theta_0 \approx 30^\circ$, suggesting that the foil properties in group III are ideal for efficient continuous propulsion. At the values of $\theta_0 \approx 30^\circ$ and $St \approx 0.2 - 0.3$, the maximum angle of attack is reasonably low, at $\alpha_{max} \approx 5^\circ - 7^\circ$, which is below the expected static stall angle of the foil, $\alpha_{static-stall} \approx 8^\circ$. This may suggest that steadily swimming fish do not necessarily use unsteady flow mechanisms to generate propulsive forces.

Group	Set	$\frac{h_0}{c}$	$\theta_0(^{\circ})$	χ	$St_{0,simp}$	$St_{0,qs}$	$St_{h,0,simp}$	$St_{h,0,qs}$
I	1	0.75	0	∞	0	0.11	0	0.11
	2	0.50			0	0.11		
	3	0.25			0	0.11		
II	4	0.75	15	2.80	0.09	0.10	0.09	0.1
	5	0.50		1.87	0.09	0.11		
	6	0.25		0.93	0.11	0.13		
III	7	0.75	30	1.30	0.21	0.22	0.18	0.19
	8	0.5		0.87	0.23	0.25		
	9	0.25		0.43	0.33	0.35		
IV	10	0.75	45	0.75	0.41	0.42	0.32	0.32
	11	0.50		0.50	0.49	0.50		
	12	0.25		0.35	0.75	0.76		

Table 3.2: Results for St_0 based on the quasi-steady model

3.11.2 Wake dynamics

Figures 3.9 and 3.10 display the numerical results of the wake dynamics as predicted using the Q-S model, for cases where $\frac{h_0}{c} = 0.75$ (sets 1, 4, 7, and 10) and $\frac{h_0}{c} = 0.5$ (sets 2, 5, 8, and 11) respectively. Unlike the results for the foil kinematics shown in Figure 3.8, the wake dynamics are dependent on the foil heave amplitude, and hence the results for the wake dynamics, in particular the non-dimensional wake width \tilde{A}_c , and thus \tilde{M}_Γ , do not collapse within each foil kinematic group.

Figure 3.9a displays the relationship between St_h and $\tilde{\Gamma}_{total,c}$, which clearly reflects the fact that the wake produced by the foil is modelled using two independent vorticity generating mechanisms, namely the “primary” and “secondary” vorticity generating mechanisms, as discussed in Section 3.10. At low St_h , corresponding to $St_h \lesssim St_{h,0,qs} \lesssim 0.15 - 0.3$, the lift forces generated by the foil are expected to be small due to the low values of α_{max} , and hence Γ_{total} is dominated

3.11 Numerical results

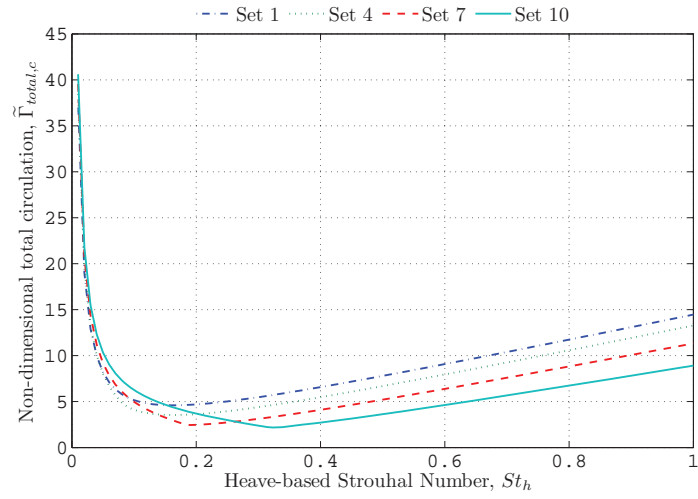
by the vorticity shed at the foil trailing edge (secondary vorticity), which is approximately proportional to U_∞^2 . Therefore $\tilde{\Gamma}_{total,c} = \frac{\Gamma_{total}}{U_\infty c} \propto U_\infty$. It then follows that at low St_h , where U_∞ is large, $\tilde{\Gamma}_{total,c}$ is also very large. However, at larger Strouhal numbers, $St_h \gtrsim St_{h,0,qs}$, the lift forces increase and Γ_{total} becomes more dominated by the changes in the bound circulation on the wing. The changes in the bound circulation on the wing produce primary vorticity, which is generated at a rate approximately proportional to $\sin \alpha$ (see equations 3.31 and 3.33). Thus, at large Strouhal numbers, the value of $\tilde{\Gamma}_{total,c}$ is observed to increase steadily with St_h , due to the fact that α_{max} is generally large at high St_h .

The foil kinematic parameters $\frac{h_0}{c}$ and θ_0 only have an indirect effect on $\tilde{\Gamma}_{total,c}$ (see Figures 3.9a and 3.10a). At low Strouhal numbers, the differences between foil sets are negligible, due to the fact that the generation of secondary vorticity is a strong function of U_∞ at low St_h . Large Strouhal numbers (sets 1 & 4), where χ is large, have larger $\tilde{\Gamma}_{total,c}$ than sets 7 & 10, where χ is small. Furthermore, sets 1 & 4, where $\frac{h_0}{c} = 0.75$ have larger $\tilde{\Gamma}_{total,c}$ than sets 2 & 5, where $\frac{h_0}{c} = 0.5$, indicating that when the foil heave amplitude is large, $\tilde{\Gamma}_{total,c}$ increases. This is due to the fact that α_{max} tends to be large when the non-dimensional heave amplitude is large relative to the pitch amplitude (i.e., χ is large).

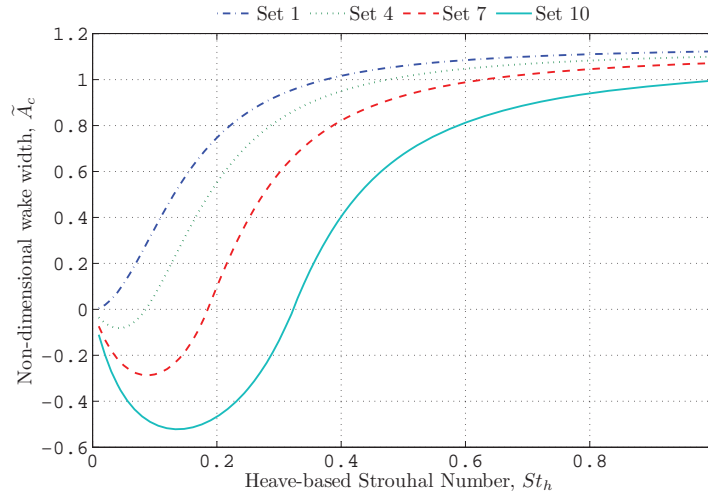
Figures 3.9b and 3.10b show the relationship between St_h and the non-dimensional centroidal wake width, \tilde{A}_c for sets where $\frac{h_0}{c} = 0.75$ and $\frac{h_0}{c} = 0.5$ respectively. It is evident that the heave amplitude has a strong effect on the wake width; larger heave amplitudes produce larger wakes. This is particularly clear when St_h is large, where \tilde{A}_c approximately approaches 1 when $\frac{h_0}{c} = 0.75$ (Figure 3.9b), while \tilde{A}_c approximately approaches 0.75 when $\frac{h_0}{c} = 0.5$ (Figure 3.10b). This is intuitively correct as larger heave amplitudes should generate vorticity at locations more distant from the time-averaged foil centreline.

It also should be noted that for most cases (except set 1), when $St_h \approx St_{h,0,qs}$, the non-dimensional wake widths $\tilde{A}_c \approx 0$ (see Table 3.3), indicating that the time-averaged thrust coefficient produced by the foil, C_t , is zero when the vorticity in the foil wake is distributed such that the centroidal wake width is zero. The discrepancy in the quasi-steady model results for set 1 is attributed to the fact that α_{max} is generally larger in this group (possibly leading to a break-down in the Kutta condition).

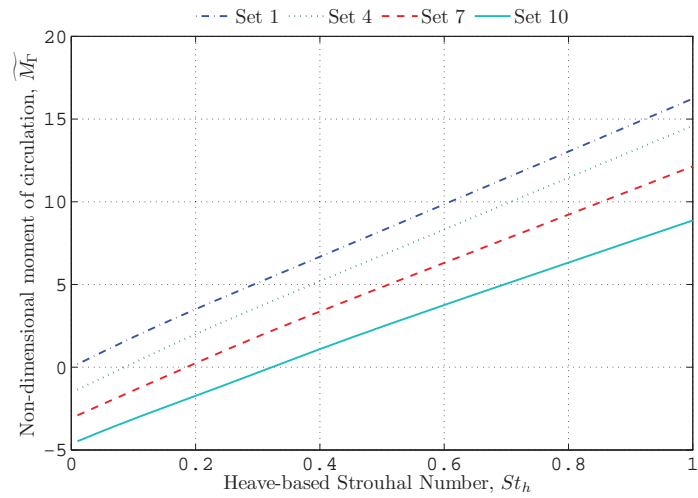
The relationship between \tilde{M}_Γ and St_h is shown in Figures 3.9c and 3.10c. Interestingly, \tilde{M}_Γ increases approximately linearly with St_h , and since C_t is approximately $\propto St_h^2$, therefore C_t is approximately proportional to \tilde{M}_Γ^2 , suggesting that within the context of the Q-S model, the simple idea that the time-averaged thrust can be increased by either increasing the wake width, or increasing the strength of the shed circulation, has its merits.



(a)



(b)



(c)

Figure 3.9: Wake dynamics predicted by the Q-S model, for sets 1, 4, 7 and 10

3.11 Numerical results

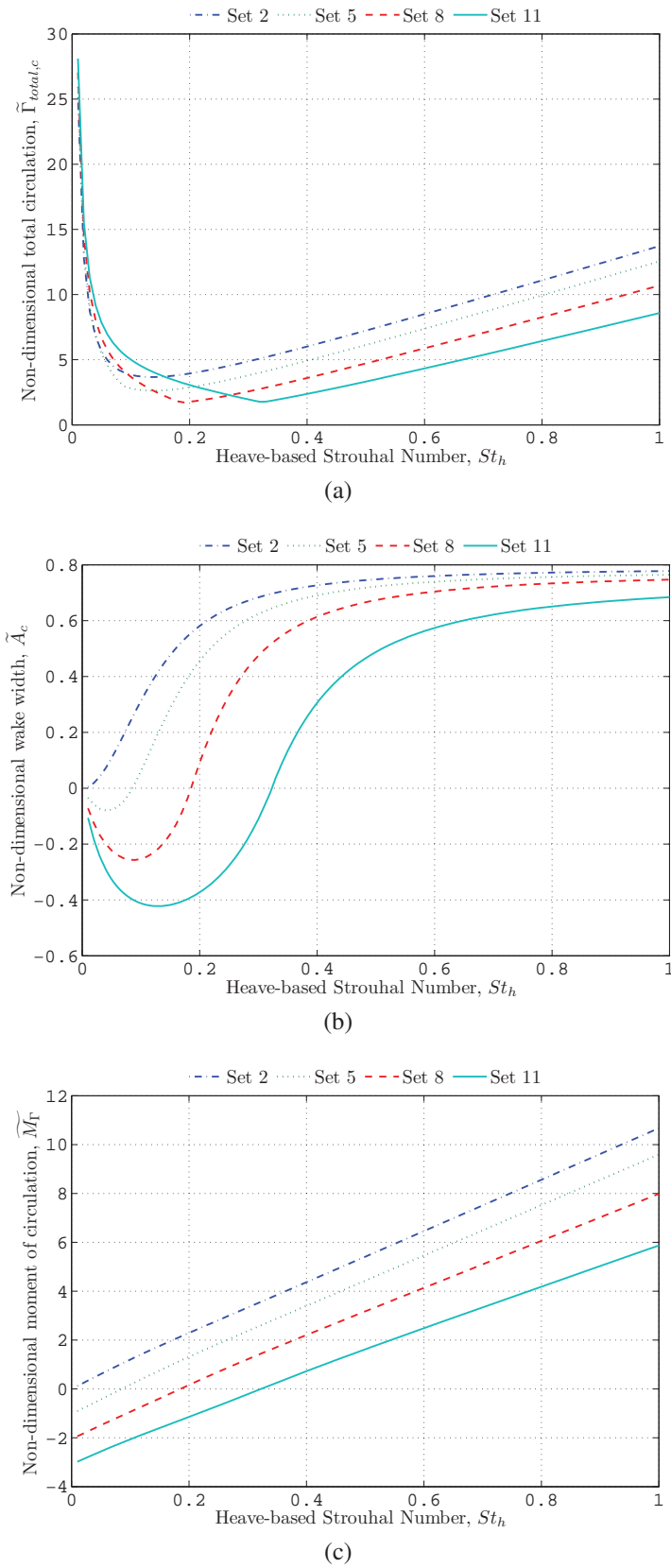


Figure 3.10: Wake dynamics predicted by the Q-S model for sets 2, 5, 8 and 11

Group	Set	$\frac{h_0}{c}$	$\theta_0(^{\circ})$	$St_{h,0,qs}$	\tilde{A}_c when $St_h = St_{h,0,qs}$	\tilde{M}_{Γ} when $St_h = St_{h,0,qs}$
I	1	0.75	0	0.11	0.4	0.18
	2	0.50			0.35	0.12
	3	0.25			0.25	0.06
II	4	0.75	15	0.1	0.06	0.26
	5	0.50			0.06	0.17
	6	0.25			0.06	0.09
III	7	0.75	30	0.19	0.03	0.08
	8	0.5			0.03	0.05
	9	0.25			0.02	0.03
IV	10	0.75	45	0.32	-0.02	-0.04
	11	0.50			-0.02	-0.03
	12	0.25			-0.01	-0.01

Table 3.3: Foil wake width \tilde{A}_c and moment of circulation \tilde{M}_{Γ} when $St_h = St_{h,0,qs}$

3.12 A note on the limitations of the Q-S model

At this stage it would be prudent to highlight the limitations of the Q-S model in its current implementation. Firstly, the Q-S model, as outlined in this section, does not take into account the time-dependent nature of the flow around the unsteady foil, and hence the Q-S model neglects the evolution of the wake. Essentially, the Q-S model assumes that the flow around the foil “forgets” its history.

Furthermore, the Q-S model neglects any effect of the rotation of the foil on the flow. In particular, the forces induced on the foil by the change of the strength of the bound circulation on the foil due to rotation (the Magnus effect) is completely neglected. However, the contribution of the Magnus effect is estimated to be small (Wu and Sun, 2004).

The Q-S model also neglects the Wagner effect - which predicts that a foil is able to generate lift only after a finite time (or distance) after the start of the foil’s translation, due to the detrimental effect of the starting vortex shed by the foil. However, studies have found that foils can generate

3.13 Chapter summary

lift forces very quickly after they are impulsively started (e.g. Dickinson and Gotz, 1993), which suggests that the Wagner effect is small.

The most significant assumption of the Q-S model is the neglect of viscous effects, including the assumption that the Kutta condition holds for all flow conditions and foil parameters. Without viscosity, the model does not predict flow separation, and stall, and therefore the sudden loss of lift and the sudden increase in drag are totally ignored. Therefore, the Q-S model is predicted to overestimate the thrust forces, productivities and propulsive efficiencies of the heaving and pitching foil, particularly for cases where α_{max} is large.

Nonetheless, although the Q-S model has many limitations, when used with caution it is expected to provide a reasonable approximation to the true kinematics of the unsteady foil. Deviations from the quasi-steady behaviour is expected to be most significant when the non-dimensional heave amplitudes are large relative to the pitch amplitude, (i.e., χ is large), where α_{max} is expected to be large. These deviations are attributed to viscous effects such as flow separation and the Wagner effect.

3.13 Chapter summary

A theoretical quasi-steady model of the heaving and pitching foil was developed based on, a) experimental results obtained for a NACA 0026 foil in a steady flow performed at the University of Adelaide, and b) published empirical results of NACA 00-series foils. A conservative approach was taken in choosing steady values of lift and drag coefficients - when in doubt, higher values of steady lift coefficients and lower values of drag coefficients were used. Therefore, it is expected that the thrust values, and hence propulsive efficiency values, obtained using the Q-S model will over-estimate the true values.

Based on the simplified Q-S model, we predict a Strouhal number $St_{0,qs}$ at which the foil starts to produce a nett forward thrust. When $St \rightarrow St_{0,qs}$, the maximum angle of attack of the foil across an entire oscillating cycle approaches $\alpha_{max} \approx 0$. The foil subsequently produces very little lift, just enough to balance any drag forces produced. Therefore, in a time-averaged sense, the foil is not expected to produce any nett thrust or drag when $St \approx St_{0,qs}$. This value of $St_{0,qs}$, which compares well with the simplified analytic values of $St_{0,simp}$, is highly dependent on the foil dynamic parameters $\frac{h_0}{c}$ and θ_0 , and increases when the foil pitch amplitude becomes large compared to the non-dimensional heave amplitude.

Furthermore, the Q-S model predicts that propulsive efficiencies are at their highest at St slightly above $St_{0,qs}$, where thrust coefficients are small. The efficiencies increase for cases where the

foil pitch amplitude is large relative to the non-dimensional heave amplitude (i.e., χ is small), although it has to be noted that the Q-S model tends to overestimate efficiencies at large pitch amplitudes due to the fact that it neglects the power required to rotate the foil.

Time-averaged thrust coefficients generated by the foil, C_t , appears to increase approximately as a function of St_h^2 , and therefore C_t can be very large at high Strouhal numbers. The thrust coefficients are particularly large when the foil becomes more heave dominated (groups I and II), although this increase in thrust coincides with a decline in productivity, η , and propulsive efficiency, η_F .

Thus, based on the Q-S thrust and efficiency predictions, we suggest two different modes of propulsion:

1. An “acceleration” mode (Group I) - The unsteady foil, undergoing large heave motions and small pitch motions, can develop very large thrust coefficients at the expense of efficiency, especially at large St . Within this mode, angles of attack are very large, with $\alpha_{max} \gtrsim 60^\circ$ at $St_h = 1$;
2. A “cruise” mode (Group III) - The unsteady foil can produce a reasonable balance of thrust and efficiency if it undergoes moderate pitching and heaving motions, particularly at St slightly larger than St_0 . Within this mode, angles of attack are very small, on order of $\alpha_{max} \approx 5 - 7^\circ$ at $St_h \approx 0.2$, which is below the static stall angle of the foil, $\alpha_{static-stall} \approx 8^\circ$.

Finally, the Q-S model also shows a link between the wake dynamics and the foil kinematics. In particular, both the wake width \tilde{A}_c and the total amount of vorticity shed (in terms of normalised circulation), $\tilde{\Gamma}_{total,c}$ increases with St . The thrust coefficient can be shown to be approximately proportional to the square of the product of these two values, which we define as the non-dimensional moment of circulation, $\tilde{M}_\Gamma = \tilde{\Gamma}_{total,c} \times \tilde{A}_c$, and hence implies that an increase in the total vorticity shed by the foil, or an increase in the wake width behind the foil, can lead to an increase in the thrust coefficient. This finding may have implications for the study of the development of optimal vortical structures behind the wake of an unsteady foil, as will be discussed in Chapter 6.

Chapter 4

Experimental Force and Efficiency Measurements

4.1 Introduction

In this chapter, we discuss the experimentally measured unsteady foil dynamics, consisting of the time-averaged thrust coefficient, C_t , the time-averaged side force coefficient, C_s , the productivity, η , and the propulsive efficiency, η_F , as previously defined in Chapter 3. Two methods have been employed to measure the time-averaged forces on the foil.

Firstly, the two-dimensional time-averaged velocity field measured using particle image velocimetry is numerically integrated around the foil to obtain the thrust and side force, per unit span, developed by the foil. This is then extended to three dimensions using the assumption that the forces developed by the foil is constant along the span of the foil. Secondly, strain gauges were employed to measure the thrust, side force, and the moment developed by the foil. The methods used to obtain these measurements are discussed in more detail in Appendix B. These experimental results will be directly compared to the results predicted using the quasi-steady theory, discussed in Chapter 3.

The individual results, corresponding to particular foil heave-pitch combinations, are grouped according to whether the motion of the foil is heave dominated or pitch dominated, as first noted in Table 2.1 in Chapter 2. Within each group, thrust and side force data are shown for all individual cases, however, only selected cases of productivity and propulsive efficiency are displayed for brevity (the reader may refer to Appendix A for the results of all experimental cases). These results, shown in Figures 4.1 to 4.15, are plotted against the Strouhal number (based on the trailing edge of the foil), St_{te} .

4.2 Group I : Pure heave (sets 1-3)

Figures 4.1 to 4.3 show the force coefficient results for cases with $\frac{h_0}{c} = 0.75, 0.5, 0.25$ and $\theta_0 = 0^\circ$. The results show that the purely heaving hydrofoil can develop thrust at very low Strouhal numbers; thrust starts to develop at approximately $St > 0.15$. This is probably due to the fact that a purely heaving hydrofoil develops a positive non-zero maximum angle of attack, α_{max} at very low Strouhal numbers (as discussed in Chapter 3).

It is also evident that the purely heaving hydrofoil can generate very large thrust and side force coefficients, approximately twice the amount of the predicted values using the quasi-steady theory, particularly at large Strouhal numbers. The maximum thrust coefficients are approximately $C_t \approx 12$ at $St \approx 0.7$. At this value of Strouhal number, the maximum angle of attack α_{max} is large, approaching 70° . This is far beyond the static stall angle of the foil, which is estimated to be approximately $\alpha_{static-stall} \approx 8^\circ$ (see Chapter 3), and this demonstrates the fact that the foil still can generate large forces beyond the static stall angle of the foil.

As the pitch amplitude for this group is zero, the discrepancy between the quasi-steady model and the experimental results cannot be attributed to the exclusion of rotational effects from the quasi-steady model. Therefore, the difference between theoretical and experimental results is evidence that the oscillating foil can potentially use unsteady flow mechanisms to generate large forces.

For this foil kinematic group, the efficiencies and productivities are low to moderate, and are on order of what is expected using the Q-S theory (see Figure 4.4). This indicates that the development of large thrust coefficients on the foil are also accompanied by the generation of large side forces. This suggests that the large thrust coefficient arises from the generation of large instantaneous lift coefficients on the foil, as opposed to the tilting of the lift vector towards the upstream direction.

Although this group exhibits large thrust coefficient values which would have great practical benefits, this occurs at fairly low efficiencies ($\eta_F \approx 10 - 30\%$), making this group an unlikely candidate for continuous propulsion. Nonetheless, it may prove useful in situations where short bursts of thrust are required.

4.3 Group II : Heave dominant (sets 4-6)

Figures 4.5 to 4.7 show force coefficient results for cases with $\frac{h_0}{c} = 0.75, 0.5, 0.25$ and $\theta_0 = 15^\circ$. The results in this group show good agreement to the quasi-steady theory, although at larger

4.3 Group II : Heave dominant (sets 4-6)

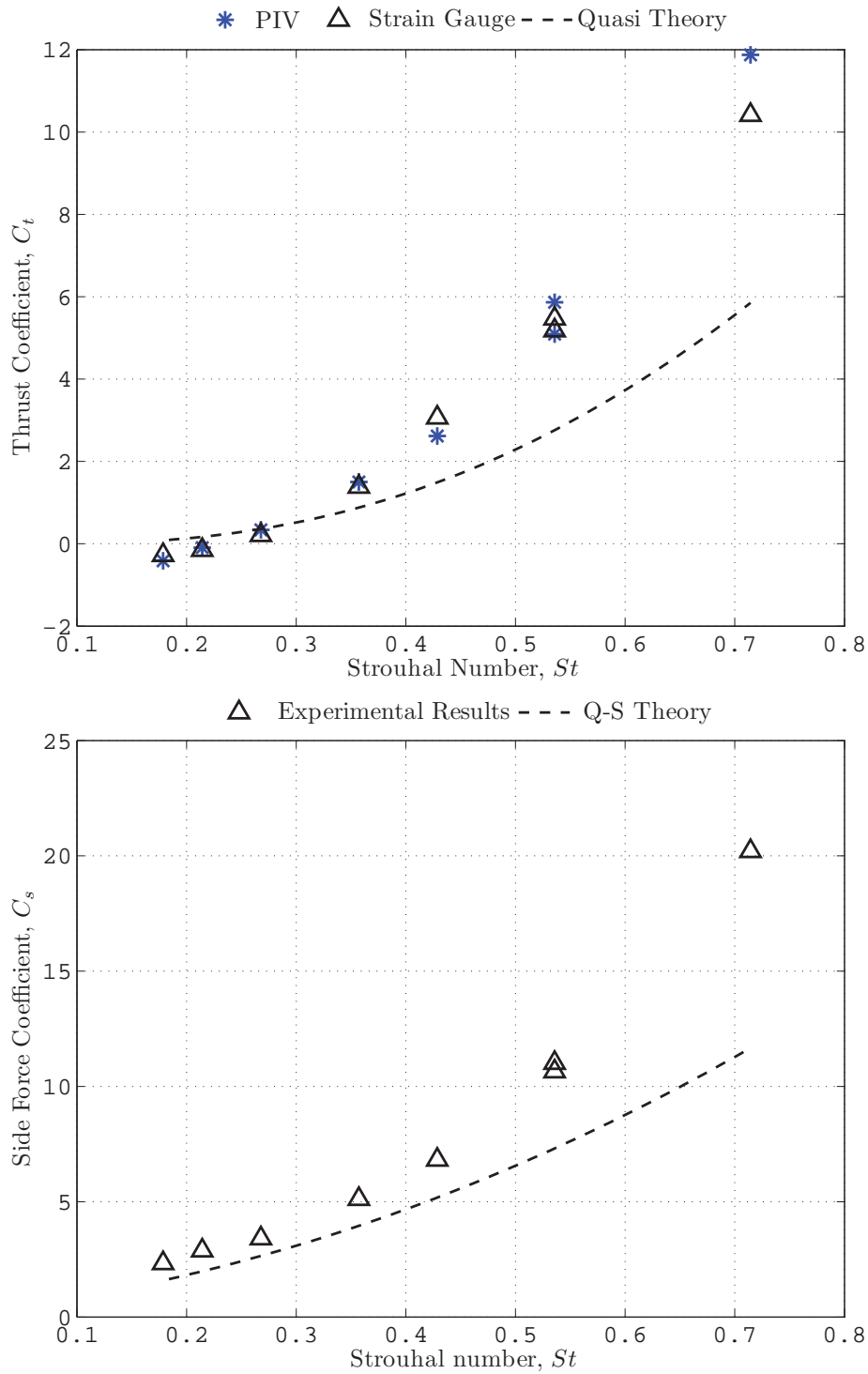


Figure 4.1: Thrust and side force coefficients, C_t and C_s , for set 1 : $\frac{h_0}{c} = 0.75$, $\theta_0 = 0^\circ$

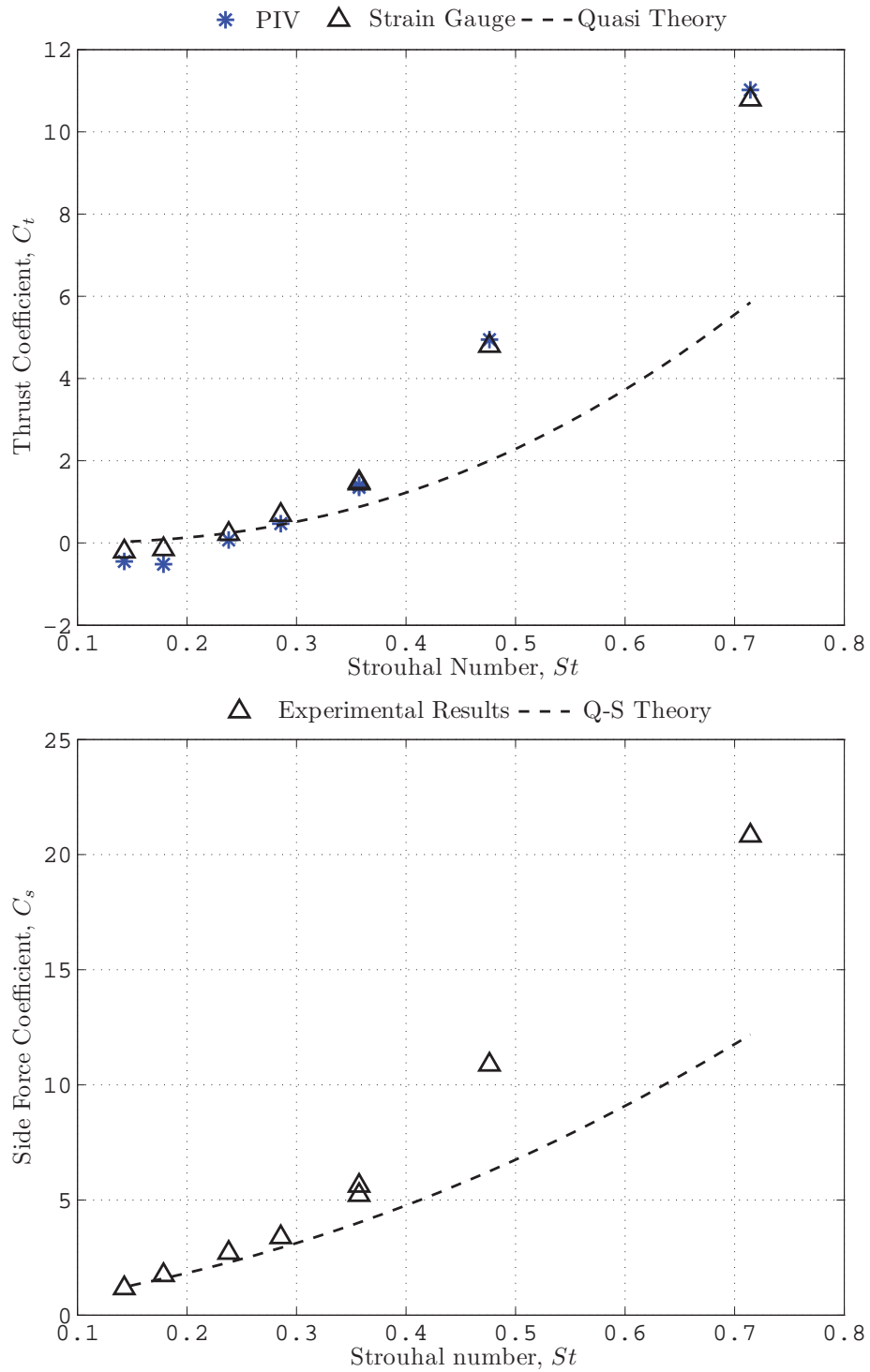


Figure 4.2: Thrust and side force coefficients, C_t and C_s , for set 2 : $\frac{h_0}{c} = 0.5$, $\theta_0 = 0^\circ$

4.3 Group II : Heave dominant (sets 4-6)

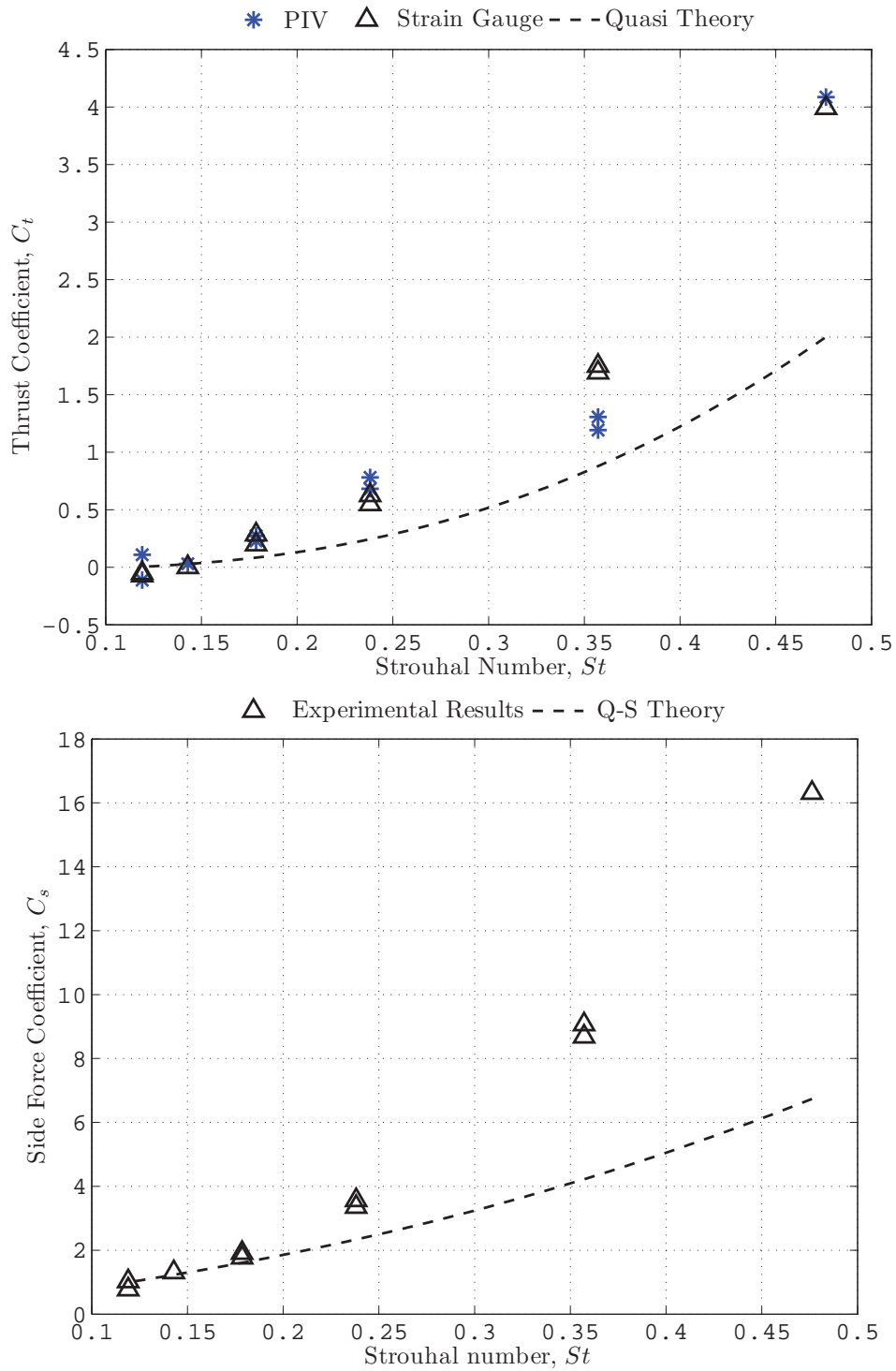


Figure 4.3: Thrust and side force coefficients, C_t and C_s , for set 3 : $\frac{h_0}{c} = 0.25$, $\theta_0 = 0^\circ$

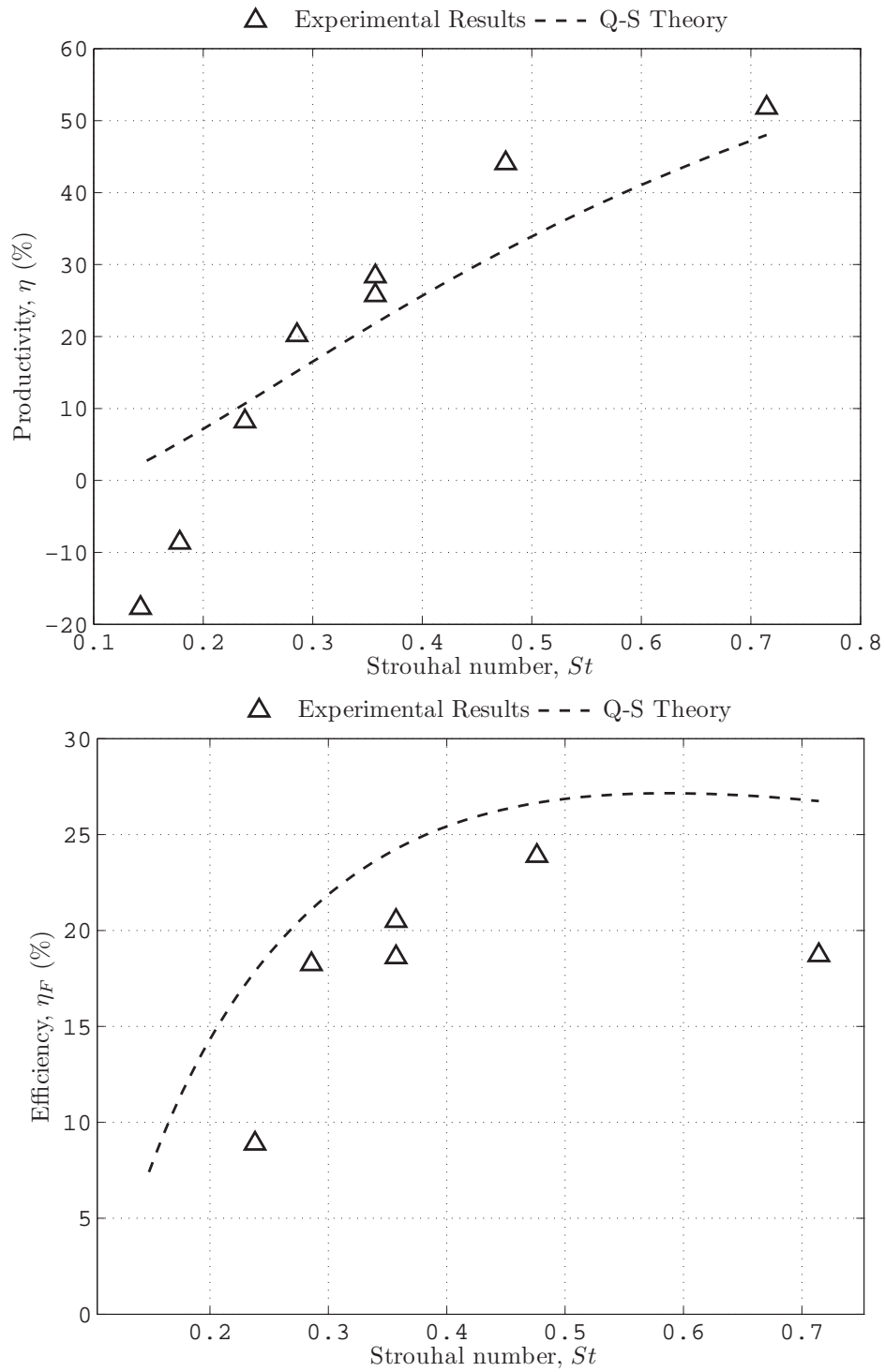


Figure 4.4: Productivity, η and Froude efficiency, η_F for set 2 : $\frac{h_0}{c} = 0.5$, $\theta_0 = 0^\circ$

4.4 Group III : Moderate pitch & heave (sets 7-9)

Strouhal numbers, the thrust and side force coefficients still exceed the predicted values. This should not be surprising, considering the large measured force coefficients in group I.

Productivity and efficiency values (Figure 4.8) also follow the same trends as the Q-S theory, however, the experimental efficiency results are consistently approximately 15% lower than the Q-S model. This could be due to the failure of the Q-S model to incorporate the work used to rotate the foil, resulting in an over-estimation of the foil propulsive efficiency.

Nevertheless, the results show that the productivity increases approximately linearly with St , whereas the propulsive efficiency slowly decreases as St increases. Efficiencies in this group are slightly higher than group I at the same corresponding St , and generally fall in the range of $\eta_F \approx 20 - 40\%$.

4.4 Group III : Moderate pitch & heave (sets 7-9)

Figures 4.9 to 4.11 show force coefficient results for cases with $\frac{h_0}{c} = 0.75, 0.5, 0.25$ and $\theta_0 = 30^\circ$. A comparison of the experimental and theoretical thrust coefficient results show remarkable agreement, and indicates that the quasi-steady model can prove to be a useful tool in predicting the forces on an unsteady foil under some conditions. The thrust coefficients produced are moderate, approximately $C_t \approx 2$ at $St \approx 0.5$, where the maximum angle of attack, $\alpha_{max} \approx 20^\circ$, is still beyond the static stall angle of the foil. The Strouhal number where thrust starts to develop is approximately $St_{0,exp} \approx 0.2 - 0.25$, which is close to the range of $St_{0,qs} \approx 0.2 - 0.35$ predicted using the quasi-steady model (see Table 3.2).

The side force coefficients in Figures 4.9 and 4.10 show excellent agreement with theory, however, for the case where $\frac{h_0}{c} = 0.25$, the side force coefficient deviates slightly from the theory, although general trends and values are still in good agreement. This is probably because the Strouhal numbers involved are close to the value of St_0 , where the angles of attack are small (close to zero), and therefore the forces developed are small and thus more susceptible to errors. More specifically, any deficiencies in the in the Q-S model, such as the simplified modelling of added (or virtual) mass effects due to the dynamics of the foil, will be more obvious when C_t and C_s are small.

As expected, the productivity values are in excellent agreement with the Q-S theory, whereas the theoretical propulsive efficiencies overestimate the experimental results by approximately 20% (Figure 4.12), probably due to the higher pitch amplitudes in this group. The propulsive efficiencies recorded in group III, are reasonable, in the range of $\eta \approx 30 - 60\%$, while thrust coefficients are moderate to large. It then follows that an unsteady foil with dynamic properties

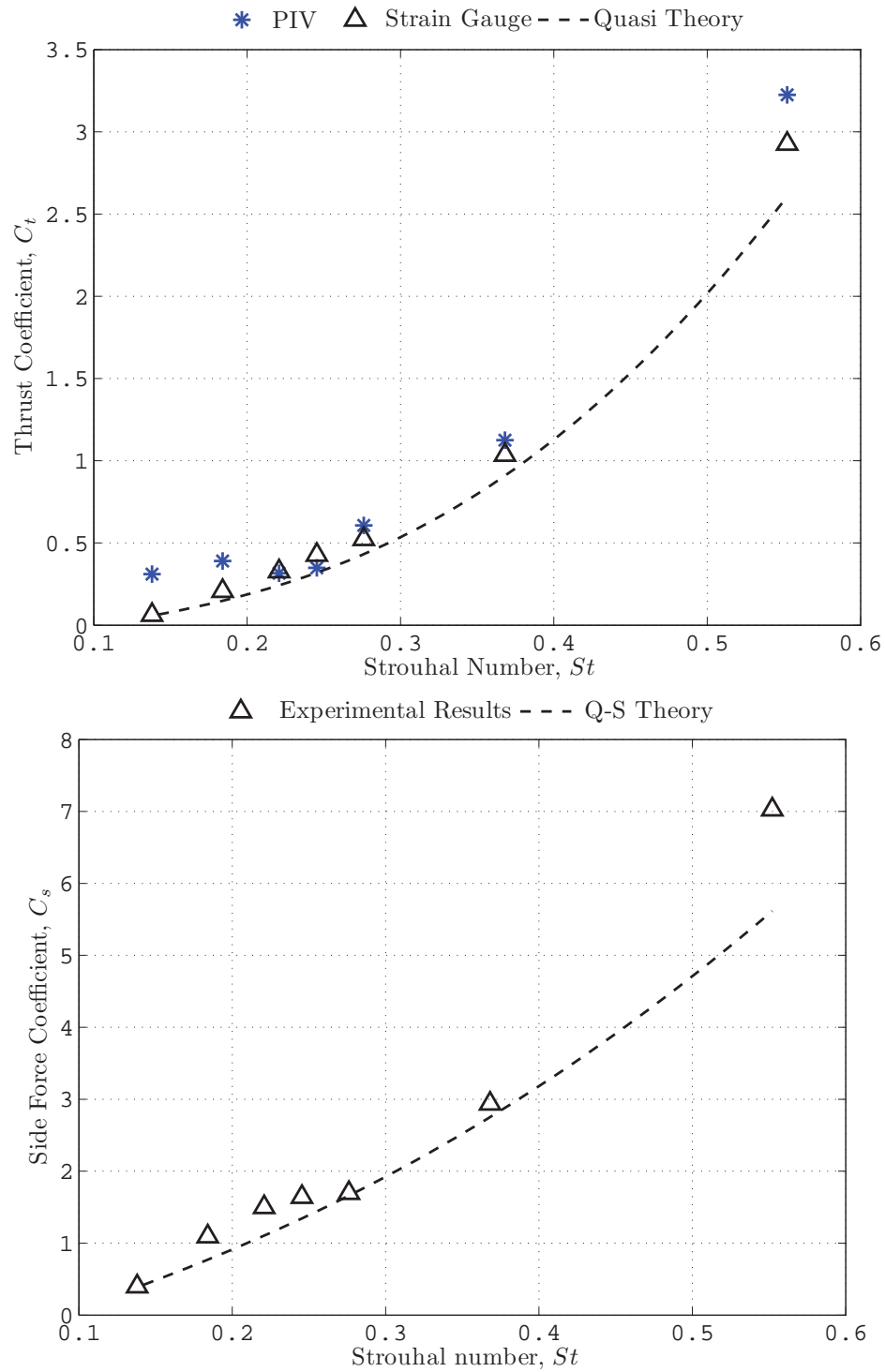


Figure 4.5: Thrust and side force coefficients, C_t and C_s , for set 4 : $\frac{h_0}{c} = 0.75$, $\theta_0 = 15^\circ$

4.4 Group III : Moderate pitch & heave (sets 7-9)

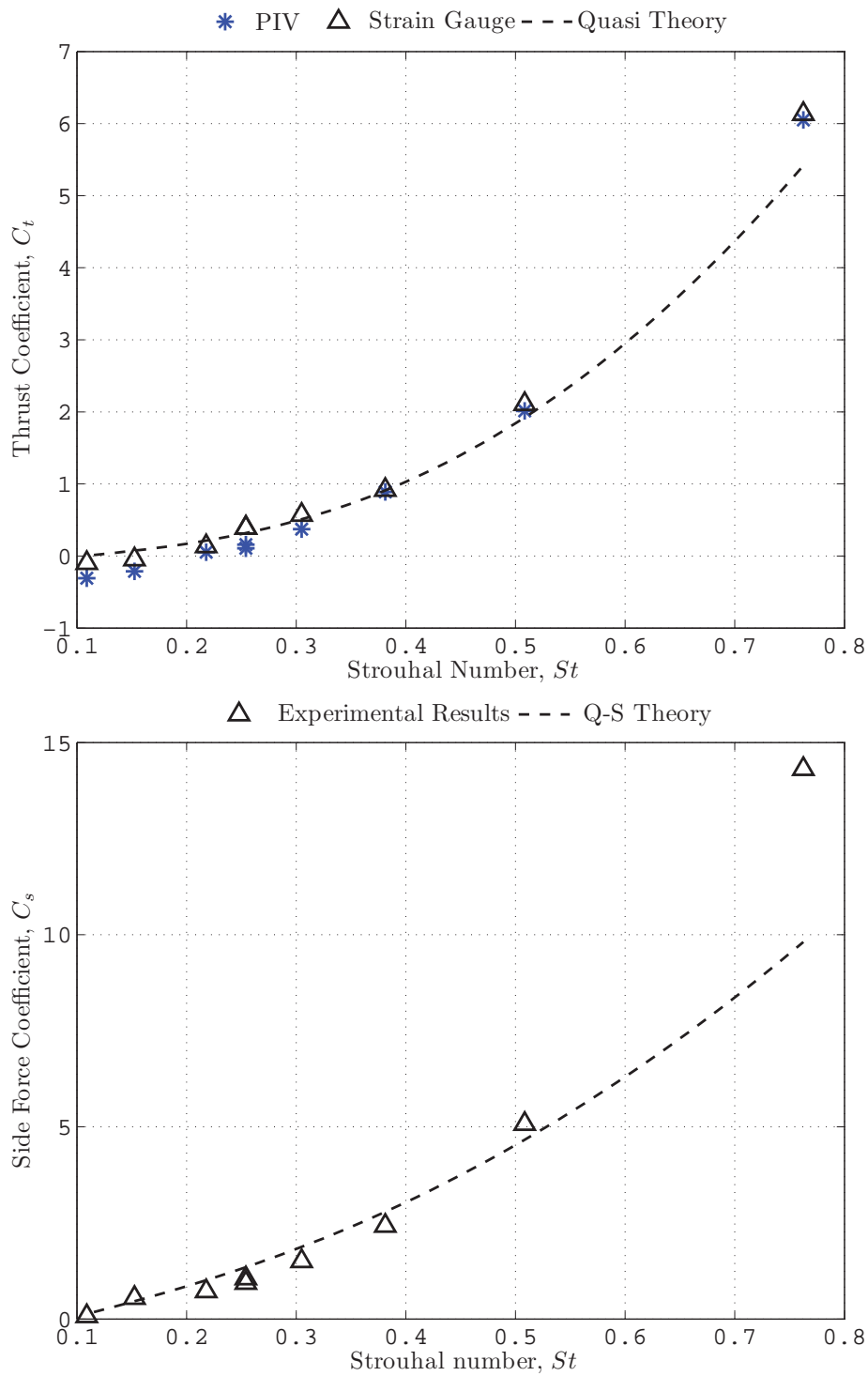


Figure 4.6: Thrust and side force coefficients, C_t and C_s , for set 5 : $\frac{h_0}{c} = 0.5$, $\theta_0 = 15^\circ$

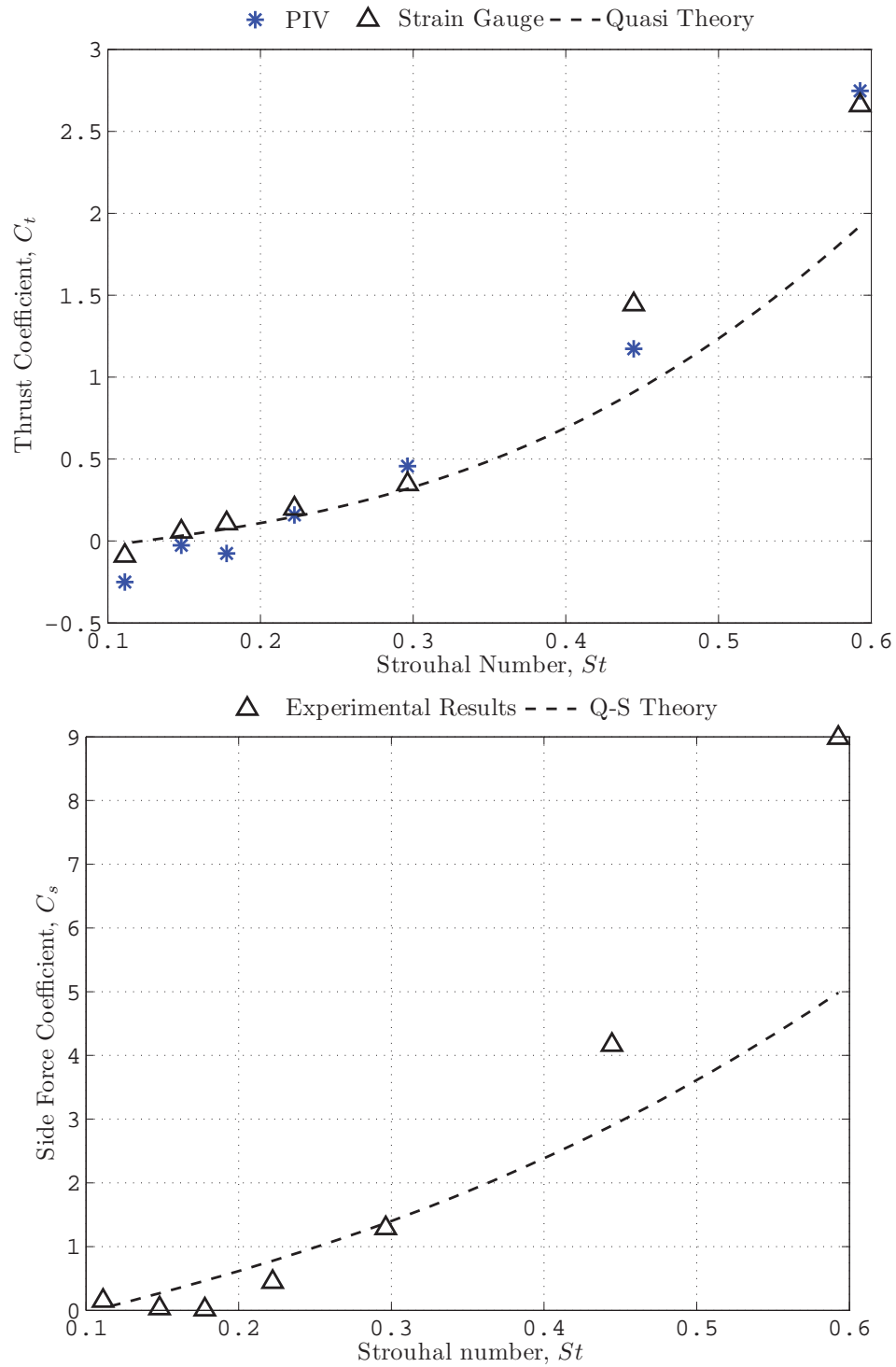


Figure 4.7: Thrust and side force coefficients, C_t and C_s , for set 6 : $\frac{h_0}{c} = 0.25$, $\theta_0 = 15^\circ$

4.4 Group III : Moderate pitch & heave (sets 7-9)

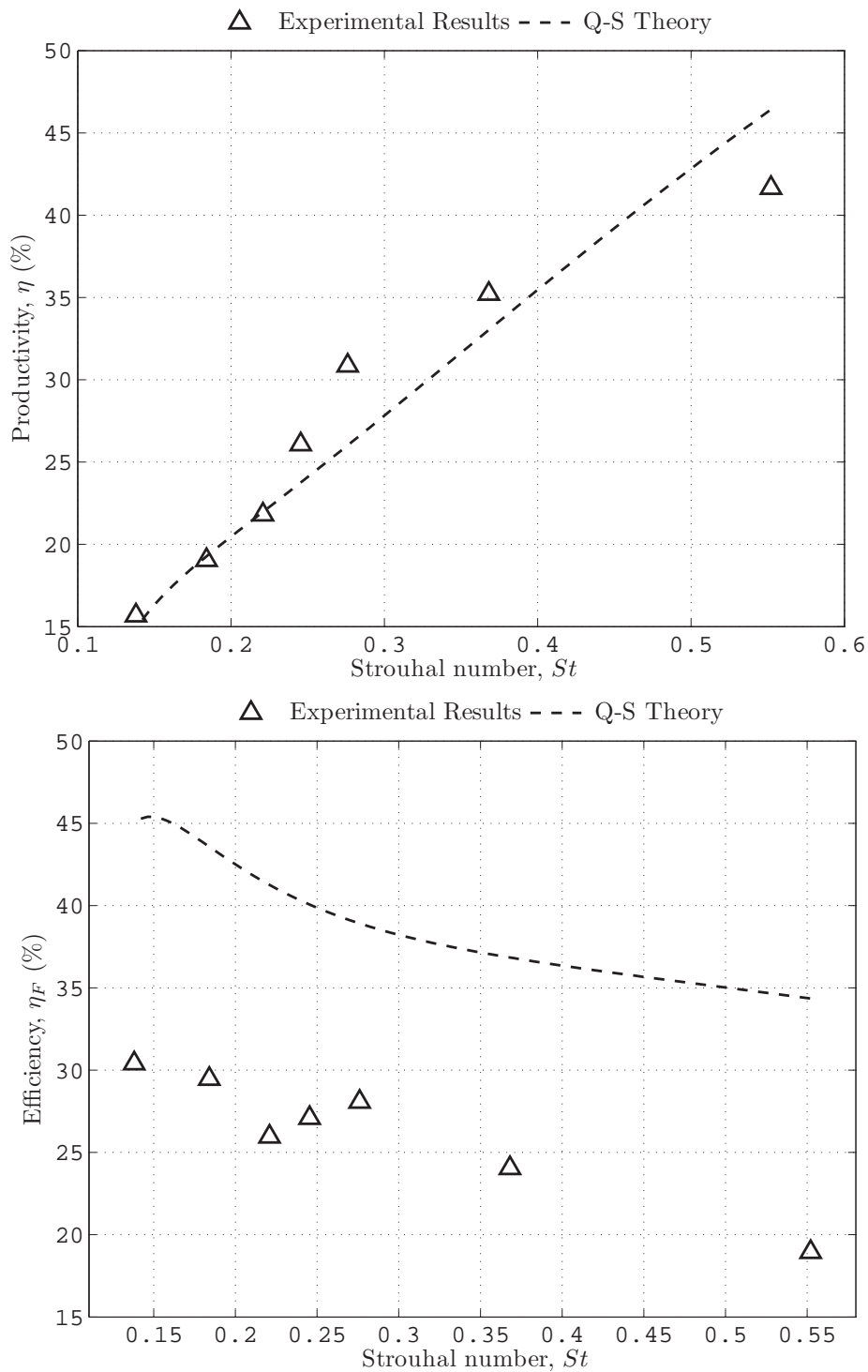


Figure 4.8: Productivity, η and Froude efficiency, η_F for set 4 : $\frac{h_0}{c} = 0.75$, $\theta_0 = 15^\circ$

within this group may provide the necessary balance of thrust and propulsive efficiency required for practical steady propulsion.

4.5 Group IV : Pitch dominant (sets 10-12)

Figures 4.13 to 4.15 show force coefficient results for cases with $\frac{h_0}{c} = 0.75, 0.5, 0.25$ and $\theta_0 = 45^\circ$. The thrust coefficient values for the cases where the heave amplitude is moderate to large, that is, $\frac{h_0}{c} = 0.5, 0.75$ (Figures 4.13 and 4.14), show very good agreement with the theoretical estimates. The highest recorded thrust coefficient in this group is $C_t = 7$, occurring at the very large Strouhal number value of $St = 1.45$, at which point the maximum angle of attack, $\alpha_{max} \approx 36^\circ$. This suggests that even in the cases where the pitch amplitude is large relative to the non-dimensional heave amplitude, large thrust coefficients still can be developed without obvious signs of static stall. The side force coefficients show reasonable agreement with theory, except that the Q-S theory underestimates the side forces particularly at larger Strouhal numbers, consistent with the observations in Groups II and III above.

For the case where the heave amplitude is small ($\frac{h_0}{c} = 0.25$), the quasi-steady model breaks down due to the large pitch amplitudes, and the theoretical thrust and side force estimates exceed the experimental values (see Figure 4.15). The experimental thrust values for this particular case are only moderate, on order of $C_t \approx 2$, even when the Strouhal numbers are very large, $St = 1.68$.

Productivity and efficiency values (Figure 4.16) within this group also fail to match the theoretical estimates, and it is evident that the Q-S model is a poor predictor of efficiency within this group, overestimating propulsive efficiencies by up to 60%. Experimentally recorded efficiencies are surprisingly low, within the range of $\eta_F \approx 10 - 40\%$.

In summary, this group displays low propulsive efficiencies, and generally low thrust coefficients. Furthermore, within this group, the value of $St_{0,exp}$ has clearly increased, relative to other foil kinematic groups, to a value approaching $St_{0,exp} \approx 0.45 - 0.5$ (which is in-line with what is predicted) resulting in the development of thrust only at large St . It is then apparent that this foil kinematic group offers little in terms of practical propulsive application.

4.6 Discussion

Generally, for all cases, the thrust coefficient results measured using the strain gauges, $C_{t,sg}$, and the thrust coefficients evaluated from the PIV velocity field, $C_{t,piv}$, show good agreement, indicating that the experimental results are most likely to be accurate.

4.6 Discussion

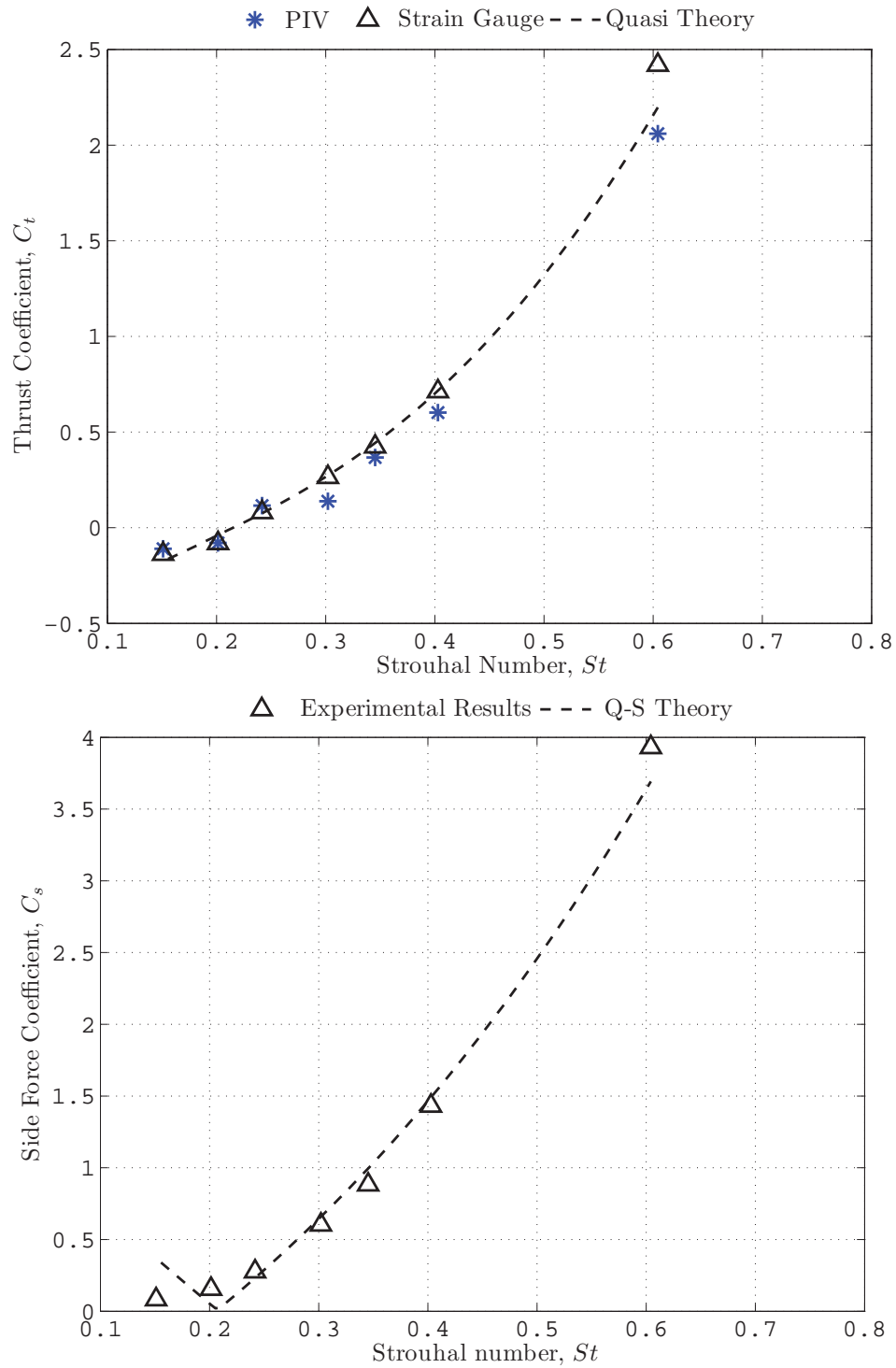


Figure 4.9: Thrust and side force coefficients, C_t and C_s , for set 7 : $\frac{h_0}{c} = 0.75$, $\theta_0 = 30^\circ$

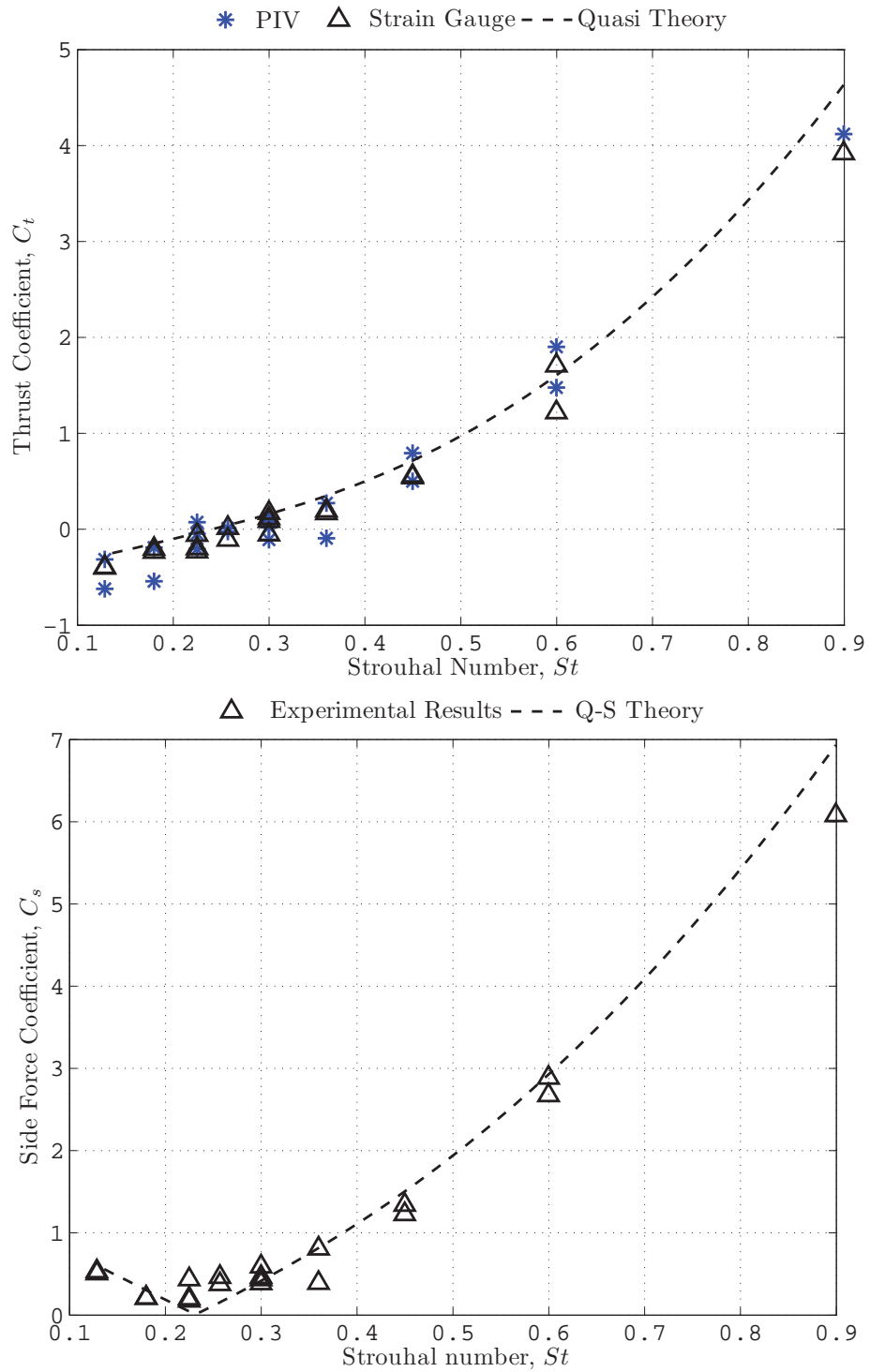


Figure 4.10: Thrust and side force coefficients, C_t and C_s , for set 8 : $\frac{h_0}{c} = 0.5$, $\theta_0 = 30^\circ$

4.6 Discussion

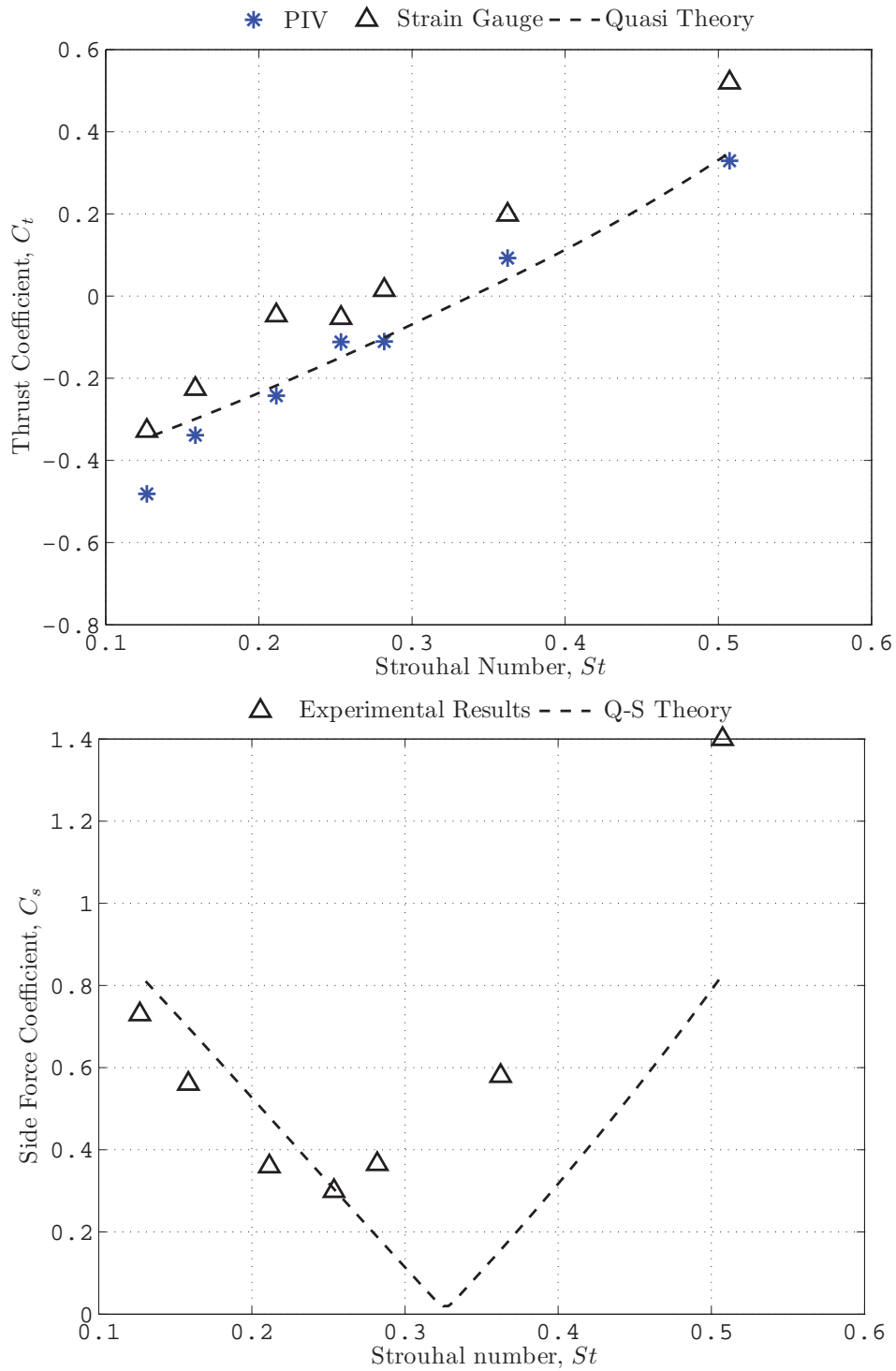


Figure 4.11: Thrust and side force coefficients, C_t and C_s , for set 9 : $\frac{h_0}{c} = 0.25$, $\theta_0 = 30^\circ$

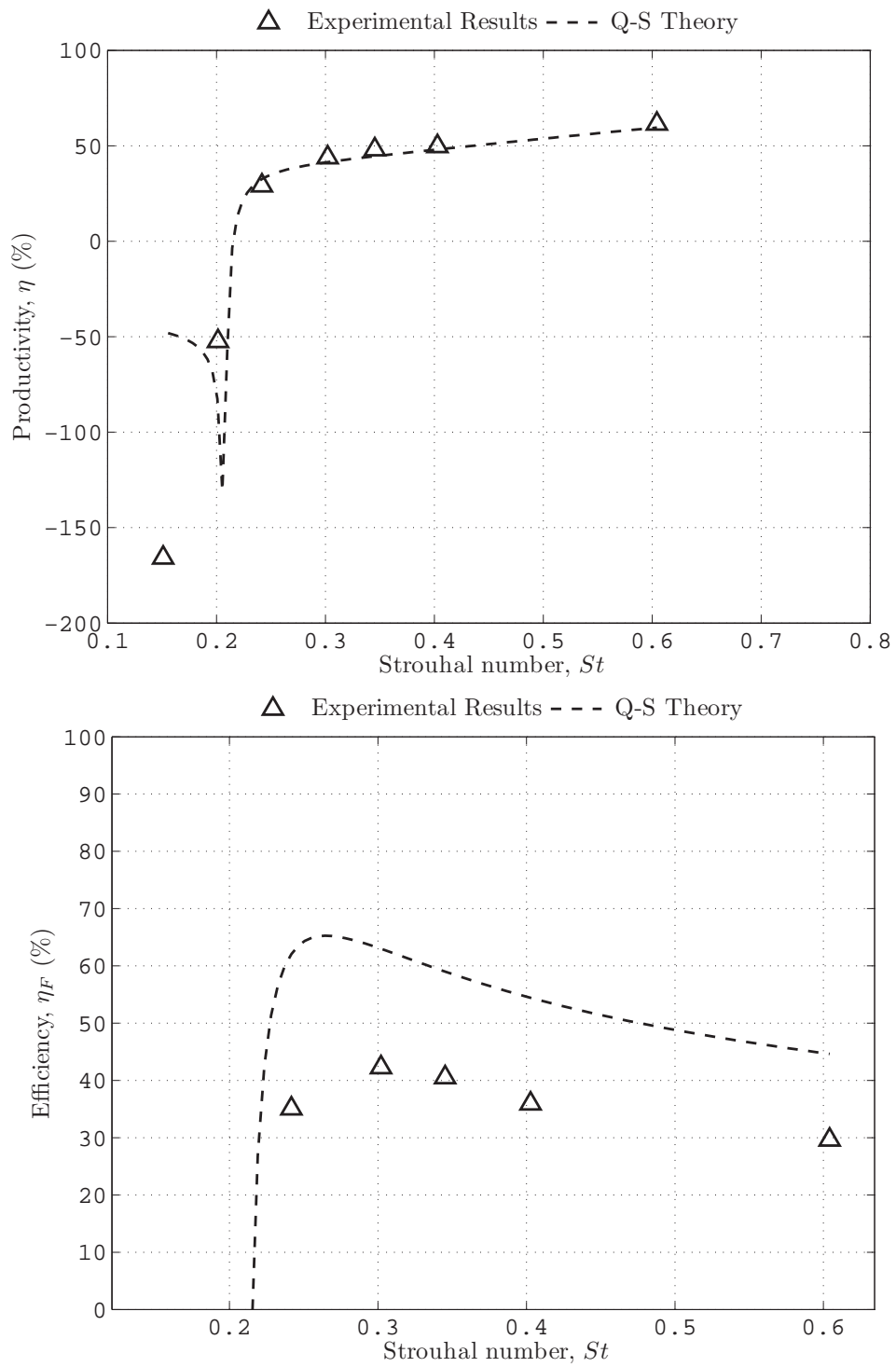


Figure 4.12: Productivity, η and Froude efficiency, η_F for set 7 : $\frac{h_0}{c} = 0.75$, $\theta_0 = 30^\circ$

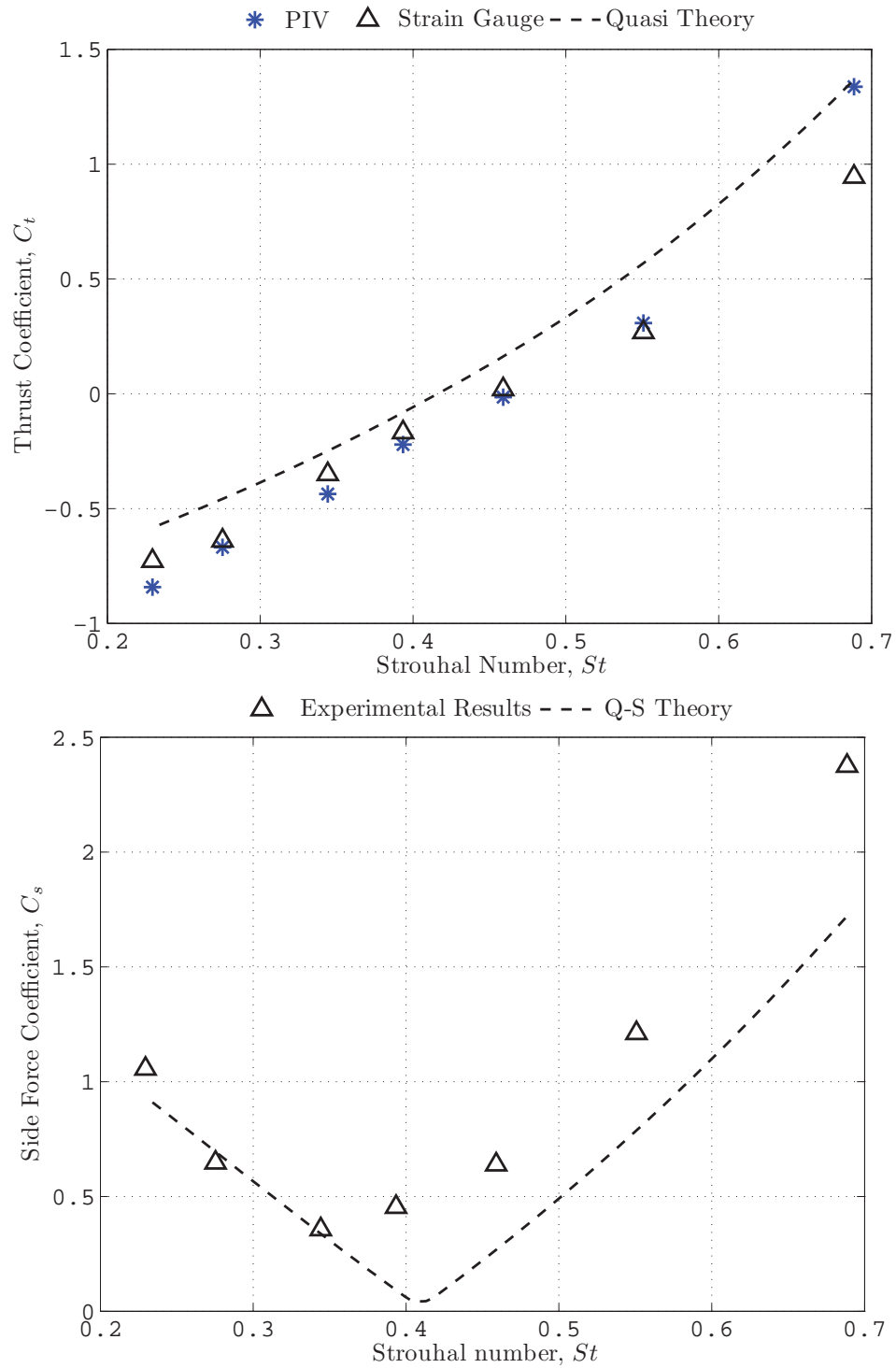


Figure 4.13: Thrust and side force coefficients, C_t and C_s , for set 10 : $\frac{h_0}{c} = 0.75$, $\theta_0 = 45^\circ$

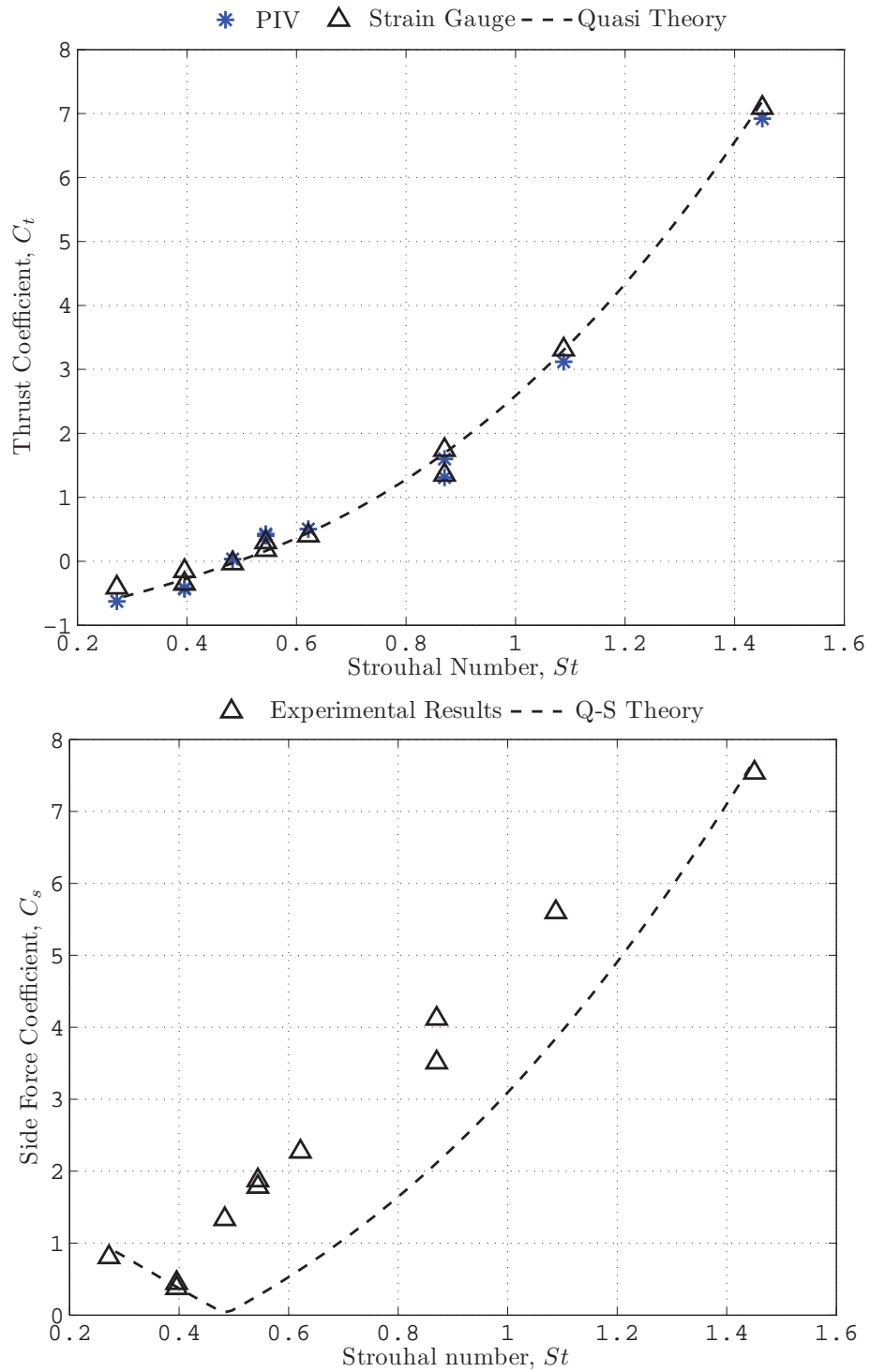


Figure 4.14: Thrust and side force coefficients, C_t and C_s , for set 11 : $\frac{h_0}{c} = 0.5$, $\theta_0 = 45^\circ$

4.6 Discussion

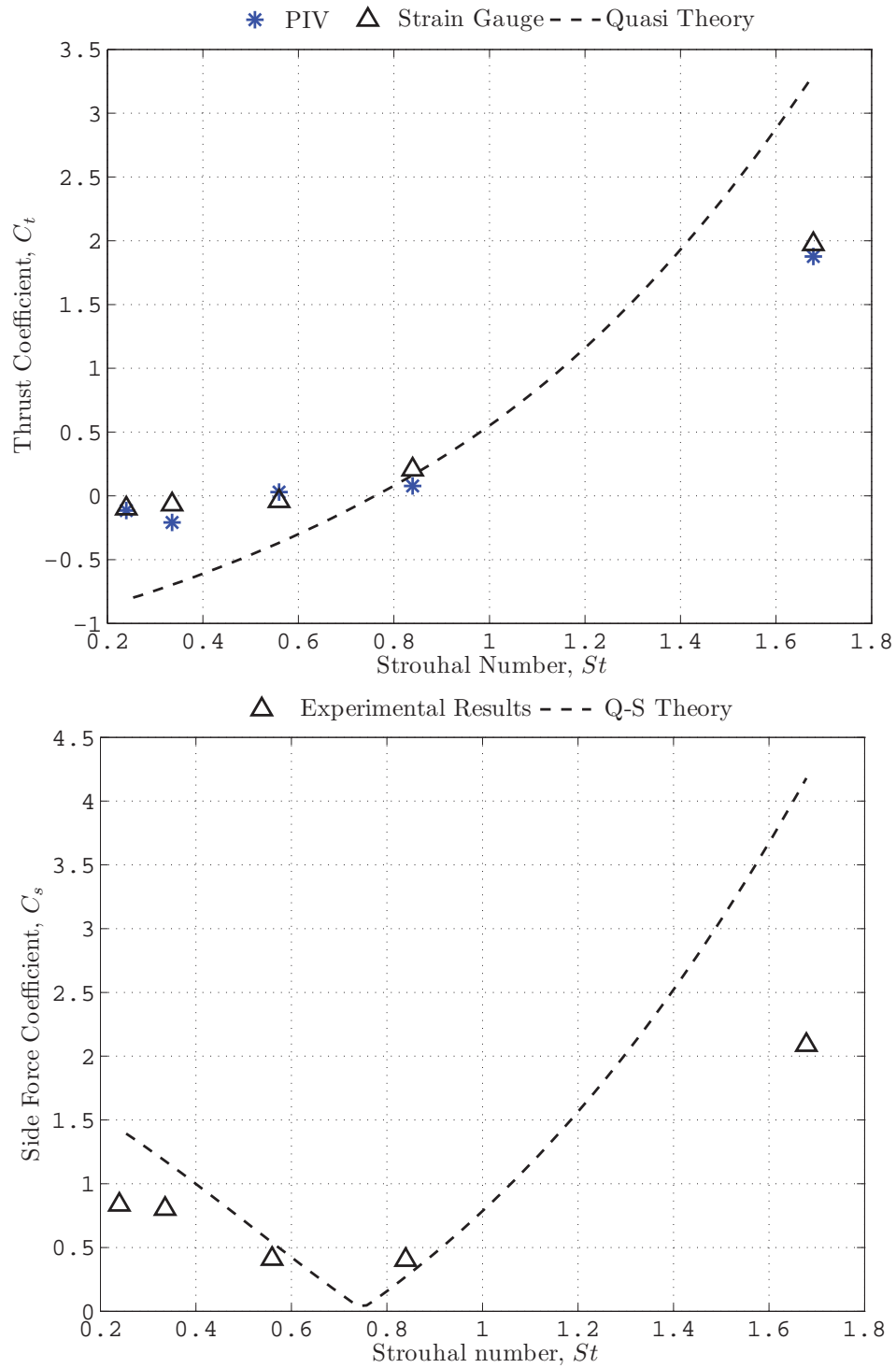


Figure 4.15: Thrust and side force coefficients, C_t and C_s , for set 12 : $\frac{h_0}{c} = 0.25$, $\theta_0 = 45^\circ$

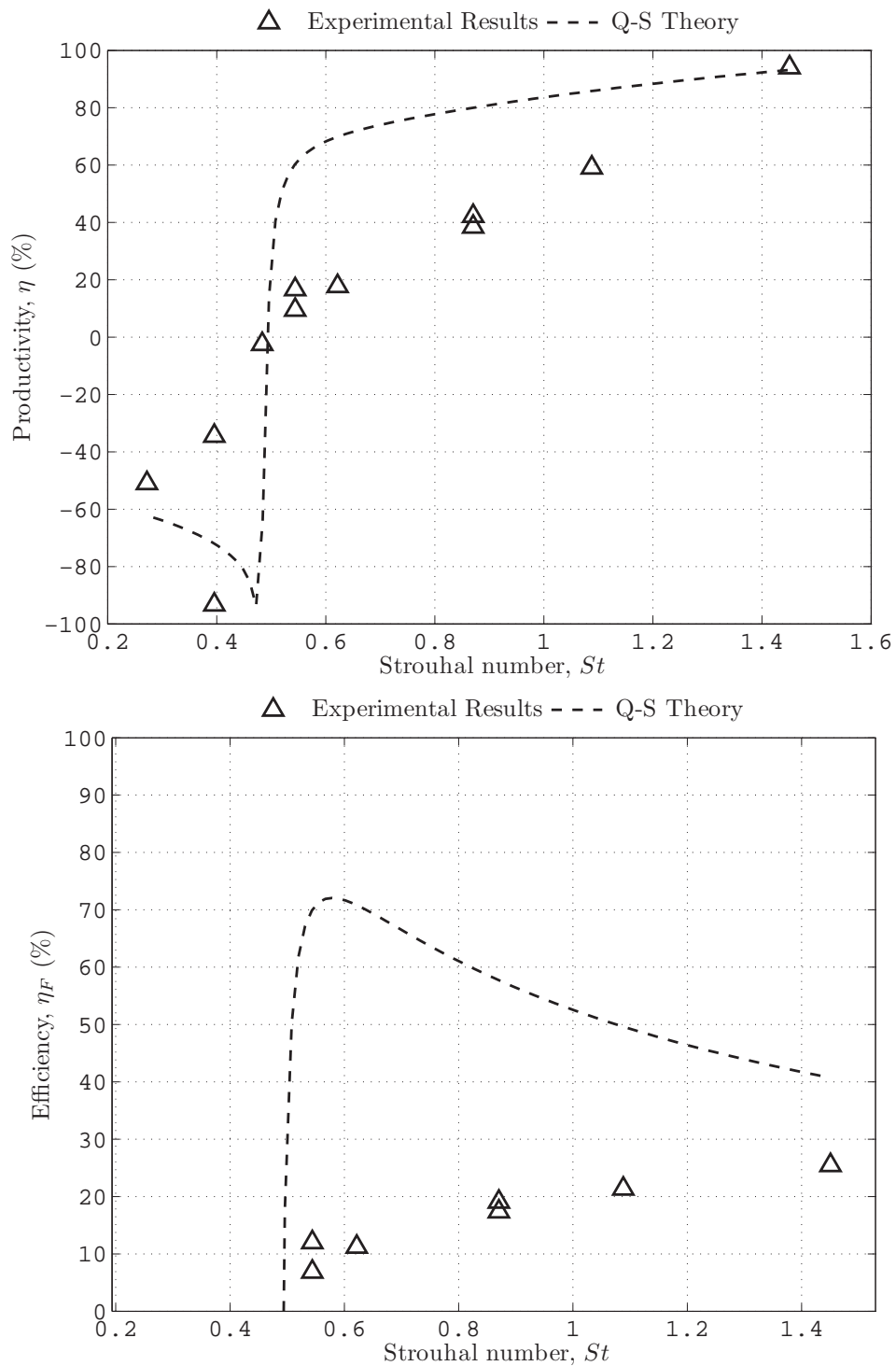


Figure 4.16: Productivity, η and Froude efficiency, η_F for set 11 : $\frac{h_0}{c} = 0.5$, $\theta_0 = 45^\circ$

4.6 Discussion

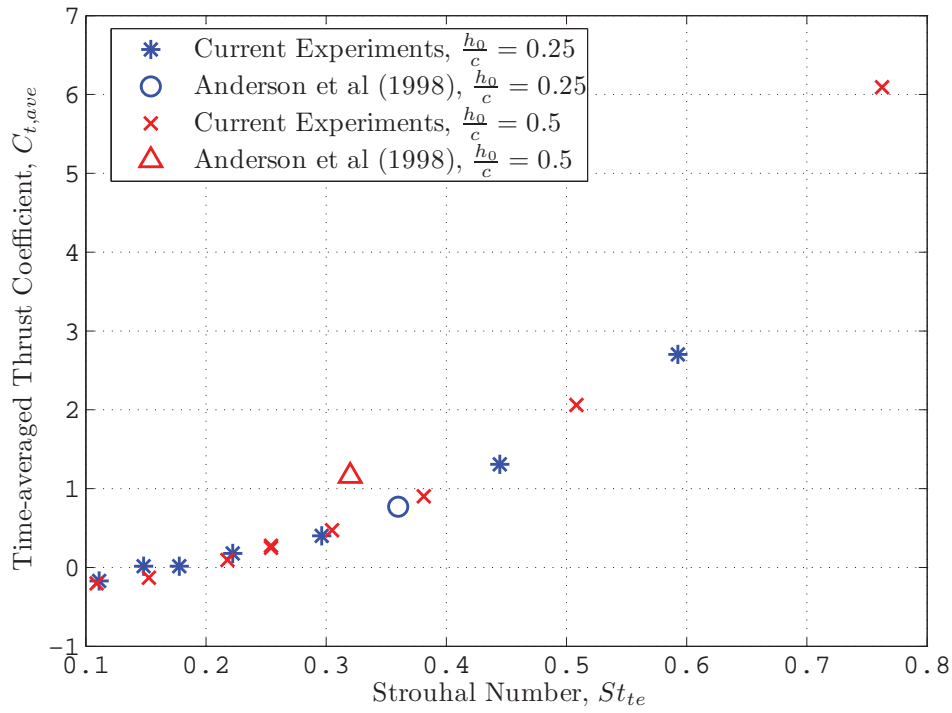


Figure 4.17: Comparison of current experimental results with results from Anderson *et al.* (1998), for $\theta_0 = 15^\circ$

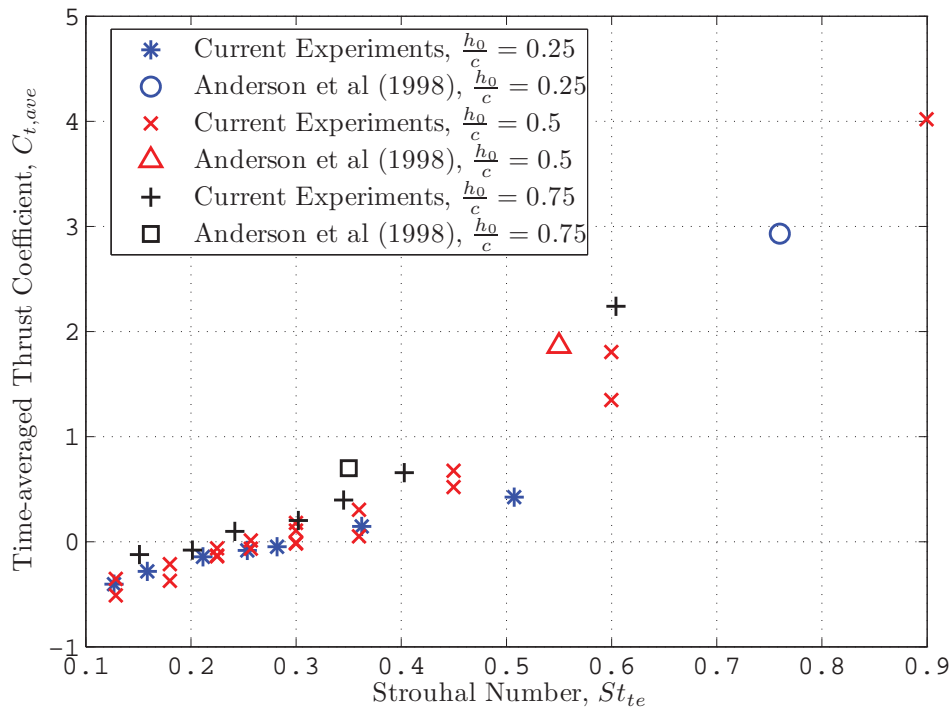


Figure 4.18: Comparison of current experimental results with results from Anderson *et al.* (1998), for $\theta_0 = 30^\circ$

A summary of the average thrust coefficient data, $C_{t,ave} = \frac{C_{t,piv} + C_{t,ave}}{2}$, plotted against the heave-based Strouhal number, St_h for all flow conditions tested is shown in Figure 4.19. It is evident from the results that the thrust coefficient data from each group collapse and show a roughly quadratic relationship with St_h , particularly at larger Strouhal numbers. The thrust coefficient data in Figure 4.19 can also be compared to similar flapping foil results performed by Triantafyllou *et al.* (1993), Anderson *et al.* (1998), Read *et al.* (2003), and Schouveiler *et al.* (2005). Their thrust coefficient results also show a similar quadratic relationship between C_t and St_h , and generally their results fall in the range of $C_t \approx 0 - 1$ in the range of $St_h \approx 0 - 0.5$, which is also consistent with the current experimental results.

Figures 4.17 and 4.18 show the results of the current force measurements when directly compared to the results by Anderson *et al.* (1998). The results appear to be in good agreement, with the results of Anderson *et al.* slightly higher than the current experiments.

The experimental results show that the Strouhal number at which the foil starts to develop thrust, $St_{0,exp}$, increases as the foil motion becomes more dominated by pitching motions, as shown in Table 4.1. This result, which is consistent with the Q-S model, is due to the fact that at larger pitch amplitudes, and smaller heave amplitudes, the Strouhal number at which the angles of attack become positive increases.

The experimental thrust coefficient and side force coefficient results also show an excellent agreement with the theoretical predictions made with the quasi-steady theory. The main deviations occur in group I, where the foil undergoes pure heaving motion, and also in set 12 in group IV, where the non-dimensional heave amplitude is small ($\frac{h_0}{c} = 0.25$) and the pitch amplitude is simultaneously large ($\theta_0 = 45^\circ$). As the Q-S model should, theoretically, perform better when the pitch amplitudes are small, it is postulated that the reason for the discrepancy in theoretical and experimental results in group I is the development of unsteady leading edge separation at large heave amplitudes, possibly leading to the break-down in the Kutta-Joukowski theorem, leading to larger-than-predicted thrust coefficients. On the other hand, the reason for the failure of the Q-S model in set 12 is probably due to the fact that the Q-S model fails to take into account the effects of the foil rotation. The strong agreement between experimental and theoretical thrust results for all other cases demonstrates that the Q-S model performs admirably, and can be used to predict the hydrodynamic forces on the unsteady foil.

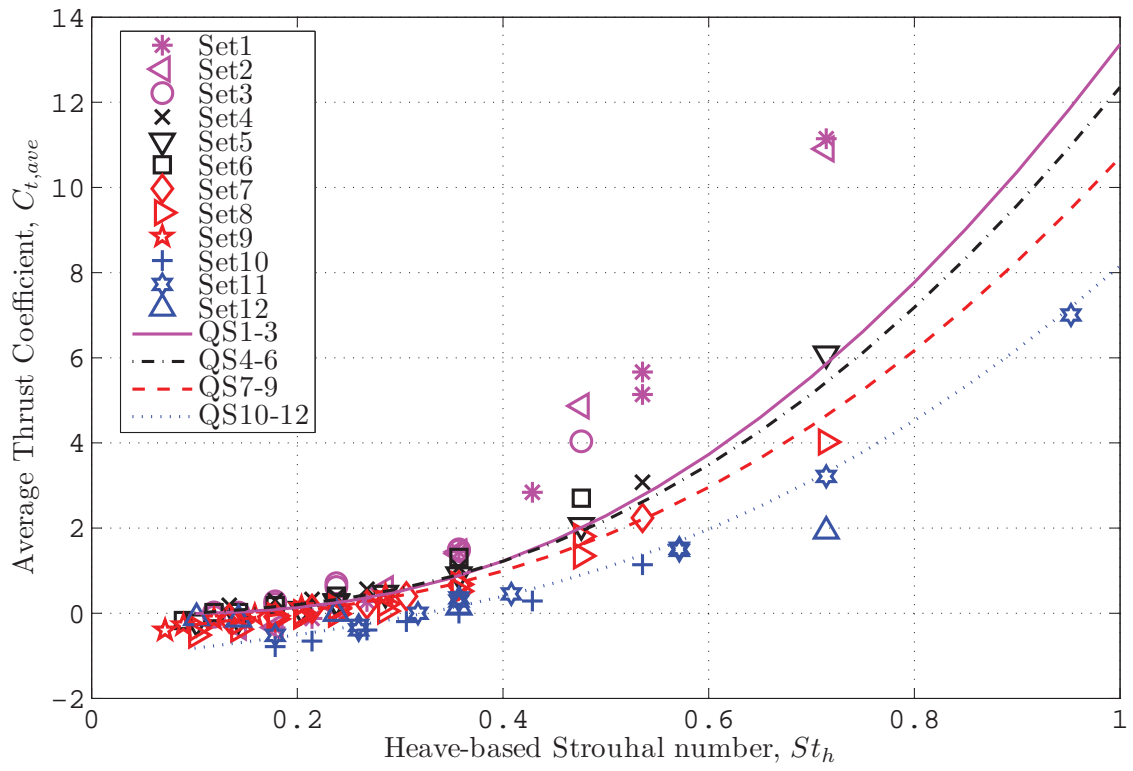


Figure 4.19: Time-averaged thrust coefficient based on an average of the PIV and strain gauge measurements, $C_{t,ave}$ vs St_h for all flow cases. For a definition of set numbers, please refer to Table 2.1 or Table 4.1

Group	Set	$\frac{h_0}{c}$	$\theta_0(^{\circ})$	χ	$St_{0,simp}$	$St_{0,q-s}$	$St_{0,exp}$
I	1	0.75	0	∞	0	0.11	≈ 0.21
	2	0.50	0	∞	0	0.11	≈ 0.20
	3	0.25	0	∞	0	0.11	≈ 0.14
II	4	0.75	15	2.80	0.09	0.10	≈ 0.12
	5	0.50	15	1.87	0.09	0.11	≈ 0.20
	6	0.25	15	0.93	0.11	0.13	≈ 0.18
III	7	0.75	30	1.30	0.21	0.22	≈ 0.23
	8	0.5	30	0.87	0.23	0.25	≈ 0.26
	9	0.25	30	0.43	0.33	0.35	≈ 0.32
IV	10	0.75	45	0.75	0.41	0.42	≈ 0.45
	11	0.50	45	0.50	0.49	0.50	≈ 0.50
	12	0.25	45	0.35	0.75	0.76	≈ 0.70

Table 4.1: Summary of experimentally measured values of St_0

The largest measured thrust coefficients generally fell within group I, with a maximum recorded $C_t \approx 12$, occurring at $St = 0.7$, and $\frac{h_0}{c} = 0.75$. For almost all flow conditions examined, no sudden loss of thrust was observed, suggesting that the concept of static stall is not applicable to an unsteady foil, and therefore even larger thrust coefficients can be produced if the Strouhal number is further increased.

The efficiency results predicted using the Q-S model only has a fair agreement with the experimental results. The Q-S model consistently overestimates the efficiency of the unsteady foil, particularly at large pitch amplitudes. This is probably due to the fact that the Q-S model does not take into account the energy required to rotate the foil, and therefore underestimates the energy required to move the foil in a flow (as predicted in Chapter 3).

Generally, the experimentally evaluated efficiencies rise sharply at low St , and show a very broad peak centered at $St \approx St_0$ (where angles of attack and thrust coefficients are small), and slowly decrease as the Strouhal number increases further.

4.7 Conclusion

Typical propulsive efficiencies tend to increase as the pitch amplitude increases from $\theta_0 = 0^\circ$, where $\eta_F \approx 10 - 30\%$ to $\theta_0 = 30^\circ$, where $\eta_F \approx 30 - 60\%$. This increase is consistent with the Q-S model, however, when the pitch amplitude is increased further to $\theta_0 = 45^\circ$, the typical efficiencies drop to $\eta_F \approx 10 - 40\%$. The reason for this is unclear.

The highest efficiency recorded was $\eta_F = 64\%$, which occurred at $\frac{h_0}{c} = 0.75$, $\theta_0 = 30^\circ$, and $St = 0.22$, although there is some doubt about the accuracy of the efficiency results, especially when the angles of attack are low and the hydrodynamic forces are small (compared to the inertia of the foil).

From the experimental results, we can determine the foil dynamic properties which would potentially provide practical applications. For short bursts of acceleration, the dynamic properties of group I ($\frac{h_0}{c} = 0.25, 0.5, 0.75$, $\theta_0 = 0^\circ$) would be highly suitable, due to the large thrust coefficients developed, albeit at low efficiencies. For continuous propulsion, however, the foil dynamic properties of group III ($\frac{h_0}{c} = 0.25, 0.5, 0.75$, $\theta_0 = 30^\circ$) would be more suitable, due to its balance of moderate efficiency and thrust production.

4.7 Conclusion

From the comparison of the experimental data with the results from the quasi-steady model, it can be concluded that:

- In almost all flow conditions, the experimental thrust and side force coefficients are in excellent agreement with the theoretical estimates, demonstrating that the quasi-steady theory is a useful predictor of forces on an unsteady foil;
- There are discrepancies between the experimental and theoretical force results when:
 - a) the foil is purely heaving; very large thrust and side force coefficients are developed, approximately twice as large as theoretically predicted. As the Q-S model is expected to be more accurate when pitching amplitudes are small, it is postulated that this discrepancy is due to unsteady effects on the foil, in particular leading edge separation and the breakdown of the Kutta-Joukowski condition, which is not accounted for in the Q-S model;
 - b) the non-dimensional heave amplitudes are small ($\frac{h_0}{c} = 0.25$) and the pitch amplitudes are simultaneously large ($\theta_0 = 45^\circ$); the theoretical thrust and side forces are overestimated, due to the failure of the Q-S model to account for the effects of rotation on the flow around the foil;

- The Q-S model tends to over-estimate the efficiency values, particularly when the pitch amplitudes are large, probably due to the failure of the Q-S model to account for the rotation of the foil;
- The thrust coefficients follow approximately a quadratic relationship with St ;
- The experimentally-determined efficiencies show a broad peak at $St \approx St_0$, where hydrodynamic forces and angles of attack are low;
- As a method of locomotion, the unsteady foil has two distinct modes of practical application:
 - a) A “quick burst” mode, developed when the foil undergoes pure heaving ($\frac{h_0}{c} = 0.25, 0.5, 0.75, \theta_0 = 0^\circ$) where very large thrust coefficients can be developed ($C_t \approx 12$ at $St \approx 0.7$), at the expense of propulsive efficiency ($\eta_F \approx 20\%$);
 - b) A “cruise” mode, occurring when the foil undergoes moderate heave and pitch amplitudes ($\frac{h_0}{c} = 0.25, 0.5, 0.75, \theta_0 = 30^\circ$), where moderate thrust ($C_t \approx 2$ at $St \approx 0.5$) and propulsive efficiencies ($\eta_F \approx 40 - 50\%$) can be simultaneously developed.

Chapter 5

Wake Patterns of an Unsteady Foil

5.1 Introduction

In this chapter, we investigate the effect of the foil dynamic parameters on the wake patterns produced behind the foil. To study the wake patterns of the foil, three methods have been employed, a) two dimensional dye visualisation ($Re = 900 - 3,500$), b) three dimensional hydrogen bubble visualisation ($Re = 500 - 3,500$) and c) two dimensional flow visualisation based on the PIV-derived vorticity fields ($Re = 1,250 - 12,500$). The details of these methods have already been discussed in chapter 2.

The intention of this chapter is to make a survey of the various wake patterns behind the flapping foil for a large range of foil parameters and flow conditions, and to identify any key vortical structures that may be essential to the development of thrust on the foil. The results of the qualitative flow visualisation based on each method are discussed individually below.

5.2 Dye visualisation

Preliminary investigations of the flow around the unsteady foil using dye visualisation indicate that for most flow cases and foil parameters tested, the wake consists of a combination of two qualitatively different vortical structures, which we name “P” vortices and “S” vortices. “P” vortices are only noticeable at moderate to large Strouhal numbers, and are shed into the wake at a rate of one per foil half-cycle. “S” vortices, on the other hand, are clearly generated regardless of the value of St , and are usually shed into the wake in a path approximately traced by the trailing edge of the foil. There may be more than one “S” vortex generated per half cycle, depending on the foil parameters and flow conditions.

Based on the arrangements and the relative strengths of the “P” and “S” vortices, we observe three different flow regimes : a “drag” regime, a “transitional” regime, and a “thrust” regime. These flow regimes are differentiated by the resulting vortex wake patterns and are highly dependent on the Strouhal number, or more specifically, whether the Strouhal number is below or above the critical Strouhal number St_0 . The foil heave and pitch amplitudes, as well as the chord-based Reynolds number, Re , only have a secondary effect on the wake patterns. We attempt to illustrate the observed differences between the “P” and “S” vortices, and show how these vortices form the final wake pattern behind the unsteady foil, based on a brief discussion on each flow regime below:

In the “drag” regime, occurring at low Strouhal numbers roughly corresponding to $St \lesssim St_0$ (Figure 5.1), the observed wake pattern consists of a series of alternating counter-rotating vortices (“S” vortices). These vortices are shed along a path that approximately corresponds to the location of the trailing edge of the foil, therefore the resulting wake pattern can be interpreted as a localised (or foil-relative) regular von Karman vortex street (LK). The direction of rotation of the “S” vortices suggests that there is a nett momentum deficit in the wake of the foil, and hence the unsteady foil is expected to produce nett drag across the entire flapping cycle. The frequency of shedding of “S” vortices of both rotational directions is typically higher than the flapping frequency of the foil, indicating that the “free” shedding of “S” vortices is not phase-locked to the flapping motion of the foil.

In the second flow regime, corresponding to $St \approx St_0$, the wake pattern noticeably changes to one of three possibilities. In the first pattern, shown in Figure 5.2a, the wake consists of a single “P” vortex which is shed once per foil half-cycle. This “P” vortex is shed at a location approximately corresponding to the time-averaged foil centreline, roughly forming a line that is parallel to the free-stream flow, and thus implying that the width of the wake is approximately zero. This wake pattern suggests that the foil is neither producing nett thrust nor drag. This pattern will be referred as the in-line vortex wake pattern (I-P), and usually occurs when the foil trailing edge amplitude, A_{te} is small. In the second flow pattern, shown in Figure 5.2b, one relatively large “P” vortex is shed per foil half-cycle, at a location vertically (i.e., along the y-axis) distant from the time-averaged foil centreline. “P” vortices are also accompanied by a number of “S” vortices. The number of “S” vortices shed per foil half-cycle is dependent on the foil kinematic properties and flow conditions, however, large values of A_{te} typically result in more “S” vortices. For the special case where there is exactly one shed “S” vortex per half-cycle, we obtain a wake pattern as shown in Figure 5.2c. These wake patterns are dubbed the P+XS and P+S patterns respectively. In both these flow patterns, the shedding of “S” vortices is phase-locked to the flapping motion of the foil, as highlighted by the fact that “S” vortices of only one particular rotational direction are generated per foil half-cycle. In both these wake

5.2 Dye visualisation

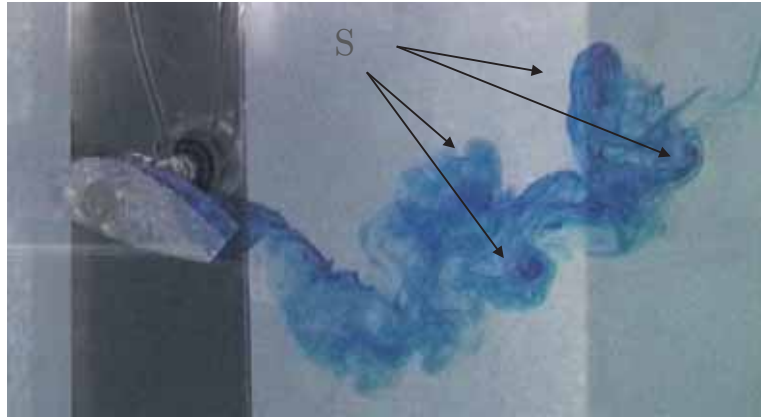
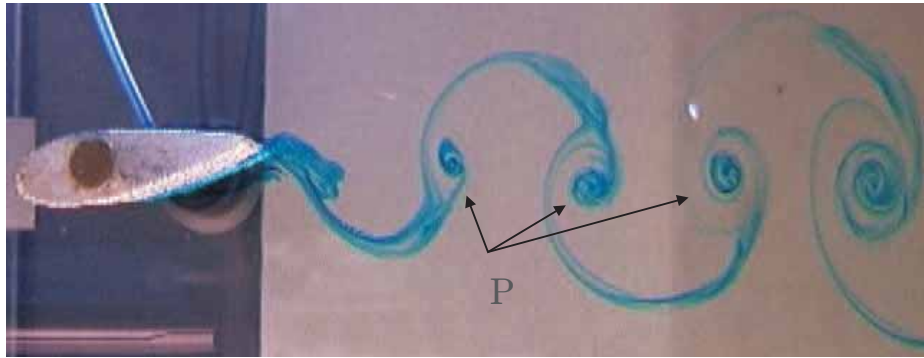


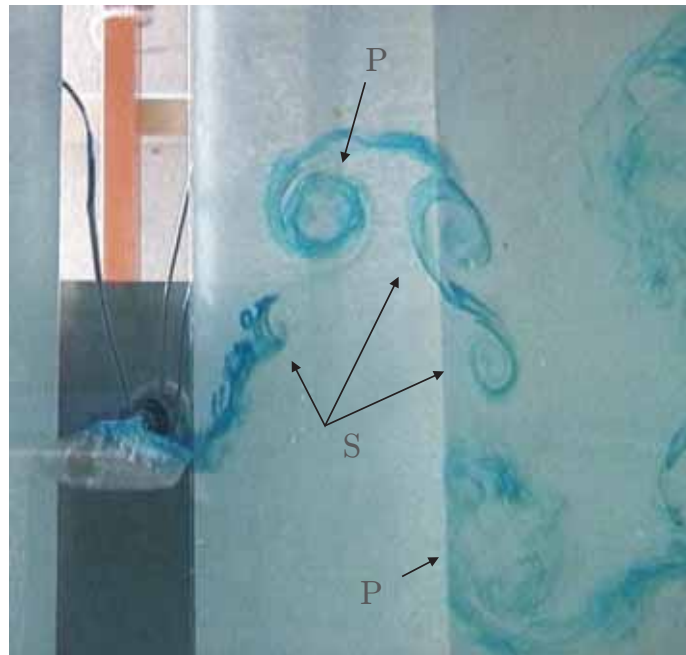
Figure 5.1: Dye flow visualisation for $St < St_0$, $\frac{h_0}{c} = 0.5$, $\theta_0 = 45^\circ$, $St = 0.14$, $St_{0,exp} = 0.5$, $Re = 3,500$.

patterns, the locations of the shed “S” vortices form an approximately regular Karman vortex sheet, while the shed “P” vortices form a reverse Karman vortex street (for example, see Figure 5.2c). We judge the strength of the “P” and “S” vortices to be of similar magnitude, due to their physical size and rate of rotation (seen on video). Therefore, it is expected that the P+XS and P+S wake patterns produce a “neutral” wake, whereby the foil is neither producing nett thrust nor drag forces.

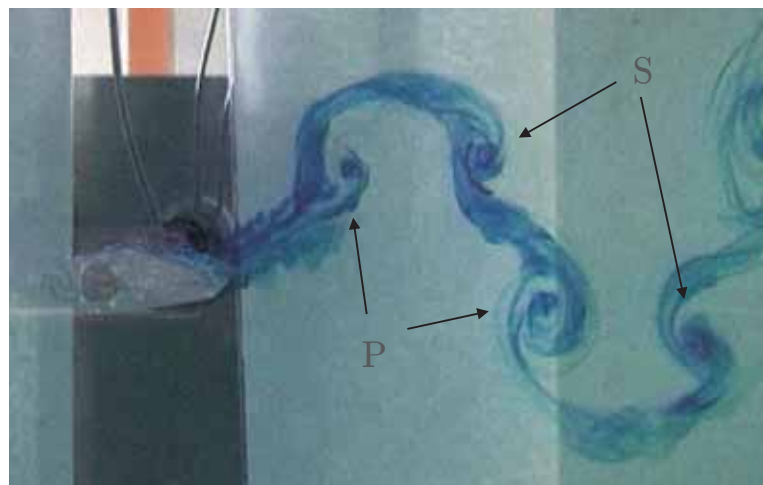
At large Strouhal numbers, corresponding to $St > St_0$ (Figure 5.3), the “P” vortices are observed to be strong relative to the “S” vortices. The “P” vortices, which are shed once per foil half-cycle, are shed away from the foil centreline such that the wake forms a reverse Karman vortex street. The rotational directions of the shed “P” vortices implies that there is a positive momentum surplus downstream of the foil, and therefore indicates that the foil is producing nett thrust. The “P” vortices may be accompanied by clear “S” vortices, as shown in Figures 5.3a and 5.3c, or the “P” vortices may be so large that they totally dominate the flow, resulting in little or no observed “S” vorticity (Figure 5.3b). Of additional interest is the fact that in cases where the non-dimensional heave amplitude is large compared to the pitch amplitude (i.e., at large χ), it was observed that the “P” vortices are predominantly generated close to the leading edge of the foil (Figure 5.3c). We link the generation of strong vorticity near the leading edge of the foil with the phenomenon of leading edge separation. Vorticity generated due to leading edge separation is labelled as “LE” vorticity. In cases where the heave amplitude is not particularly large, the “P” vortices are predominantly generated closer to the trailing edge of the foil (Figures 5.3a and 5.3b).



(a) $\frac{h_0}{c} = 0.25$, $\theta_0 = 15^\circ$, $St = 0.18$, $St_{0,exp} = 0.18$, $Re = 2,000$



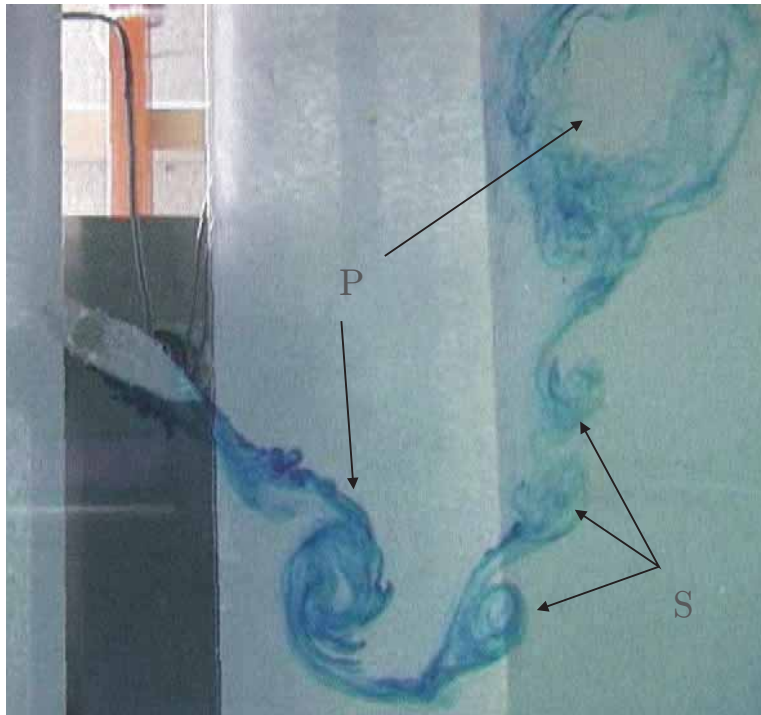
(b) $\frac{h_0}{c} = 0.75$, $\theta_0 = 15^\circ$, $St = 0.22$, $St_{0,exp} = 0.12$, $Re = 2,000$



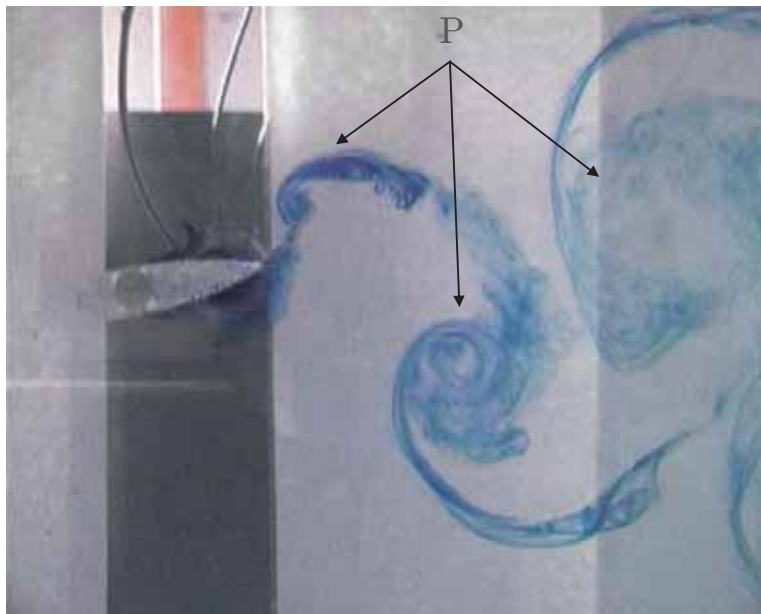
(c) $\frac{h_0}{c} = 0.25$, $\theta_0 = 30^\circ$, $St = 0.21$, $St_{0,exp} = 0.32$, $Re = 2,400$

Figure 5.2: Dye flow visualisation for $St \approx St_0$

5.2 Dye visualisation

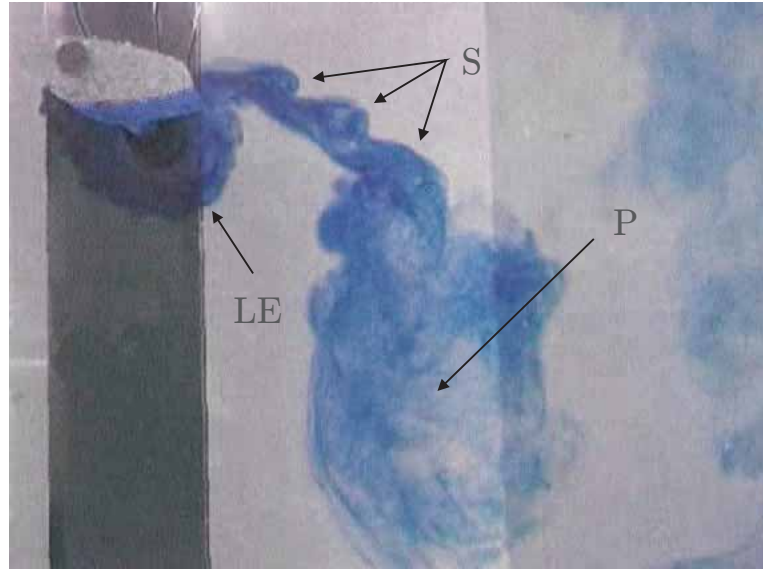


(a) $\frac{h_0}{c} = 0.75$, $\theta_0 = 45^\circ$, $St = 0.69$, $St_{0,exp} = 0.45$, $Re = 1,500$



(b) $\frac{h_0}{c} = 0.25$, $\theta_0 = 15^\circ$, $St = 0.44$, $St_{0,exp} = 0.18$, $Re = 1,500$

Figure 5.3: Dye flow visualisation for $St > St_0$



(c) $\frac{h_0}{c} = 0.75$, $\theta_0 = 0^\circ$, $St = 0.43$, $St_{0,exp} = 0.21$, $Re = 2,000$

Figure 5.3: Dye flow visualisation for $St > St_0$ (continued)

5.3 Three-dimensional hydrogen bubble visualisation

In the previous section, the results of the dye flow visualisation indicate that for the majority of foil parameters and flow conditions, the wake patterns generally fall into three regimes, depending on the value of St relative to St_0 . In general, the wake patterns within each regime are qualitatively similar, regardless of the foil heave and pitch amplitude. The only exception to this is when the non-dimensional heave amplitude is very large (relative to the pitch amplitude), where leading edge vortices are clearly observed.

Therefore, we proceed to further study the three-dimensional flow around the unsteady foil in more detail for “representative” foil kinematic parameters of $\frac{h_0}{c} = 0.5$ and $\theta_0 = 30^\circ$ (moderate $\chi \approx 1$), and for a purely heaving case of $\frac{h_0}{c} = 0.5$ and $\theta_0 = 0^\circ$ (large $\chi = \infty$), at Strouhal numbers corresponding to each flow regime.

It should be noted that in the following discussion, the terms “top dead centre” and “bottom dead centre” are frequently used to describe the location of the foil at the extremities of the heave cycle (that is, at $\phi = 90^\circ$ and $\phi = 270^\circ$). This is illustrated in 5.4.

5.3 Three-dimensional hydrogen bubble visualisation

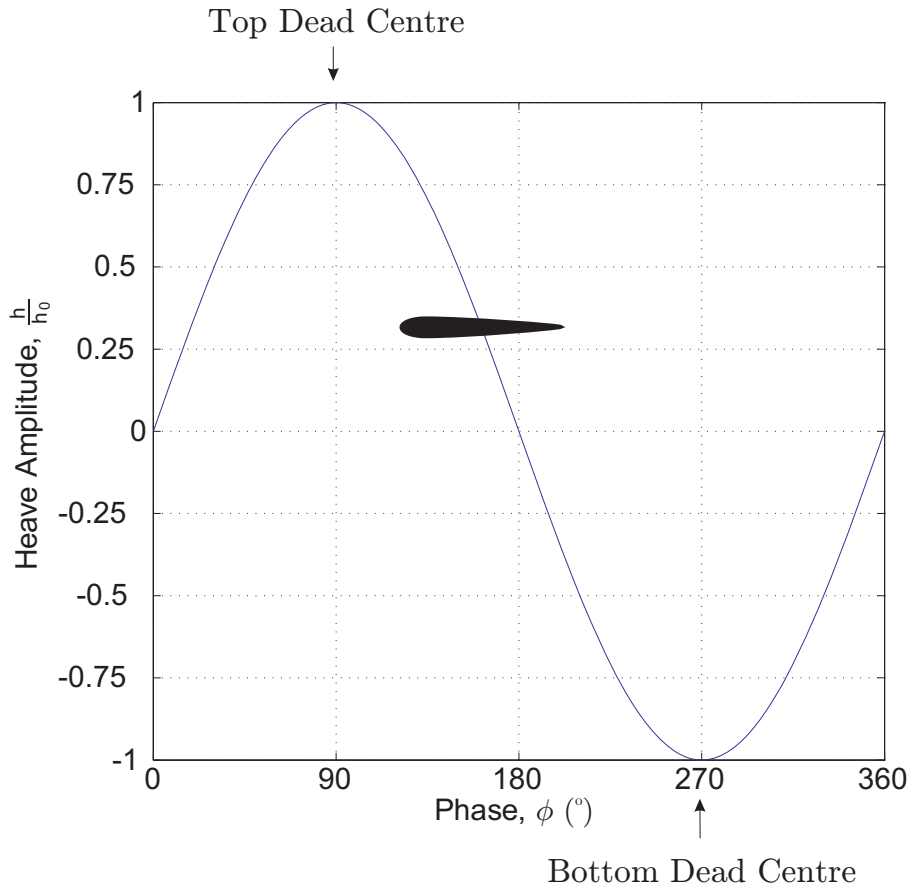


Figure 5.4: Definition of top dead centre (TDC) and bottom dead centre (BDC)

5.3.1 Spanwise view

5.3.1.1 Group III, set 8 : $\chi = 0.87$, $\frac{h_0}{c} = 0.5$, $\theta_0 = 30^\circ$

At $St = 0.13 < St_0$ (Figure 5.5), the wake pattern does not appear to contain any distinguishable large scale vortical structures. There is some hint of roll-up of vorticity (see Figure 5.5f), however, the roll-ups are either too small, or too weak to be clearly observed.

Figure 5.6 shows the flow around the foil at $St = 0.29 \approx St_0$. The wake pattern now consists of a number of discrete and observable vortical structures. Every foil half-cycle, one moderately large “P” vortex is shed, while two smaller “S” vortices are shed (for example, vortices P_1 , S_1 and S_2 in Figure 5.6a).

The generation of the “P” vortices is rooted in the development of flow separation, typically occurring near the leading edge of the foil as shown in Figures 5.6a to 5.6g. In this instance, the vorticity generated due to separation near the leading edge of the foil rolls up into a distinct leading edge vortex, LE_1 as the foil approaches the maximum downstroke (Figures 5.6a and

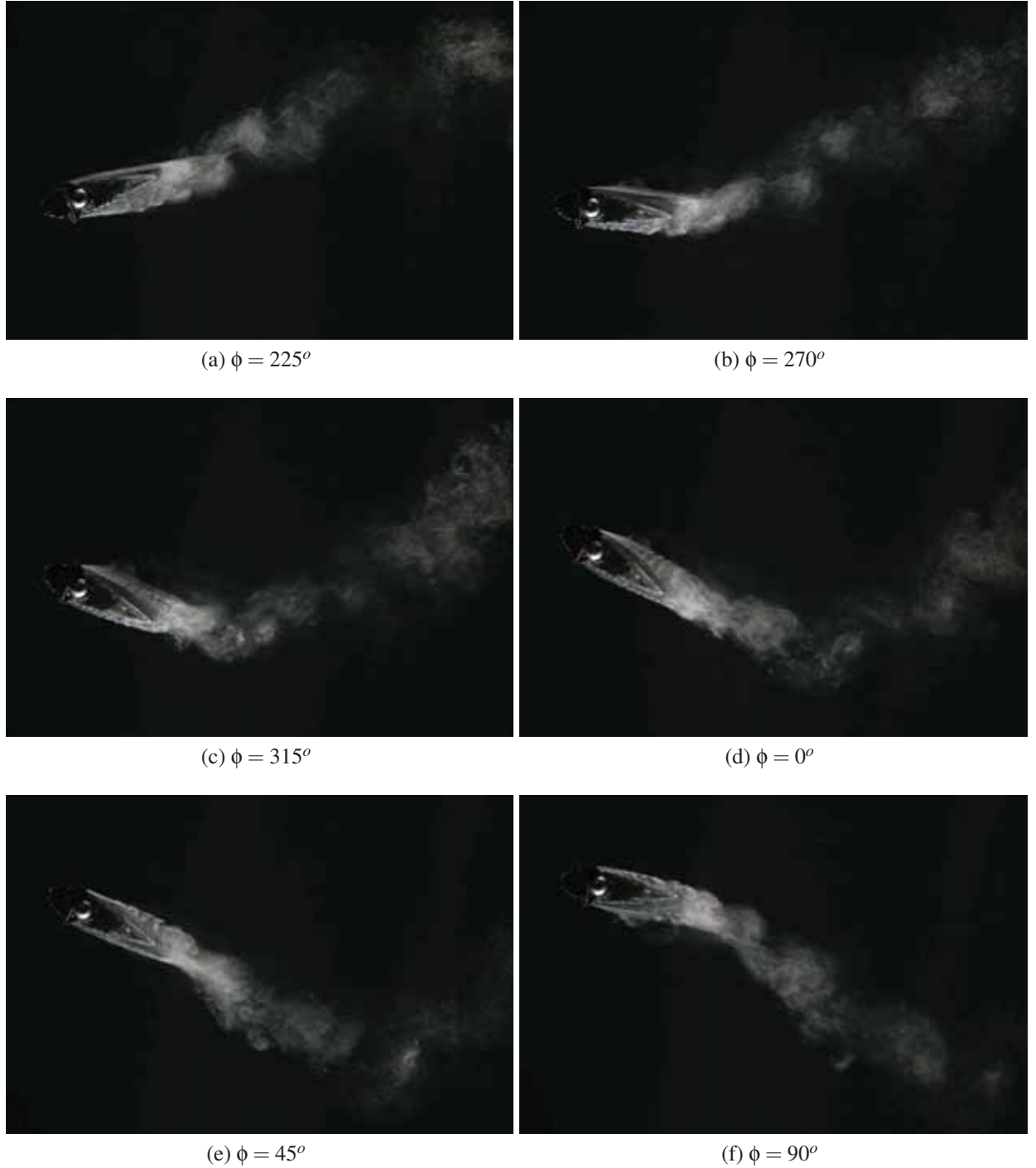


Figure 5.5: Hydrogen bubble image sequence, spanwise view, for group III, set 8 : $\frac{h_0}{c} = 0.5$, $\theta_0 = 30^\circ$, $St = 0.13$, $St_{0,exp} = 0.26$, $Re = 2,800$

5.3 Three-dimensional hydrogen bubble visualisation

5.6b). LE_1 then starts to slowly propagate towards the trailing edge of the foil (Figures 5.6c-f), where it finally sheds into the foil wake as a “P” vortex, P_3 (Figure 5.6g).

Figure 5.6a and 5.6b show the first sign of the generation of an “S” vortex, S_3 , which occurs just after the shedding of the “P” vortex, P_2 . One further “S” vortex, S_4 , is shed close to the end of the foil downstroke (Figure 5.6e). These “S” vortices are generated closer to the trailing edge of the foil, and appear to be smaller and more compact than the “P” vortices. The S_4 vortex appears to be particularly weak, possibly due to the low trailing edge velocities when the foil is close to the extremities of the heave cycle. Nevertheless, the weak S_4 vortex is shed as an individual vortical structure, even though it is shed in relatively close proximity to the strong LE_1 vortex.

The positions of the shed “P” and “S” vortices (P_1 - S_1 - S_2 and P_2 - S_3 - S_4) indicate that the wake profile is qualitatively similar to the P+XS pattern observed in the dye flow visualisation (Figure 5.2b).

As the Strouhal number is increased to $St = 0.44 > St_0$ (Figure 5.7), the wake pattern is now dominated by strong “P” vortices, which are shed at once per foil half-cycle. The locations and rotational directions of the “P” vortices clearly form a reverse Karman vortex street pattern.

Similar to the flow at $St = 0.29$ above, the leading edge vortex, LE_1 , starts to develop during the latter part of the foil downstroke (Figure 5.7a-c). However, this leading edge vortex now appears to merge with a “S” vortex, S_4 , to form a single vortical structure P_3 (Figures 5.7e-h), which is shed close to the maximum foil trailing edge excursion.

Further “S” vortices are also generated as the trailing edge moves within the flow, however, these vortices are either strongly influenced by the shed “P” vortices (for example, in Figure 5.7d-h, vortex S_2 merges with a much larger and stronger vortex P_2), or are shed as very weak vortical structures that are barely noticeable (for example, vortices S_1 and S_3).

The presence of strong “P” vortices arranged in a reverse Karman vortex street, and the lack of strong “S” vortices in the wake suggest that within this flow regime, the foil is expected to produce nett thrust over an entire foil flapping cycle.

5.3.1.2 Group I, set 2 : $\chi = \infty$, $\frac{h_0}{c} = 0.5$, $\theta_0 = 0^\circ$

For the purely heaving foil, the value of $St_{0,exp} \approx 0.1 - 0.2$ is small, and therefore we do not expect the foil to display wake patterns corresponding to the “drag” regime.

At low $St = 0.14 \approx St_0$, the wake pattern consists of a moderately strong leading edge vortex (LE_1) that is shed approximately along the foil centreline (as shown in Figure 5.8), indicating an

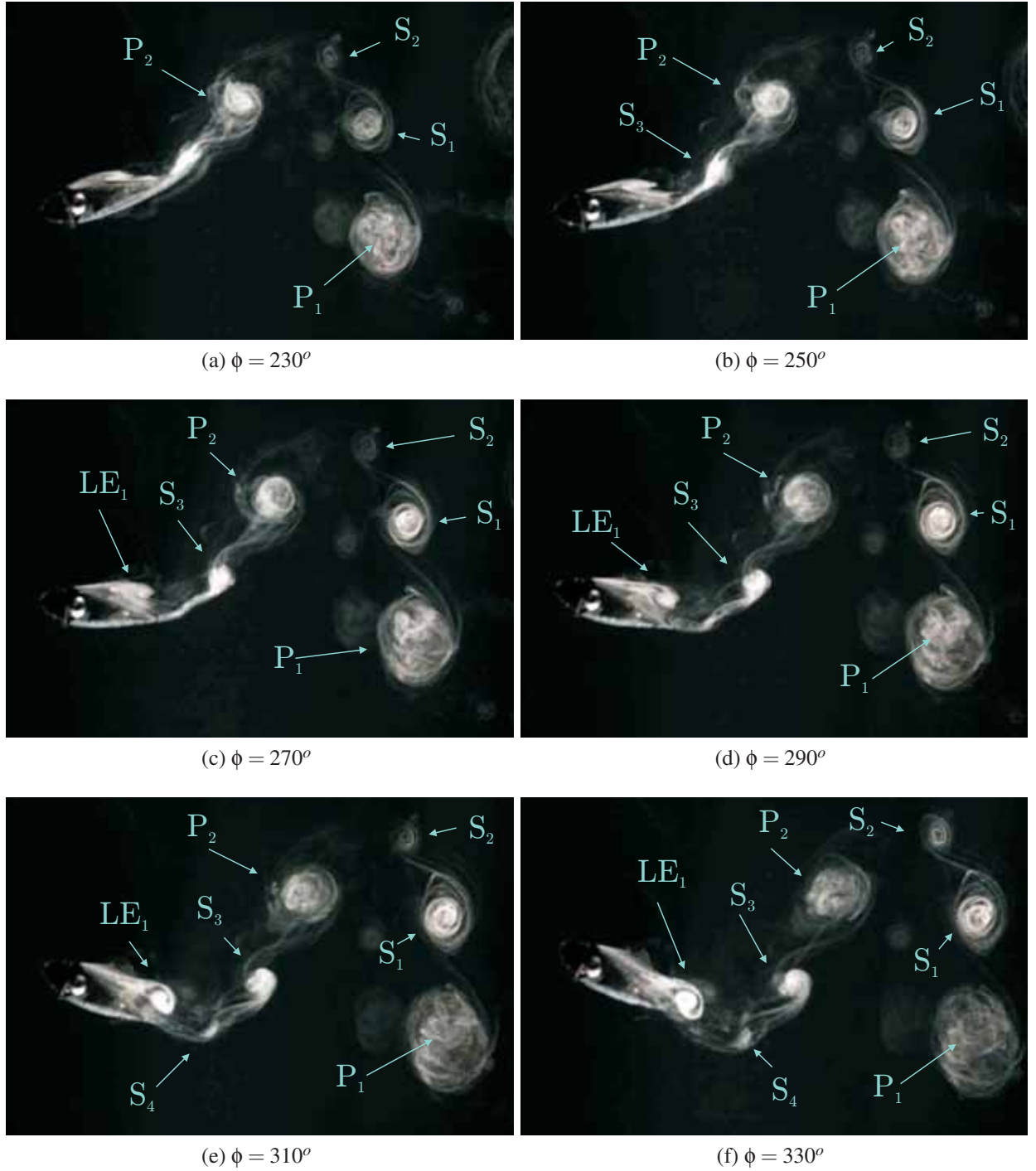


Figure 5.6: Hydrogen bubble image sequence, spanwise view, for group III, set 8 : $\frac{h_0}{c} = 0.5$, $\theta_0 = 30^\circ$, $St = 0.29$, $St_{0,exp} = 0.26$, $Re = 2,500$ (continued on following page)

5.3 Three-dimensional hydrogen bubble visualisation

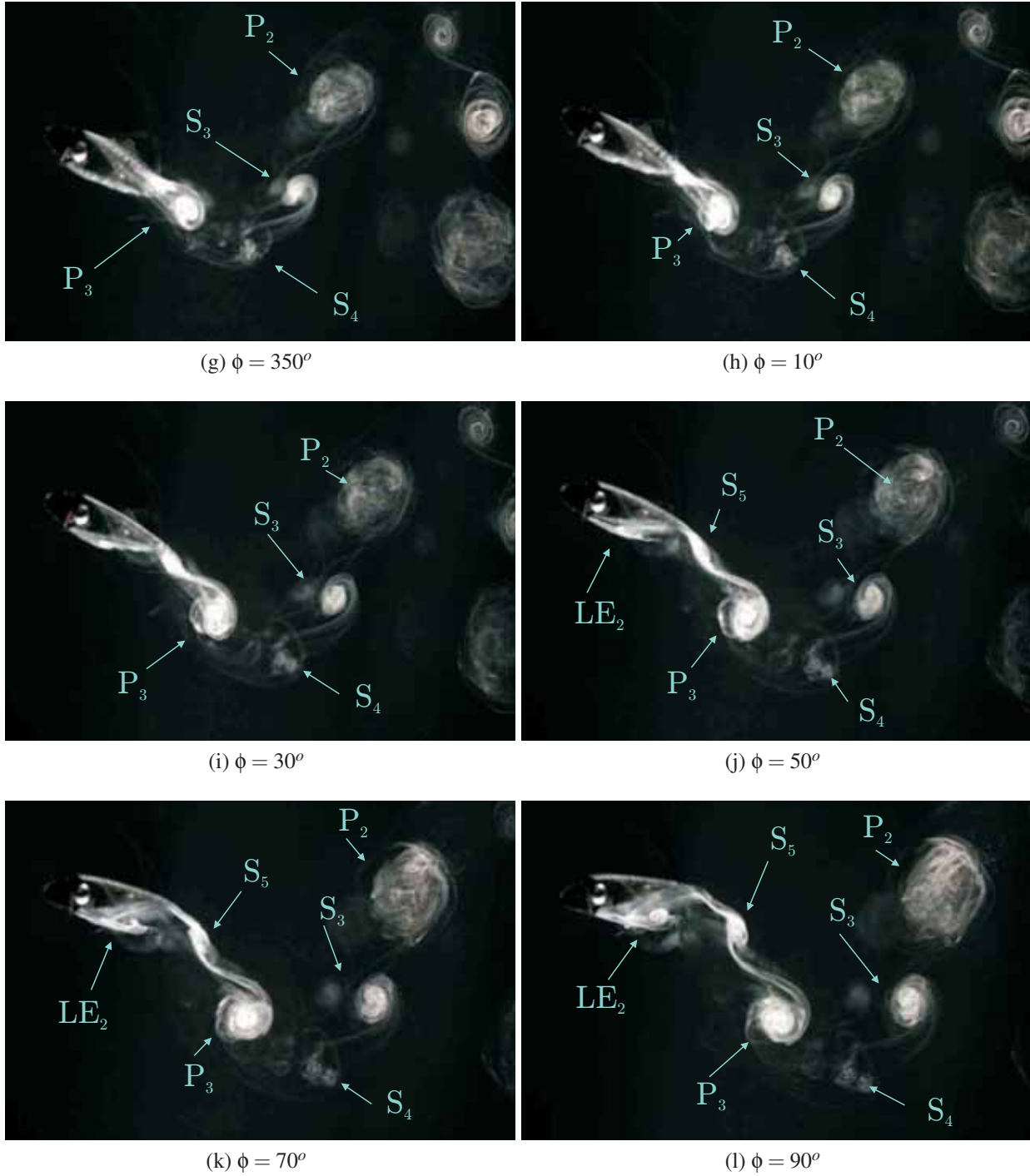


Figure 5.6: Hydrogen bubble image sequence, spanwise view, for group III, set 8 : $\frac{h_0}{c} = 0.5$, $\theta_0 = 30^\circ$, $St = 0.29$, $St_{0,exp} = 0.26$, $Re = 2,500$ (continued)

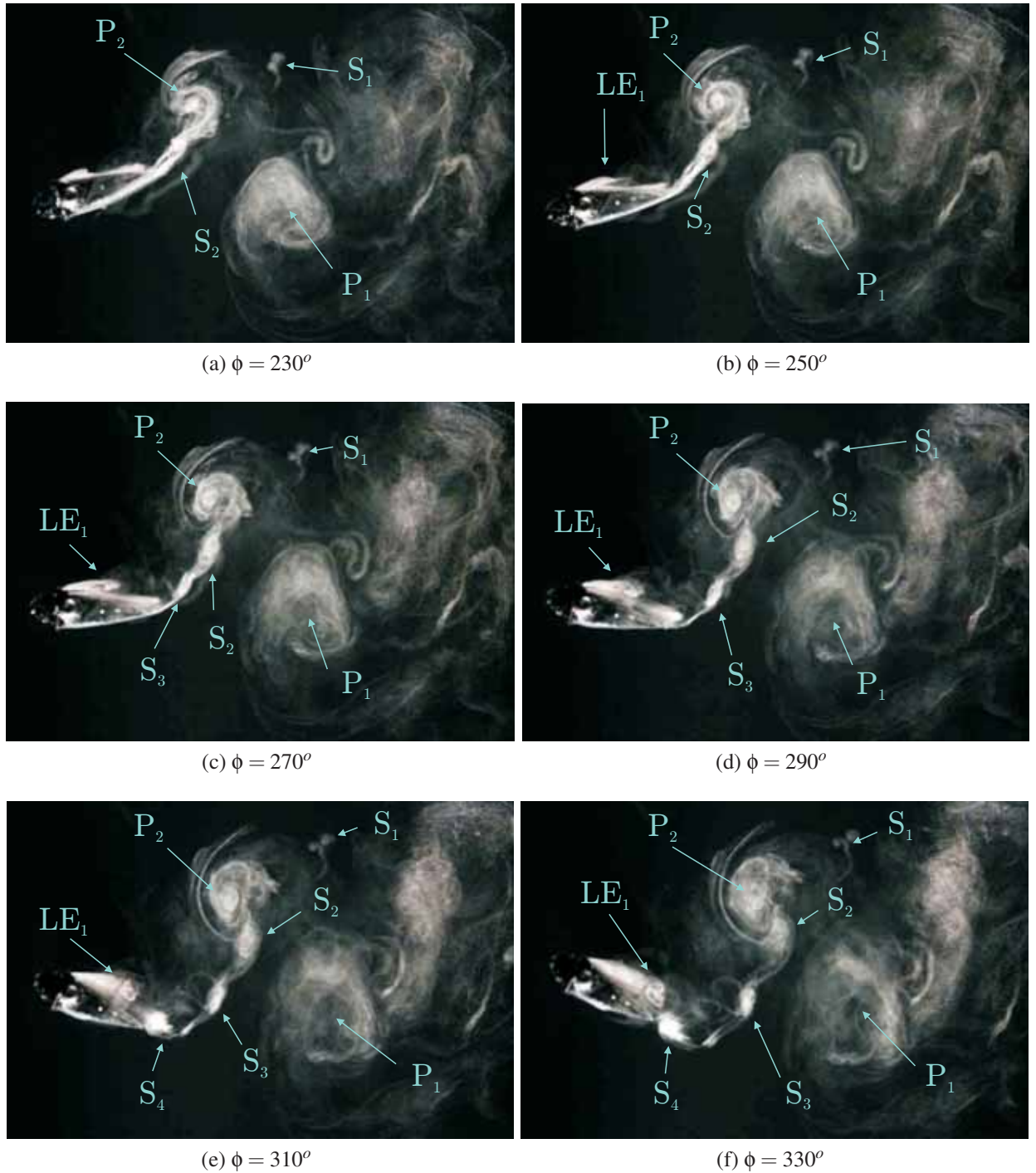


Figure 5.7: Hydrogen bubble image sequence, spanwise view, for group III, set 8 : $\frac{h_0}{c} = 0.5$, $\theta_0 = 30^\circ$, $St = 0.44$, $St_{0,exp} = 0.26$, $Re = 1,500$ (continued on following page)

5.3 Three-dimensional hydrogen bubble visualisation

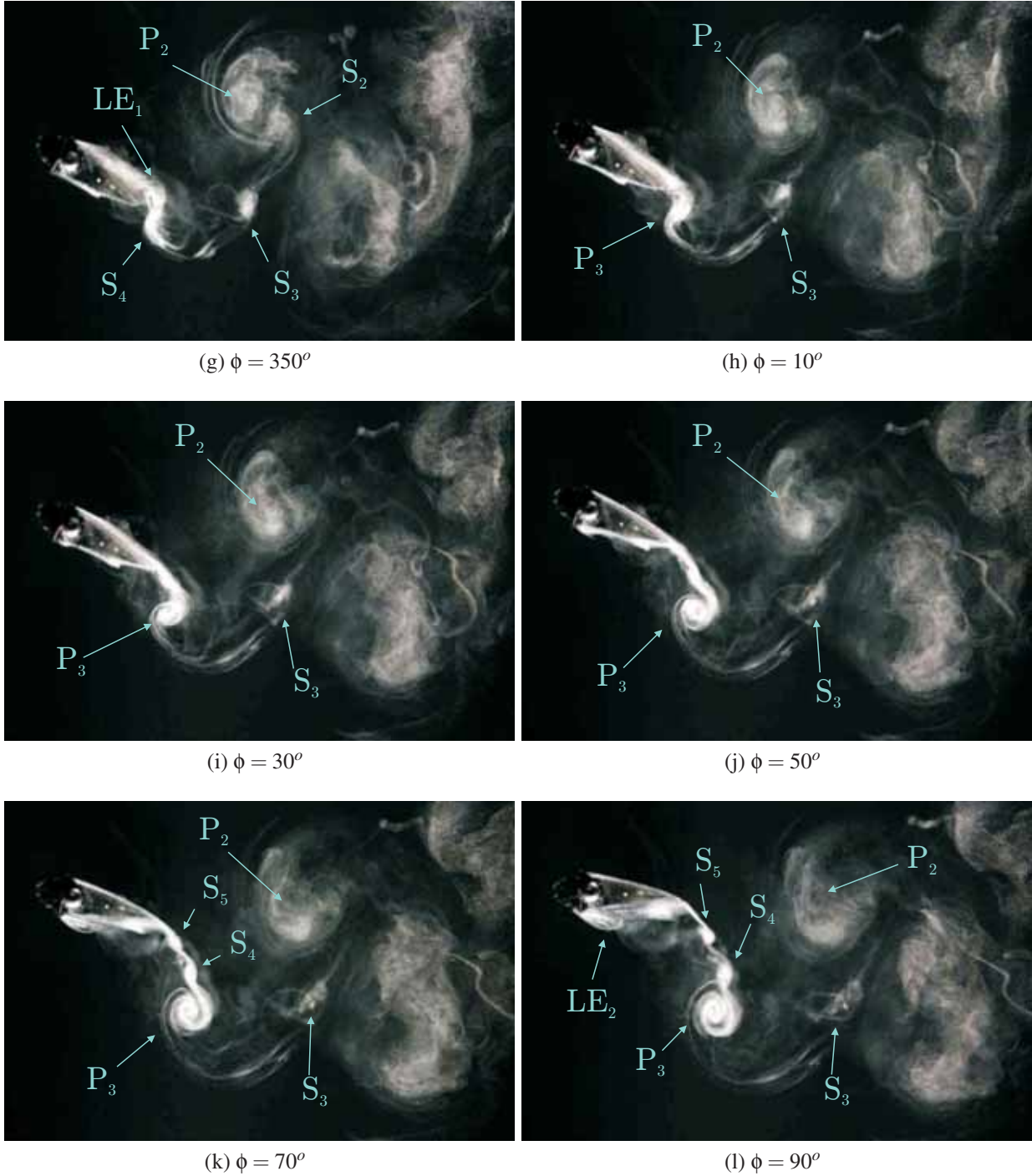


Figure 5.7: Hydrogen bubble image sequence, spanwise view, for group III, set 8 : $\frac{h_0}{c} = 0.5$, $\theta_0 = 30^\circ$, $St = 0.44$, $St_{0,exp} = 0.26$, $Re = 1,500$ (continued)

in-line vortex wake pattern (I-P), and thus the flow is in the “transitional” regime. This leading edge vortex is moderately large but diffuse, and is shed into the wake at a rate of one per foil half-cycle as a “P” vortex (P_1 and P_2). “S” vortices, S_1 and S_2 , are also observed to shed at once per foil half-cycle, out-of-phase with the shedding of the “P” vortices. Additional “S” vortices may be present, however, it may be masked by the fact that a) the “P” vortex is large and b) the Reynolds numbers are relatively large and thus the hydrogen bubbles may not be able to seed the flow with sufficiently high density.

Figure 5.9 shows the flow around the purely heaving foil at $St = 0.24 > St_0$. A leading edge vortex, LE , is again apparent, developing as the foil reaches its lowest position (Figure 5.9b-f). Close to bottom dead centre, $\phi \approx 270^\circ$ (Figures 5.9e-f), a small vortex is shed at the trailing edge of the foil (S_4), while LE_1 appears to remain attached to the foil. As S_4 is shed into the wake away from the foil centreline position, the leading edge structure, LE_1 , propagates slowly along the foil boundary towards the trailing edge, where it eventually sheds close to the foil centreline as vortex P_3 (Figure 5.9i). The vertical separation between vortices P_2 and P_3 is small, but non-zero, indicating that P_2 and P_3 form a reverse Karman vortex street pattern, albeit with a very small wake width. There is some indication of the existence of further “S” vortices (e.g., S_1 , S_2 and S_5), however, these vortices are very weak and are not clearly observed in the flow, due to the presence of the large and diffuse “P” vortices. As the “P” vortices dominate the flow, we expect the flow to be on the verge of entering the “thrust” regime.

When the Strouhal number is increased to $St = 0.36 > St_0$ (Figure 5.10), the “P” vortices P_1 and P_2 are now much stronger, and are clearly shed further away from the foil centreline position. The generation of strong “P” vortices is attributed to the generation of large leading edge vortex structures. As an example, leading edge vorticity LE_1 , which starts to develop during the foil downstroke (as shown in Figure 5.10b), engulfs the numerous small “S” vortices generated at the trailing edge of the foil to generate one large vortex, P_3 (Figures 5.10e and f). The resulting “P” vortices form a clear reverse Karman vortex street pattern.

5.3.2 Planform view

To obtain an overall representation of the three-dimensional flow around the foil, we examine the hydrogen bubble images of the flow around the unsteady foil for two flow cases, a) for the case of moderate heave and pitch amplitude, $\frac{h_0}{c} = 0.5$ and $\theta_0 = 30^\circ$ respectively, at moderate $St = 0.29$, where both “P” and “S” vortices have been clearly observed (see section 5.3.1.1) and b) for the purely heaving foil and at moderately large Strouhal numbers, $\frac{h_0}{c} = 0.5$, $\theta_0 = 0^\circ$ and $St = 0.36$, where strong “P” vortices were observed (see section 5.3.1.1).

5.3 Three-dimensional hydrogen bubble visualisation

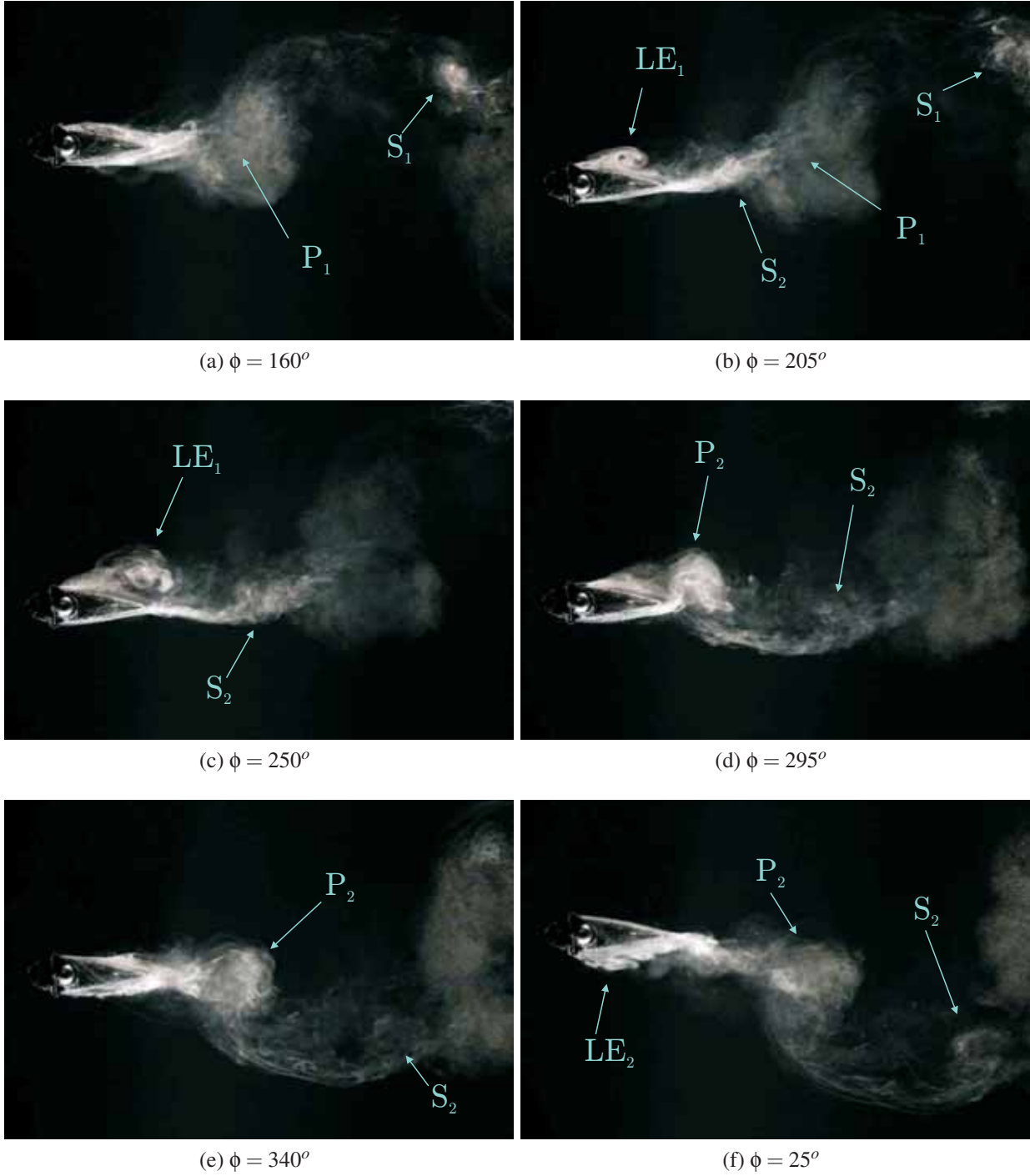


Figure 5.8: Hydrogen bubble image sequence, spanwise view, for group I, set 2 : $\frac{h_0}{c} = 0.5$, $\theta_0 = 0^\circ$, $St = 0.14$, $St_{0,exp} = 0.20$, $Re = 2,000$

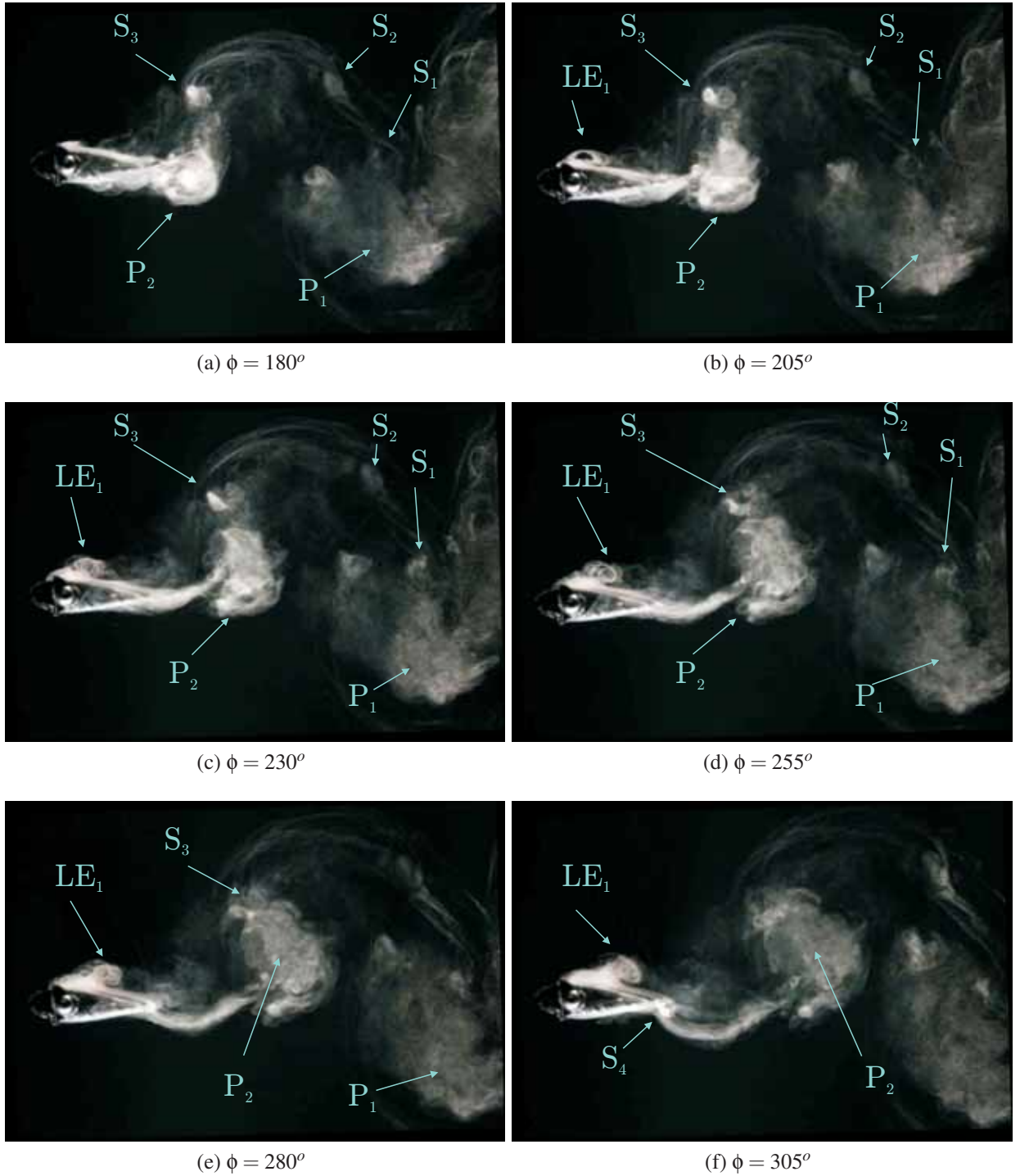


Figure 5.9: Hydrogen bubble image sequence, spanwise view, for group I, set 2 : $\frac{h_0}{c} = 0.5$, $\theta_0 = 0^\circ$, $St = 0.24$, $St_{0,exp} = 0.20$, $Re = 1,200$ (continued on following page)

5.3 Three-dimensional hydrogen bubble visualisation

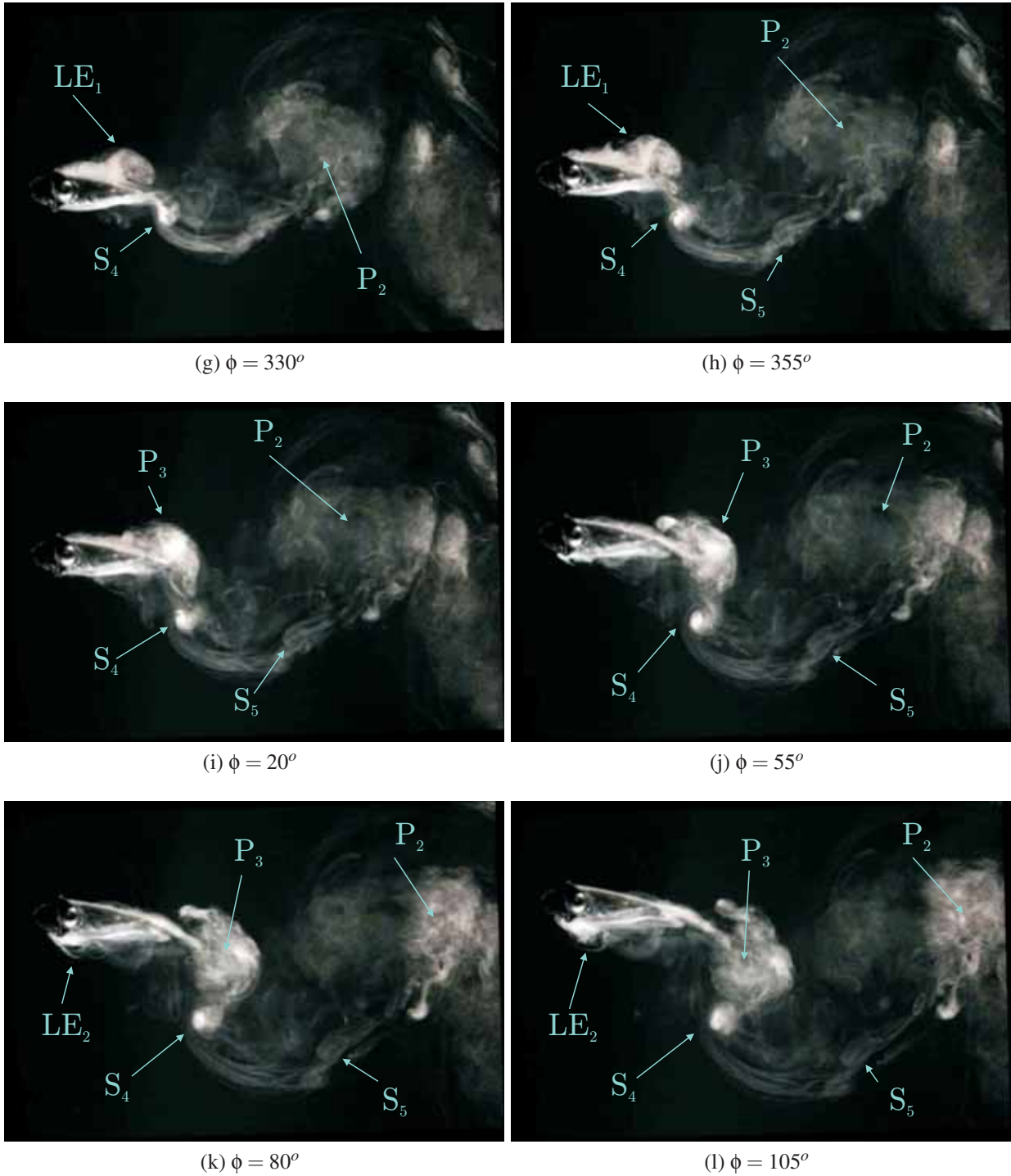


Figure 5.9: Hydrogen bubble image sequence, spanwise view, for group I, set 2 : $\frac{h_0}{c} = 0.5$, $\theta_0 = 0^\circ$, $St = 0.24$, $St_{0,exp} = 0.20$, $Re = 1,200$ (continued)

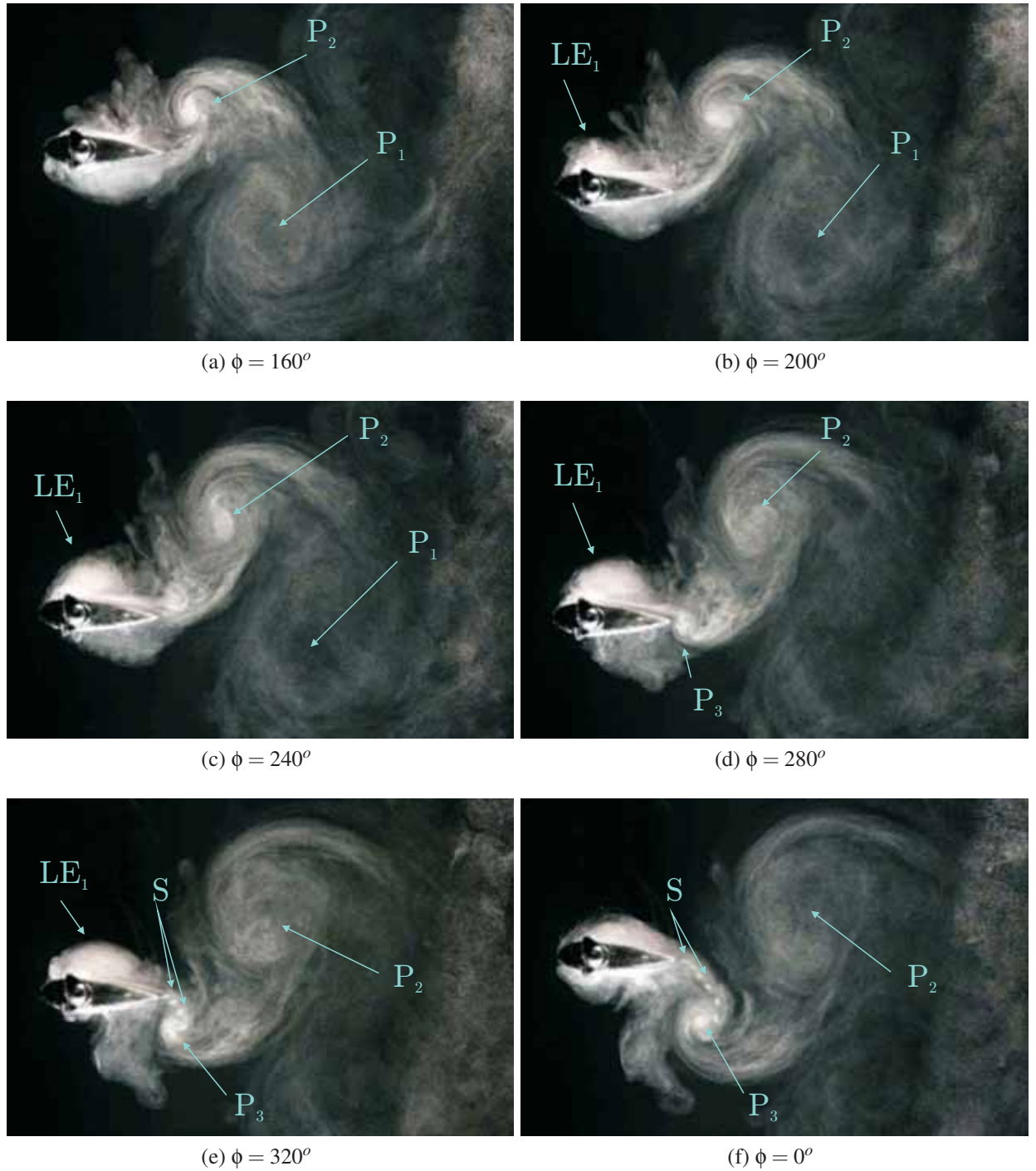


Figure 5.10: Hydrogen bubble image sequence, spanwise view, for group I, set 2 : $\frac{h_0}{c} = 0.5$, $\theta_0 = 0^\circ$, $St = 0.36$, $St_{0,exp} = 0.20$, $Re = 1,500$

5.3 Three-dimensional hydrogen bubble visualisation

Figure 5.11 shows the planform view of the flow previously shown in Figure 5.6. This view illustrates the three-dimensional nature of the flow, and in particular, shows that the “P” vortices (P_1 , P_2 and so on) have very strong spanwise flow (towards the foil mid-span). This is not observed in the much more compact “S” vortices (S_1 , S_2 and so forth), which hardly show any sign of spanwise flow. The difference in the three-dimensional characteristics of the “P” and “S” vortices are interesting, as it provides us a clear method for distinguishing “P” and “S” vortices which, for some flow cases, may look qualitative similar in two dimensions (for example, see Figure 5.2b). The strong spanwise flow within the “P” vortices is even more evident for the case where the foil is undergoing purely heaving motions (as shown in Figure 5.12), possibly due to the larger maximum angles of attack incurred ($\alpha_{max} \approx 48.5^\circ$ for $\frac{h_0}{c} = 0.5$, $\theta_0 = 0^\circ$ and $St = 0.36$ versus $\alpha_{max} \approx 12.5^\circ$ for $\frac{h_0}{c} = 0.5$, $\theta_0 = 30^\circ$ and $St = 0.29$).

In both cases, the development of the “P” vortices is linked to the generation of vorticity close to the leading edge of the foil, LE , which also has very strong spanwise flow towards the midspan of the foil. This vortex, which appears to be generated closer to the foil leading edge for the case of the purely heaving foil, starts to develop as the foil moves between the ends of the excursions (roughly corresponding to $\phi \approx 0^\circ$ and $\phi \approx 180^\circ$), and is shed close to the foil maximum/minimum heave location, where it tends to overwhelm neighbouring “S” vortices. The resulting “P” vortices are observed to form closed vortical loops (e.g.. P_1 and P_2 in Figures 5.11 and 5.12) with the vortices shed at the foil wingtips.

The strong spanwise flow in the “P” vortices causes the “P” vortices to appear large and diffuse, but more importantly, is indicative of spanwise pressure gradients within the cores of these vortices. Therefore, the existence of leading edge vortices, and the subsequent positioning of the shed “P” vortices may be fundamental to the control of low pressure regions within the flow, which in turn controls the development of forces on the foil.

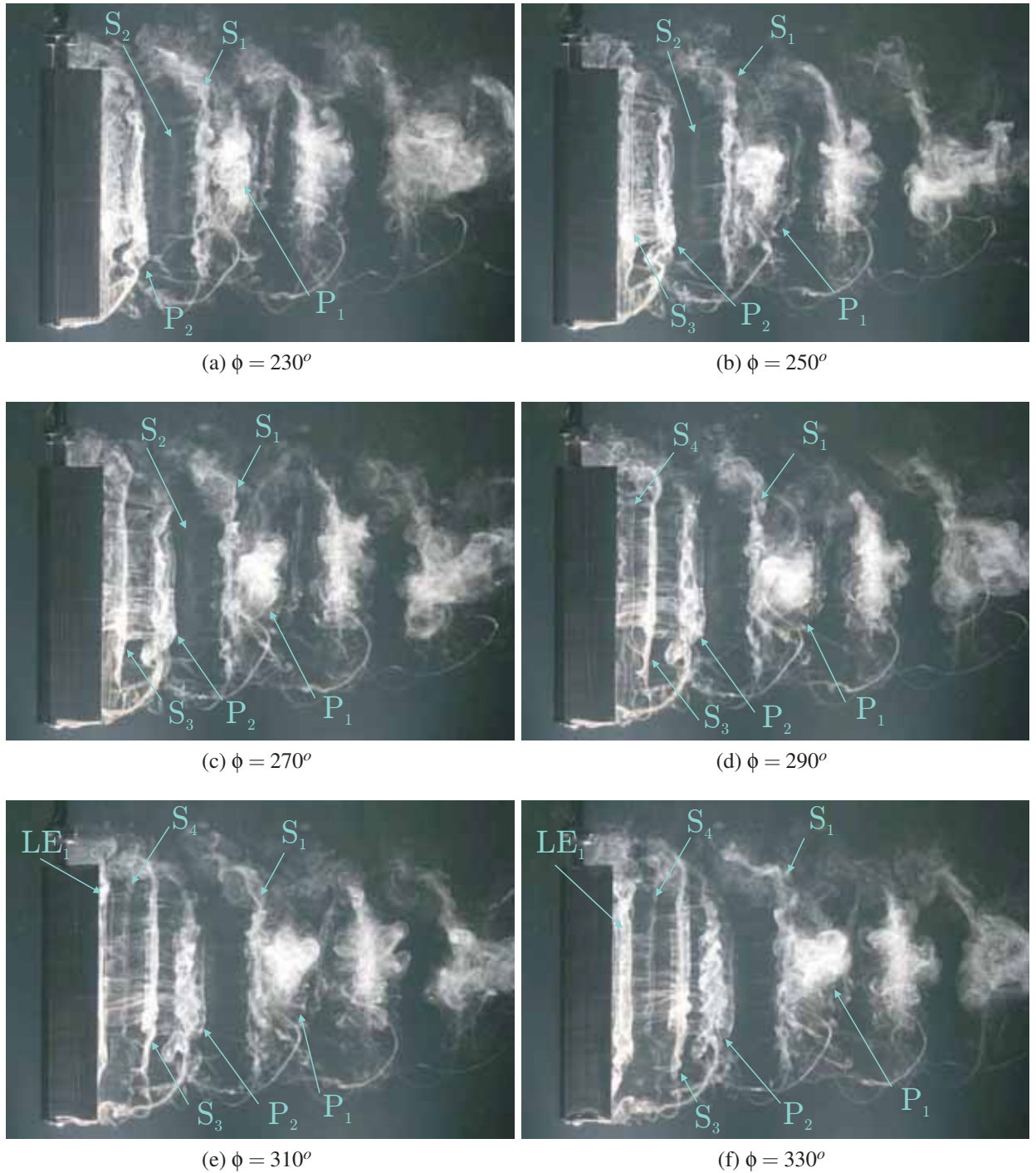


Figure 5.11: Hydrogen bubble image sequence, planform view, group III, set 8: $\frac{h_0}{c} = 0.5$, $\theta_0 = 30^\circ$, $St = 0.29$, $St_{0,exp} = 0.26$, $Re = 2,500$ (continued on following page)

5.3 Three-dimensional hydrogen bubble visualisation

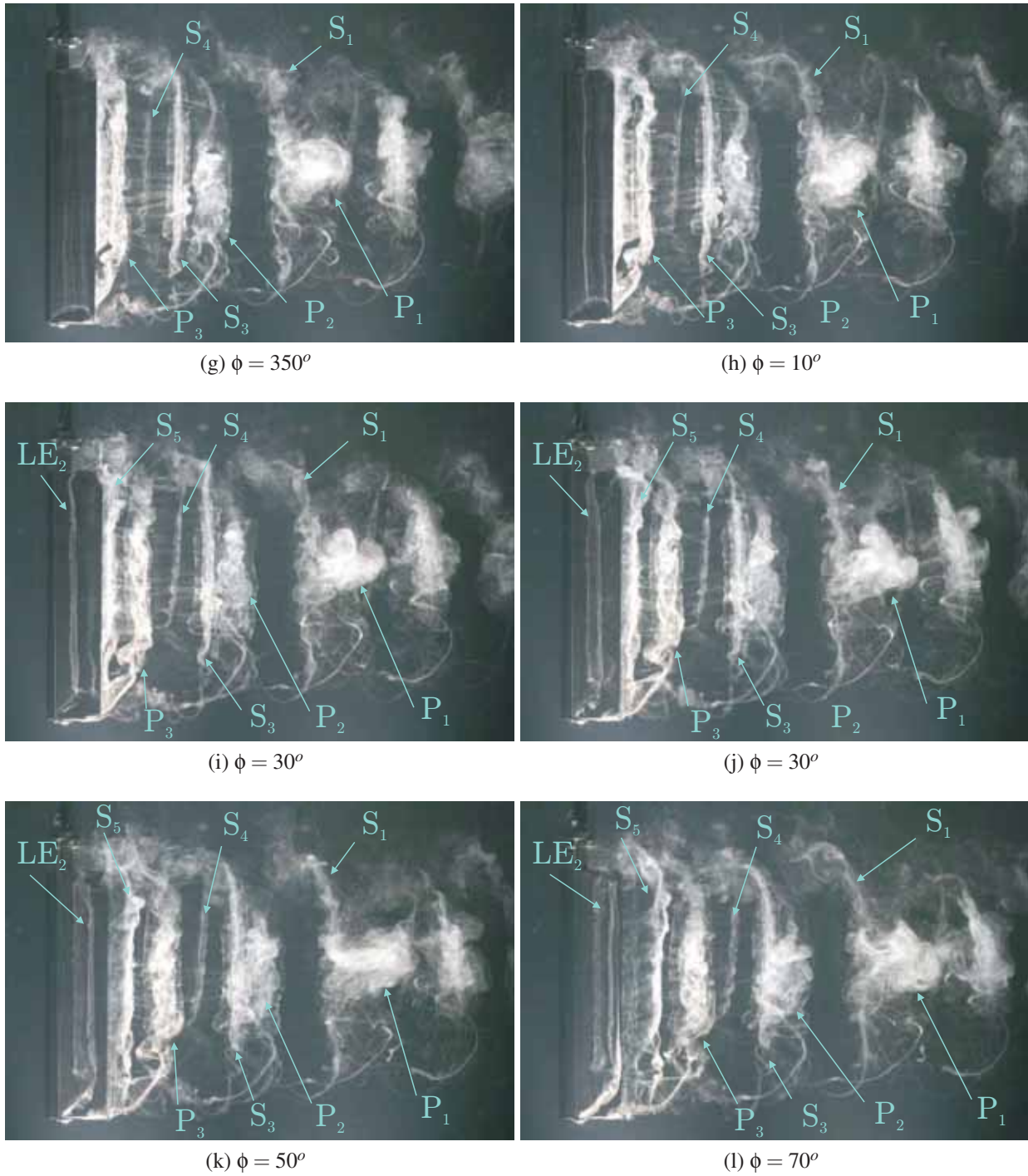


Figure 5.11: Hydrogen bubble image sequence, planform view, group III, set 8: $\frac{h_0}{c} = 0.5$, $\theta_0 = 30^\circ$, $St = 0.29$, $St_{0,exp} = 0.26$, $Re = 2,500$ (continued)

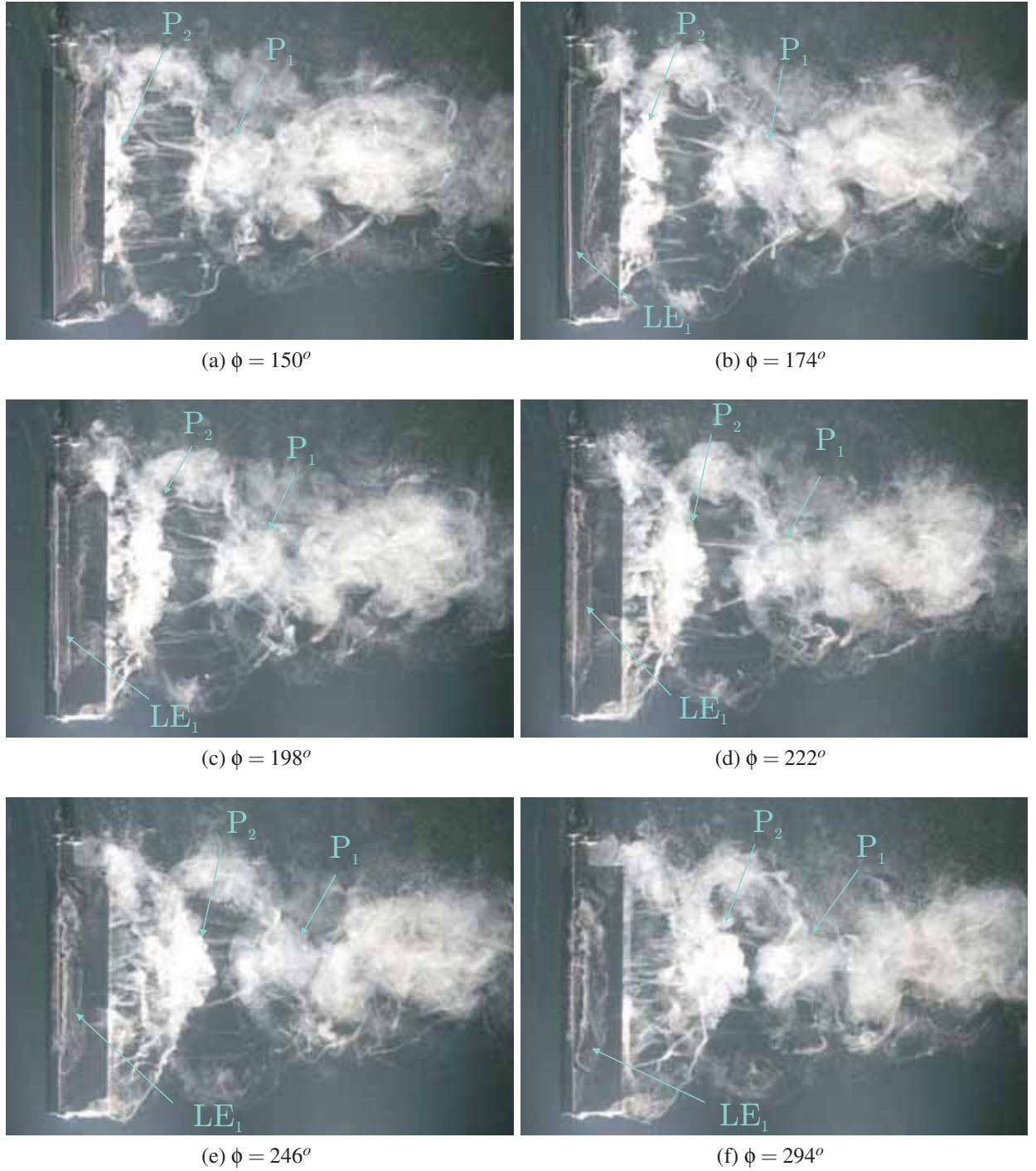


Figure 5.12: Hydrogen bubble image sequence, planform view, group I, set 2: $\frac{h_0}{c} = 0.5$, $\theta_0 = 0^\circ$, $St = 0.36$, $St_{0,exp} = 0.20$, $Re = 1,500$ (continued on following page)

5.3 Three-dimensional hydrogen bubble visualisation

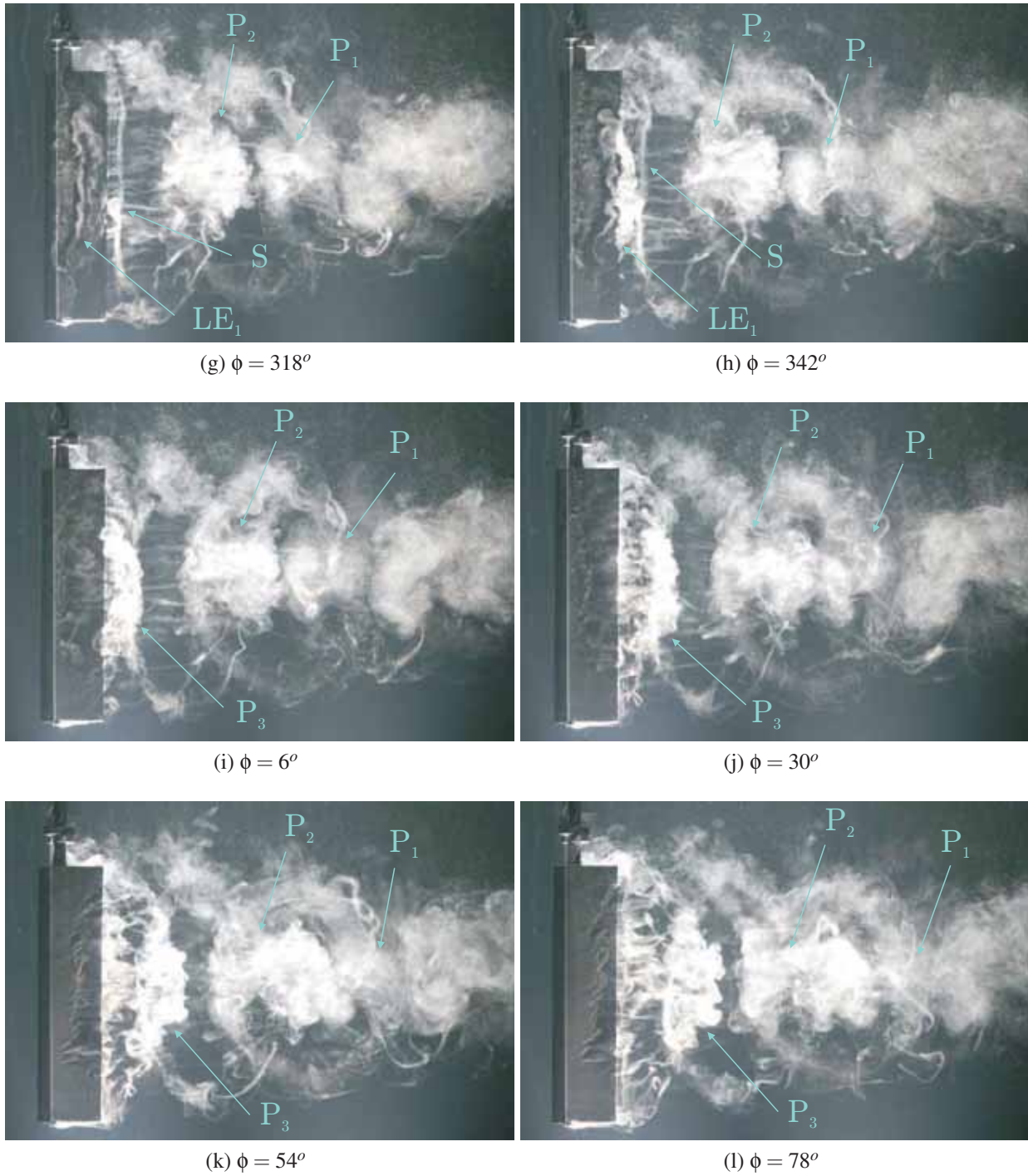


Figure 5.12: Hydrogen bubble image sequence, planform view, group I, set 2: $\frac{h_0}{c} = 0.5$, $\theta_0 = 0^\circ$, $St = 0.36$, $St_{0,exp} = 0.20$, $Re = 1,500$ (continued)

5.4 PIV-derived vorticity fields

We employ a third method to visualise the wake structure behind the unsteady foil, namely the vorticity fields derived from measured PIV velocity fields. Although the vorticity fields exist for all foil conditions listed in Table 2.1, we shall limit our discussion to the two foil conditions analysed with the hydrogen bubble visualisation (section 5.3), albeit at a much larger range of Strouhal numbers. Note that the PIV experiment was performed at $Re = 1,250 - 12,500$, while dye visualisation was performed at $Re = 900 - 3,500$ and hydrogen bubble visualisation was performed at $Re = 500 - 3,500$.

5.4.1 Wake patterns for group III, set 8: $\chi = 0.87$, $\frac{h_0}{c} = 0.5$, $\theta_0 = 30^\circ$

Figures 5.13 to 5.19 show the phase-averaged vorticity patterns behind the foil at $\frac{h_0}{c} = 0.5$ and $\theta_0 = 30^\circ$ (Group III) for increasing Strouhal numbers. All vorticity contours are shown at a foil phase angle of $\phi = 90^\circ$ (top dead centre), corresponding to the location of the maximum foil heave amplitude. Note that for all vorticity contours, the flow is from left to right, and the vorticity units are $\frac{1}{s}$. Also, it should be noted that there is a region in the flow which is obscured by the shadow of the foil. Within this region, velocity measurements cannot be made, and therefore all velocity vectors within this region is set to zero (as previously discussed in Chapter 2). This has the unfavourable effect of causing artificial vorticity measurements between the measured region, and the shadowed region. This artificial vorticity should be ignored.

At very low $St = 0.13 < St_0$ (Figure 5.13), the vorticity generated at the boundary of the foil initially sheds as a continuous shear layer. The unstable shear layer then eventually rolls up into weak, diffuse vortices, and forms a regular Karman street pattern that traces the path of the foil trailing edge (i.e., a “localised” regular Karman street). As the Strouhal number is increased to $St = 0.18$ (Figure 5.14) and $St = 0.22$ (Figure 5.15), the vorticity generated by the foil clearly rolls up into clear distinct vortices of approximately equal strengths. These vortices, which were labelled as “S” vortices in sections 5.2 and 5.3, are shed across the wake as a localised regular Karman street pattern with a vortex shedding frequency, $f_{shedding}$, that is much higher than the flapping frequency of the foil, f . In fact, the Strouhal number of the shedding frequency, normalised to the maximum thickness of the foil, $A_{foil,max}$, is close to $St_{shed} = \frac{f_{shedding} \cdot A_{foil,max}}{U_\infty} \approx 0.2$, which, intuitively, implies that the flow around the foil at low St is similar to the flow around a fixed bluff body in a uniform freestream. At this stage it should be noted that the roll up of the shear layer behind the foil into the “S” vortices were possibly due to the unwanted physical vibration of the foil (see Section 2.6). This possibility though, is unlikely, due to the fact that the vortex shedding frequency $f_{shedding}$ was not equal to the

5.4 PIV-derived vorticity fields

frequency of vibration of the foil, and that the vortex shedding frequency varied as a function of the free-stream velocity.

At $St = 0.29 \approx St_0$ (Figure 5.16), the vortex shedding behind the foil becomes asymmetrical. When $St = 0$, the vorticity generated at the boundaries of both sides of the foil flows into the shear layer symmetrically. However, when St increases, the vorticity generated on each side becomes cyclic. Thus, at the phase shown ($\phi = 90^\circ$), the shear layer vorticity asymmetry can be expected to increase as St increases. This asymmetrical shedding of secondary vorticity is a sign that the vortex shedding behind the foil is starting to be strongly influenced by the flapping frequency of the foil, that is, the shedding of vorticity is now phase-locked to the flapping motion of the foil. Furthermore, the vortices shed by the foil are now not of equal strengths; the vortex shed at the beginning of the foil half-cycle (“P” in Figure 5.16) has slightly larger strength (circulation) than the remaining vortical structures. This is due to the fact that leading edge vorticity is now being generated by the foil within this “transitional” flow regime, which combines with the “S” vorticity of the same sign at the trailing edge of the foil to form one vortical structure.

This vortical structure, “P”, eventually grows in strength as the Strouhal number increases, and is shed as strong, diffuse vortical structures. This is more clearly seen in Figure 5.17, where the foil Strouhal number is $St = 0.35 > St_0$. The vortex “P” has higher circulation than the remaining shed vorticity. Not surprisingly, the positions of the “P” vortices form a reverse Karman vortex street. The wake patterns also show a continual generation of “S” vortices, which is now completely phase-locked to the flapping foil frequency.

As the Strouhal number is increased further to $St = 0.44 > St_0$ (Figure 5.18), the strength and size of the “P” vorticity increases, and the distribution of vorticity within the entire shear structure is weighted more heavily away from the foil centreline position. The shed “S” vorticity typically forms small, compact structures, except when they are shed in close proximity to the “P” vorticity, at which point the “P” and “S” vorticity interact and merge to form a larger vortical structure.

At $St = 0.59$ (Figure 5.19), the shear layer, which is shed across the width of the wake, clearly has more vorticity located at the far extremities of the visualised wake, which therefore suggests that the wake width has increased, and that the wake pattern is roughly that of the reverse Karman street. The “S” vorticity is again observed to shed as small, compact vortical structures, except if shed close to the large primary vorticity.

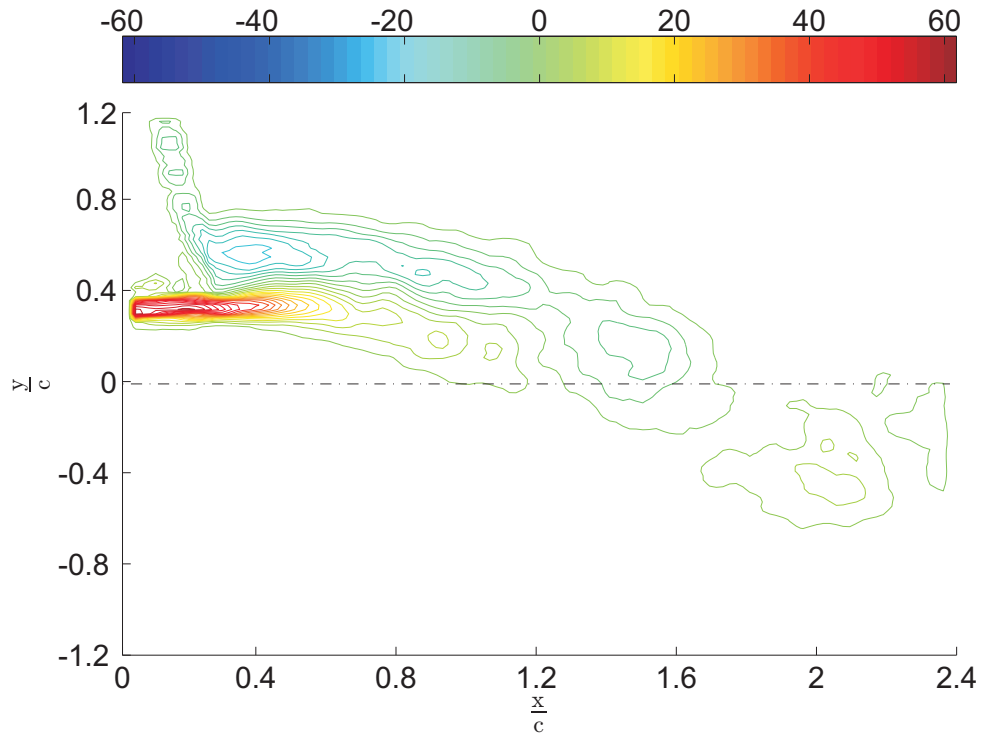


Figure 5.13: Vorticity contours for group III, set 8 : $\frac{h_0}{c} = 0.5$, $\theta_0 = 30^\circ$, $St = 0.13$, $St_{0,exp} = 0.26$, $Re = 12,000$

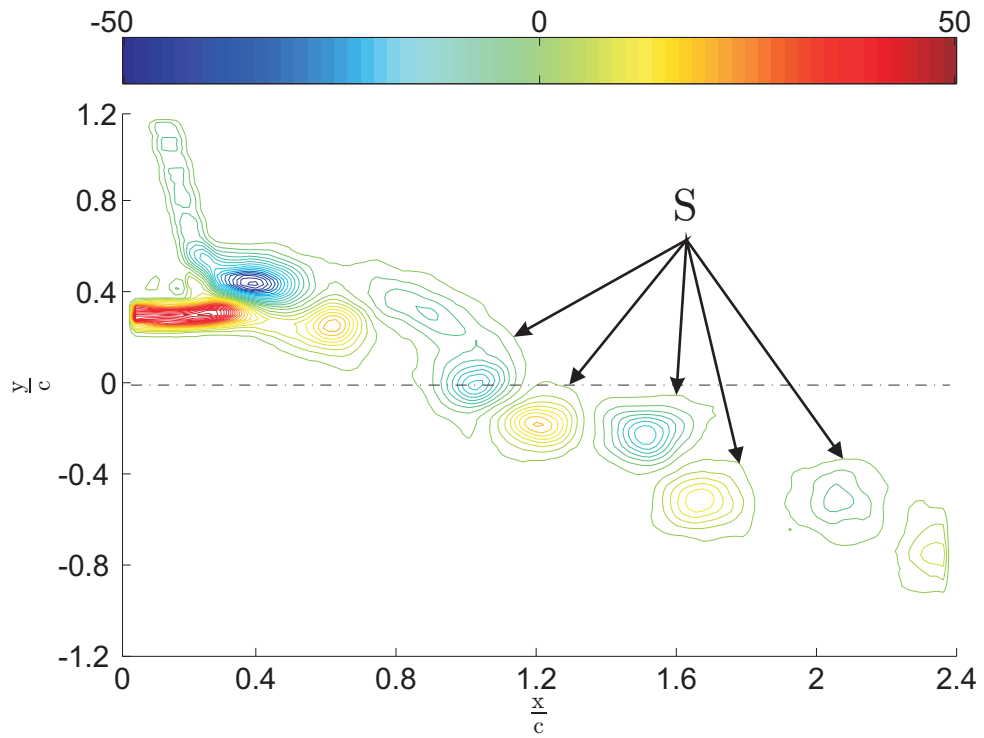


Figure 5.14: Vorticity contours for group III, set 8 : $\frac{h_0}{c} = 0.5$, $\theta_0 = 30^\circ$, $St = 0.18$, $St_{0,exp} = 0.26$, $Re = 9,000$

5.4 PIV-derived vorticity fields

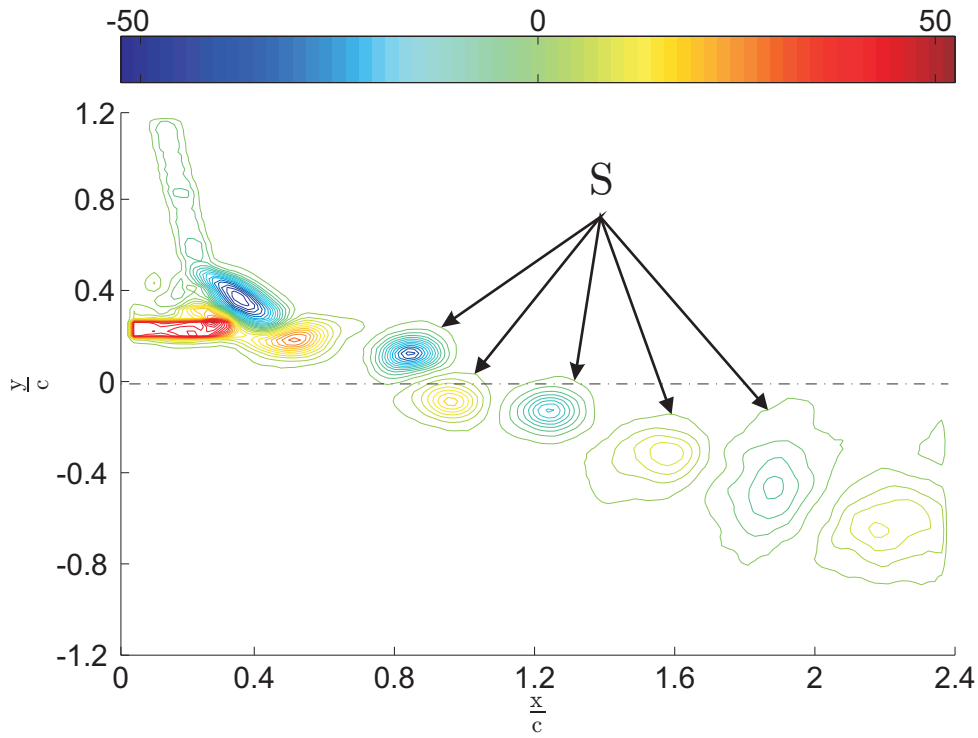


Figure 5.15: Vorticity contours for group III, set 8 : $\frac{h_0}{c} = 0.5$, $\theta_0 = 30^\circ$, $St = 0.22$, $St_{0,exp} = 0.26$, $Re = 7,000$

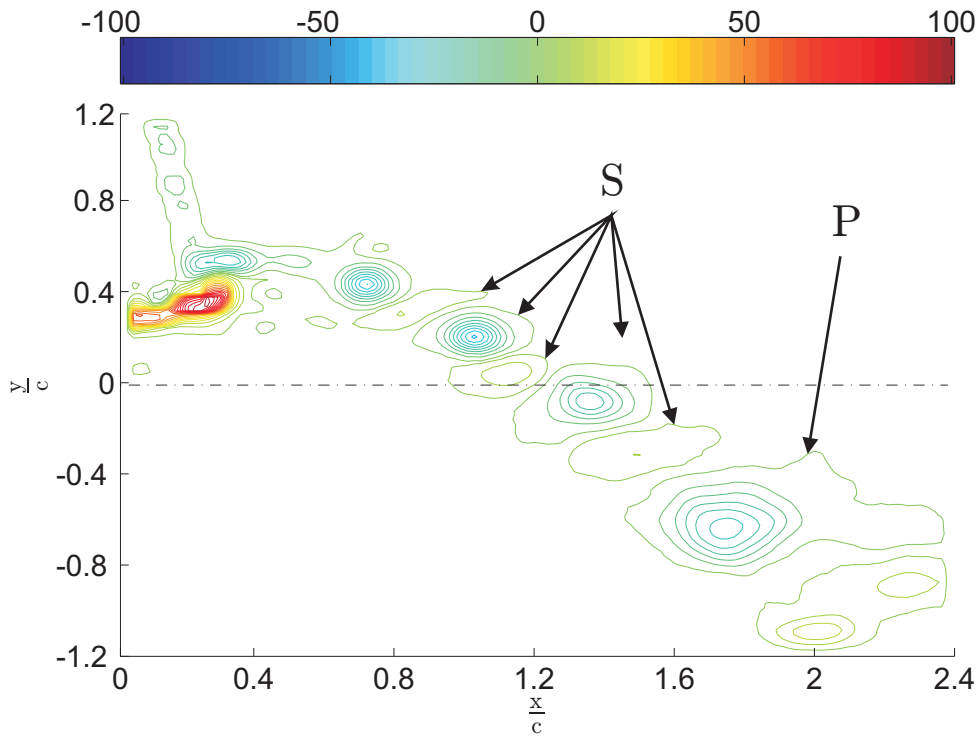


Figure 5.16: Vorticity contours for group III, set 8 : $\frac{h_0}{c} = 0.5$, $\theta_0 = 30^\circ$, $St = 0.29$, $St_{0,exp} = 0.26$, $Re = 10,500$

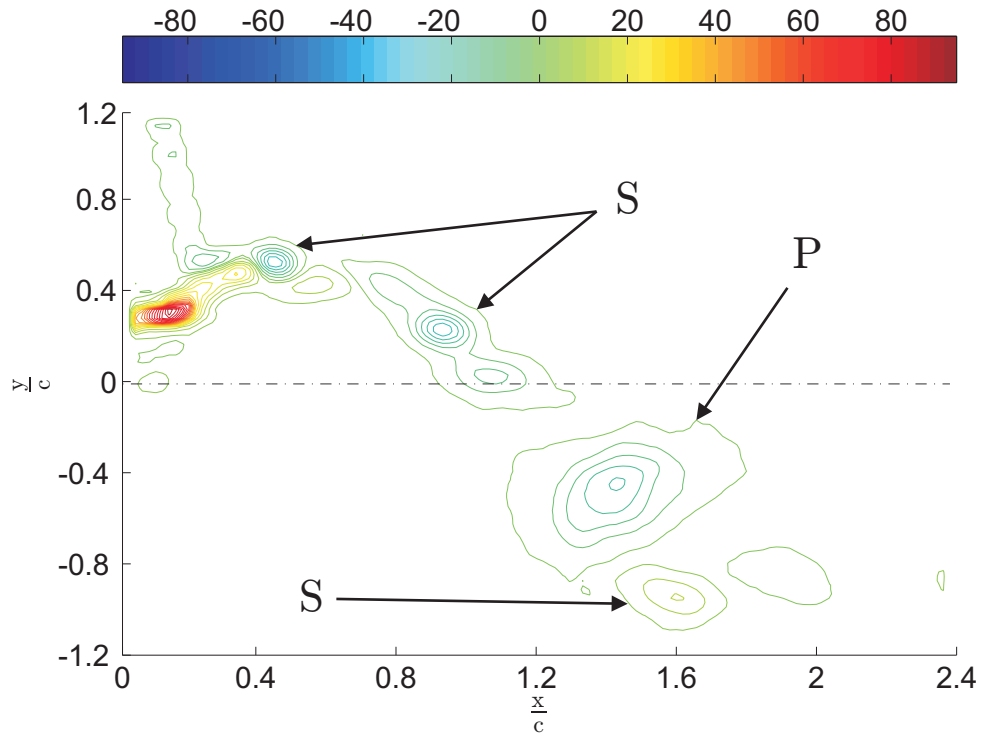


Figure 5.17: Vorticity contours for group III, set 8 : $\frac{h_0}{c} = 0.5$, $\theta_0 = 30^\circ$, $St = 0.35$, $St_{0,exp} = 0.26$, $Re = 8,750$

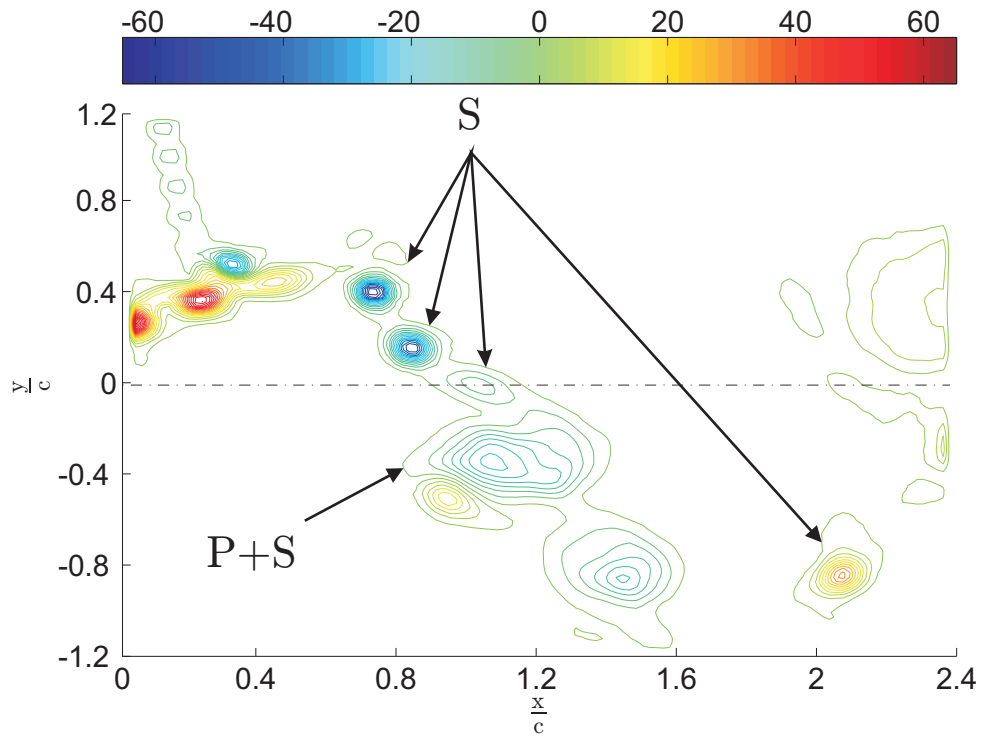


Figure 5.18: Vorticity contours for group III, set 8 : $\frac{h_0}{c} = 0.5$, $\theta_0 = 30^\circ$, $St = 0.44$, $St_{0,exp} = 0.26$, $Re = 7,000$

5.4 PIV-derived vorticity fields

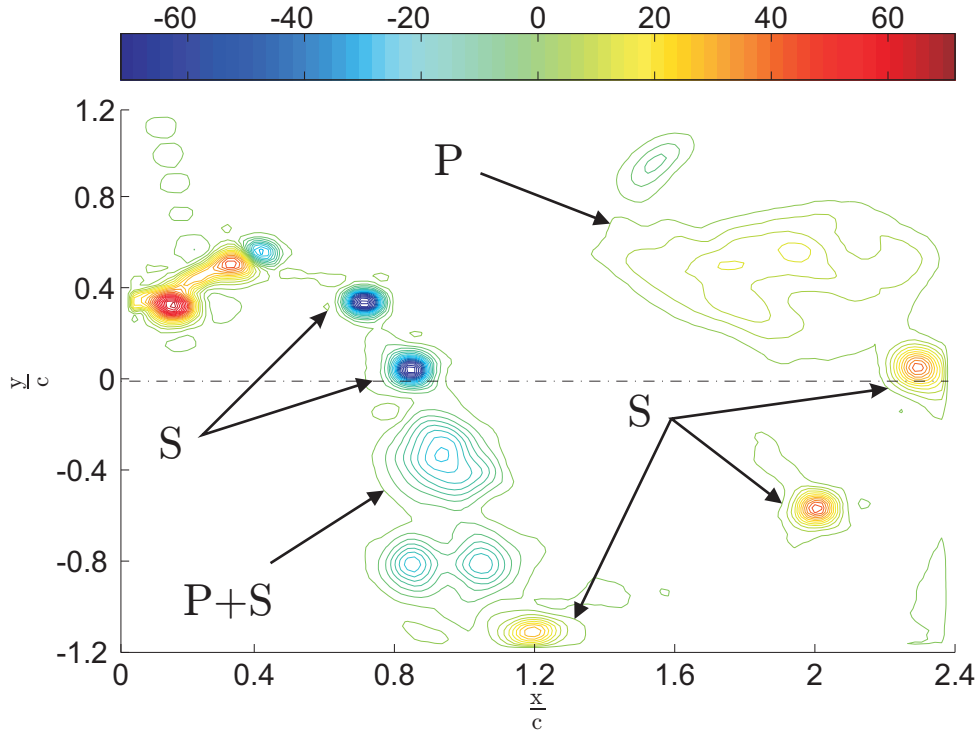


Figure 5.19: Vorticity contours for group III, set 8 : $\frac{h_0}{c} = 0.5$, $\theta_0 = 30^\circ$, $St = 0.59$, $St_{0,exp} = 0.26$, $Re = 5,000$

5.4.2 Wake patterns for group I, set 2 : $\chi = \infty$, $\frac{h_0}{c} = 0.5$, $\theta_0 = 0^\circ$

Figures 5.20 to 5.24 display the phase-averaged vorticity contours behind the foil for the purely heaving case of $\frac{h_0}{c} = 0.5$ and $\theta_0 = 0^\circ$ (Group I), at various Strouhal numbers. The purely heaving cases have been shown to produce large thrust coefficients (see chapter 4), and are therefore of particular interest. As with the contour plots discussed in section 5.4.1, the contour plots in Figures 5.20 to 5.24 are displayed at the foil phase of $\phi = 90^\circ$.

At the low Strouhal number $St = 0.14$ (Figure 5.20), the wake pattern behind the unsteady foil appears to be a combination of “S” vortex shedding and the shedding of one “P” vortex per half-cycle. The wake pattern is qualitatively similar to the wake pattern shown in Figure 5.17, where the “S” vorticity shows signs of phase-locking to the foil flapping frequency. The “P” vorticity is relatively large, especially at such a low Strouhal number, owing to the fact that large leading edge vortices were observed in sections 5.2 and 5.3 for the purely heaving foil.

At $St = 0.18$ (Figure 5.21), the “P” vortex is now clearly distinguishable from the surrounding “S” vorticity. The “P” vorticity, interestingly, is shed close to the centreline of the foil, suggesting that the wake pattern is approximately an in-line pattern. The “S” vorticity is shed unevenly across the wake, with the generation of negative vorticity biased towards the upstroke, while

the generation of positive vorticity is biased towards the downstroke. Therefore the shedding of “S” vortices is in-phase with the flapping motion of the foil.

As the Strouhal number is increased to $St = 0.24$ (Figure 5.22), the phase-locking process is complete and the shedding of “S” vorticity is locked-in to the flapping motion of the foil. The “S” vorticity is shed as compact vortical structures, however, the generated “P” vorticity is so large and strong that it tends to engulf neighbouring “S” vorticity to form one large vortical structure, consistent with observations made in sections 5.2 and 5.3. This shear-like vortical structure contains, spatially, an uneven distribution of vorticity, whereby the vorticity is stronger at locations slightly away from the foil centreline position. The resulting pattern can therefore be interpreted as a reverse Karman vortex street.

The reverse Karman street wake pattern is clearly observed in Figures 5.23 and 5.24, taken at $St = 0.36$ and $St = 0.48$ respectively. All generated vorticity by the foil is now encompassed in a single vortical structure, which is dominated by very strong “P” vorticity. The distribution of the vorticity within this structure is now located away from the foil centreline. Considering that the main vortical structure is large and strong, this would indicate that there should be a strong velocity excess in the wake of the foil, and therefore we would expect the foil to generate large thrust coefficients at these Strouhal numbers.

5.4.3 The interaction of leading edge and trailing edge vorticity

Results from dye and hydrogen bubble visualisation indicate that when the heave amplitude is large, strong leading edge vortices can be observed. Furthermore, the results from all three flow visualisation experiments indicate that when the heave amplitude is large, strong “P” vortices are generated by the foil. To explain the correlation between the leading edge vortices, and the “P” vortices, we take a closer look at the vorticity fields for the purely heaving case of $\frac{h_0}{c} = 0.5$, $\theta_0 = 0^\circ$ and $St = 0.36$, shown in Figure 5.25 for all measured foil phases.

At $\phi = 90^\circ$ (Figure 5.25a), the foil is at its maximum heave location, and vorticity is observed to be generated at the trailing edge of the foil (S_1). As the foil moves downward, the vorticity at the trailing edge, S_1 , rolls up into a compact vortex (Figure 5.25b). The compact vortex S_1 is contained within a larger, more diffuse vortical structure, P_2 , which was generated close to the leading edge of the foil. As the foil continues its downstroke, more “S” vortices are generated close to the trailing edge of the foil (Figure 5.25d). Meanwhile, the leading edge vorticity continues to feed the vortical structure P_2 , which still clearly contains the compact vortical structure S_1 . As the foil reaches its minimum heave position ($\phi = 270^\circ$), most of the “S” vorticity generated at the trailing edge of the foil is now encompassed within a dominant

5.4 PIV-derived vorticity fields

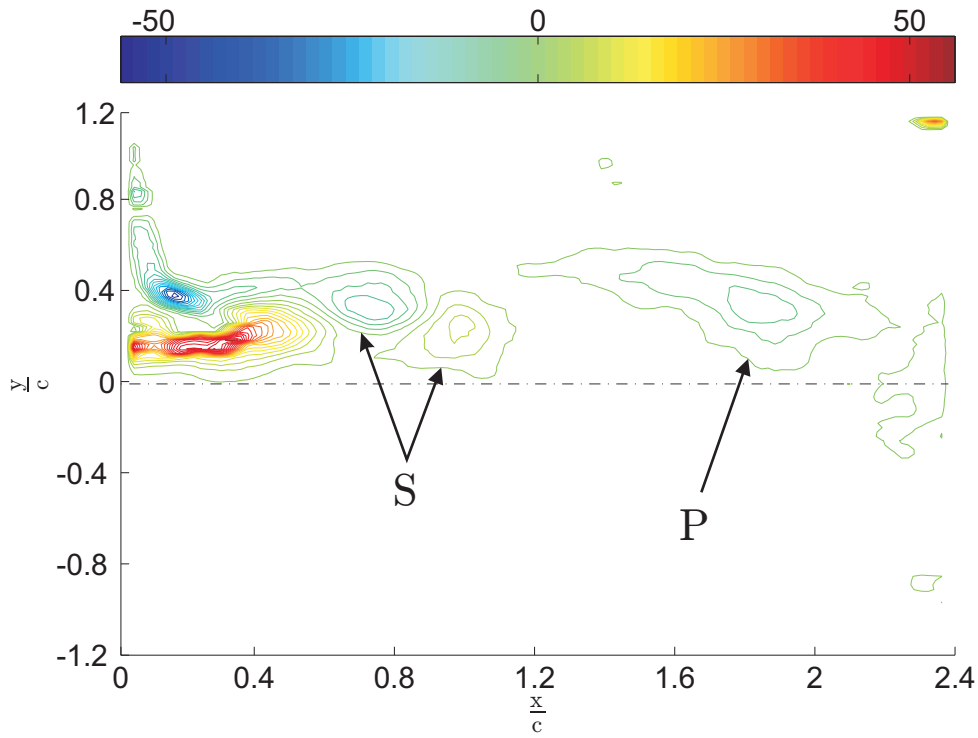


Figure 5.20: Vorticity contours for group I, set 2 : $\frac{h_0}{c} = 0.5$, $\theta_0 = 0^\circ$, $St = 0.14$, $St_0 = 0.2$, $Re = 8,750$

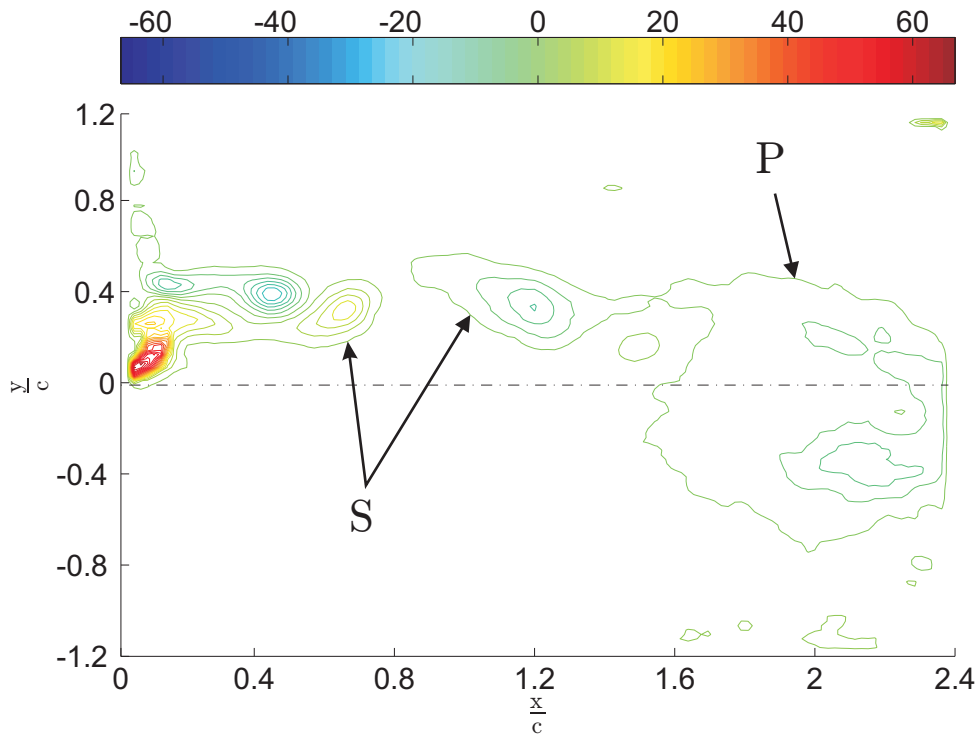


Figure 5.21: Vorticity contours for group I, set 2 : $\frac{h_0}{c} = 0.5$, $\theta_0 = 0^\circ$, $St = 0.18$, $St_0 = 0.2$, $Re = 7,000$

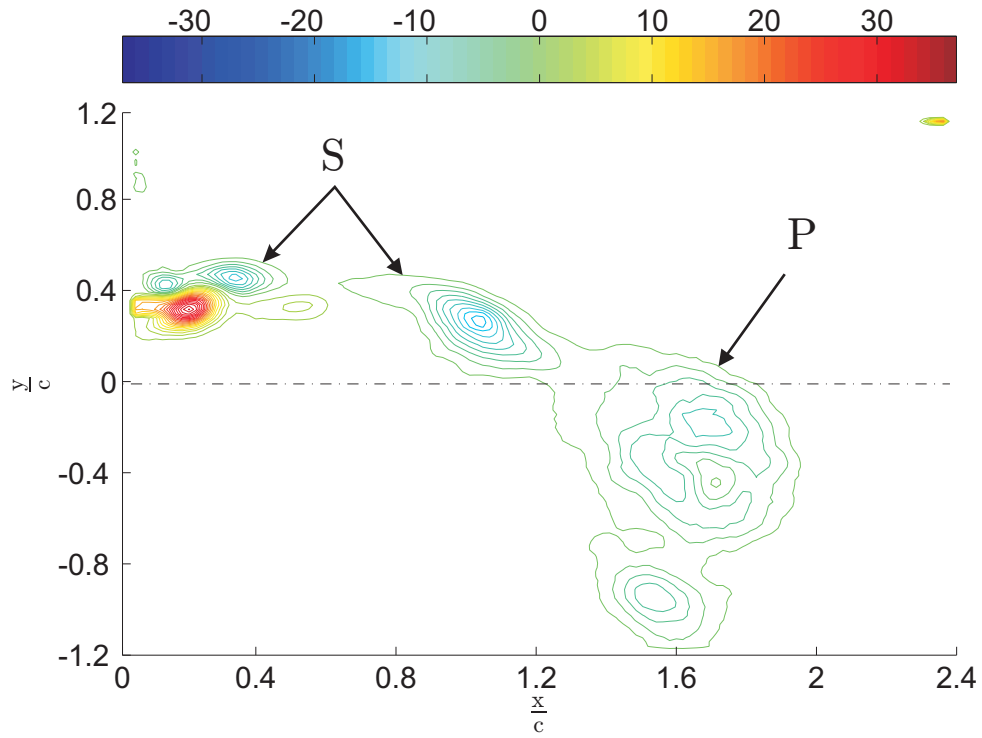


Figure 5.22: Vorticity contours for group I, set 2 : $\frac{h_0}{c} = 0.5$, $\theta_0 = 0^\circ$, $St = 0.24$, $St_0 = 0.2$, $Re = 5,000$

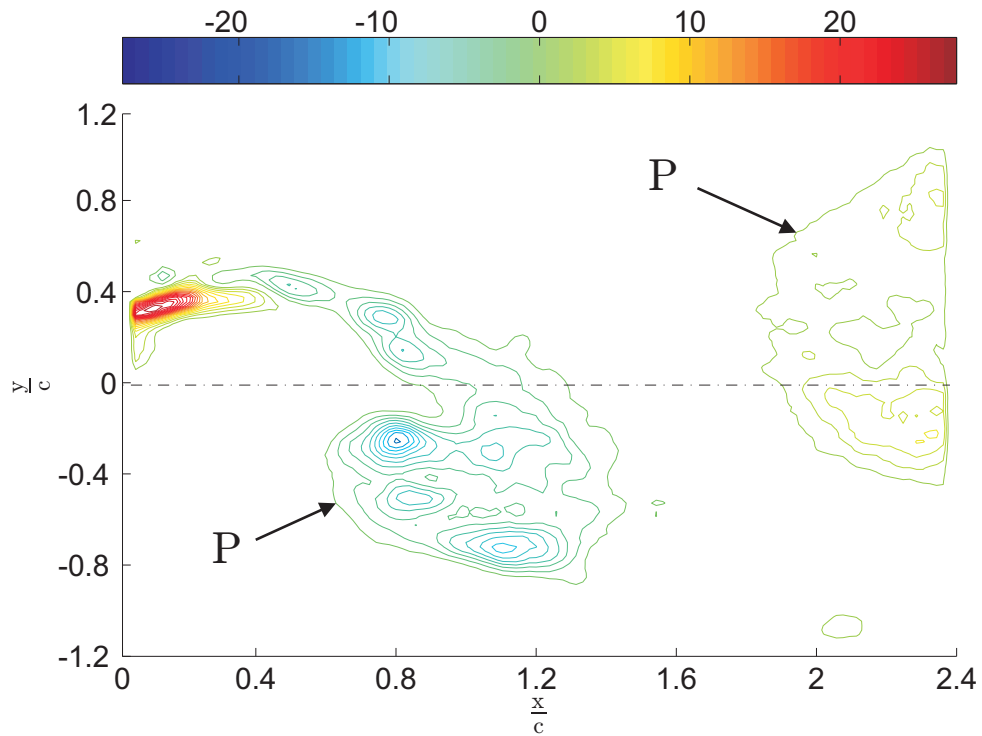


Figure 5.23: Vorticity contours for group I, set 2 : $\frac{h_0}{c} = 0.5$, $\theta_0 = 0^\circ$, $St = 0.36$, $St_0 = 0.2$, $Re = 3,500$

5.5 Interpretation of unsteady foil wake structure

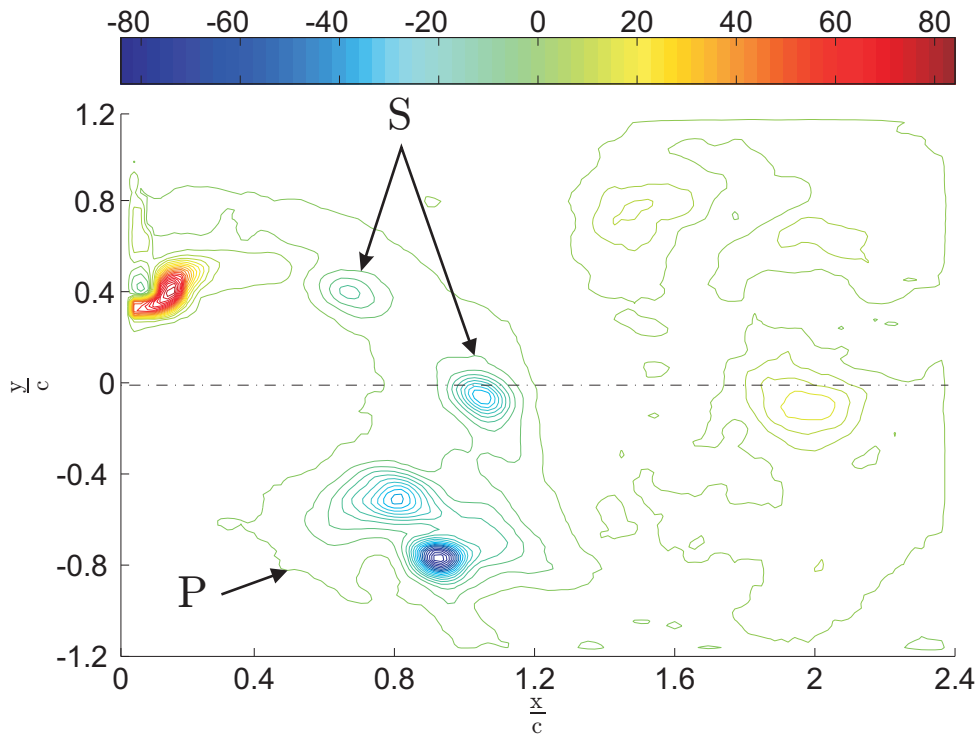


Figure 5.24: Vorticity contours for group I, set 2 : $\frac{h_0}{c} = 0.5$, $\theta_0 = 0^\circ$, $St = 0.48$, $St_0 = 0.2$, $Re = 5,000$

vorticity structure P_2 (Figure 5.25e), which is shed into the wake such that its vorticity centroid location is located vertically distant from the foil centreline (Figure 5.25f). This entire process is repeated for the foil upstroke (Figures 5.25f-j).

5.5 Interpretation of unsteady foil wake structure

After considering all the qualitative flow visualisation based on the PIV vorticity fields, we can produce a generalised schematic interpretation of the wake structure behind the heaving and pitching foil, at various heave and pitch amplitudes, and across all the measured Strouhal numbers. This schematic representation of the unsteady foil wake is shown in Figure 5.26.

The wake structure is interpreted as a linear combination of two different vorticity generating mechanisms. The first mechanism is the generation of vorticity due to the foil acting as a lifting device. The temporally changing lift produced by the foil, and therefore the changing strength of the bound circulation around the foil, manifests itself as shed vorticity, as first described in section 3. This shed vorticity, which is sometimes called the starting or stopping vortex (Dickinson, 1996), is dubbed the “primary” vorticity. The second vorticity generation mechanism

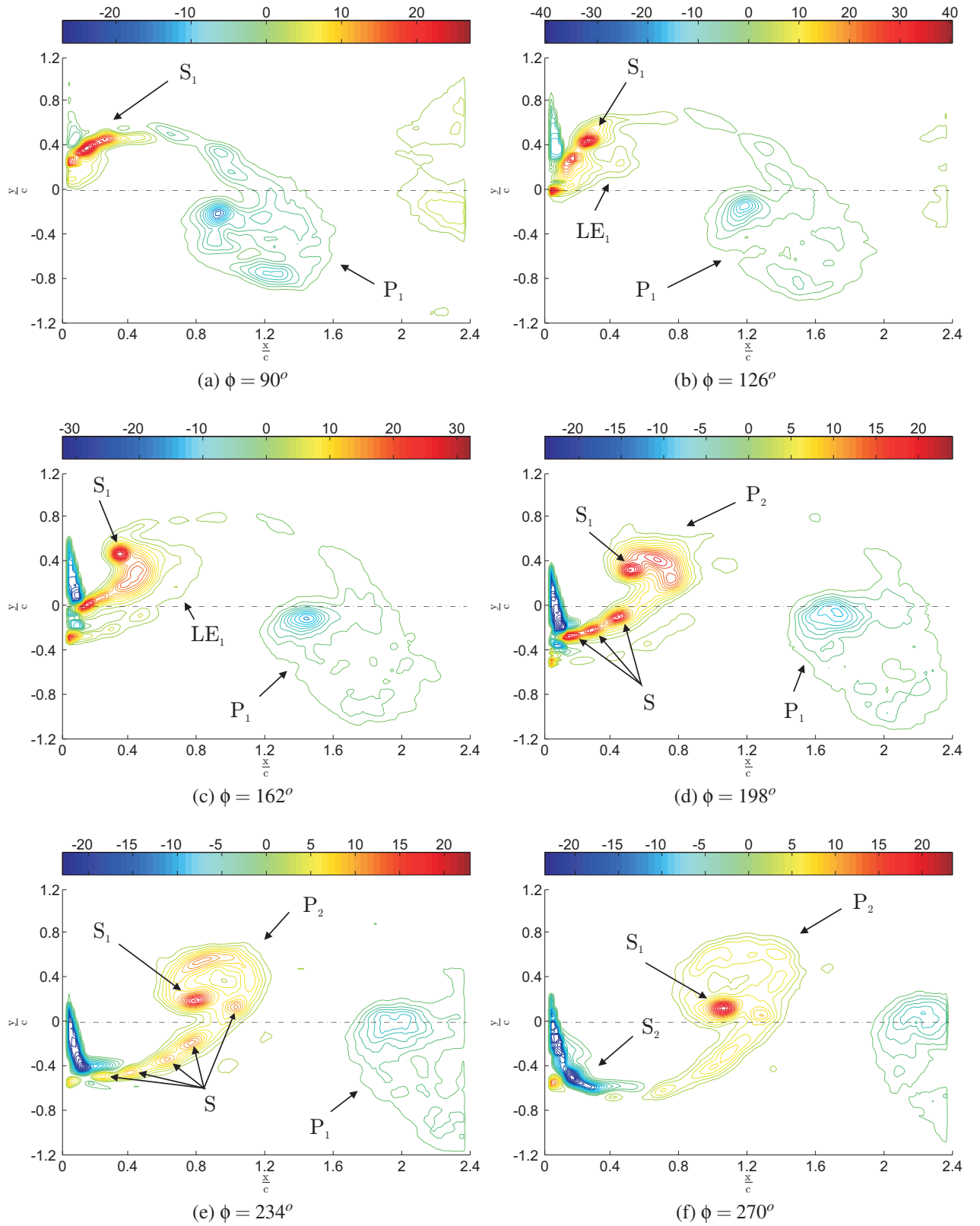


Figure 5.25: The interaction of leading edge and trailing edge vorticity. Foil parameters : $\frac{h_0}{c} = 0.5$, $\theta_0 = 0^\circ$ and $St = 0.36$, $St_0 = 0.2$, $Re = 3,500$ (continued on following page)

5.5 Interpretation of unsteady foil wake structure

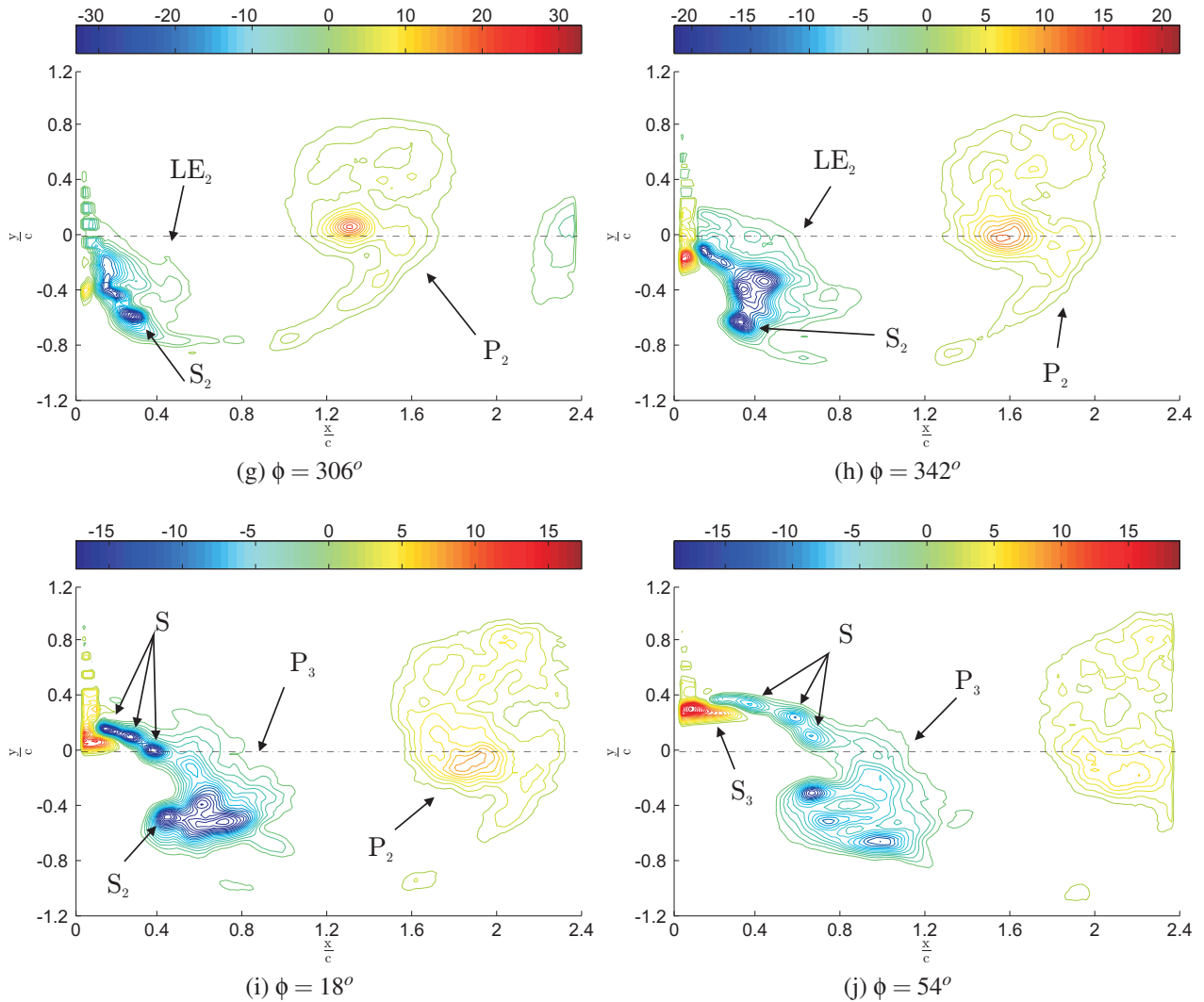


Figure 5.25: The interaction of leading edge and trailing edge vorticity (continued). Foil parameters : $\frac{h_0}{c} = 0.5$, $\theta_0 = 0^\circ$ and $St = 0.36$, $St_0 = 0.2$, $Re = 3,500$

is attributed to the fact that vorticity is generated in the foil boundary layer due to the no-slip boundary condition on the foil's surface. The no-slip condition causes vorticity to be generated at the surface of the foil, which is shed as vortical structures, called “secondary” vortices. These secondary vortices, which are associated with drag forces on the foil, are generated even if the foil is not in motion, as long as the free-stream velocity is non-zero.

We interpret the general wake pattern as a combination of the primary vorticity (shown as $\sigma_{n,L}$ in Figure 5.26), which is shed once per half-cycle (if it is generated), and any number of secondary vortices (shown as $\sigma_{n,1-3}$ and $\sigma_{p,1-4}$ in Figure 5.26) shed per foil half-cycle. The number of secondary vortices generated per foil cycle generally depends on the foil heave and pitch amplitude, or more specifically, the size of the trailing edge excursion, A_{te} . In general,

more secondary vortices are generated for larger values of A_{te} . The qualitative aspects of the shedding of the secondary and in particular, the primary vorticity, are dependent on the Strouhal number, and hence the wake pattern is highly dependent on St .

At low St , the strength of the primary vorticity is very low, and the existence of primary vorticity is not clearly noticeable. The secondary vorticity is shed with a pattern which can be roughly described as a regular Karman vortex street which is organised by the motion of the foil. In the flow visualisation experiments, these shed secondary vortices are called “S” vortices. The frequency of the secondary vortex shedding is much higher than St , and is therefore not phase locked to the foil flapping frequency.

As the Strouhal approaches $St \approx St_0$, the strength of the primary vorticity increases, and is shed once per foil half-cycle. The primary vorticity, which may combine with secondary vortices of the same rotational direction, is usually shed as large, and diffuse vortices (relative to the neighboring secondary vortices, which typically are smaller and more compact). In the flow visualisation experiments, these large and diffuse vortical structures, which may contain a combination of primary and secondary vorticity, are called “P” vortices. At $St \approx St_0$, the shedding of secondary vortices shows signs of being phase-locked to the flapping motion of the foil, whereby the shedding negative secondary vorticity ($\sigma_{n,1-3}$) is limited to the foil upstroke, and the shedding of positive secondary vorticity is limited to the foil downstroke ($\sigma_{p,1-3}$). The primary vortex sheds approximately along the foil mean centreline position, and therefore the wake loosely forms an in-line wake pattern.

As the Strouhal number increases beyond $St > St_0$, the shedding of secondary vorticity becomes completely phase-locked to the foil flapping frequency, and there is little or no sign of positive secondary vorticity during the upstroke, nor is there any sign of negative secondary vorticity during the downstroke. The strength of the primary vortex increases, and the primary vortical structure now sheds further away from the foil centreline. The primary vortex tends to strongly influence the neighbouring secondary vorticity, resulting in a agglomeration of vortices of the same rotational sense. The corresponding wake pattern then forms an approximate reverse Karman vortex street.

Depending on the foil dynamic parameters, the primary and secondary vorticity generated by the foil can be shed either as discrete vortical structures ($\sigma_{n,1-3}$, $\sigma_{p,1-3}$ and $\sigma_{n,L}$), or as a large agglomeration of vorticity (τ_p and τ_n), or, more usually, a combination of discrete vortical structures embedded within a shear layer. Generally, it is observed that cases where the heave amplitudes are large tend to produce larger, more diffuse vorticity structures, while cases where the pitch amplitude dominates the foil motion tends to produce clearly distinct vortical structures. This is probably a consequence of the fact that the flow around the unsteady foil at

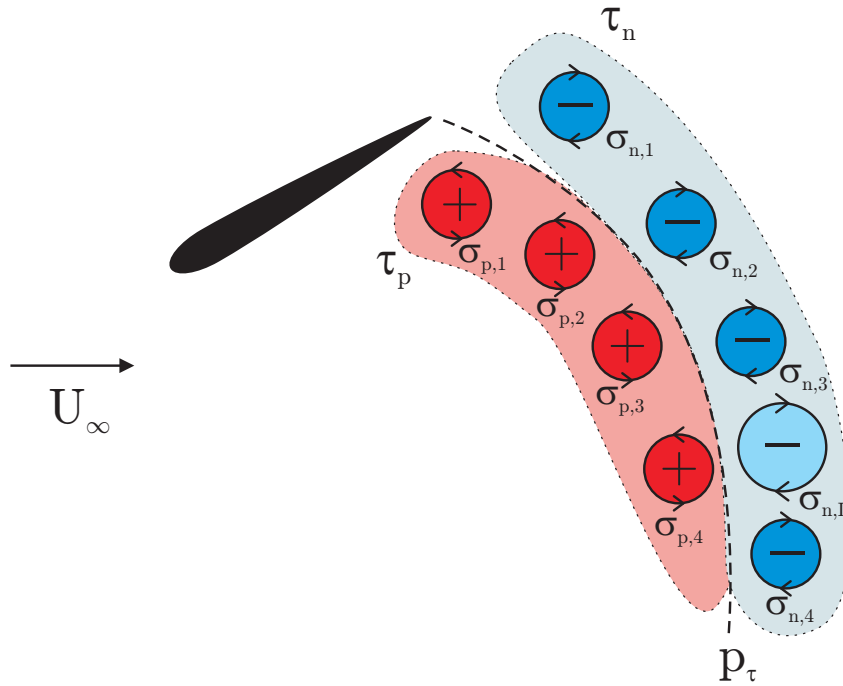


Figure 5.26: Schematic of wake patterns behind the unsteady hydrofoil

large heave amplitudes produces large leading edge vortices, whereas the the flow around the unsteady foil undergoing large pitch motions is dominated by the high effective velocities of the sharp trailing edge of the foil, which may introduce instabilities into the shed shear layer, promoting the roll-up of vorticity into clear distinct vortical structures.

The path along which the vorticity is shed, p_τ , is also dependent on the foil dynamic properties. When the trailing edge excursion A_{te} and St are large, the width of the wake tends to be large, and typically more secondary structures are observed. Conversely, when the trailing edge excursion is small, or the St is small, the wake width tends to be small, and fewer secondary vortical structures are evident.

In three dimensions, we propose that the pairs of secondary vorticity (for example, γ_1 , γ_2 and so forth), and the primary vorticity (γ_L) form closed loops with the vorticity shed at the trailing edge of the foil. A proposed vortex skeleton (see Perry and Chong 1987) is shown in Figure 5.27, for the case where the shedding of secondary vorticity is phased locked to the flapping motion of the foil. The pattern is simplified to improve its clarity. The connections between the spanwise vortices may not be so distinct in the real flow, where vortex lines may connect an individual vortex, γ_1 say, with many other vortices.

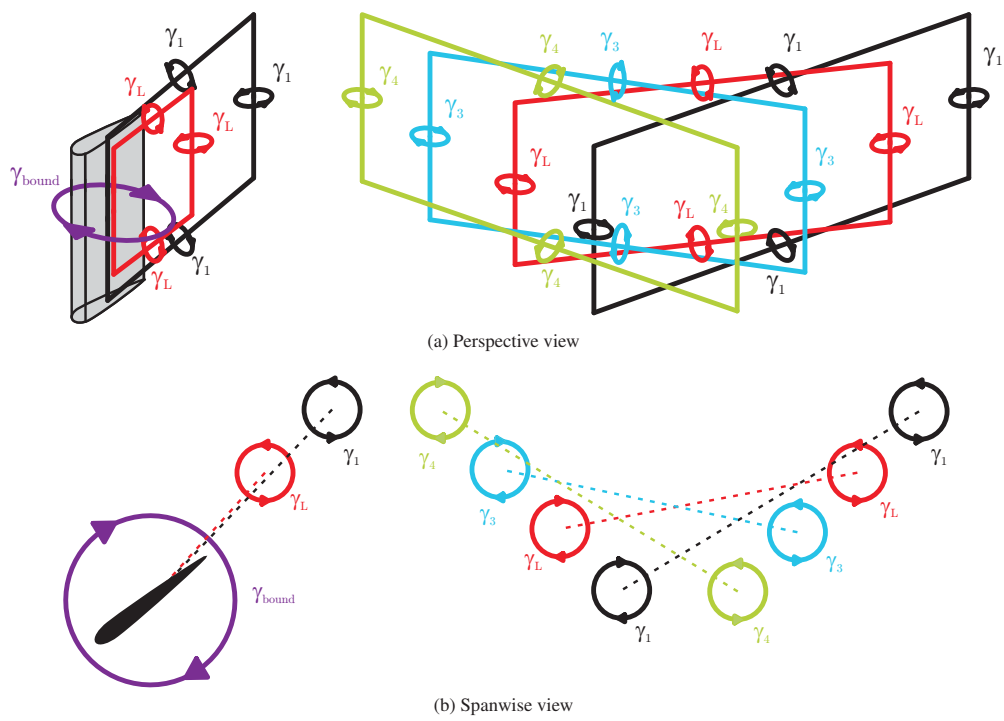


Figure 5.27: Proposed vortex skeleton of the 3D unsteady foil wake

5.6 Conclusions

An extensive qualitative analysis of the wake patterns produced behind the unsteady hydrofoil was performed using a combination of dye visualisation, hydrogen bubble visualisation, and particle image velocimetry. Dye visualisation was performed on a large number of flow conditions and foil dynamic parameters, while hydrogen bubble visualisation was performed only on a selected number of foil parameters. Dye visualisation was performed for 113 different flow combinations, ranging from $Re = 900 - 3,500$, while hydrogen bubble visualisation was performed for 38 different flow cases, in the range of $Re = 500 - 3,500$.

Vorticity fields, derived from the PIV velocity fields, were also used to analyse the wake patterns behind the foil. PIV was performed on the unsteady foil for 106 different flow conditions, corresponding to $1,250 < Re < 12,500$.

Observations of the flow around the unsteady foil reveal that the foil is capable of producing qualitatively different wake patterns, based on the foil parameters (as shown in Figure 5.28). These observed wake patterns are interpreted as a linear combination of two independent vorticity generating mechanisms.

Firstly, “primary” vorticity is generated by the foil acting as a lift-producing surface. The transient lift produced by the foil coincides with a change in the strength (and at times, direction) of the bound vortex around the foil. The change in the bound circulation around the foil is then accompanied by shed “primary” vortices. These shed primary vortices are sometimes called “starting” or “stopping” vortices (or are a combination of both - see 1.2.3, or Dickinson (1996); Vogel (1996)). The “primary” vorticity is therefore associated with lift forces on the foil.

Secondly, vorticity is continuously generated at the foil boundary due to the no-slip condition, as long as the effective velocity of the foil relative to the surrounding fluid is non-zero (which is true for all foil parameters and flow conditions tested). This vorticity is dubbed “secondary” vorticity, and is associated with drag forces on the foil.

Visually, secondary vorticity is typically shed as small, compact vortices, with little or no spanwise flow evident, and is observed to shed close to the trailing edge of the foil. On the other hand, primary vorticity is observed to be generated close to the leading edge of the foil. This vorticity flows downstream, where it combines with adjacent trailing edge secondary vorticity to form strong, diffuse vortical structures with large spanwise flow (towards the mid-span of the foil). The generation of strong leading edge vorticity is particularly evident in cases with where the foil undergoes large heave amplitudes (relative to the pitch amplitudes), possibly due to the large maximum angles of attack, α_{max} that the foil produces under high heave conditions. The large spanwise flow through the cores of the primary vorticity suggests that the primary vortices

	Wake designation	Brief wake description
A	-	No distinct vortical structures observed. Wake consists of shear layer from the boundary of the foil.
B	LK-H	Shed “S” vortices form a “localised” regular Karman vortex street; Heave-dominated.
C	LK-R	Shed “S” vortices form a “localised” regular Karman vortex street; Pitch-dominated.
D	I-P	One “P” vortex is shed per half-cycle, shed in-line with the foil average centreline location.
E	P+S	A single “P” and “S” vortex pair, of approximately same strength, is shed per foil half-cycle.
F	P+XS	One “P” vortex, which forms a reverse Karman vortex street, and a number of significantly strong “S” vortices, are shed per foil half-cycle.
G	P+0S	One “P” vortex is shed per half-cycle, forming a reverse Karman vortex street.
H	P+Xs	One “P” and a number of small “S” vortices are shed per half-cycle. “P” vortices form a reverse Karman vortex street.

Table 5.1: Summary of observed wake patterns behind the unsteady foil. For a schematic representation of these wake patterns, refer to Figure 5.28.

coincide with regions of low pressure, and therefore the control of these primary vortices may be pivotal to the generation of thrust forces on the foil.

Depending on the positions and relative strengths of the shed primary and secondary vortical structures, each of the wake patterns can be categorised into one of three flow regimes, namely the “drag regime”, the “transitional regime” and the “thrust regime” (as shown in Table 5.1 and Figure 5.28). These flow regimes are highly dependent on the value of St relative to St_0 , while the foil heave and pitch amplitude, and the Reynolds number, were found to only have a secondary effect on the observed wake patterns. Each flow regime is subtly different, and has unique characteristics:

1. Drag regime - Occurs at low Strouhal numbers, roughly corresponding to $St < St_0$. Wake patterns consists of secondary vorticity which may shed as two shear layers of opposing

5.6 Conclusions

vorticity (pattern A), or the secondary vorticity may roll up into discrete vortical structures (“S”) which are shed into the wake corresponding to the location of the trailing edge of the foil, forming a “localised” regular Karman vortex (wake pattern B for heave dominated cases, and wake pattern C for pitch dominated cases). There is little or no sign of primary vorticity. The frequency of vortex shedding is much higher than the foil flapping frequency f , and it is estimated that the vortex shedding corresponds approximately to $St_{shed} = \frac{f_{shedding} \cdot A_{foil,max}}{U_{\infty}} \approx 0.2$. This indicates that the shedding of these vortices is not phase-locked to the flapping frequency of the foil. The rotational directions of the shed vorticity implies that there is a momentum deficit in the wake, and hence the foil is expected to produce nett drag across an oscillating cycle;

2. Transition Regime - Roughly occurring at $St \approx St_0$. Wake patterns now consist of primary vorticity, which is shed at a rate of once per foil half-cycle, and secondary vorticity, which may be shed multiple times per foil half-cycle. The shedding of secondary vorticity shows sign of phase-locking to the flapping of the foil, whereby secondary vorticity of one particular sign is shed per foil half-cycle. The combination of primary and secondary vorticity may result in three slightly different wake patterns. Firstly, if the trailing edge excursion is small, the shedding of secondary and primary vorticity become completely synchronised, and is shed as a single vortical structure (“P”), resulting in an in-line vortex wake pattern (pattern D). For larger trailing edge excursions, only a proportion of the total secondary vorticity generated combines with the primary vorticity (forming a “P” vortex), while the remaining secondary vorticity is shed as a number of discrete “S” vortical structures (pattern E). For the special case where only one “S” and one “P” vortex of approximately the same strength are shed per half-cycle respectively, we obtain pattern F. In all three wake patterns, the relative directions of the shed vortices indicates that there is neither a momentum deficit nor a momentum excess in the wake, and hence the foil is expected to be in the transition between drag and thrust production;
3. Thrust Regime - Observed to occur at large Strouhal numbers, approximately corresponding to $St > St_0$. The wake pattern is dominated by strong diffuse vortical structures which are shed once per foil half-cycle. These structures are an agglomeration of strong primary vorticity, and relatively weak secondary vorticity. These structures may contain all of the secondary vorticity generated by the foil, and if so, a pure reverse Karman street wake pattern develops (wake pattern G). Otherwise, some secondary vorticity (“S”) may be shed separately from the main vortical structure (“P”), therefore generating wake pattern H. Typically, wake pattern G is observed when either the trailing edge excursion is small (causing the primary and secondary vortices are shed in close proximity to each other),

or when the heave amplitude and the Strouhal number are simultaneously large (causing the primary vorticity to be so large that it envelops all generated secondary vorticity). Nonetheless, in both wake patterns, the rotational directions and relative strengths of the shed vortices indicate that there is a momentum excess in the wake, and therefore the foil is producing nett time-averaged thrust.

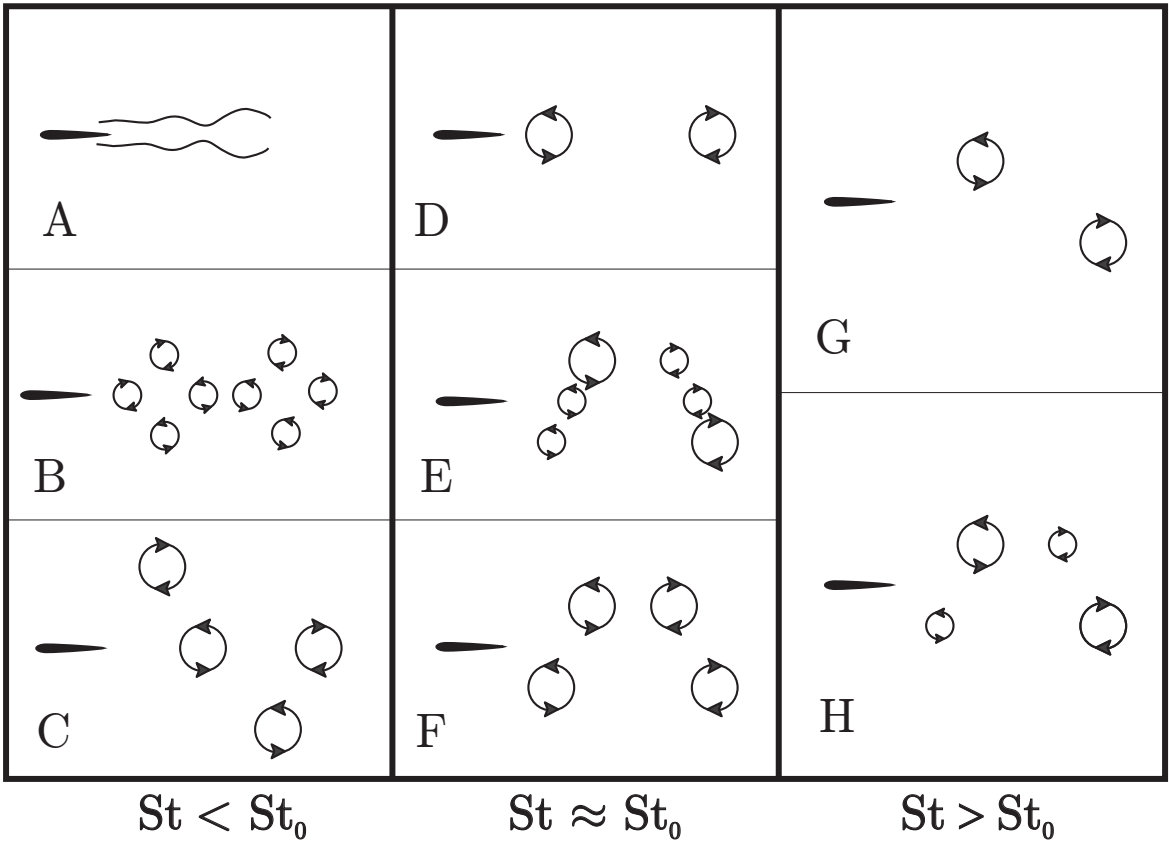


Figure 5.28: Observed vortex patterns in the wake of an unsteady hydrofoil. For a brief description of these wake patterns, please refer to Table 5.1.

Chapter 6

Quantitative Wake Measurements

6.1 Introduction

In Chapter 5, it was found that the flow around the heaving and pitching foil can result in a range of wake patterns. These wake patterns are interpreted as a combination of lift-inducing primary vortices, and drag-related secondary vortices. In this chapter, we attempt to investigate the effect of the foil kinematic parameters on the flow behind the unsteady foil by making quantitative measurements of the foil wake vorticity. The intention of these investigations is to determine if there are any particular foil kinematic parameters that will lead to the formation of optimal vortical structures, and whether the generation of these optimal vortical structures can be characterised by a single non-dimensional formation number (as previously discussed in Chapter 1).

6.2 The generation of optimal vortical wake structures

Gharib *et al.* (1998) first introduced the notion of “formation time” in their experiments of vortex rings generated by an impulsively started jet issuing from a circular orifice. They discovered that the vorticity generated by the jet rolls up into a leading vortex ring, which grows in strength (circulation) up to a limiting non-dimensional time, which they call the formation time, or formation number. Beyond the non-dimensional formation number, any vorticity generated by the jet rolls up into smaller trailing structures. This is shown schematically in Figure 6.1a, where L_1 is the leading vortex ring while L_2 and L_3 are the trailing vortex ring-like structures. The generation of an optimal leading vortex ring then occurs when all the vorticity generated by the jet is contained within L_1 (and therefore L_2 and L_3 do not exist). Gharib *et al.* found that

6.2 The generation of optimal vortical wake structures

this occurs when the formation number, $FN(t) = \frac{U_j \cdot t}{D}$ is approximately between 3.6 and 4.5. This concept of formation time has also been further extended to other flows, including bluff body flows (e.g. Jeon and Gharib, 2004; Milano and Gharib, 2005; Dabiri and Gharib, 2005), as previously discussed in Chapter 1.

It is then tempting to apply the concept of formation number to the wakes of flapping foils. From Chapters 4 and 5, we have determined that the unsteady foil starts to develop thrust at approximately $St \gtrsim St_0$, where the wake patterns consists of large “P” vortices, shed at a rate of one per foil half cycle, that form a reverse Karman vortex street. These “P” vortices are sometimes accompanied by smaller “S” vortices, which can be shed more frequently than the “P” vortices, and are detrimental to the generation of thrust on the foil. By analogy, we then link these “P” vortices to the leading vortex ring (L_1) of Gharib *et al.*’s experiments, while we link the “S” vortices with the trailing vorticity (L_2 and L_3), as shown in Figure 6.1b. It then follows that the generation of optimal thrust by the flapping foil should coincide with the generation of optimal “P” (L_1) vortices.

However, it was quickly discovered that this concept is not applicable to the current experiments. In Chapter 4, it was determined that the propulsive efficiency, η_F , of the foil generally peaks at $St \approx St_0$, where the wake patterns behind the foil consist of either an in-line (I-P) or a double (P+S) vortex wake pattern, or a wake pattern which consists of a single “P” and multiple “S” shed vortices per foil half cycle (P+XS), as discussed in Chapter 5. The peak in η_F occurs at $St \approx St_0$ regardless of whether secondary “S” vortices are observed or not. In fact, in cases where the foil trailing edge excursion A_{te} is large, generally more “S” vortices are observed and η_F tends to be higher when compared to cases where A_{te} is small.

Furthermore, the “P” vortices, which are associated with the production of thrust by the foil, when observed, are shed no more than once per foil half cycle. This implies that either the circulation of the “P” vorticity does not have an upper limit, or alternatively, the formation number of the “P” vortices is not sufficiently large for all flow conditions tested to cause a saturation in the circulation of the “P” vortices. In either case, a limiting formation number cannot be determined in the current experiments.

In addition, the generation of optimal vortical structures based on the concept of formation number do not guarantee that the foil generates thrust efficiently; the formation number does not take into consideration the positions of the shed vortical structures, which, as discussed in Chapter 5, clearly plays an integral role in determining whether the foil generates nett thrust or drag.

We believe that this concept of an optimal “vortex formation number”, as it stands, is not applicable for the flow around the heaving and pitching foil because it is too simplistic to draw a

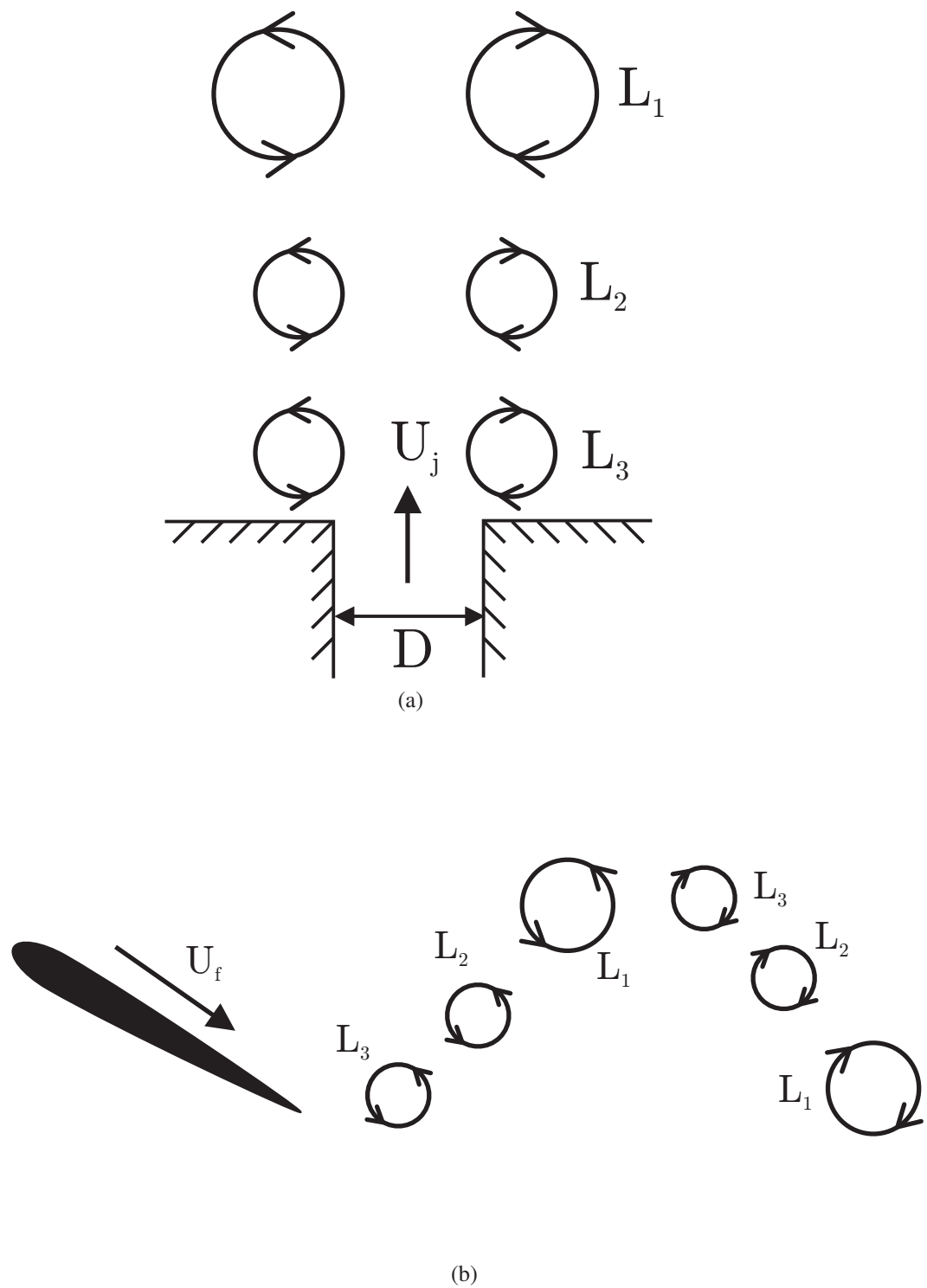


Figure 6.1: Formation of optimal vortical structures

6.3 Quasi-steady model (II) of wake dynamics

direct analogy between the flow around a unsteady foil, and the flow through a circular orifice. In Gharib *et al.*'s experiment, the flow was relatively simple, and contained a flow with a clearly distinct axi-symmetric vortex ring in a still body of fluid, while in the current experiments, the flow around the unsteady foil is highly complex and three-dimensional (von Ellenrieder *et al.*, 2003), and is more closely related to the flow through a rectangular orifice with a temporally variable exit area in a co-flow.

Furthermore, in Chapter 5, we interpreted the flow around the unsteady foil as a combination of two different, independent mechanisms for generating vorticity (that is, the primary and secondary vorticity). Therefore, the concept of formation time should be applied to each of these vorticity generating mechanisms individually, and in isolation. This cannot be done in the current unsteady foil experiments, due to the fact that in many flow cases, there is large interaction between the primary and secondary vorticity.

In light of this, we attempt an alternate quantitative measurement of the wake dynamics - the first moment of circulation of the wake of any given sign, $M_\Gamma = \Gamma_{total} \times A_c$ (first defined in Chapter 3). Here Γ_{total} is the total circulation shed of any given sign per foil period, which includes both primary and secondary vorticity, and A_c is wake width estimated from the centroid of all the shed vorticity of a particular sign, which is a measure of the average positions of the shed vortical structures. The inspiration for using M_Γ , Γ_{total} and A_c as quantitative measurements of the wake kinematics is the intuitive notion that a strong velocity surplus in the foil wake, which leads to high foil thrust coefficients, is linked with the generation of strong vortical structures which are shed away from the time-averaged foil centreline. M_Γ should then provide a quantitative link between the wake dynamics and the thrust produced by the foil. To justify the use of M_Γ as an indirect measurement of the thrust coefficient on the foil, we apply the quasi-steady concept to the vorticity patterns developed in the wake of the foil, as discussed in the following section.

6.3 Quasi-steady model (II) of wake dynamics

In Chapter 5, we showed that the flow behind the heaving and pitching hydrofoil consists of vortices that are shed anti-symmetrically across the wake. Here, we intend to show that the strengths and positions of these shed vortices can be linked to the thrust produced by the foil. This is achieved by simulating an instantaneous “snapshot” of the wake using a distribution of Oseen vortices. These Oseen vortices have an analytically defined velocity field, which can then be integrated to obtain an estimate of the thrust coefficients produced by the foil. In keeping with the spirit of the original quasi-steady model, we assume that a) no other vorticity exists outside the region of interest, or alternatively, any vorticity outside the region of interest has

very little impact on the flow within the region of interest, b) the vorticity in the region of interest does not grow or decay with time and c) that the vortices in the region of interest can be described by the analytic Oseen vortex.

It should be noted that this is different from the quasi-steady model discussed in Chapter 3, where the wake dynamics are linked to the instantaneous angles of attack and trailing edge velocities of the foil. In the current model, named the Quasi-Steady-Model-II (Q-S-II), we do not concern ourselves with the how the kinematics of the foil affect the foil wake, but instead, we are solely interested in the effect of the vorticity distribution in a particular region on the momentum balance around that region.

The modelling of the foil wake is done in two stages. In the first stage, the wake patterns generated by the foil during a foil half-cycle are assumed to consist of a discrete number of vortical structures (say $N_{vortices}$). It is assumed that these vortices, each with a circulation Γ_i , are shed from the foil at a location corresponding to the point (x_0, y_i) where $i = 1, 2, \dots, N_{vortices}$ (see Figure 6.2). Each vortex i is then assumed to propagate into the wake in the same direction and speed as the freestream velocity, U_∞ .

Each vortex i is modelled as an Oseen vortex, which has analytic velocity and vorticity distribution, given by

$$u_{oseen}(r) = \frac{\Gamma}{2\pi r} \left[1 - \exp\left(\frac{-r^2}{2L^2}\right) \right] \quad (6.1)$$

$$\omega_{oseen}(r) = \frac{\Gamma}{2\pi L^2} \left[\exp\left(\frac{-r^2}{2L^2}\right) \right] \quad (6.2)$$

where r is the radial distance from the Oseen vortex core, Γ is the circulation contained within the Oseen vortex and L is a characteristic radius of the Oseen vortex (L^2 is the variance of the Oseen vorticity distribution). Note that $u_{oseen}(r)$ is the tangential velocity component of the Oseen vortex; the radial velocity component is zero everywhere. The velocity at the vortex core, $u_{oseen}(0)$ is set to zero. It should be noted that, using the above convention, that the control volume is moving with the Oseen vortices (and is therefore moving at U_∞ relative to the foil).

The Oseen vortices are added onto a square computational grid of size $N_{field} \times N_{field}$ (as shown in Figure 6.2), with a fixed grid spacing of $\Delta = \frac{1}{50}c$, where c is the chord length of the foil. N_{field} is set to $4c$.

The time-averaged wake velocity field, $\vec{V}_T(x, y)$, and vorticity field, $\omega_T(x, y)$, behind the foil during a foil half-cycle (that is, between $0 \leq t \leq \frac{T}{2}$) are simply then the superposition of the velocity and vorticity fields from each Oseen vortex respectively, averaged across all time steps.

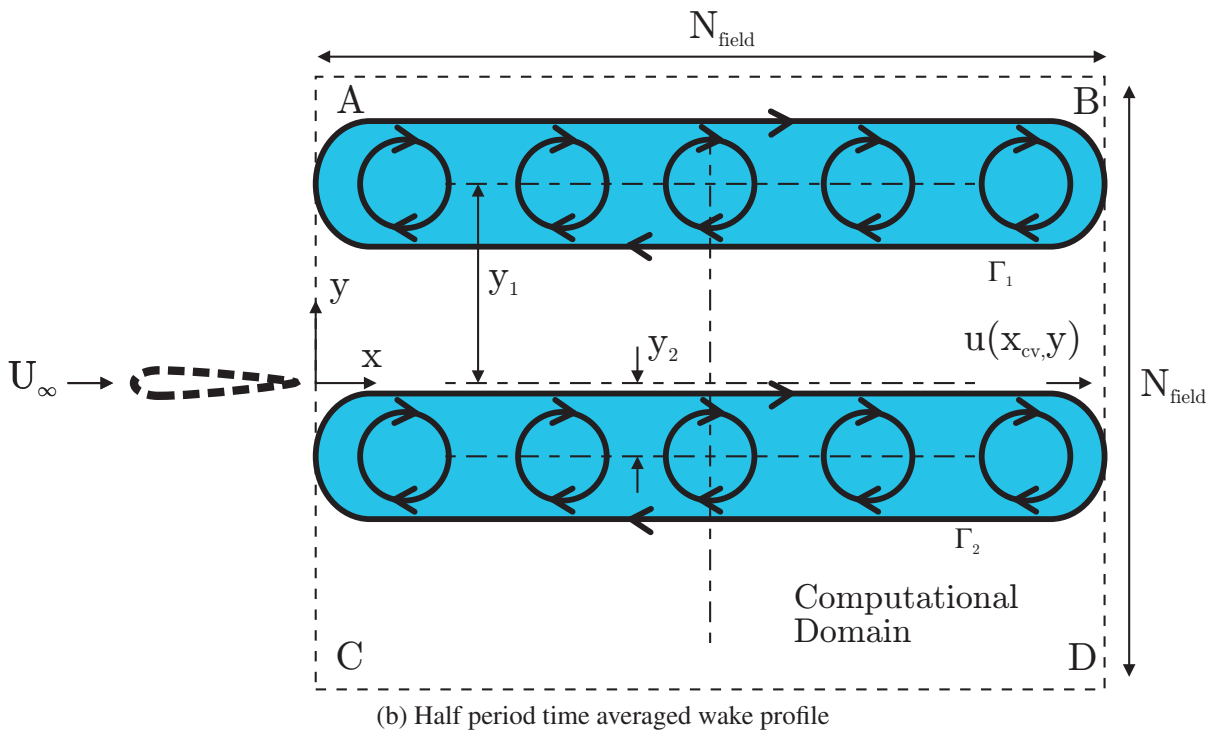
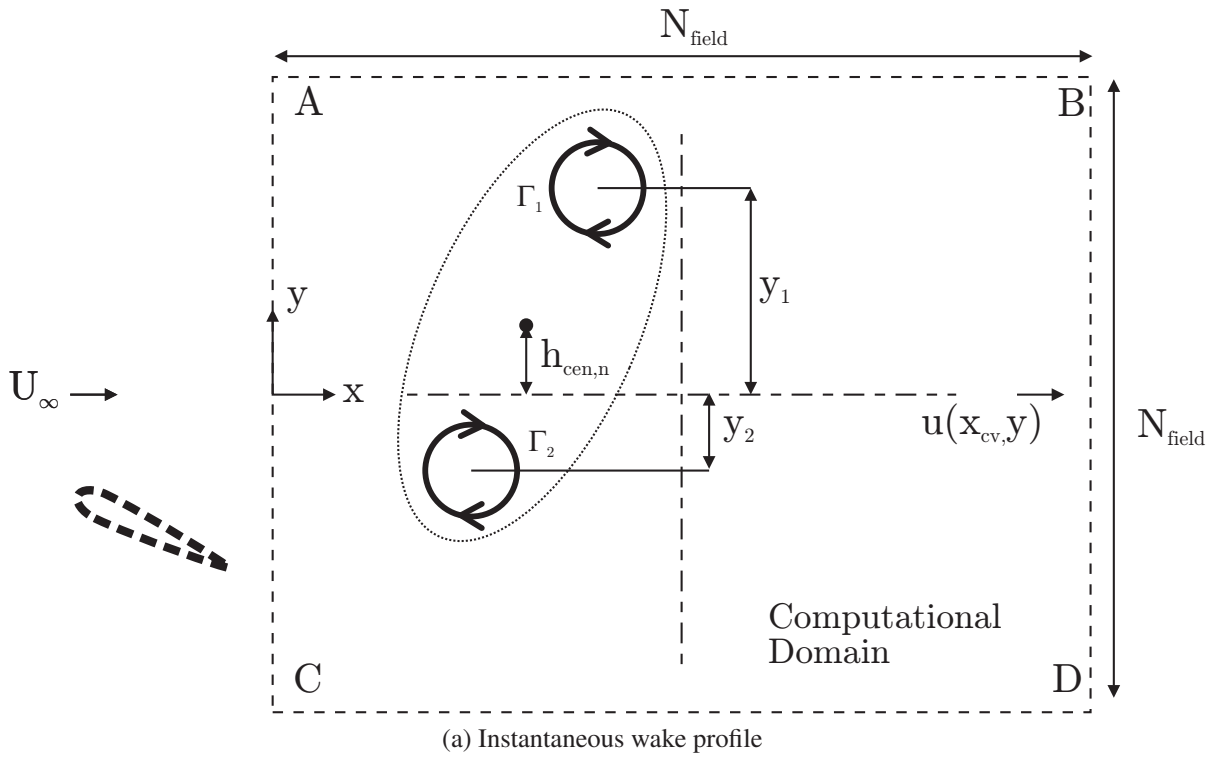


Figure 6.2: Schematic of possible simulated wake patterns with $N_{\text{vortices}} = 2$ (continued on following page)

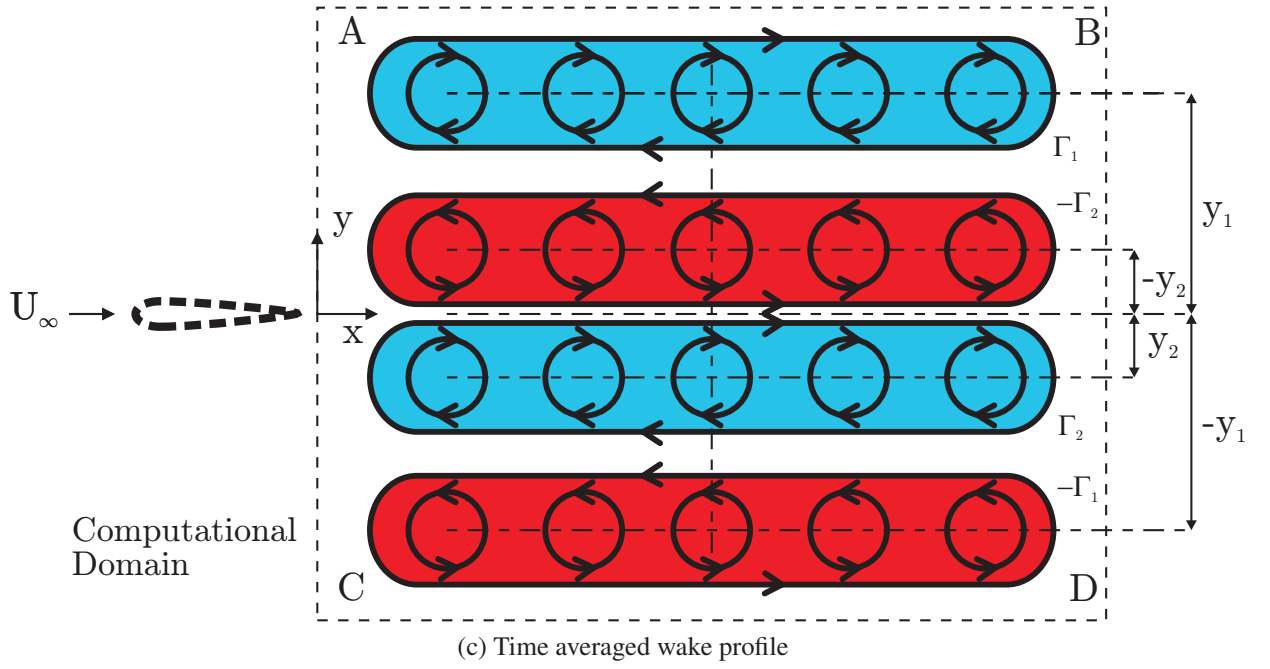


Figure 6.2: Schematic of possible simulated wake patterns with $N_{vortices} = 2$ (continued)

In the second stage of the Q-S-II simulations, the motion of the unsteady foil is assumed to be symmetric, and thus the time averaged wake velocity and vorticity field behind the foil across an entire foil oscillating cycle, $\vec{V}(x, y)$ and $\omega(x, y)$ respectively, are simply $\vec{V}(x, y) = \vec{V}_{\frac{T}{2}}(x, y) + \left\{ \vec{V}_{\frac{T}{2}}(x, y) \right\}_{-1}$ and $\omega(x, y) = \omega_{\frac{T}{2}}(x, y) + \left\{ \omega_{\frac{T}{2}}(x, y) \right\}_{-1}$ where $\left\{ \vec{V}_{\frac{T}{2}}(x, y) \right\}_{-1}$ and $\left\{ \omega_{\frac{T}{2}}(x, y) \right\}_{-1}$ are the mirrored fields of $\vec{V}_{\frac{T}{2}}(x, y)$ and $\omega_{\frac{T}{2}}(x, y)$ about the time-averaged foil centreline, respectively.

The total circulation in the computational field is obtained by numerically approximating

$$\Gamma_{total} = \int_{ROI} \omega_n(x, y) dA \quad (6.3)$$

where the region of integration, ROI , is the entire computational domain, and $\omega_n(x, y)$ is the negative component of the time-averaged vorticity field, $\omega(x, y)$. This is simply achieved by summing $\omega_n(x, y)$ across the whole computational domain, and multiplying the calculated value with $dA = \Delta^2$.

Γ_{total} is then normalised by the free-stream velocity, and foil chord length,

$$\tilde{\Gamma}_{total, c} = \frac{\Gamma_{total}}{U_{\infty} c} \quad (6.4)$$

6.3 Quasi-steady model (II) of wake dynamics

The non-dimensional wake width, on the other hand, is defined as

$$\tilde{A}_c = \frac{2h_{cen,n}}{c} \quad (6.5)$$

where $h_{cen,n}$ is the centroid of the negative vorticity field $\omega_n(x, y)$,

$$h_{cen,n} = \frac{\oint_{S_{i,s}} \omega_n(x, y) y dy}{\oint_{S_{i,s}} \omega_n(x, y) dy} \quad (6.6)$$

It should be noted that, by convention, if $\tilde{A}_c < 0$, then it is expected that there is a momentum deficit in the wake, and therefore the foil is expected to produce drag.

The non-dimensional first moment of circulation is

$$\tilde{M}_\Gamma = \tilde{\Gamma}_{total,c} \cdot \tilde{A}_c \quad (6.7)$$

Since the flow is two dimensional, we can then obtain an estimate of the thrust coefficient due to the induced velocities of the Oseen vortices using equation B.25 (see Appendix B),

$$C_t \approx -\frac{2 \int_{BD} u(x_{cv}, y) [U_\infty - u(x_{cv}, y)] dy}{U_\infty^2 \cdot c \cdot s} \quad (6.8)$$

where s is the span of the foil, set to $s = 1$, U_∞ is the free-stream velocity, which is typically fixed at $\frac{U_\infty}{c} = 1 \frac{1}{s}$, and u is the x-component of the velocity. Nominally, $\frac{L}{c} \approx 0.15$, although the results of the Q-S-II simulations is independent of the choice of L , as long as $L \ll N_{field}$. x_{cv} is the location of the control volume boundary BD relative to the origin (see Figure 6.2).

The Q-S-II simulations are divided into two parts. In part 1, the foil is assumed to shed one single vortex (thus $N_{vortices} = 1$) of strength Γ_1 , per foil half cycle. The strength of the vortex was systematically varied between $0.05 \lesssim \frac{|\Gamma_1|}{U_\infty c} \lesssim 3$, while the location of the shed vortex, y_1 , was varied such that $-c \lesssim y_1 \lesssim c$. This facilitates a direct investigation into the effect of $\tilde{\Gamma}_{total}$ and \tilde{A}_c (and hence \tilde{M}_Γ) on the thrust coefficient, C_t . An example of a possible resulting vorticity field is shown in Figure 6.3a.

In part 2 of the Q-S-II simulations, the wake produced by the flapping foil is modelled as a number of Oseen vortices, $N_{vortices}$, which are shed into the wake every foil half cycle. The simulation consists of 1000 realisations, whereby in each realisation the number of vortices, $N_{vortices}$, the circulations of each vortex i , Γ_i , and the positions of these vortices, y_i , were randomly varied such that $1 \leq N_{vortices} \leq 4$, $-3 < \frac{\Gamma_i}{U_\infty c} < 3$ and $-c < y_1 < c$. An example of one possible resulting vorticity field is shown in Figure 6.3b.

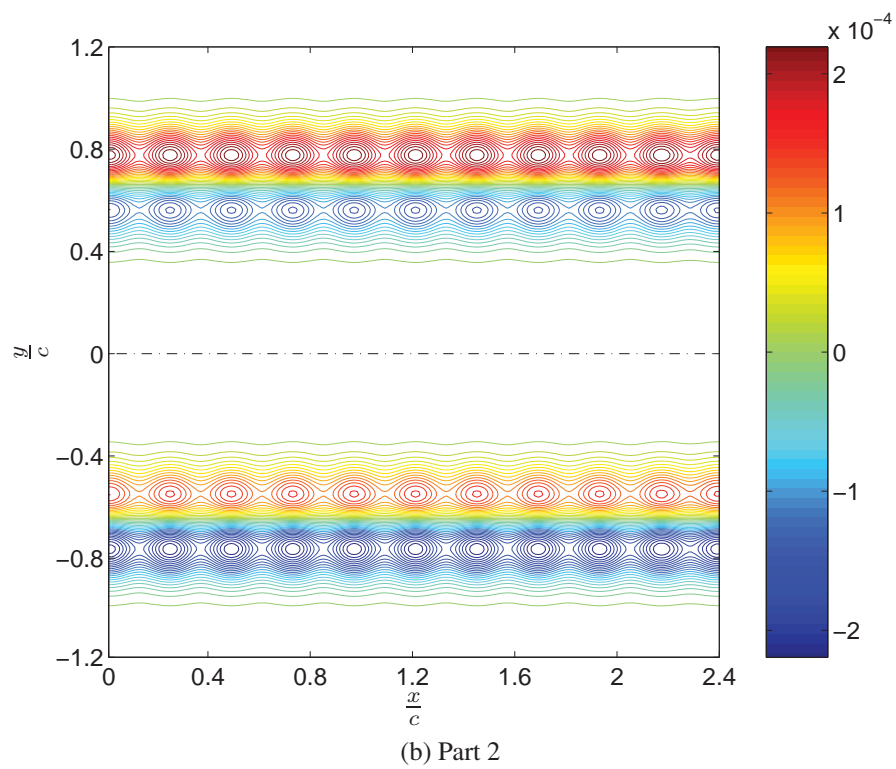
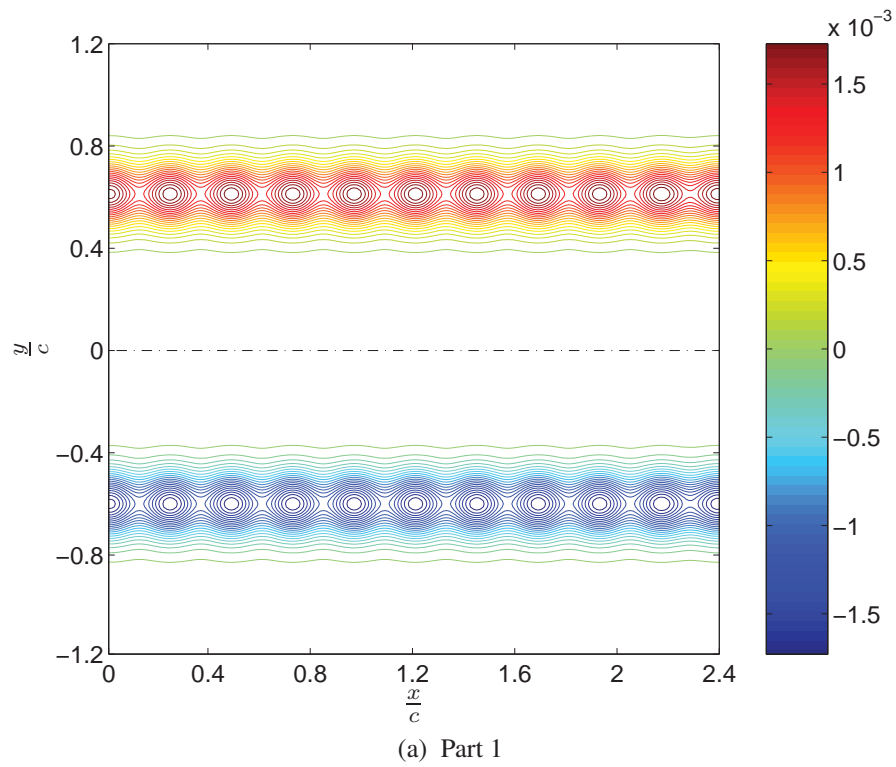


Figure 6.3: Example of vorticity fields produced in the Q-S-II simulations. Vorticity contours have units $\frac{1}{s}$

6.3.1 Q-S-II results

Figure 6.4 shows the results of part 1 of the Q-S-II wake simulations. Figure 6.4a indicates that the measured time-averaged thrust coefficient, C_t is approximately linearly proportional to $\tilde{\Gamma}_{total,c}$. This is not an unexpected result, as intuitively, the induced velocities in the region of interest are directly proportional to the strength (circulation) of the vortices (see equation 6.1).

Figure 6.4b shows the effect of varying the non-dimensional centroidal wake width, \tilde{A}_c , on the time-averaged foil thrust coefficient, C_t . The results are not surprising; a larger wake width leads to larger foil thrust coefficients. In a strict sense, the relationship between C_t and \tilde{A}_c appears to be non-linear, however, within the parameter range tested, it would seem that C_t and \tilde{A}_c are approximately linearly proportional.

Figure 6.4c shows the relationship between C_t and the non-dimensional first moment of circulation, \tilde{M}_Γ , for all tested values of $\tilde{\Gamma}_{total,c}$ and \tilde{A}_c . It is clear that all data collapse onto a single curve, demonstrating that C_t is approximately linearly proportional to \tilde{M}_Γ regardless of the positions or strength of the shed vortices in the wake.

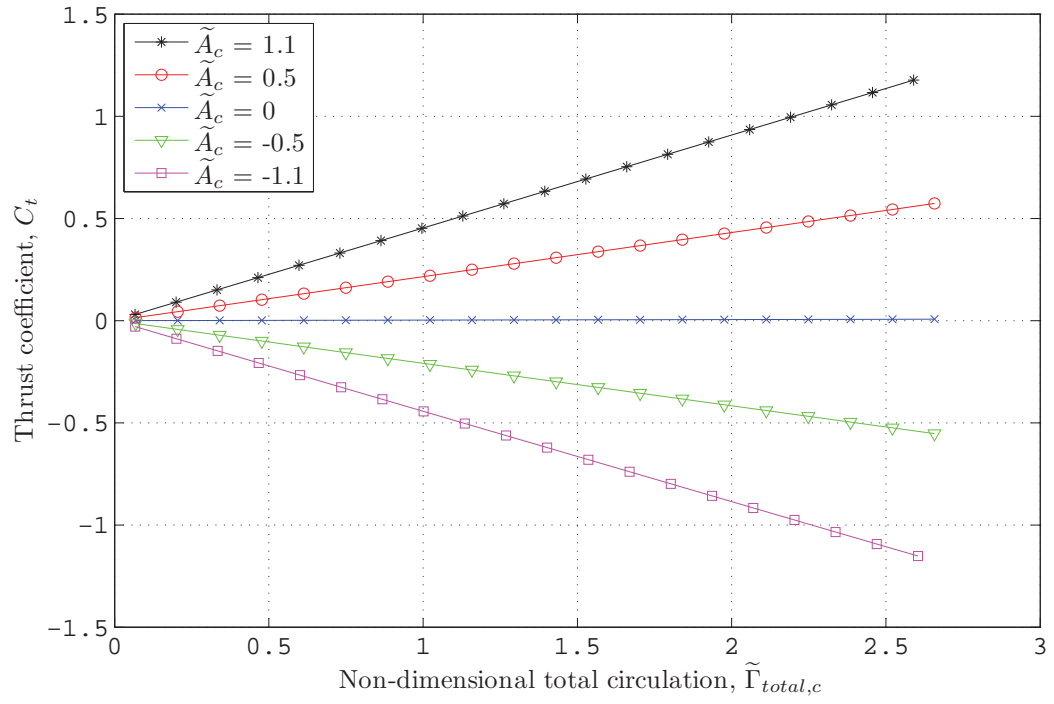
Figure 6.5 shows the results of part 2 of the Q-S-II wake simulations. Figures 6.5a-c mirror the results of part 1 shown in Figures 6.4a-c respectively, however, what is of particular interest is the result shown in Figure 6.5c, which is exactly the same result obtained in part 1 of the wake simulations. This is an important result because it indicates that \tilde{M}_Γ is a useful wake parameter because it shows a consistent trend relative to C_t regardless of the number of vortices in the wake, the positions of the vortices, and the relative strengths of the shed vortices.

It should be noted that these simulations were also repeated for an additional 10 different values of L and U_∞ respectively (not shown here for brevity). The results approximately match that of Figure 6.5c. In all cases, the relationship between C_t and \tilde{M}_Γ can be expressed empirically as

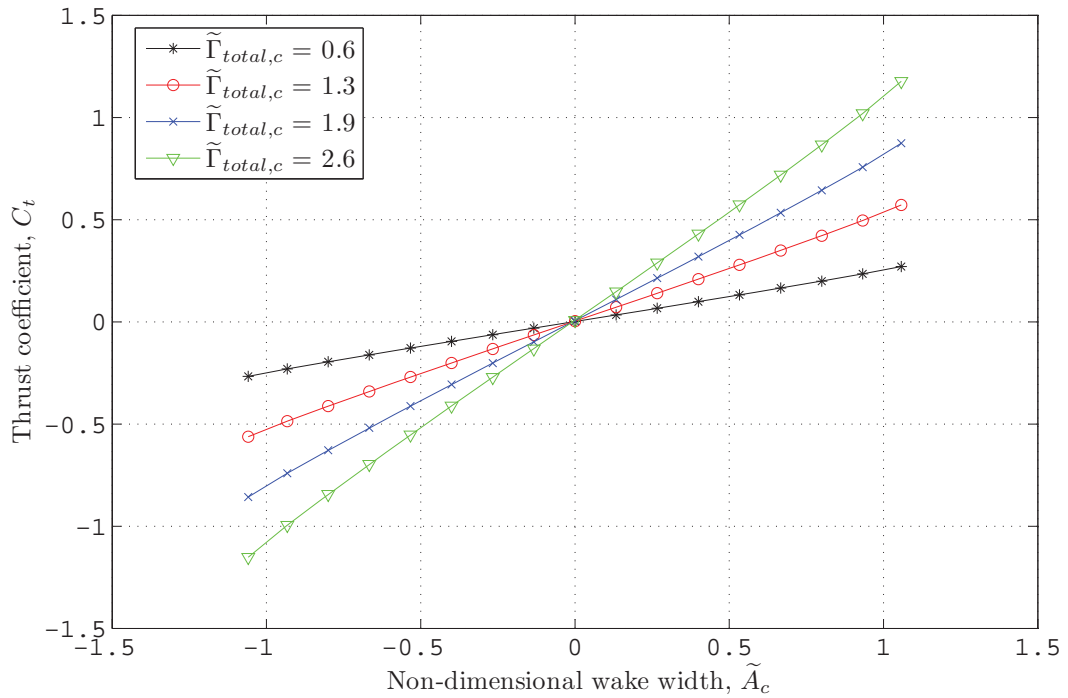
$$C_t \approx k_{\Gamma, sim} \tilde{M}_\Gamma \quad (6.9)$$

where $k_{\Gamma, sim}$ was found to be $k_{\Gamma, sim} \approx 0.41$.

Since equation 6.9 is consistent for all tested parameters, the Q-S-II wake simulations indicate that regardless of a) the number of vortices shed into the wake, b) the relative circulations of the shed vortices, c) the positions of the shed vortices, d) the free-stream velocity, and e) the size of the modelled vortices (that is, L), the thrust coefficient produced by the foil shows approximately a linear relationship with the non-dimensional first moment of circulation \tilde{M}_Γ . Therefore, it is expected experimentally that \tilde{M}_Γ can be used as a useful, indirect, qualitative measurement of the time-averaged thrust produced by the foil.



(a)



(b)

Figure 6.4: Results of Q-S-II wake simulations, part 1 (continued on following page)

6.4 Experimental measurement of M_Γ , $\Gamma_{total,c}$ and A_c

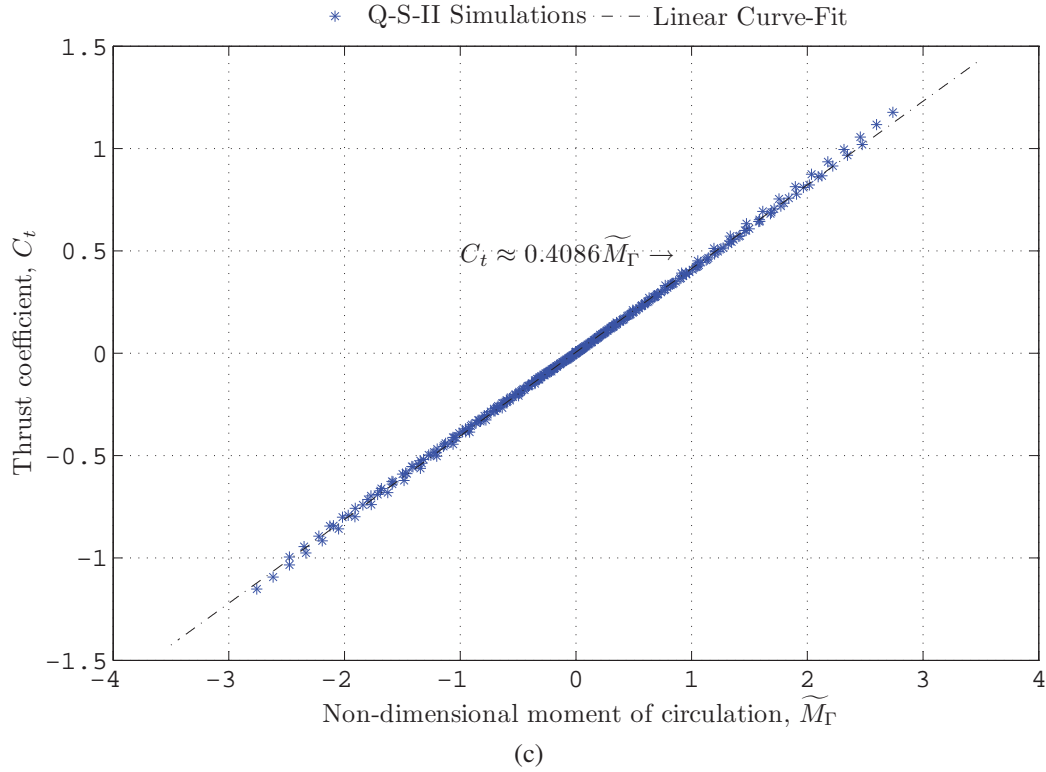
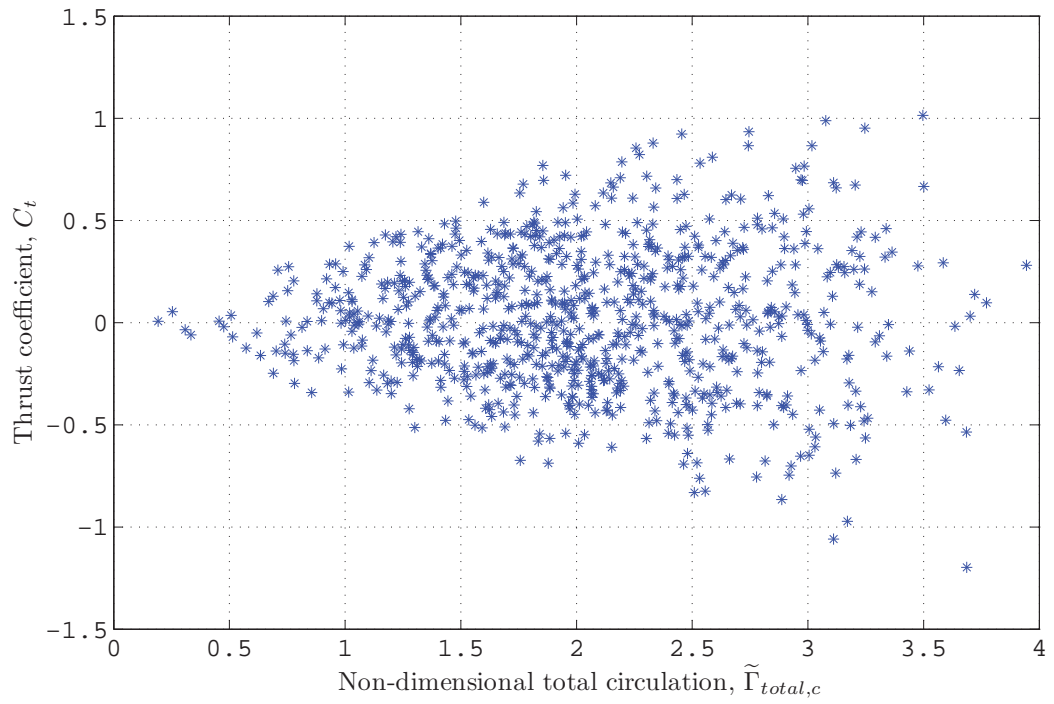


Figure 6.4: Results of Q-S-II wake simulations, part 1 (continued)

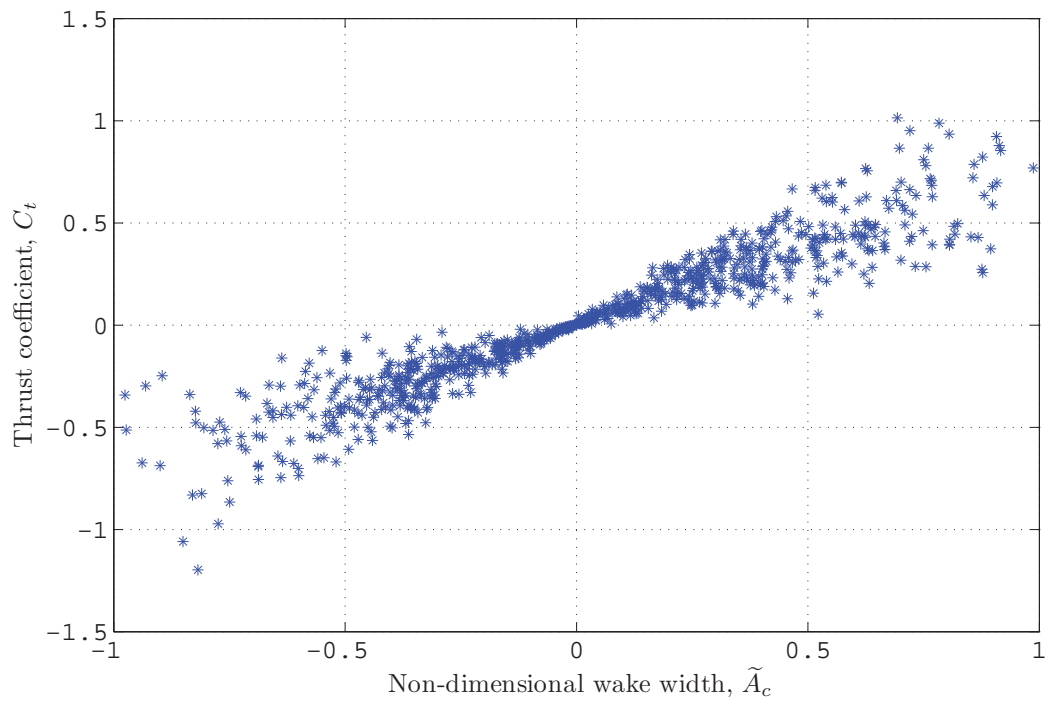
6.4 Experimental measurement of M_Γ , $\Gamma_{total,c}$ and A_c

We proceed by experimentally measuring the first moment of circulation, M_Γ , for all experimental flow conditions and foil dynamic parameters. To achieve this, we first have to measure the total circulation shed of any given sign per foil period, $\Gamma_{total,c}$, and the wake width estimated from the centroid of all the shed vorticity of a particular sign, A_c , which can be determined experimentally. $\Gamma_{total,c}$ and A_c (and consequently M_Γ) can also be determined numerically using the quasi-steady model (as discussed in Chapter 3). This provides us with the opportunity to compare the experimental and theoretical results to determine if there are any particular flow conditions which display wake dynamics that are beyond the theoretical predictions.

The qualitative wake survey in Chapter 5 indicates that, in the majority of cases, the vorticity generated by the unsteady foil is either shed as a large agglomeration of vorticity, or as a number of discrete vortical structures, or a combination of both. Very little, or no observed cross-annihilation of vorticity was observed, although the experimental PIV results close to the foil boundary are poorly resolved and could be a source of significant errors. Nonetheless, we proceed using the assumption that all the vorticity generated by the unsteady foil is subsequently shed into the wake as measurable, in-plane vortical structures.



(a)



(b)

Figure 6.5: Results of Q-S-II wake simulations, part 2 (continued on following page)

6.4 Experimental measurement of M_Γ , $\Gamma_{total,c}$ and A_c

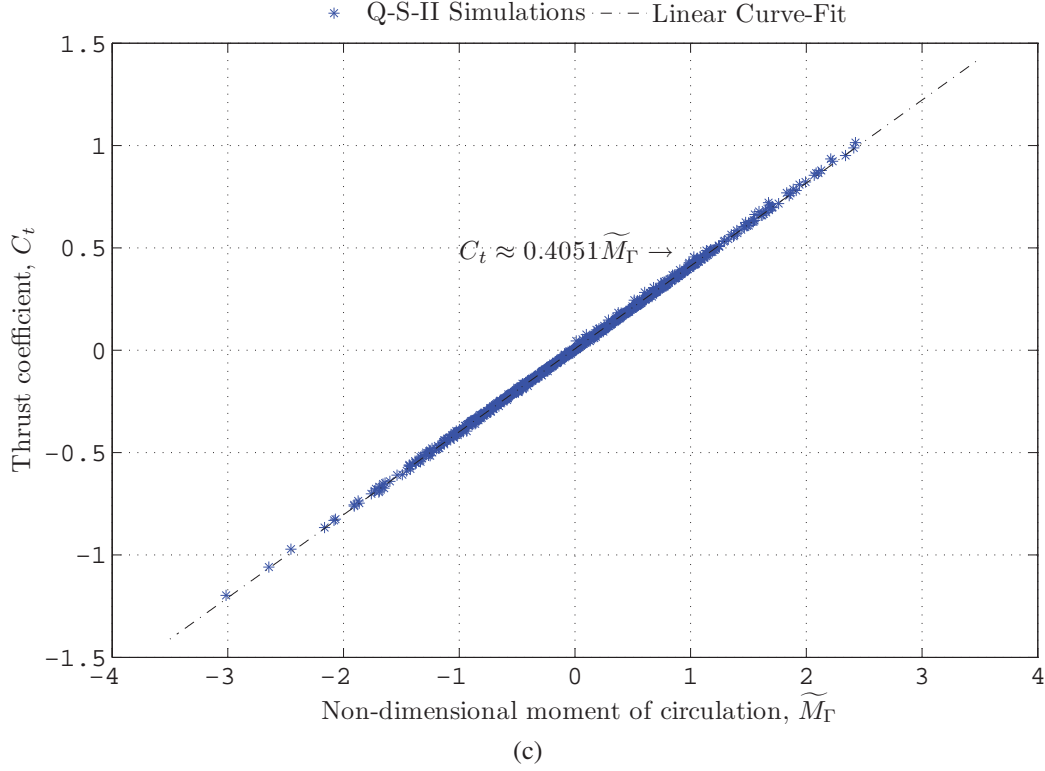


Figure 6.5: Results of Q-S-II wake simulations, part 2 (continued)

To measure the total amount of shed vorticity of any given sign $\Gamma_{total,c}$ and the centroidal wake width A_c , we denote the individual circulation $\Gamma_{i,s}$ and the individual vorticity centroid location $h_{cen,i,s}$ for each identifiable vortical structure i of a particular sign s (where $s = p, n$ for positive and negative vorticity respectively).

The boundaries of the individual vortical structures, $S_{s,i}$ are defined by an iso-vortical contour with fixed vorticity threshold, $\omega_t = 0.4 \frac{1}{s}$ (note that peak vorticity is generally within the range of $\omega_{peak} \approx 25 - 80 \frac{1}{s}$). The evaluation of the circulation of these vortical structures is based on the method discussed in Appendix C. The location of the vorticity centroid of each vortical structure is based on a numerical evaluation of

$$h_{cen,s,i} = \frac{\oint_{S_{i,s}} \omega y dy}{\oint_{S_{i,s}} \omega dy} \quad (6.10)$$

The circulation of any vortical structure, $\Gamma_{s,i}$ and the location of its vorticity centroid, $h_{cen,s,i}$ is evaluated as soon as it is shed from the boundary of the foil, as shown in Figure 6.6.

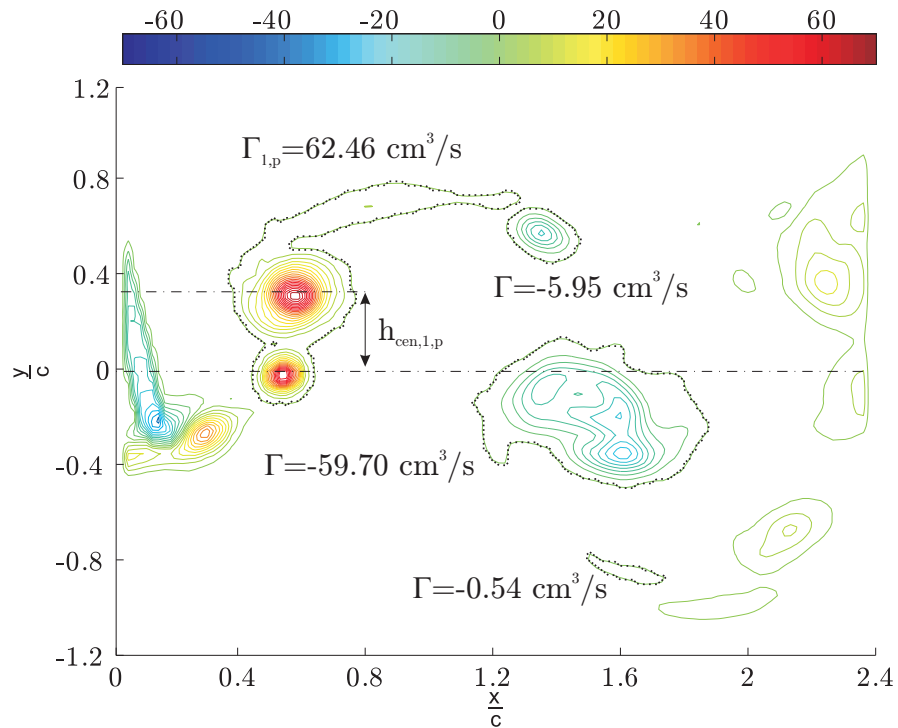
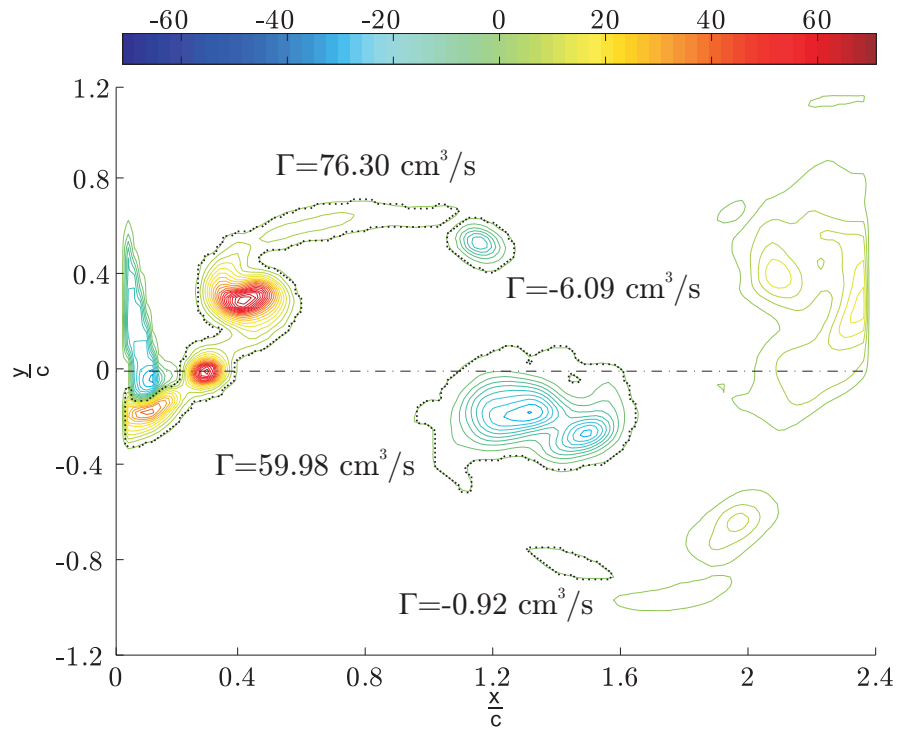
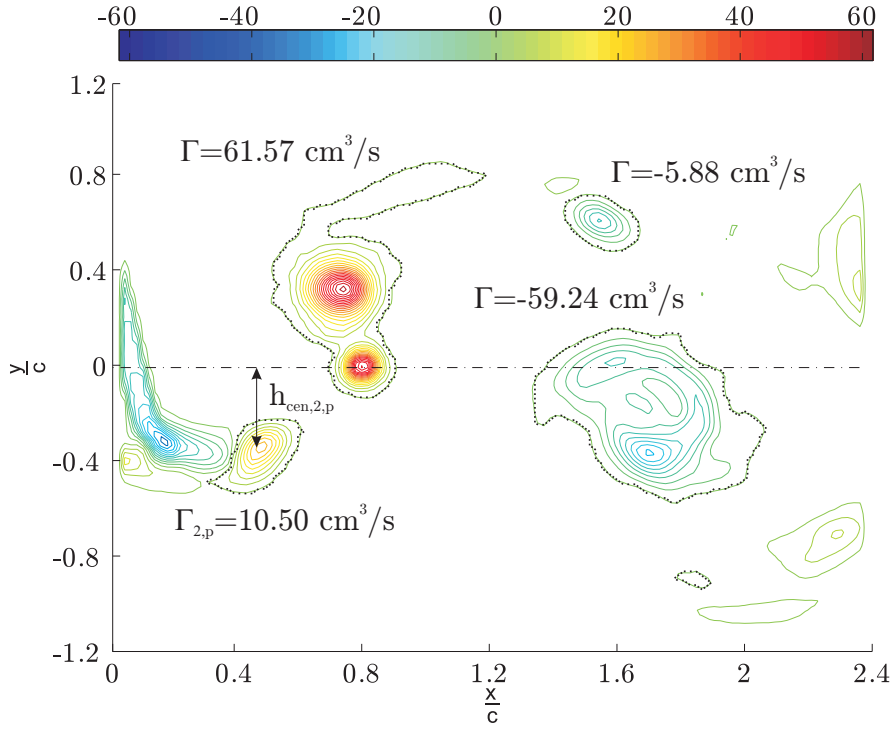


Figure 6.6: Evaluation of circulation of shed vortical structures behind the foil. Flow is from left to right. Foil kinematic parameters: $\frac{h_0}{c} = 0.25$, $\theta_0 = 15^\circ$, and $St = 0.44$ (continued on following page)

6.4 Experimental measurement of M_Γ , $\Gamma_{total,c}$ and A_c



(c) Additional positive vorticity is shed into the wake of the foil

Figure 6.6: Evaluation of circulation of shed vortical structures behind the foil. Flow is from left to right. Foil kinematic parameters: $\frac{h_0}{c} = 0.25$, $\theta_0 = 15^\circ$, and $St = 0.44$ (continued)

Thus, for $N_{vortices,s}$ discrete vortical structures shed into the foil wake, the circulation of all the shed vortices of a particular sign s is

$$\Gamma_{total,s} = \sum_{i=1}^{N_{vortices,s}} \Gamma_{s,i} \quad (6.11)$$

As the motion of the foil is approximately symmetrical, we can then take the average of the circulation of the positive and negative shed vorticity magnitudes,

$$\Gamma_{total} = \frac{\Gamma_{total,p} - \Gamma_{total,n}}{2} \quad (6.12)$$

Finally, we normalise Γ_{total} with the chord and the freestream velocity to obtain a non-dimensional measurement of the strength of the shed vorticity produced by the unsteady foil of any particular sign,

$$\tilde{\Gamma}_{total,c} = \frac{\Gamma_{total}}{U_\infty \cdot c} \quad (6.13)$$

To obtain the centroidal wake width, we first calculate the centroid of all the shed vorticity of sign s ,

$$h_{cen,s} = \frac{\sum_{i=1}^{N_{vortices,s}} h_{cen,s,i} \cdot \Gamma_{s,i}}{\Gamma_{total,s}} \quad (6.14)$$

Again, assuming that the motion of the foil is symmetrical, the wake width is

$$A_c = h_{cen,p} - h_{cen,n} \quad (6.15)$$

We normalise the wake width by the chord length to obtain a non-dimensional wake width,

$$\tilde{A}_c = \frac{A_c}{c} \quad (6.16)$$

Following this, we can also define a single non-dimensional term that takes into account both the total circulation and the positions of shed vorticity, dubbed the moment of circulation

$$\tilde{M}_\Gamma = \tilde{\Gamma}_{total,c} \cdot \tilde{A}_c \quad (6.17)$$

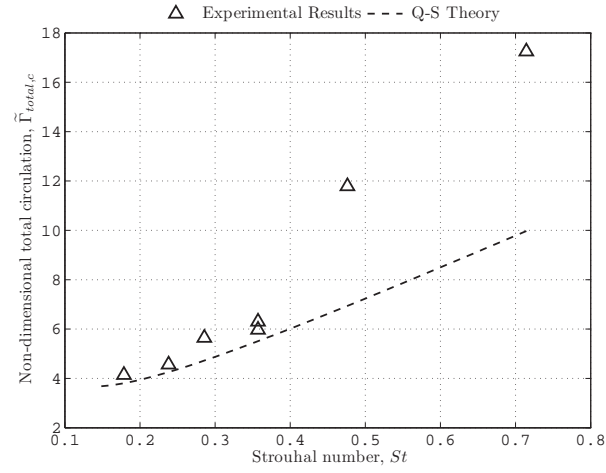
6.5 Experimental and numerical results

A selection of experimental wake measurements for each foil dynamic group are shown in Figures 6.7 to 6.10, plotted together with the wake dynamics estimated using the quasi-steady model (see Section 3.10). Note that some results are omitted due to the fact that in some cases, particularly at low St (i.e. U_∞ is large), the vorticity does not fully shed² from the foil before leaving the PIV field of view.

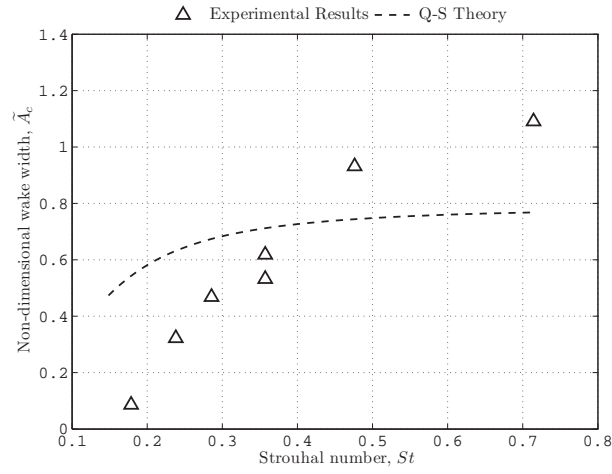
Figure 6.7a shows the experimentally measured value of $\tilde{\Gamma}_{total,c}$ for the purely heaving foil. This value of $\tilde{\Gamma}_{total,c}$ is larger than that predicted by the quasi-steady theory for all St , but $\tilde{\Gamma}_{total,c}$ is particularly large at high St , indicating that the purely heaving foil produces vortical structures with large circulation at large Strouhal numbers. Although this large value of $\tilde{\Gamma}_{total,c}$ could be linked to the generation of large leading edge vortices observed in the flow visualisation experiments (as discussed in Chapter 5), the large $\tilde{\Gamma}_{total,c}$ does not necessarily correlate with optimal thrust production by the foil, as $\tilde{\Gamma}_{total,c}$ does not differentiate between primary vorticity (which we associate with thrust), and secondary vorticity (which we associate with drag). To get some indication of whether $\tilde{\Gamma}_{total,c}$ contains a large proportion of primary vorticity relative

²A vortical structure is considered to be fully shed from the foil when the iso-vortical contour with fixed threshold $\omega_t = 0.4 \frac{1}{s}$ forms a closed loop around the vortex, but does not enclose or encroach on the boundaries of the foil.

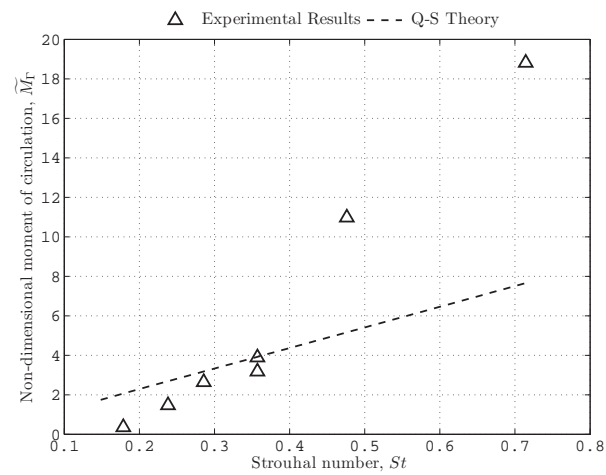
6.5 Experimental and numerical results



(a)

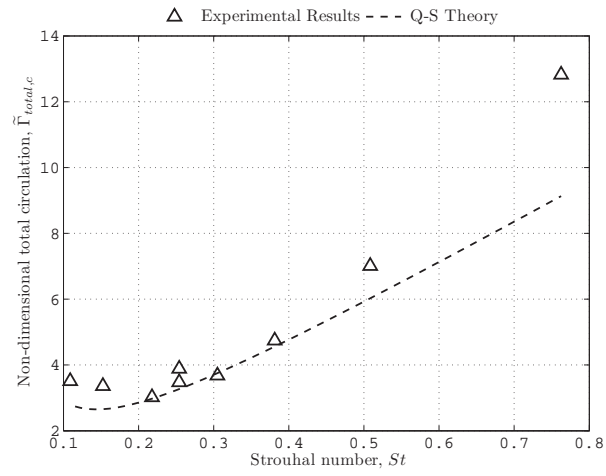


(b)

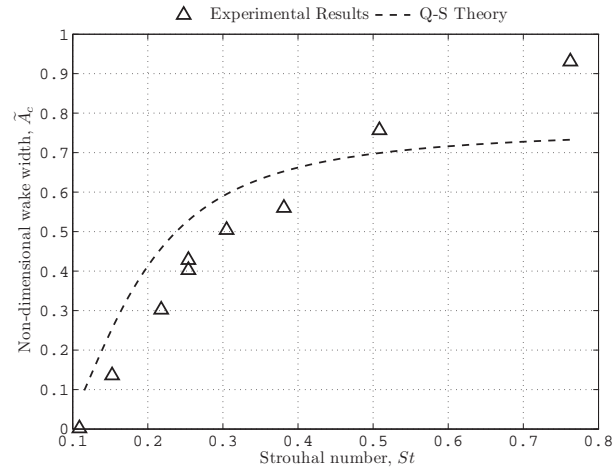


(c)

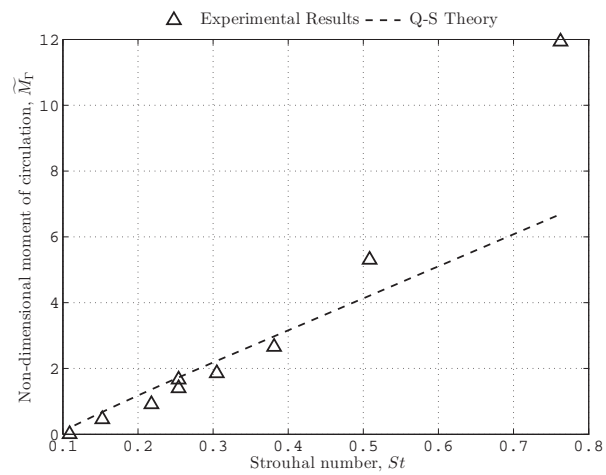
Figure 6.7: Wake dynamics for set 2 : $\frac{h_0}{c} = 0.5$, $\theta_0 = 0^\circ$ (Group I)



(a)



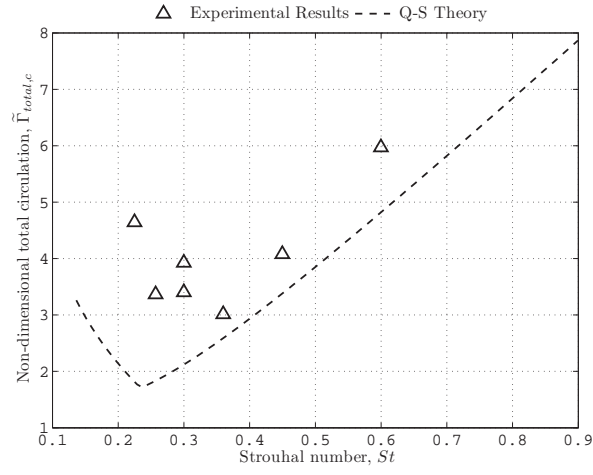
(b)



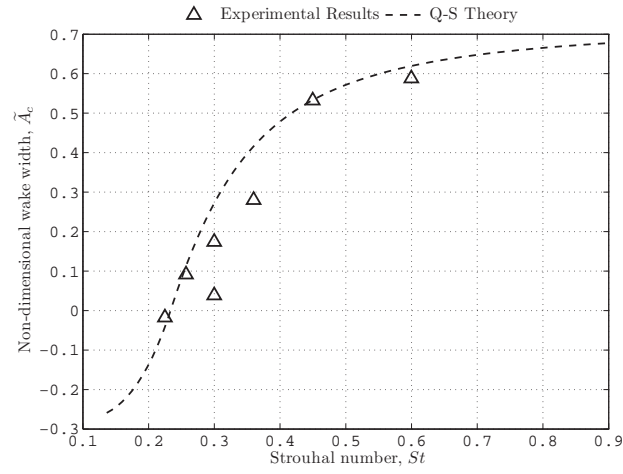
(c)

Figure 6.8: Wake dynamics for set 5 : $\frac{h_0}{c} = 0.5$, $\theta_0 = 15^\circ$ (Group II)

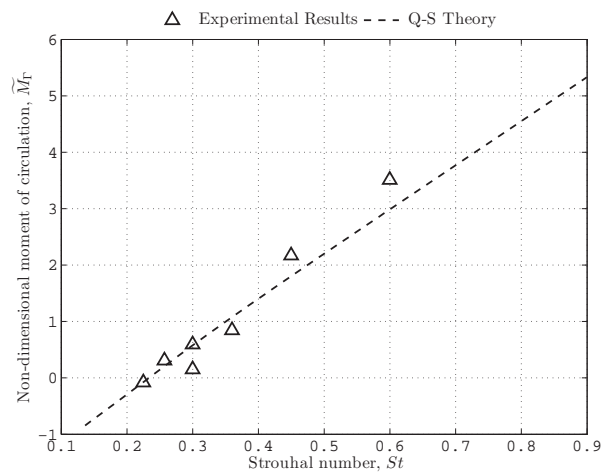
6.5 Experimental and numerical results



(a)

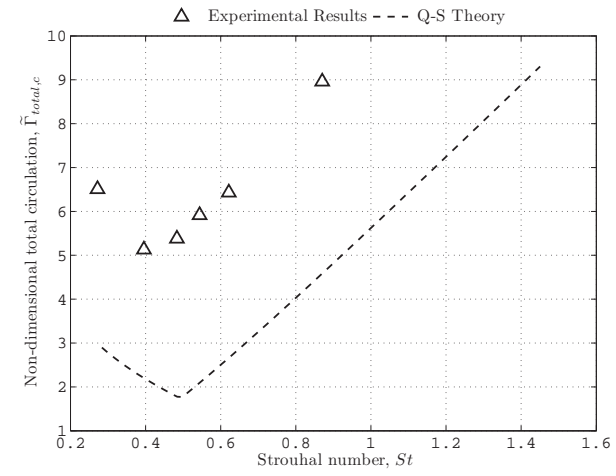


(b)

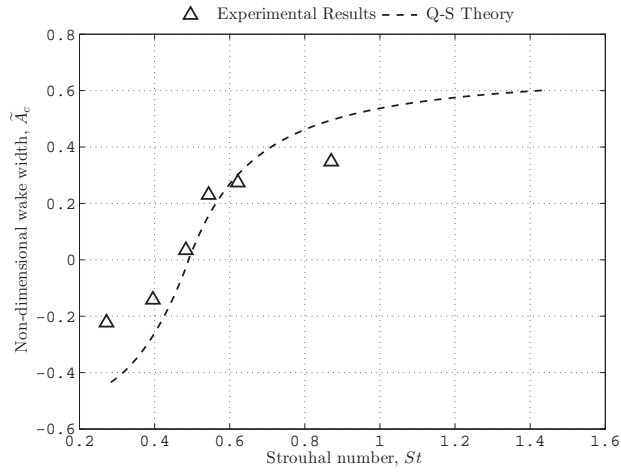


(c)

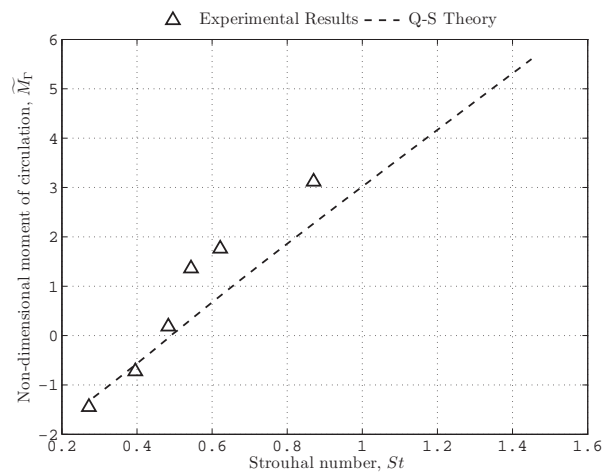
Figure 6.9: Wake dynamics for set 8 : $\frac{h_0}{c} = 0.5$, $\theta_0 = 30^\circ$ (Group III)



(a)



(b)



(c)

Figure 6.10: Wake dynamics for set 11 : $\frac{h_0}{c} = 0.5$, $\theta_0 = 45^\circ$ (Group IV)

6.5 Experimental and numerical results

to the secondary vorticity, we have to look at the centroidal wake width, \tilde{A}_c , as shown in Figure 6.7b. Large amounts of primary vorticity (relative to secondary vorticity), theoretically, should result in large wake widths. For the purely heaving foil, the centroidal wake widths are smaller than predicted using the quasi-steady theory at low St , but at $St > 0.35$, \tilde{A}_c increases beyond the theoretical predictions. The fact that both $\tilde{\Gamma}_{total,c}$ and \tilde{A}_c (see Figures 6.7a and b respectively) simultaneously increase beyond theoretical predictions at $St > 0.35$ is strong indication that the purely heaving foil generates vortical structures with large circulation, which is consistent with the results of flow visualisation (as discussed in Chapter 5).

In groups II and III, where the foil undergoes moderate heave and pitch amplitudes, the results obtained experimentally matches closely with the results obtained using the quasi-steady model (Figures 6.8 to 6.9). This emphasises the fact that the quasi-steady model is accurate for both predicting the time-averaged forces (as discussed in Chapter 3), and also the wake dynamics produced by the unsteady foil when it undergoes heave and pitch motions with moderate amplitudes.

The quasi-steady model, however, breaks down when the pitch amplitudes are large (Figure 6.10), as expected (previously discussed in Chapter 3). $\tilde{\Gamma}_{total,c}$ is strongly underestimated by the Q-S model for group IV (Figure 6.10a), possibly due to the fact that the Q-S model neglects the effect of the rotation of the foil on the surrounding fluid, and therefore does not take into account the complex transient pressure gradients along the boundary of the foil, which may be an additional source of vorticity (Morton, 1984). The wake widths, \tilde{A}_c for group IV are generally slightly smaller than the wake widths predicted with the Q-S theory (Figure 6.10b). The small wake widths at large θ_0 suggests that the large amounts of measured shed vorticity behind the foil consists of secondary vorticity, as opposed to primary vorticity, due to the fact that the presence of strong primary vorticity should increase the centroidal wake width \tilde{A}_c . We postulate that this will lead to unfavorable thrust production.

A summary of available $\tilde{\Gamma}_{total,c}$ values for all tested flow cases is shown in Figure 6.11a. When plotted against the heave-based Strouhal number, St_h , the data show good collapse within each Group. $\tilde{\Gamma}_{total,c}$ appears to reach a minimum at $St_h \approx St_{h,0}$, which is as expected, due to the fact that the angles of attack are low at these Strouhal numbers. Beyond $St_h > St_{h,0}$, $\tilde{\Gamma}_{total,c}$ shows an approximate linear relationship to St_h . The relative magnitudes of $\tilde{\Gamma}_{total,c}$ between foil kinematic groups are close, however, Group I (pure heave) does portray a larger $\tilde{\Gamma}_{total,c}$ than the other foil dynamic groups. This result suggests that the purely heaving foil generates vortical structures with large circulation, which is consistent with the observations made in Chapter 5, where the purely heaving foil was observed to generate large, strong leading edge vortices. For all other cases (groups II to IV), however, the variation in $\tilde{\Gamma}_{total,c}$ is small, which suggests that

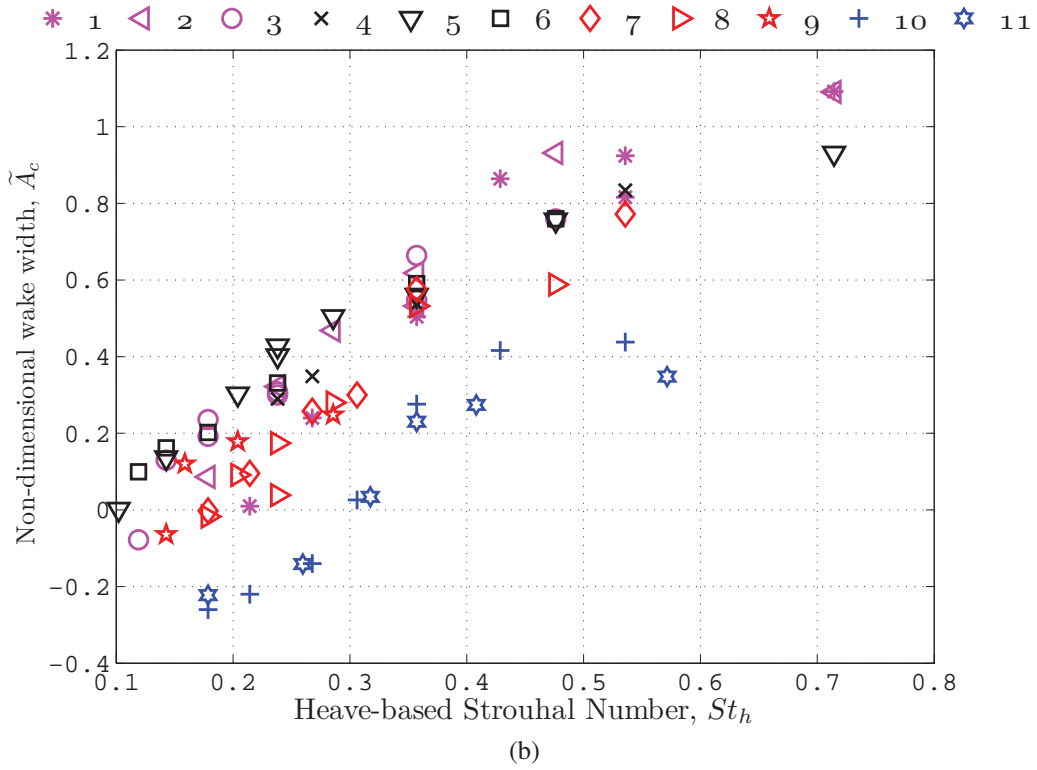
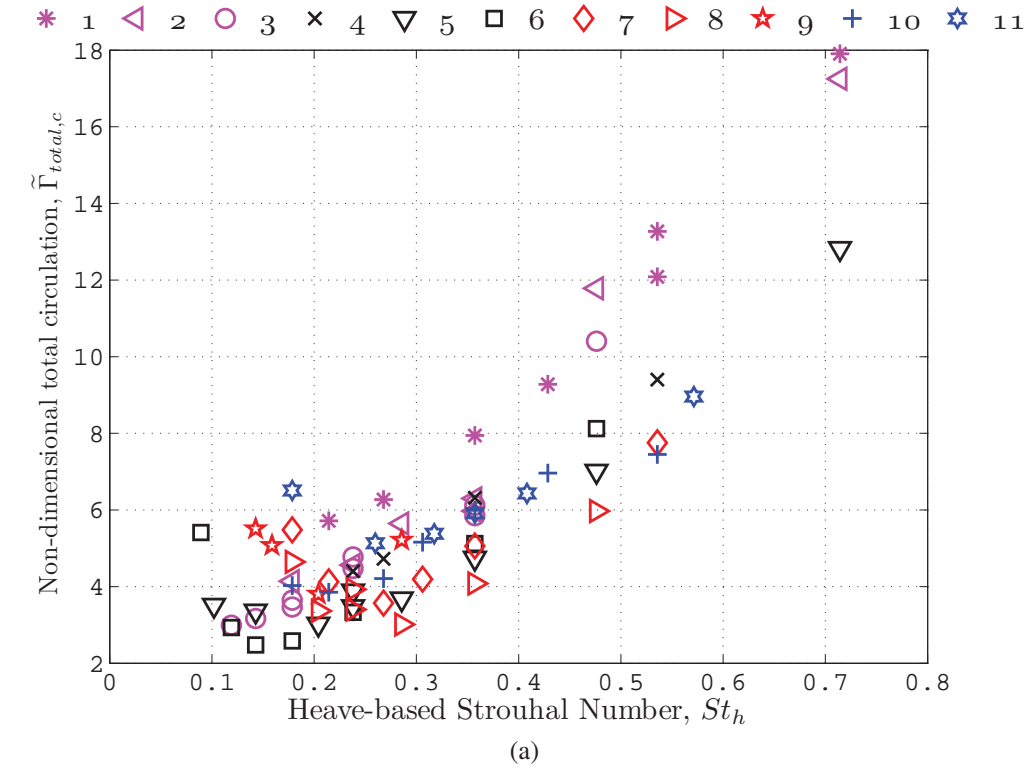


Figure 6.11: Summary of wake measurements for all flow cases. Set numbers refer to foil kinematic parameters defined in Table 2.1 (continued on following page)

6.5 Experimental and numerical results

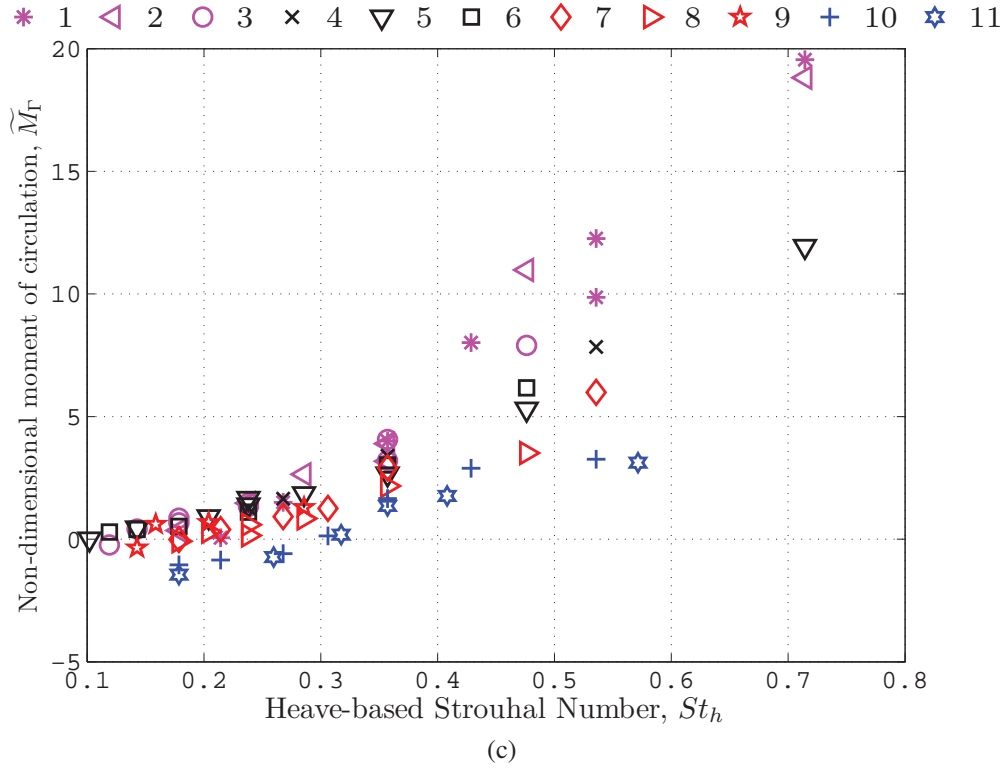


Figure 6.11: Summary of wake measurements for all flow cases. Set numbers refer to foil kinematic parameters defined in Table 2.1 (continued)

the strengths of the total shed vorticity $\tilde{\Gamma}_{total,c}$ is insensitive to variations in the foil heave and pitch amplitude when the heave dominance is not extremely large ($\chi = \frac{h_0}{c \cdot \tan \theta_0} \neq \infty$).

Figure 6.11b shows a summary of available non-dimensional centroidal wake widths, \tilde{A}_c for all experimental flow conditions. The data show reasonable consistency, particular for groups I to III. There is, however, a variation in \tilde{A}_c between groups I and III, where the wake width is generally larger when χ increases. When χ is small (group IV), the wake widths are noticeably small. Since a large wake width is theoretically desirable for thrust production (see Section 6.3), it appears that large non-dimensional heave amplitudes, relative to the pitch amplitude (i.e. large χ) should be employed by the unsteady foil for optimal propulsion.

At $St_h \approx 0.1 - 0.3 \approx St_{h,0}$, the wake widths approach zero, indicating that the wake patterns are within the “transitional” regime (see Chapter 5), whereby there is neither a velocity deficit, nor a velocity excess in the wake, and therefore the foil does not produce any nett thrust or drag across an entire flapping cycle, further reinforcing the findings of the flow visualisation experiments discussed in Chapter 5.

Figure 6.11c shows the non-dimensional first moment of circulation, \tilde{M}_Γ for all available flow conditions. As discussed in Section 6.3, \tilde{M}_Γ takes into account both the total strength and

the positions of the shed vorticity, and therefore \tilde{M}_Γ should be able to provide a reasonable qualitative measurement of the thrust generated by the unsteady foil; larger \tilde{M}_Γ should produce larger thrust coefficients. The results in Figure 6.11c clearly indicate that flow cases where χ is large tends to produce larger \tilde{M}_Γ values, with Group I producing the highest moment of circulation values of all foil dynamic parameters. It is also obvious from Figure 6.11c that group IV produces the lowest values of \tilde{M}_Γ , suggesting that the foil undergoing large pitch amplitudes produces very low thrust coefficients when compared to other foil dynamic groups.

Due to the fact that the variation in $\tilde{\Gamma}_{total,c}$ between groups is generally smaller than the variation in \tilde{A}_c (see Figure 6.11a), we conclude that the large and small \tilde{M}_Γ values at heave-dominated and pitch-dominated flow conditions respectively are mainly caused by the large variation in the measured wake widths between the groups. As previously noted, larger foil wake widths are associated with higher time-averaged thrust coefficients, and thus, based on the wake measurements, we would expect that the unsteady foil produces larger thrust coefficients when the non-dimensional heave amplitude, relative to the pitch amplitude, is large. The time-averaged force measurements of the unsteady foil, discussed in Chapter 4, have already confirmed this finding.

It is interesting to note that the relationship between the measured values of \tilde{M}_Γ and St_h show a similar non-linear trend to the relationship between C_t and St_h (see Figure 4.19), as previously discussed in Chapter 4. To determine the relationship between the thrust coefficient and the dynamics of the wake produced by the foil, C_t is plotted against \tilde{M}_Γ , as shown in Figure 6.12a. The collapse of data is excellent. It appears that C_t exhibits an approximate quadratic trend with \tilde{M}_Γ , as indicated by an order-2 curve fit of all the available experimental data, shown in Figure 6.12b. The resultant order-2 curve fit of the data can be expressed as

$$C_t \approx 0.0127 \tilde{M}_\Gamma^2 + 0.3369 \tilde{M}_\Gamma - 0.0831 \quad (6.18)$$

However, within the range of $-2 \lesssim \tilde{M}_\Gamma \lesssim 10$, C_t shows an approximately linear relationship with \tilde{M}_Γ . This linear relationship was also predicted in the Q-S-II wake simulations (see Section 6.3). A linear curve is fitted to the data in Figure 6.12 in the range of $-2 \lesssim \tilde{M}_\Gamma \lesssim 10$ such that it passes through the origin, resulting in the empirical relationship,

$$C_t \approx 0.4034 \tilde{M}_\Gamma \quad (6.19)$$

Equation 6.19 displays an excellent agreement to the results obtained using the Q-S-II simulations (see Figure 6.5), particularly at $\tilde{M}_\Gamma \lesssim 10$. Here, the constant of proportionality is within $\approx 0.2\%$ of the predicted value (that is, $k_{\Gamma, sim} \approx 0.4051$). At $\tilde{M}_\Gamma \gtrsim 10$, which mainly consists of

6.5 Experimental and numerical results

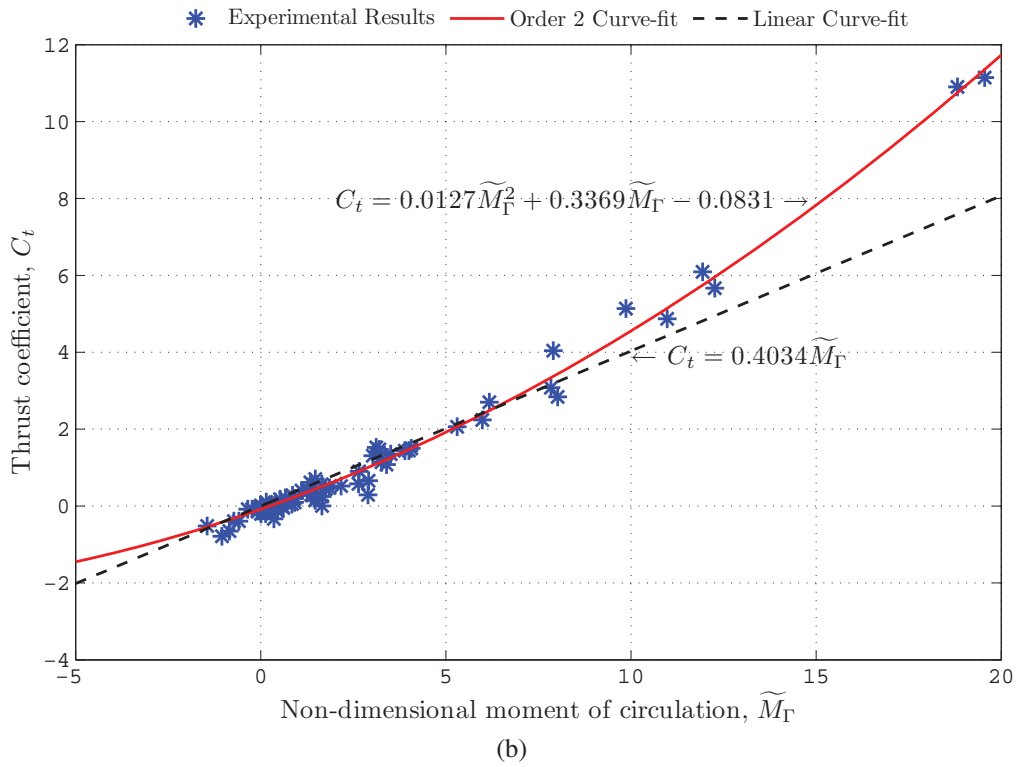
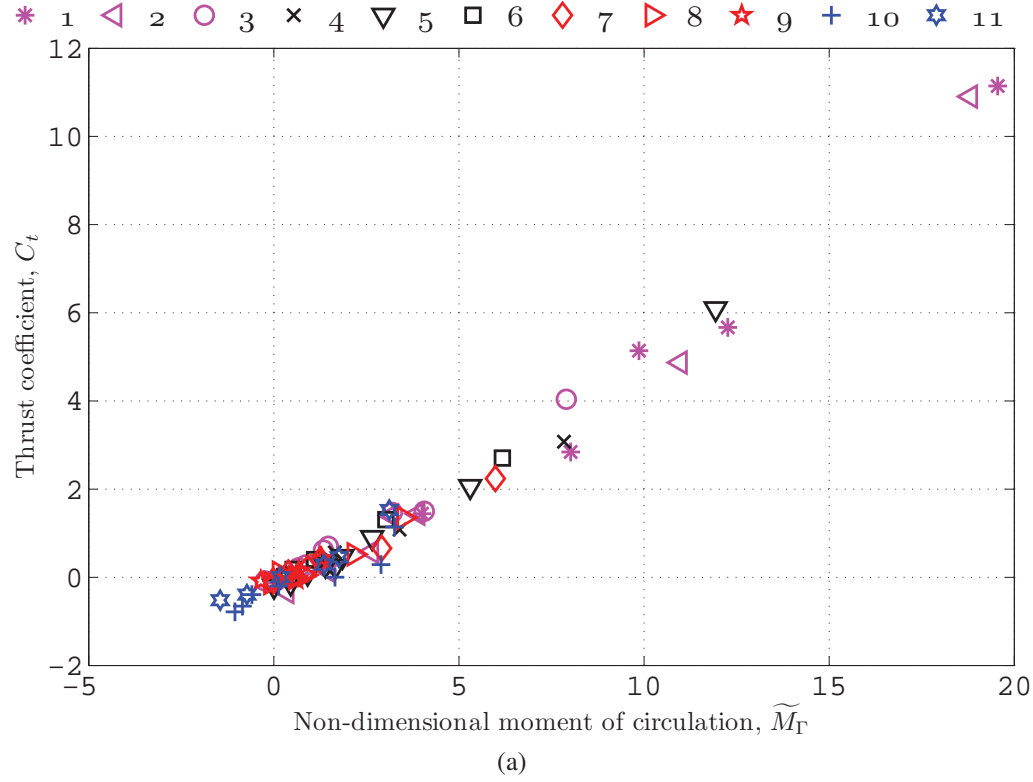


Figure 6.12: Relationship between the foil time-averaged thrust coefficient, C_t and the non-dimensional first moment of circulation, \widetilde{M}_Γ . Set numbers refer to foil kinematic parameters defined in Table 2.1

cases where St_h and χ are very large (see Figures 6.11c and 6.12a), the time-averaged thrust coefficients produced are slightly larger than predicted. These results therefore strongly indicate that:

1. The non-dimensional first moment of circulation \tilde{M}_Γ is an excellent indirect measurement of the time-averaged thrust coefficients on the foil, C_t . Therefore, the measurement of the wake dynamics (via PIV, for example), may be used as a substitute in cases where direct force measurements are impractical (on a live swimming fish, for example). This result can also be applied to any object, whether producing thrust or drag, and is therefore a general result;
2. For the great majority of flow conditions and foil dynamic parameters tested, there is an approximately linear relationship between C_t and \tilde{M}_Γ , which is consistent with results obtained using a quasi-steady (II) foil wake simulation. The experiments indicate that this relationship is of the form $C_t \approx 0.4034 \tilde{M}_\Gamma$. This implies that the foil can increase thrust production, in the time-averaged sense, by generating vortices with strong circulation while simultaneously controlling and shedding these vortices such that the wake widths are large;
3. Some cases produce slightly larger ($\approx 10 - 20\%$) time-averaged thrust coefficients than predicted with the Q-S-II wake simulations. These cases occur when the foil non-dimensional heave amplitude is larger than the pitch amplitude (χ is large), and the Strouhal number is large.

Although the results clearly indicate that C_t increases proportionally to \tilde{M}_Γ , they do not explicitly describe the flow mechanisms that link the generation of large thrust coefficients to the generation of large values of \tilde{M}_Γ . However, based on the results in this chapter, the flow visualisation results in Chapter 5, and the force measurements discussed in Chapter 4, it is proposed that the unsteady foil develops large time-averaged thrust coefficients by the generation of strong leading edge vortices. These leading edge vortices, most noticeably seen when χ is large (where the flow is heave-dominated) and the Strouhal number is high, have strong circulation, leading to large values of $\tilde{\Gamma}_{total,c}$. These leading edge vortices are also interpreted as lift-associated primary vortices, which are shed away from the time-averaged foil centreline location, which leads to larger centroidal wake widths, \tilde{A}_c . Simultaneously large $\tilde{\Gamma}_{total,c}$ and \tilde{A}_c then leads to large \tilde{M}_Γ , which has been shown both computationally, and experimentally, to lead to high time-averaged thrust coefficients.

6.6 Conclusions

The wake dynamics behind the heaving and pitching hydrofoil were investigated by measuring two quantitative parameters, the non-dimensional circulation of the total vorticity (of any given sign) shed by the foil into the wake during an entire flapping period, $\tilde{\Gamma}_{total,c}$ and the non-dimensional wake width based on the location of the centroid of the shed vorticity behind the foil, \tilde{A}_c . Initially, these measurements were intended to determine if the foil is capable of producing “optimal vortical structures”, however, this approach proved to have little merit.

Instead, we propose an alternative quantitative measurement of the wake dynamics - a single non-dimensional parameter $\tilde{M}_\Gamma = \tilde{\Gamma}_{total,c} \times \tilde{A}_c$, which is defined as the first moment of circulation of the wake behind the unsteady foil. Based on the quasi-steady concept, simulations of the effect of the time-averaged wake vorticity distribution on the time-averaged thrust coefficient were performed (dubbed the Q-S-II simulations). These simulations indicate that the thrust coefficient developed by the foil, C_t is approximately linearly dependent on \tilde{M}_Γ , regardless of the flow conditions, or the foil dynamic settings.

When the experimental results of C_t , obtained in Chapter 4, are plotted against the experimentally measured \tilde{M}_Γ , the data show excellent collapse. C_t portrays an approximately quadratic relationship with \tilde{M}_Γ , however, of particular interest is the fact that C_t within the range $-2 \lesssim \tilde{M}_\Gamma \lesssim 10$ (which includes $\approx 95\%$ of the available data) show an approximately linear trend with \tilde{M}_Γ , showing an excellent agreement to the results predicted by the Q-S-II simulations. The relationship between the time-averaged thrust coefficient produced by the foil, C_t , and the non-dimensional first moment of circulation of the wake produced by the foil, \tilde{M}_Γ , can then be expressed empirically as

$$C_t \approx 0.4034 \tilde{M}_\Gamma \quad (-2 \leq \tilde{M}_\Gamma \leq 10) \quad (6.20)$$

Equation 6.20 is shown to hold true for most flow conditions and foil dynamic parameters. This important finding implies that the thrust coefficient produced by the foil can be increased by directly increasing either the strength of the shed vorticity, such that $\tilde{\Gamma}_{total,c}$ increases (as long as $\tilde{A}_c > 0$), or by the positioning of shed vorticity to locations further away from the time-averaged foil centreline such that \tilde{A}_c increases, or both. Furthermore, in situations where direct force measurements are difficult (for example, force measurements on live swimming fish), equation 6.20 can potentially be used as an indirect measurement of the time-averaged force purely based on velocity measurements in the wake. However, it should be noted that the flow around the foil is inherently three-dimensional, and therefore equation 6.20 may not be valid for foil with different aspect ratios and/or different profiles from the one investigated here (NACA 0026, $AR = 4$). Furthermore, equation 6.20, as well as the results of the Q-S-II model, break

down when the heave amplitude is large. We propose that the reason for this break-down in the Q-S-II model at large heave amplitudes is due to the generation of leading edge vorticity of large circulation.

The experimentally measured $\tilde{\Gamma}_{total,c}$, \tilde{A}_c and \tilde{M}_Γ are also compared to the results predicted using the quasi-steady theory (see Chapter 3). The experimental and theoretical results show good agreement, particularly for groups II and III, which occur when the non-dimensional foil heave amplitude, relative to the pitch amplitude, is moderate (i.e., $\chi \approx 1 - 2$). When χ is small, the experimentally measured values of $\tilde{\Gamma}_{total,c}$ are higher while \tilde{A}_c is significantly lower than theoretically predicted. This implies that when the foil undergoes large pitch motion, relative to the heave motion, the foil generates larger than predicted secondary vorticity, which is detrimental to the production of thrust on the foil. However, when χ and St_h are simultaneously large, the experimentally measured values of $\tilde{\Gamma}_{total,c}$, \tilde{A}_c , and \tilde{M}_Γ are all significantly larger than the theoretically predicted values, implying that the foil generates large, strong primary vorticity when it undergoes large heave motions, relative to the pitch motions, at large Strouhal numbers. These results are consistent with the force measurements made in Chapter 4.

We therefore conclude, based on the force measurements made in Chapter 4, the flow visualisation experiments discussed in Chapter 5, and the wake measurements made in this chapter, that when the foil parameter χ and the Strouhal number St_h are simultaneously large, large values of C_t are produced due to the generation of strong primary vorticity, which is observed as a large leading edge vortex, and which simultaneously increases both $\tilde{\Gamma}_{total,c}$ and \tilde{A}_c leading to large values of \tilde{M}_Γ .

Chapter 7

Concluding Remarks

7.1 Discussion and summary

The main aim of this thesis was to investigate the flow around a fish-inspired heaving and pitching hydrofoil in a constant free-stream. In particular, the objectives of this investigation were to study the effect of the foil dynamics on the wake structure behind the foil, and on the hydrodynamic forces on the foil. A secondary objective of this thesis was to investigate whether a simple quasi-steady theoretical model of the unsteady foil would be able to predict the true hydrodynamic forces on the foil. A comparison between theoretical and experimental data may be able to provide evidence of whether fish employ unsteady flow control mechanisms during propulsion.

To achieve these goals, an extensive investigation of the flow around a harmonically pitching and heaving hydrofoil was performed, employing a combination of digital planar particle image velocimetry, strain gauge force & moment measurements, dye flow visualisation and hydrogen bubble visualisation. The details of these techniques are discussed in more detail in Chapter 2.

The experiments were performed by systematically varying the non-dimensional heave amplitude, $\frac{h_0}{c} = 0.25, 0.5, 0.75$, the pitch amplitude $\theta_0 = 0, 15, 30, 45^\circ$, and the free-stream velocity, $U_\infty = 10 - 250 \frac{\text{mm}}{\text{s}}$ resulting in Strouhal numbers of $0.1 \lesssim St \lesssim 1.7$. The phase between the heaving and pitching motion was fixed at $\Psi = 90^\circ$ (heaving lagging behind the pitching). Simultaneous PIV and force measurement experiments consisted of 106 different flow conditions, resulting in $Re = 1,250 - 12,500$. Dye visualisation was performed for 113 different flow conditions, at $Re = 900 - 3,500$, while hydrogen bubble visualisation was performed for 38 flow cases, at $Re = 500 - 3,500$.

Two parameters were defined to characterise the foil kinematics. Firstly, the foil heave dominance parameter $\chi = \frac{h_0}{c \tan(\theta_0)}$ is a convenient method to specify the ratio of the non-dimensional heave amplitude relative to the pitch amplitude. A second useful parameter, St_0 , is defined as the Strouhal number at which the foil neither produced nett thrust nor drag across an oscillating cycle. An approximation to the true value of St_0 can be obtained by assuming that this value occurs when $\alpha_{max} = 0$, whereby we obtain $St_{0,simp} = \frac{A_{te}}{2\pi c} \chi$. The values of χ and $St_{0,simp}$ for each foil heave and pitch amplitude are summarised in table 7.2.

In Chapter 3, a quasi-steady model (Q-S model) of the heaving and pitching hydrofoil was developed to provide the experimental results with a basis for comparison. The Q-S model is based on two main assumptions; a) that the instantaneous flow around an unsteady foil is equivalent to the flow around a similar static foil with the same angle of attack, i.e., the unsteady foil does not “remember” its history, and b) that the unsteady foil does not portray steady “stall” characteristics, even at large angles of attack. The results of the Q-S model are divided into two parts, namely, the foil dynamics, which includes force and efficiency predictions, and the wake dynamics, which includes predictions on the amount of vorticity shed by the foil into the wake, and the width of the foil wake.

Based on the Q-S model, the time-averaged thrust coefficient, C_t , appears to be approximately proportional to St_h^2 , and thus the thrust coefficients can be substantially large, $C_t > 10$, at high Strouhal numbers ($St_h \approx 1$). The thrust coefficient also appears to increase when the heave dominance parameter χ increases, however, when χ is large, both the productivities, η , and the propulsive efficiencies, η_F , are small. By definition, the thrust coefficients are zero at $St_h = St_{h,0}$, where $St_{h,0}$ is a function of $\frac{h_0}{c}$ and θ_0 . When χ is small, $St_{h,0}$ tends to be large, however, in general, the value of $St_{h,0}$ predicted using the Q-S model is approximately $St_{h,0,qs} \approx 0.1 - 0.3$ (summarised in table 7.2). Furthermore, at $St_h \approx St_{h,0}$, the propulsive efficiencies generally peak, decreasing slowly as St_h increases. The propulsive efficiency generally tends to increase as θ_0 increases (i.e., χ decreases), although it is estimated that the Q-S model overestimates the propulsive efficiencies at large θ_0 , due to the fact that the Q-S model neglects the moments produced by the pitching foil.

By design, the Q-S model assumes that the vorticity shed into the wake of the unsteady foil is generated using two independent mechanisms. Firstly, “primary” vorticity is generated and shed due to the transient change in the bound circulation around the unsteady foil, and is therefore associated with the production of thrust by the foil. “Secondary” vorticity, on the other hand, is shed due to the no-slip condition on the foil surface, and the fact that the Kutta condition is assumed to hold for any given flow condition. Secondary vorticity is then associated with the production of drag by the foil. The relationship between St_h and the normalised total circulation

7.1 Discussion and summary

shed by the foil (of any given sign) per foil period, $\tilde{\Gamma}_{total,c}$ (which is a combination of primary and secondary vorticity), indicates that secondary vorticity is dominant when $St_h \lesssim St_{h,0}$, while the primary vorticity is dominant when $St_h \gtrsim St_{h,0}$, indicating that the foil should produce thrust at $St_h \gtrsim St_{h,0}$. The fact that the foil is expected to produce thrust at $St_h \gtrsim St_{h,0}$ is also reflected by the fact that the non-dimensional wake width, based on the centroids of the shed vorticity, $\tilde{A}_c \gtrsim 0$ at $St_h \gtrsim St_{h,0}$. Following this, a single non-dimensional parameter $\tilde{M}_\Gamma = \tilde{\Gamma}_{total,c} \times \tilde{A}_c$ was defined, which takes into account both the value of strength of the total shed vorticity, $\tilde{\Gamma}_{total,c}$ and the locations of the shed vorticity, \tilde{A}_c . This term, dubbed the non-dimensional first moment of circulation, was found to be approximately linearly proportional to St_h .

Experimentally measured forces on the foil were evaluated using two different methods (as explained in Appendix B). Firstly, the time-averaged velocity field acquired using PIV was integrated (based on a conservation of momentum analysis) to obtain time-averaged thrust coefficients. Secondly, strain gauges were used to measure the instantaneous thrust, side force, and moments on the foil, which were also time-averaged to provide thrust & side force coefficients, and propulsive efficiencies. The time-averaged thrust coefficients, based on both PIV and strain gauges, show excellent agreement, and therefore suggests that the experimental force measurements are accurate.

In Chapter 4, the experimentally measured thrust coefficient, side force coefficient, and propulsive efficiency, are compared directly to the Q-S theoretical estimates. For most flow cases, the thrust and side force coefficients predicted using the Q-S model show an excellent agreement to the experimental results (as summarised in figure 7.1), indicating that the Q-S model is a highly competent theoretical model. However, there are two particular flow conditions where there is a deviation between the experimental and theoretical thrust measurements. Firstly, when the heave amplitude is small ($\frac{h_0}{c} = 0.25$) and the pitch amplitude is simultaneously large ($\theta_0 = 45^\circ$), the quasi-steady model over-estimates the thrust on the unsteady foil, which is due to the fact that the Q-S model fails to account for the pitching rotation of the unsteady foil. Secondly, when the unsteady foil undergoes purely heaving motion ($\theta_0 = 0^\circ$), the experimental results show that the thrust and side force coefficients are much larger, up to twice as large as Q-S estimates. This latter deviation is of particular interest due to the fact that the Q-S model should, theoretically, be more accurate at lower pitch amplitudes, therefore suggesting that the purely heaving foil uses unsteady flow mechanisms to generate large hydrodynamic forces.

Furthermore, the value of St_0 obtained experimentally, $St_{0,exp}$ was shown to be very close to that obtained using the Q-S model for all groups except group I, where there is a slight discrepancy (please refer to table 7.2).

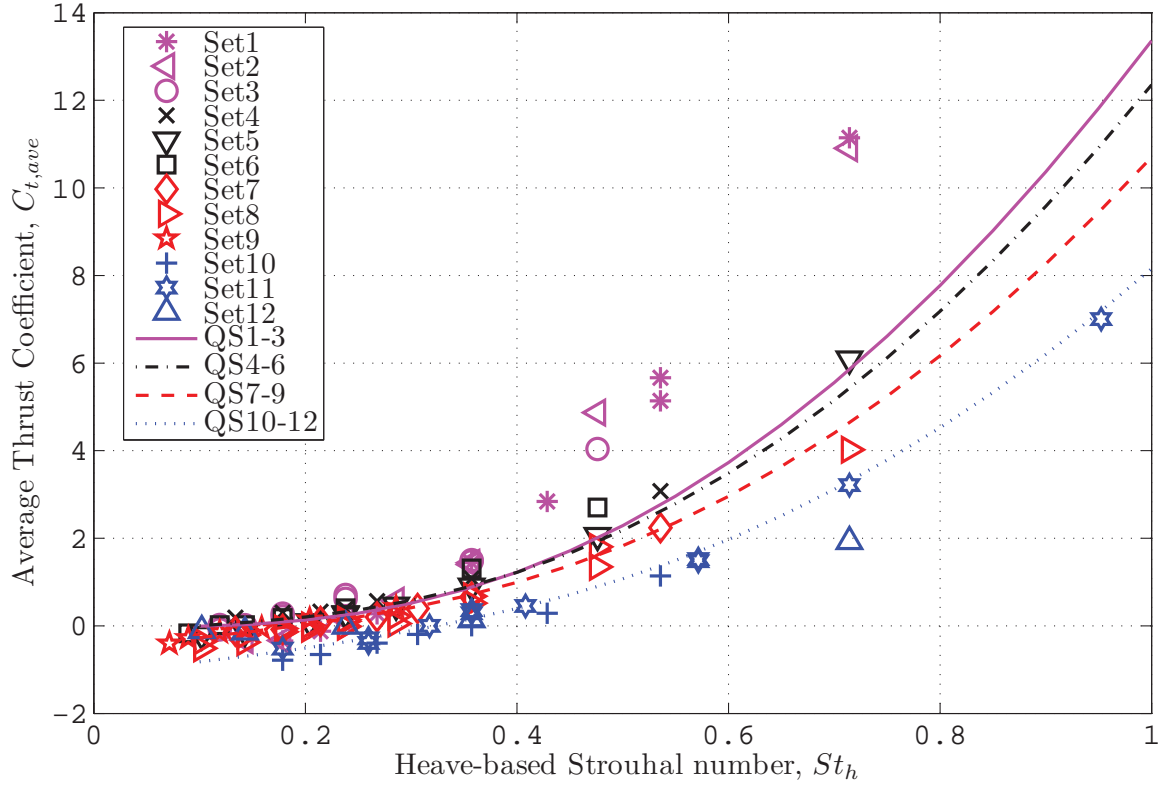


Figure 7.1: Summary of experimentally measured time-averaged foil thrust coefficients, $C_{t,ave}$ vs the heave-based Strouhal number, St_h . Set numbers refer to foil kinematic parameters defined in table 7.2

Of additional interest is the fact that the experimentally measured thrust coefficients do not show a sudden drop at large St_h , even when the angles of attack are very large, α_{max} . Since C_t is approximately proportional to St_h^2 , this leads to very large thrust coefficients at large Strouhal numbers; the maximum recorded thrust coefficient was $C_t \approx 12$, occurring at $St_h \approx 0.7$ where the angle of attack $\alpha_{max} \approx 60^\circ$.

Experimentally measured propulsive efficiencies, η_F , are generally lower than that predicted using the Q-S model, as expected. Propulsive efficiencies are particularly low when χ is very large (Group I), or very small (Group IV). At moderate $\chi \approx 1$ (Group III), propulsive efficiencies are the highest amongst all foil groups, and may reach values of $\eta_F \approx 60\%$. For all groups, the peak in η_F corresponds to $St_h \approx St_{h,0}$, where C_t and α_{max} are very low.

In Chapter 5, the wake of the foil was analysed using a combination of flow visualisation tools, including dye, hydrogen bubbles, and PIV. It was discovered that a number of qualitatively differing wake patterns were produced by the foil, depending on the flow conditions and foil kinematic parameters, in particular, the Strouhal number. These wake patterns are interpreted as a combination of two different vortical structures, namely “P” and “S” vortices. “P” vortices

7.1 Discussion and summary

consists mainly of primary vorticity, which may coalesce with neighbouring secondary vorticity to form one single vortical structure. “P” vortices are shed at a rate of once per foil half cycle, and typically the rotational directions of the “P” vortices imply a momentum surplus in the wake. “P” vortices, are therefore, associated with the production of time-averaged thrust by the foil. “P” vortices typically appear large and diffuse, and in three-dimensions, have moderate to strong axial flow through their cores towards the mid-span of the foil. This possibly indicates strong axial pressure gradients along the axes of the vortices and, by implication, low pressures in the cores at the mid-span of the foil. “S” vortices, on the other hand, consists purely of secondary vorticity, are typically small, compact structures which are shed multiple times per foil half cycle. In all cases, there was no observed spanwise flow through the cores of the “S” vortices towards the mid-span of the foil.

The flow visualisation also indicated that the “S” vortices are generated close to the trailing edge of the foil, while the “P” vortices are generated closer to the leading edge of the foil. In particular, when $\frac{h_0}{c}$ is large compared to θ_0 and St_h is large, the leading edge vortex is very large, and appears to be generated much closer to the leading edge of the foil than observed in any other foil kinematic group. Interestingly, this generation of large leading edge vortices occurs under the same flow conditions and foil kinematic parameters where large time-averaged thrust coefficients were experimentally measured. This correlation may be indicative of the capability of the oscillating foil to use unsteady flow mechanisms to generate large forces.

Depending on the number of “P” and “S” vortices shed per foil half cycle, and the relative positions of the “P” and “S” vortices, we can distinguish 6 qualitatively different wake patterns, summarised in figure 7.2. These wake patterns are organised into three distinct flow regimes, namely the “drag”, “transitional” and “thrust” regimes, based on the value of St relative to St_0 . When $St < St_0$, the flow is in the “drag” regime, whereby the wake mainly consists of “S” vortices, shed in a foil-relative regular Karman vortex street pattern. The rotational directions of these “S” vortices implies that there is a momentum deficit in the wake of the foil, and hence the foil should be producing nett drag across an entire oscillating cycle. When $St > St_0$, the wake of the foil is dominated by “P” vortices, which are shed in a reverse Karman street pattern. The resulting wake patterns imply that there is a momentum surplus in the wake, and hence the foil should producing time-averaged thrust within this flow regime. When $St \approx St_0$, the flow is making a transition between a “drag” and “thrust” wake, and the wake consists of both “P” and “S” vortices of comparable strength. The foil is expected to produce neither nett thrust nor drag.

Finally, in Chapter 6, the dynamics of the unsteady foil wake was quantitatively analysed using the PIV velocity and vorticity fields. The wake quantities $\tilde{\Gamma}_{total,c}$ and \tilde{A}_c were measured from

	Wake designation	Brief wake description
A	-	No distinct vortical structures observed. Wake consists of shear layer from the boundary of the foil.
B	LK-H	Shed “S” vortices form a “localised” regular Karman vortex street; Heave-dominated.
C	LK-R	Shed “S” vortices form a “localised” regular Karman vortex street; Pitch-dominated.
D	I-P	One “P” vortex is shed per half-cycle, shed in-line with the foil average centreline location.
E	P+S	A single “P” and “S” vortex pair, of approximately same strength, is shed per foil half-cycle.
F	P+XS	One “P” vortex, which forms a reverse Karman vortex street, and a number of significantly strong “S” vortices, are shed per foil half-cycle.
G	P+0S	One “P” vortex is shed per half-cycle, forming a reverse Karman vortex street.
H	P+Xs	One “P” and a number of small “S” vortices are shed per half-cycle. “P” vortices form a reverse Karman vortex street.

Table 7.1: Summary of observed wake patterns behind the unsteady foil. For a schematic representation of these wake patterns, refer to figure 7.2.

the PIV data, and the wake parameter \tilde{M}_Γ was derived from these measurements. These results, when compared to the results based on the quasi-steady model, show reasonable agreement for foil groups II and III. However, for group I, where χ is very large, the foil appears to generate larger than predicted values of $\tilde{\Gamma}_{total,c}$ and \tilde{A}_c , possibly indicating that the foil produces large amounts of beneficial primary vorticity, which is linked to the production of large thrust coefficients by the foil. When χ is small (group IV), $\tilde{\Gamma}_{total,c}$ is large while \tilde{A}_c is small, indicating that the foil produces large amounts of detrimental secondary vorticity, and thus it is expected that the unsteady foil produces thrust sub-optimally when θ_0 is large relative to $\frac{h_0}{c}$.

In an important finding, it was discovered that the experimentally measured value of \tilde{M}_Γ , for all available flow cases and foil kinematic parameters, collapsed onto a single curve when plotted against the heave-based Strouhal number (as shown in figure 7.3). This result indicates that,

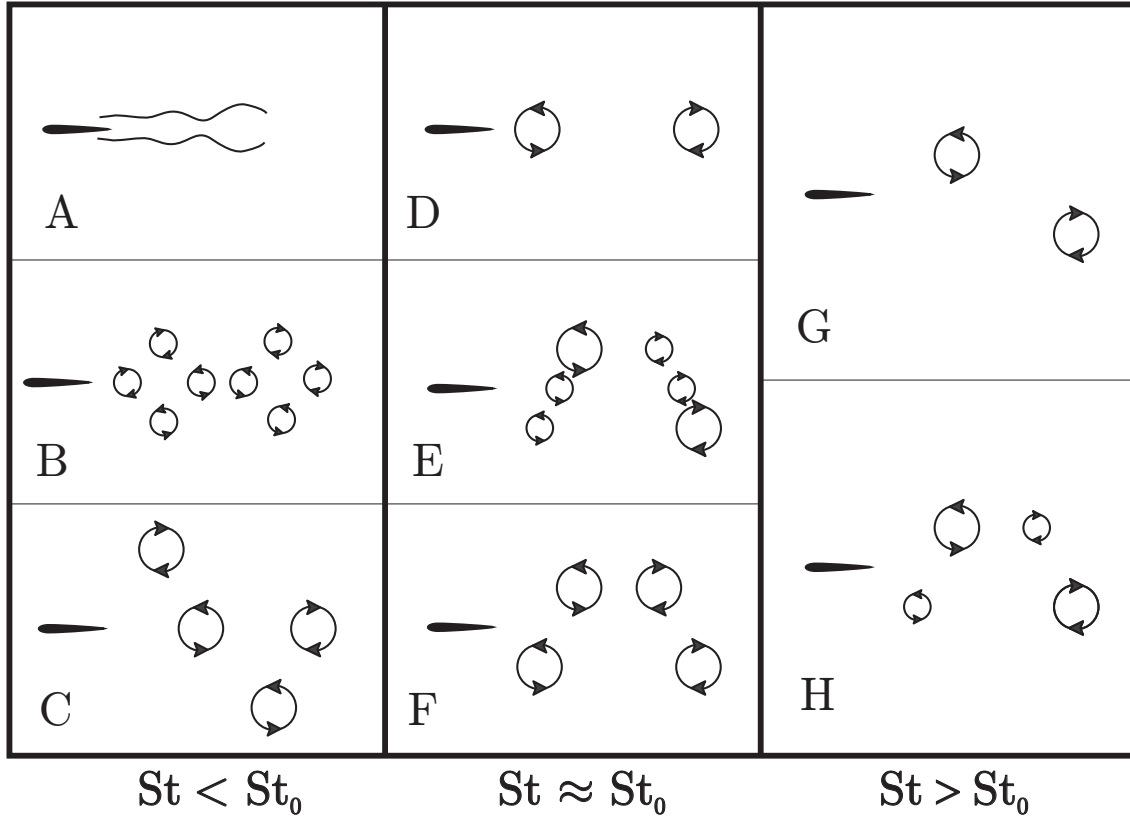


Figure 7.2: Schematic representation of possible wake profiles behind an unsteady foil

within the flow cases tested, the time-averaged thrust coefficient produced by the foil is only a function of \tilde{M}_Γ , and can be empirically approximated as

$$C_t \approx 0.0127 \tilde{M}_\Gamma^2 + 0.3369 \tilde{M}_\Gamma - 0.0831 \quad (7.1)$$

However, within the range of $-2 \lesssim \tilde{M}_\Gamma \lesssim 10$ (which encompasses $\approx 95\%$ of the available data), the relationship between C_t and \tilde{M}_Γ can be approximated by a linear curve fit of the form

$$C_t \approx 0.4034 \tilde{M}_\Gamma \quad (7.2)$$

Furthermore, equation 7.2 was also shown to be consistent with results obtained from simple simulations of the vorticity patterns behind the unsteady foil, based on the quasi-steady principle. The results from the wake simulations indicates that the relationship between C_t and \tilde{M}_Γ collapses onto an approximately linear curve, regardless of any other flow condition, supporting the idea that \tilde{M}_Γ is a useful wake parameter that may be used to characterise the capability of the foil to produce thrust.

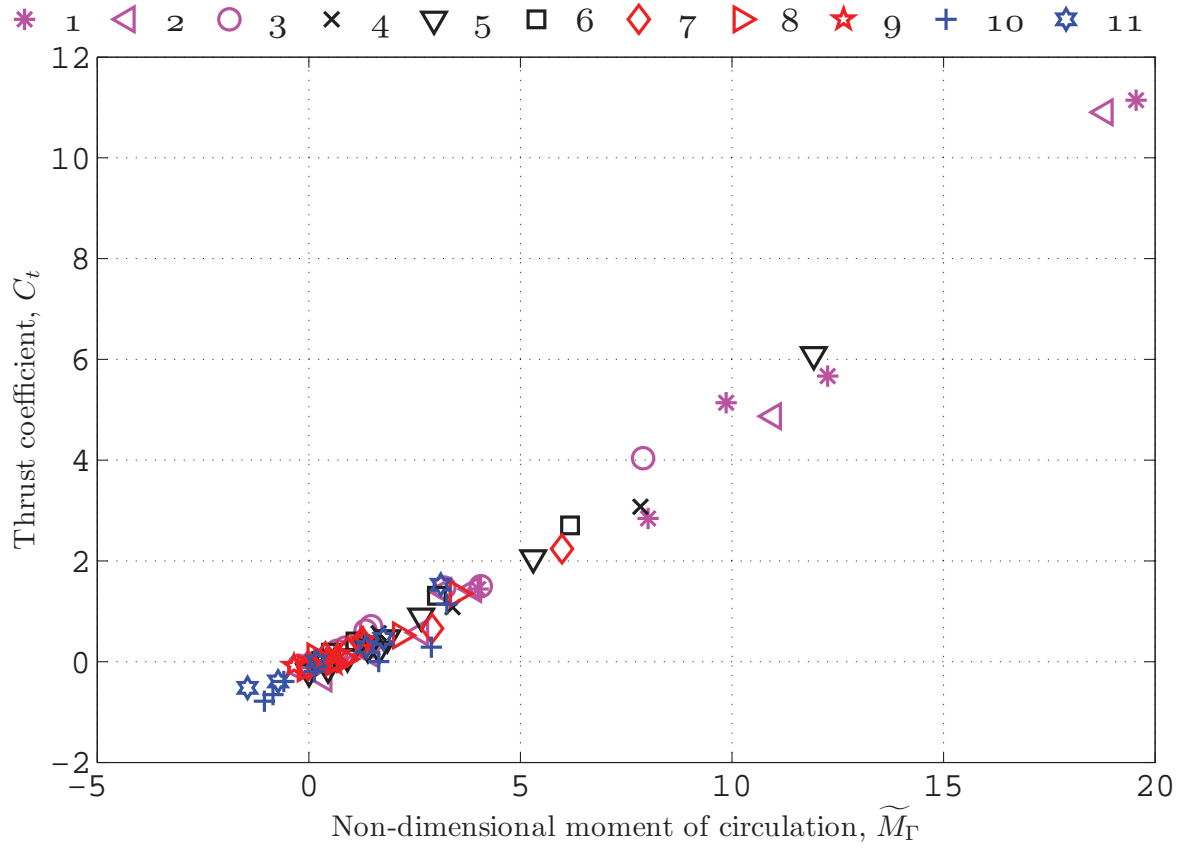


Figure 7.3: Summary of experimentally measured time-averaged foil thrust coefficients, $C_{t,ave}$ vs the non-dimensional moment of circulation, \widetilde{M}_Γ . Set numbers refer to foil kinematic parameters defined in table 7.2

Based on the discussion above, it is evident that the forces developed by the foil, and the wake dynamics, are a function of not only the Strouhal number, but also the foil heave and pitch amplitude. In particular, the foil and wake dynamics are functions of St (relative to St_0) and χ . Thus, the significant results of this thesis can be summarised as both a function of St , St_0 and χ , as shown in tables 7.2 to 7.4.

7.2 Implications of research findings

The major findings of this thesis, summarised in section 7.1, have a number of important implications, as described in the following paragraphs;

7.2 Implications of research findings

Group	Set	$\frac{h_0}{c}$	$\theta_0(^{\circ})$	χ	$St_{0,simp}$	$St_{0,q-s}$	$St_{0,exp}$	$\frac{St}{St_h}$
I	1	0.75	0	∞	0	0.11	≈ 0.21	1.00
	2	0.50	0	∞	0	0.11	≈ 0.20	1.00
	3	0.25	0	∞	0	0.11	≈ 0.14	1.00
II	4	0.75	15	2.80	0.09	0.10	≈ 0.12	1.03
	5	0.50	15	1.87	0.09	0.11	≈ 0.20	1.07
	6	0.25	15	0.93	0.11	0.13	≈ 0.18	1.25
III	7	0.75	30	1.30	0.21	0.22	≈ 0.23	1.13
	8	0.5	30	0.87	0.23	0.25	≈ 0.26	1.26
	9	0.25	30	0.43	0.33	0.35	≈ 0.32	1.78
IV	10	0.75	45	0.75	0.41	0.42	≈ 0.45	1.29
	11	0.50	45	0.50	0.49	0.50	≈ 0.50	1.52
	12	0.25	45	0.35	0.75	0.76	≈ 0.70	2.35

Table 7.2: Summary of foil kinematic parameters

1) Oscillating foil is capable of unsteady flow control

We have provided compelling evidence to show that the heaving and pitching hydrofoil is capable of unsteady flow control to generate large time-averaged thrust coefficients. This has been shown to occur when $\frac{h_0}{c}$ is large relative to θ_0 , and at large St_h , where α_{max} is also very large. Under these conditions, the thrust developed by the foil is much larger than that predicted using the Q-S theory, and flow visualisation has indicated that large vortical structures are generated close to the leading edge of the foil. These large leading-edge vortical structures have also been shown to have strong spanwise flow through their cores (towards the foil mid-span), possibly indicating that these vortical structures coincide with low-pressure flow regions. Additionally, when χ and St_h are simultaneously large, \tilde{M}_Γ is shown to be large, indicating that the wake width is large, and that the wake contains vortices with large circulation.

Therefore, we suggest that the foil can generate large thrust coefficients by “tripping” leading edge separation at large α_{max} . The leading edge separation coincides with a low pressure

	Typical observations
$St \lesssim St_0$	<ul style="list-style-type: none"> * “Drag” flow regime * Experimentally measured time-averaged thrust coefficients, $C_t < 0$ * “P” vortices are not observed * The shedding of “S” vortices are not locked-in to the oscillating motion of the foil * LK wake pattern
$St \approx St_0$	<ul style="list-style-type: none"> * “Transitional” flow regime * Angles of attack are low, $\alpha_{max} \approx 0$ * Experimentally measured time-averaged thrust coefficients are very low, $C_t \approx 0$ * For cases where C_t is slightly above zero, propulsive efficiencies, η_F are relatively high * Wake patterns are either the I-P, P+XS or the P+S * “P” vortices are relatively weak, and show little axial (spanwise) flow * For cases where “S” vortices are observed, the total strength of the “S” vortices are similar to the strength of the shed “P” vortices * The shedding of “S” vortices, when observed, is locked-in to the oscillation of the foil * Circulation of shed vorticity, $\tilde{\Gamma}_{total,c}$ is relatively low * The wake width is very low, $\tilde{A}_c \approx 0$
$St \gtrsim St_0$	<ul style="list-style-type: none"> * “Thrust” flow regime * $C_t \gtrsim 0$ * Wake consists of large, strong “P” vortices shed in a reverse Karman street pattern, which may (P+Xs) or may not (P+0S) be accompanied by weak “S” vortices * “P” vortices are observed to have very strong axial flow * Leading edge separation is observed, particularly when χ is large * Circulation of shed vorticity, $\tilde{\Gamma}_{total,c}$ is high * The wake width, \tilde{A}_c is large

Table 7.3: Summary of significant experimental observations as a function of St . For definitions of wake pattern abbreviations (LK-H, P+Xs, etc), refer to 7.1)

7.2 Implications of research findings

	Typical observations
Group I	<ul style="list-style-type: none"> * $\frac{h_0}{c}$ is large relative to θ_0, i.e. χ is large ($3 \lesssim \chi \lesssim \infty$) * The value of St_0 is low, $St_{0,exp} \approx 0.1 - 0.2$ * At large Strouhal numbers, the angles of attack are typically large (eg. $\alpha_{max} \approx 65^\circ$ at $St_h = 0.7$) * Experimentally measured time-averaged thrust coefficients can be very large, $C_t > 12$ * Q-S theory underestimates C_t, suggesting that the foil uses unsteady flow mechanisms to augment thrust when χ is large * Propulsive efficiencies are generally low, on order of $\eta_F \approx 20 - 30\%$ * Very large vortices, generated very close to the foil leading edge were observed * $\tilde{\Gamma}_{total,c}$ and \tilde{A}_c are both larger than predicted, suggesting that the foil is generating more primary vorticity than expected
Groups II and III	<ul style="list-style-type: none"> * $\frac{h_0}{c}$ is moderate relative to θ_0, resulting in intermediate values of χ ($0.75 \lesssim \chi \lesssim 3$) * The value of St_0 is moderate, $St_{0,exp} \approx 0.2 - 0.3$ * Maximum recorded thrust coefficient is moderately large, $C_t > 6$ * Q-S theory shows excellent agreement with experimental results, suggesting that the foil does not use unsteady flow mechanisms within this foil kinematic group * Recorded propulsive efficiencies are relatively high, particularly at $St \approx St_0$, where the efficiencies may reach $\eta_F \approx 60\%$
Group IV	<ul style="list-style-type: none"> * $\frac{h_0}{c}$ is small relative to θ_0, that is, χ is small ($0 \lesssim \chi \lesssim 0.75$) * The value of St_0 is large, $St_{0,exp} \approx 0.45 - 0.7$ * Maximum achievable thrust coefficients are typically small, on order of $C_t \approx 2 - 3$ * Q-S theory performs only fairly, and in particular, over-estimates both C_t and the propulsive efficiency, η_F, due to the fact that the Q-S theory neglects the effects of foil rotation * Maximum recorded propulsive efficiencies are generally low, on order of $\eta_F \approx 15 - 25\%$ * $\tilde{\Gamma}_{total,c}$ are relatively high, while the wake widths, \tilde{A}_c are relatively low, indicating that the foil generates more detrimental secondary vorticity than expected

Table 7.4: Summary of significant experimental observations as a function of foil kinematic parameters

region, which, due to its position upstream of the foil centreline, augments thrust production. Furthermore, these strong lift-producing vortical structures are controlled and shed by the foil at locations laterally distant from the foil mean centreline, resulting in a large wake width, which is desirable for thrust production.

The oscillating foil showcases a second form of unsteady flow control that is not observed in steady foils - the lack of static-stall. In all flow cases tested, even at very large angles of attack, $\alpha_{max} \gtrsim 60^\circ$ which are much larger than the experimentally measured static stall angle of $\alpha_{static-stall} \approx 7 - 8^\circ$, there was no observed sudden drop-off in the forces produced by the foil. This indicates that the concept of “stall”, usually used for foils in steady flow, is not necessarily applicable in unsteady foils. This may be due to the fact that static stall is an inherently transient mechanism, and thus requires a finite amount of time where the foil is static to cause a reduction in lift. The motion of the unsteady foil may be able to “bypass” the flow phase where there is a reduction in lift due to foil’s ability to continuously change its angle of attack.

2) Quasi-steady principle is applicable for most tested flow cases

Even though the oscillating foil has been shown to be capable of using unsteady flow mechanisms to generate large thrust coefficients, this has been shown to be only limited to a certain number of cases. In most other flow cases, in particular groups II and III, the experimental and the Q-S model results show excellent agreement. For group IV, the propulsive performance of the foil is below Q-S predictions, and hence it is unlikely that the oscillating foil employs unsteady flow mechanisms within this foil kinematic group. Therefore, other than the inhibition of static-stall, there is no evidence to suggest that the foil exploits unsteady flow mechanisms for optimal thrust production within all tested foil kinematic groups where $\chi \neq \infty$ (that is, groups II, III and IV). Since it has been reported that steadily swimming carangiform fish choose an approximate pitch amplitude of $\theta_0 \approx 15 - 30^\circ$, this has the added implication that steadily swimming fish do not necessarily use unsteady flow mechanisms during steady locomotion.

3) Two practical propulsion modes

The unsteady foil has been shown to be capable of producing large thrust coefficients, and producing thrust with moderately large propulsive efficiency. As a propulsor, these two characteristics are highly desirable. Unfortunately, however, the foil parameters which lead to high thrust production, and the production of thrust efficiently, are mutually exclusive, and thus we suggest two distinctive modes of propulsion:

7.2 Implications of research findings

- “Cruise” mode: During the “cruise” mode the foil produces very low thrust coefficients, $C_t \approx 0$. The thrust developed is just sufficient to balance the drag produced by the fore-body of, say, a fish or a underwater vehicle. The propulsive efficiencies are relatively high, on order of $\eta_F \approx 50 - 60\%$, which makes this mode ideal for continuous steady propulsion. Angles of attack are typically low, $\alpha_{max} \approx 0^\circ$. To achieve the cruise mode, the pitch amplitudes should be $\theta_0 \approx 15 - 30^\circ$ (i.e., groups II and III), while the Strouhal numbers should be relatively low, $St \approx St_0 \approx 0.2 - 0.3$.
- “Acceleration” mode: During the “acceleration” mode, the foil produces very large thrust coefficients ($C_t \gtrsim 12$ have been recorded). These high thrust coefficients are generated when the Strouhal numbers are very large, making it ideal for use when rapid accelerations are required, particularly when the free-stream velocities are low. However, the large thrust coefficients come at the expense of low propulsive efficiencies, $\eta_F \approx 20\%$. To achieve the “acceleration” mode, the Strouhal number and the ratio of the non-dimensional heave amplitude relative to the pitch amplitude has to be simultaneously large (for example, foil group I at large St_h).

The observations of swimming carangiform fish can then be explained within the context of these two propulsion modes. Steadily swimming carangiform fish have been reported to select flapping tail motion which results in pitch amplitudes of $\theta_0 \approx 20 - 30^\circ$ (Videler and Kamermans, 1985; Fish, 1998) and Strouhal numbers of $St \approx 0.2 - 0.3$ (Videler and Kamermans, 1985; Fish, 1998; Triantafyllou *et al.*, 1993; Rohr and Fish, 2004), as also discussed in Chapter 1. This strongly corresponds to the “cruise” mode. On the other hand, carangiform fish have also been observed to generate large tail motions during fast-start or rapid escape maneuvers (Triantafyllou *et al.*, 2000; Wolfgang *et al.*, 1999). These large tail motions can be interpreted as large heave amplitudes, consistent with the use of the “acceleration” propulsion mode. Carangiform fish have also been observed to choose a “burst and coast” swimming gait, whereby the fish swim by generating large thrust for only short periods of time. We suggest that these fish generate propulsion efficiently by exploiting the large thrust coefficients produced in the “acceleration” mode for short bursts of time.

4) Quantitative wake dynamics as an indirect measurement of C_t

The quantitative measurements of the wake dynamics show that there is a good collapse of data for all foil groups when the time-averaged thrust coefficient, C_t is plotted against the non-dimensional first moment of circulation, \tilde{M}_Γ . In the current experiment the empirical relationship is approximated with an order-2 curve fit of all available data, resulting in equation 7.1. It

is expected that this equation hold true only for the parameters tested, beyond the current experimental conditions there is insufficient evidence to make any further generalised conclusions. Nonetheless, the fact that the data of C_t versus \tilde{M}_Γ collapses suggests that an indirect measurement of the time-averaged thrust produced by an unsteady foil can be obtained by solely measuring the wake dynamics. This may be particularly useful in cases where direct force measurements are difficult or impractical (for example, in experiments of live swimming fish).

7.3 Conclusion

An extensive investigation of the flow around a heaving and pitching hydrofoil in a constant free-stream has indicated that the foil is capable of employing unsteady flow mechanisms to generate very large thrust coefficients. This occurs when the non-dimensional heave amplitude is large relative to the pitch amplitude, and when the Strouhal number is simultaneously large. We provide compelling evidence that these large thrust coefficients are generated due to the development of large leading edge vortical structures with strong circulation, which are subsequently controlled and shed by the foil at locations that are distant from the foil mean centreline, resulting in large foil wake widths.

The current study also indicates, for the majority of tested foil kinematic parameters and flow conditions that coincide with observed fish swimming dynamics (that is, Groups II and III), a quasi-steady model of the oscillating foil is sufficient to predict the dynamics of the unsteady foil. Following this, for most foil kinematic parameters (including the range $St \approx 0.2 - 0.3$), there is no evidence to suggest that the foil, and by implication, swimming fish, employ unsteady flow control to augment thrust production, or to generate optimal vortical structures in the wake.

7.4 Recommendations for future work

We have provided strong numerical and experimental evidence to show that when α_{max} is high, a heaving and pitching hydrofoil can produce very large thrust coefficients, where strong leading edge vortical structures are generated by the foil. However, at this stage, it remains unclear how these leading edge vortical structures augment thrust production by the foil. We have suggested that these leading edge structures correspond to regions of low pressure, however, without experimental pressure measurements, this remains unproven conjecture.

Thus, for future work, we propose an experiment where instantaneous surface pressure measurements are performed on the unsteady hydrofoil. These surface pressure measurements may

7.4 Recommendations for future work

be supplemented with simultaneous high resolution PIV near the boundary of the foil. The velocity field obtained with the PIV data can then provide information regarding the transient velocity flow field near the leading edge of the foil, which may be combined with the surface pressure measurements to further clarify the role of the leading edge vortex on the production of forces by the unsteady foil.

In our experiments, the motion of the foil is harmonic, and thus the transient variation of the instantaneous angle of attack, $\alpha(t)$ is also harmonic. Although we have shown that the unsteady foil can produce large thrust coefficients at large α_{max} , it remains unclear if this is due to the large average angles of attack that the foil is subjected to, or whether it is caused by large instantaneous values of α . An experiment where the angle of attack profile was varied such that it produces a low value of α for a large portion of the oscillating cycle, while generating large α for a short period of time may be useful in ascertaining whether a leading edge vortex may be “tripped” by a short instantaneous increase in α , and furthermore, whether this “tripped” leading edge vortex correlates with the generation of large thrust coefficients by the foil.

Bibliography

- Abbott, I. H. and von Doenhoff, A. E. (1959). *Theory of wing sections*. Dover Publications, New York.
- Adrian, R. J. (1991). Particle-imaging techniques for experimental fluid mechanics. *Annual Review of Fluid Mechanics*, **23**, 261 – 304.
- Akbari, M. H. and Price, S. J. (2003). Simulation of dynamic stall for a NACA 0012 airfoil using a vortex method. *Journal of Fluids and Structures*, **17**, 855 – 874.
- Aleyev, Y. G. (1977). *Nekton*. Junk, The Hague.
- Anderson, J. M. (1996). *Vorticity Control for Efficient Propulsion*. Ph.D. thesis, Massachusetts Institute of Technology and Woods Hole Oceanographic Institution.
- Anderson, J. M., Streitlien, K., Barrett, D. S., and Triantafyllou, M. S. (1998). Oscillating foils of high propulsive efficiency. *Journal of Fluid Mechanics*, **360**, 41 – 72.
- Bandyopadhyay, P. (2002). Maneuvering hydrodynamics of fish and small underwater vehicles. *Integrative and Comparative Biology*, **42**, 102 – 117.
- Barrett, D. S., Triantafyllou, M. S., Yue, D. K. P., Grosenbaugh, M. A., and Wolfgang, M. J. (1999). Drag reduction in fish-like locomotion. *Journal of Fluid Mechanics*, **392**, 183 – 212.
- Beal, D. N., Hover, F. S., Triantafyllou, M. S., Liao, J. C., and Lauder, G. V. (2006). Passive propulsion in vortex wakes. *Journal of Fluid Mechanics*, **549**, 385 – 402.
- Birch, J. M. and Dickinson, M. H. (2001). Spanwise flow and the attachment of the leading-edge vortex on insect wings. *Nature*, **412**, 729 – 733.
- Birch, J. M. and Dickinson, M. H. (2003). The influence of wing-wake interactions on the production of aerodynamic forces in flapping flight. *Journal of Experimental Biology*, **206**, 2257 – 2272.

Bibliography

- Blake, R. W. (1983a). *Fish locomotion*. Cambridge University Press.
- Blickhan, R. and Cheng, J.-Y. (1994). Energy storage by elastic mechanisms in the tail of large swimmers - a re-evaluation. *Journal of Theoretical Biology*, **168**, 315 – 321.
- Blondeaux, P., Fornarelli, F., Guglielmini, L., Triantafyllou, M. S., and Verzicco, R. (2005). Numerical experiments on flapping foils mimicking fish-like motion. *Physics of Fluids*, **17**(113601).
- Bose, N. and Lien, J. (1989). Propulsion of a fin whale (*balaenoptera physalus*): why the fin whale is a fast swimmer. *Proc. R. Soc. Lond. B*, **237**, 175 – 200.
- Breder, C. M. (1926). The locomotion of fishes. *Zoologica*, **4**, 159 – 256.
- Breuer, M. and Jovicic, N. (2001). An LES investigation of the separated flow past an airfoil at high angle of attack. In B. J. Geurts, R. Friedrich, and O. Metais, editors, *Direct and Large Eddy Simulation IV*, pages 165 – 172. Kluwer Academic Publishers, The Netherlands.
- Buchholz, J. H. J. and Smits, A. J. (2006). On the evolution of the wake structure produced by a low-aspect-ratio pitching panel. *Journal of Fluid Mechanics*, **546**, 433 – 443.
- Cheng, H. K. and Murillo, L. E. (1984). Lunate-tail swimming propulsion as a problem of curved lifting line in unsteady flow. Part 1. Asymptotic theory. *Journal of Fluid Mechanics*, **143**, 327 – 350.
- Chopra, M. G. (1974). Lunate-tail swimming propulsion. In T. Y. Wu, C. J. Brokaw, and C. Brennen, editors, *Swimming and flying in nature*, volume 2. Plenum Press, New York.
- Chopra, M. G. (1976). Large amplitude lunate-tail theory of fish locomotion. *Journal of Fluid Mechanics*, **74**, 161 – 182.
- Chopra, M. G. and Kambe, T. (1977). Hydromechanics of lunate-tail swimming propulsion. Part 2. *Journal of Fluid Mechanics*, **79**, 49 – 69.
- Clancy, L. J. (1975). *Aerodynamics*. John Wiley and Sons.
- Dabiri, J. O. (2005). On the estimation of swimming and flying forces from wake measurements. *The Journal of Experimental Biology*, **208**, 3519 – 3532.
- Dabiri, J. O. and Gharib, M. (2005). Starting flow through nozzles with temporally variable exit diameter. *Journal of Fluids Mechanics*, **538**, 111 – 136.

- Dabiri, J. O., Colin, S. P., and Costello, J. H. (2006). Fast-swimming hydromedusae exploit velar kinematics to form an optimal vortex wake. *Journal of Experimental Biology*, **209**, 2025 – 2033.
- Dickinson, M. H. (1994). The effects of wing rotation on unsteady aerodynamic performance at low Reynolds numbers. *Journal of Experimental Biology*, **192**, 179 – 206.
- Dickinson, M. H. (1996). Unsteady mechanisms of force generation in aquatic and aerial locomotion. *American Zoologist*, **36**, 537 – 554.
- Dickinson, M. H. and Gotz, K. G. (1993). Unsteady aerodynamic performance of model wings at low Reynolds numbers. *Journal of Experimental Biology*, **174**, 45 – 64.
- Dickinson, M. H., Lehmann, F.-O., and Sane, S. P. (1999). Wing rotation and the aerodynamic basis of insect flight. *Science*, **284**, 1954 – 1960.
- Dowis, H. J., Sepulveda, C. A., Graham, J. B., and Dickson, K. A. (2003). Swimming performance studies on the eastern pacific bonito sarda chiliensis, a close relative of the tunas (family scombridae). II. Kinematics. *Journal of Experimental Biology*, **206**, 2749 – 2758.
- Ellington, C. P. (1984b). The aerodynamics of hovering insect flight. *Phil. Trans. R. Soc. Lond.*, **305**(1122), 1 – 181.
- Ellington, C. P. (1995). Unsteady aerodynamics of insect flight. In C. P. Ellington and T. J. Pedley, editors, *Biological Fluid Dynamics*, pages 109 – 129. The Company of Biologists Ltd.
- Etebari, A. and Vlachos, P. P. (2005). Improvements on the accuracy of derivative estimation from DPIV velocity measurements. *Experiments in Fluids*, **39**, 1040 – 1050.
- Fish, F. E. (1993). Power output and propulsive efficiency of swimming bottlenose dolphins (*tursiops truncatus*). *Journal of Experimental Biology*, **185**, 179 – 193.
- Fish, F. E. (1998). Comparative kinematics and hydrodynamics of odontocete cetaceans: Morphological and ecological correlates with swimming performance. *Journal of Experimental Biology*, **201**, 2867 – 2877.
- Fish, F. E. and Lauder, G. V. (2006). Passive and active flow control by swimming fishes and mammals. *Annual Review of Fluid Mechanics*, **38**, 193 – 224.
- Fouras, A. and Soria, J. (1998). Accuracy of out-of-plane vorticity measurements derived from in-plane velocity field data. *Experiments in Fluids*, **25**, 409 – 430.

Bibliography

- Gharib, M., Rambod, E., and Shariff, K. (1998). A universal time scale for vortex ring formation. *Journal of Fluid Mechanics*, **360**, 121 – 140.
- Gopalkrishnan, R., Triantafyllou, M. S., Triantafyllou, G. S., and Barrett, D. (1994). Active vorticity control in a shear flow using a flapping foil. *Journal of Fluid Mechanics*, **274**, 1 – 21.
- Gray, J. (1936). Studies in animal locomotion VI. The propulsive powers of the dolphin. *Journal of Experimental Biology*, **13**, 192 – 199.
- Hart, D. P. (2000). PIV error correction. *Experiments in Fluids*, **29**, 13 – 22.
- Hassan, E. R. (2005). Personal communication.
- Hassan, E. R., Lau, T. C. W., and Kelso, R. M. (2007). Accuracy of circulation estimation schemes applied to discretised velocity field data. In *Proceedings of the Sixteenth Australasian Fluid Mechanics Conference*, Gold Coast.
- Hover, F. S., Haugsdal, O., and Triantafyllou, M. S. (2004). Effect of angle of attack profiles in flapping foil propulsion. *Journal of Fluids and Structures*, **19**, 37 – 47.
- Isshiki, H. and Murakami, M. (1984). A theory of wave devouring propulsion. *Society of Naval Architects of Japan*, **156**, 102 – 114.
- Jacobs, E. N. (1932). Airfoil section characteristics as affected by protuberances. NACA report no. 446, National Advisory Committee for Aeronautics, Virginia.
- Jeon, D. and Gharib, M. (2004). On the relationship between the vortex formation process and cylinder wake vortex patterns. *Journal of Fluid Mechanics*, **519**, 161 – 181.
- Jones, R. T. (1940). The unsteady lift of a wing of finite aspect ratio. Technical report no. 681, N. A. C. A.
- Kalt, P. (2005). Personal communication.
- Koochesfahani, M. (1989). Vortical patterns in the wake of an oscillating foil. *AIAA Journal*, **27**, 1200 – 1205.
- Kramer, M. O. (1960). The dolphin's secret. *The New Scientist*, **7**, 1118 – 1120.
- Lang, T. G. and Daybell, D. A. (1963). Porpoise performance tests in a sea-water tank. Technical report, Naval Ordnance test station, China Lake, CA.

- Lau, T. C. W., Hassan, E. R., and Kelso, R. M. (2004). Flow visualisation of a pitching and heaving hydrofoil. In M. Behnia, W. Lin, and G. D. McBain, editors, *Proceedings of the Fifteenth Australasian Fluid Mechanics Conference*, University of Sydney.
- Lighthill, J. (1975). *Mathematical Biofluidynamics*. Society for Industrial and Applied Mathematics, Pennsylvania.
- Lighthill, M. J. (1969). Hydromechanics of aquatic animal propulsion. *Annual Review of Fluid Mechanics*, pages 413 – 446.
- Lighthill, M. J. (1970). Aquatic animal propulsion of high hydromechanical efficiency. *Journal of Fluid Mechanics*, **44**, 265 – 301.
- Lighthill, M. J. (1971). Large-amplitude elongated-body theory of fish locomotion. *Proc. R. Soc. Lond. B*, **179**, 125 – 138.
- Linden, P. F. and Turner, J. S. (2001). The formation of "optimal" vortex rings and the efficiency of propulsive devices. *Journal of Fluid Mechanics*, **427**, 61 – 72.
- Linden, P. F. and Turner, J. S. (2004). "Optimal" vortex rings and aquatic propulsion mechanisms. *Proc. R. Soc. Lond. B*, **271**, 647 – 653.
- Liu, P. and Bose, N. (1993). Propulsive performance of three naturally occurring oscillating propeller planforms. *Ocean Engineering*, **20**, 57 – 75.
- Loftin Jr., L. K. and Smith, H. A. (1949). Aerodynamic characteristics of 15 NACA airfoil sections at seven Reynolds numbers from 0.7×10^6 to 9.0×10^6 . NACA technical report 1945, Washington.
- Lowe, C. G. (1996). Kinematics and critical swimming speed of juvenile scalloped hammerhead sharks. *Journal of Experimental Biology*, **199**, 2605 – 2610.
- Maxworthy, T. (1981). The fluid dynamics of insect flight. *Annual Review of Fluid Mechanics*, **13**, 329 – 350.
- McCroskey, W. J. (1982). Unsteady airfoils. *Annual Review of Fluid Mechanics*, **14**, 285 – 311.
- Melling, A. (1997). Tracer particles and seeding for particle image velocimetry. *Measurement Science and Technology*, **8**, 1406 – 1416.
- Milano, M. and Gharib, M. (2005). Uncovering the physics of flapping flat plates with artificial evolution. *Journal of Fluid Mechanics*, **534**, 403 – 409.

Bibliography

- Morton, B. R. (1984). The generation and decay of vorticity. *Geophys. Astrophys. Fluid Dynamics*, **28**, 277 – 308.
- Muller, U. K., van den Heuvel, B. L. E., Stamhuis, E. J., and Videler, J. J. (1997). Fish foot prints: Morphology and energetics of the wake behind a continuously swimming mullet (*chelon labrosus risso*). *Journal of Experimental Biology*, **200**, 2893 – 2906.
- Nakamura, Y. (1996). Vortex shedding from bluff bodies and a universal Strouhal number. *Journal of Fluids and Structures*, **10**, 159 – 171.
- Nauen, J. C. and Lauder, G. V. (2002). Quantification of the wake of rainbow trout (*oncorhynchus mykiss*) using three-dimensional stereoscopic digital particle image velocimetry. *Journal of Experimental Biology*, **205**, 3271 – 3279.
- Noca, F., Shields, D., and Jeon, D. (1999). A comparison of methods for evaluating time-dependent fluid dynamic forces on bodies, using only velocity fields and their derivatives. *Journal of Fluids and Structures*, **13**, 551 – 578.
- Ohmi, K., Coutanceau, M., Loc, T. P., and Dulieu, A. (1990). Vortex formation around an oscillating and translating airfoil at large incidences. *Journal of Fluid Mechanics*, **211**, 37 – 60.
- Ohmi, K., Coutanceau, M., Daube, O., and Loc, T. P. (1991). Further experiments on vortex formation around an oscillating and translating airfoil at large incidences. *Journal of Fluid Mechanics*, **225**, 607 – 630.
- Okamoto, M. and Azuma, A. (2005). Experimental study on aerodynamic characteristics of unsteady wings at low Reynolds number. *AIAA Journal*, **43**(12), 2526 – 2536.
- Perry, A. E. and Chong, M. S. (1987). A description of eddying motions and flow patterns using critical point concepts. *Annual Review of Fluid Mechanics*, **19**, 125 – 155.
- Prandtl, L. and Tietjens, O. G. (1934). *Applied hydro- and aeromechanics*. Dover Publications Inc., New York.
- Prasad, A. K. (2000). Particle image velocimetry. *Current Science*, **79**(1), 51 – 60.
- Pullin, D. I. and Wang, Z. J. (2004). Unsteady forces on an accelerating plate and application to hovering insect flight. *Journal of Fluid Mechanics*, **509**, 1 – 21.
- Raffel, M., Willert, C. E., and Kompenhans, J. (1998). *Particle image velocimetry : A practical guide*. Springer, Berlin.

- Rayner, J. M. V. (1995). Dynamics of the vortex wakes of flying and swimming vertebrates. In C. P. Ellington and T. J. Pedley, editors, *Biological Fluid Dynamics*, pages 131 – 155. The Company of Biologists Ltd.
- Read, D. A., Hover, F. S., and Triantafyllou, M. S. (2003). Forces on oscillating foils for propulsion and maneuvering. *Journal of Fluids and Structures*, **17**, 163 – 183.
- Rohr, J. J. and Fish, F. E. (2004). Strouhal number and optimization of swimming by odontocete cetaceans. *Journal of Experimental Biology*, **207**, 1633 – 1642.
- Saffman, P. G. (1992). *Vortex Dynamics*. Cambridge University Press, New York.
- Sane, S. P. (2003). The aerodynamics of insect flight. *Journal of Experimental Biology*, **206**, 4191 – 4208.
- Sane, S. P. and Dickinson, M. H. (2001). The control of flight force by a flapping wing : lift and drag production. *Journal of Experimental Biology*, **204**, 2607 – 2626.
- Sane, S. P. and Dickinson, M. H. (2002). The aerodynamic effects of wing rotation and a revised quasi-steady model of flapping flight. *Journal of Experimental Biology*, **205**, 1087 – 1096.
- Schouveiler, L., Hover, F. S., and Triantafyllou, M. S. (2005). Performance of flapping foil propulsion. *Journal of Fluids and Structures*, **20**, 949 – 959.
- Sfakiotakis, M., Lane, D. M., and Davies, J. B. C. (1999). Review of fish swimming modes for aquatic locomotion. *IEEE Journal of Oceanic Engineering*, **24**, 237 – 252.
- Sheldahl, R. E. and Klimas, P. C. (1981). Aerodynamic characteristics of seven symmetrical airfoil sections through 180-degree angle of attack for use in aerodynamic analysis of vertical axis wind turbines. Sand80-2114 energy report, Sandia National Laboratories, New Mexico.
- Smits, A. J. (2000). *A physical introduction to fluid mechanics*. John Wiley and Sons, Inc, New York.
- Smits, A. J. and Lim, T. T. (2000). *Flow visualization: Techniques and examples*. Imperial College Press, London.
- Spedding, G. R., Rayner, J. M. V., and Pennycuik, C. J. (1984). Momentum and energy in the wake of a pigeon. *Journal of Experimental Biology*, **111**, 81 – 102.
- Stamhuis, E. J., Videler, J. J., van Duren, L. A., and Muller, U. K. (2002). Applying digital particle image velocimetry to animal-generated flows : Traps, hurdles and cures in mapping

Bibliography

- steady and unsteady flows in Re regimes between 10^{-2} and 10^5 . *Experiments in Fluids*, **33**, 801 – 813.
- Streitlien, K., Triantafyllou, G. S., and Triantafyllou, M. S. (1996). Efficient foil propulsion through vortex control. *AIAA Journal*, **34**, 2315 – 2319.
- Tan, B. T., Thompson, M. C., and Hourigan, K. (2005). Evaluating fluid forces on bluff bodies using partial velocity data. *Journal of Fluids and Structures*, **20**, 5 – 24.
- Taylor, G. (1952). Analysis of the swimming of long and narrow animals. *Proc. R. Soc. Lond. A*, **214**, 158 – 183.
- Taylor, G. K., Nudds, R. L., and Thomas, A. L. R. (2003). Flying and swimming animals cruise at a Strouhal number tuned for high power efficiency. *Nature*, **425**, 707 – 711.
- Techet, A. H. (2001). *Experimental visualization of the near-boundary hydrodynamics about fish-like swimming bodies*. Ph.D. thesis, Massachusetts Institute of Technology and the Woods Hole Oceanographic Institution.
- Theodorsen, T. (1935). Theory of aerodynamic stability and the mechanism of flutter. Technical report no. 496, N. A. C. A.
- Tokumaru, P. T. and Dimotakis, P. E. (1991). Rotary oscillation control of a cylinder wake. *Journal of Fluid Mechanics*, **224**, 77 – 90.
- Triantafyllou, G. S., Triantafyllou, M. S., and Grosenbaugh, M. A. (1993). Optimal thrust development in oscillating foils with application to fish propulsion. *Journal of Fluids and Structures*, **7**, 205 – 224.
- Triantafyllou, M. S. and Triantafyllou, G. S. (1995). An efficient swimming machine. *Scientific American*, pages 40 – 48.
- Triantafyllou, M. S., Triantafyllou, G. S., and Yue, D. K. P. (2000). Hydrodynamics of fishlike swimming. *Annual review of fluid mechanics*, **32**, 33 – 53.
- Triantafyllou, M. S., Techet, A. H., Zhu, Q., Beal, D. N., Hover, F. S., and Yue, D. K. P. (2002). Vorticity control in fish-like propulsion and maneuvering. *Integrative and Comparative Biology*, **42**, 1026 – 1031.
- Triantafyllou, M. S., Techet, A. H., and Hover, F. S. (2004). Review of experimental work in biomimetic foils. *IEEE Journal of Oceanic Engineering*, **29**, 585 – 594.

- Tuncer, I. H. and Kaya, M. (2005). Optimization of flapping airfoils for maximum thrust and propulsive efficiency. *AIAA Journal*, **43**, 2329 – 2336.
- Usherwood, J. R. and Ellington, C. P. (2002a). The aerodynamics of revolving wings I. Model hawkmoth wings. *Journal of Experimental Biology*, **205**, 1547 – 1564.
- Usherwood, J. R. and Ellington, C. P. (2002b). The aerodynamics of revolving wings II. Propellor force coefficients from mayfly to quail. *Journal of Experimental Biology*, **205**, 1565 – 1576.
- Vallentine, H. R. (1967). *Applied Hydrodynamics*. Butterworths.
- Videler, J. and Kamermans, P. (1985). Differences between upstroke and downstroke in swimming dolphins. *Journal of Experimental Biology*, **119**, 265 – 274.
- Videler, J. J. (1993). *Fish Swimming*. Chapman and Hall, London.
- Videler, J. J., Muller, U. K., and Stamhuis, E. J. (1999). Aquatic vertebrate locomotion: Wakes from body waves. *Journal of Experimental Biology*, **202**, 3423 – 3430.
- Vogel, S. (1996). *Life in Moving Fluids*. Princeton University Press, 2nd edition.
- von Ellenrieder, K. D., Parker, K., and Soria, J. (2003). Flow structures behind a heaving and pitching finite-span wing. *Journal of Fluid Mechanics*, **490**, 129 – 138.
- Wang, Z. J. (2000). Vortex shedding and frequency selection in flapping flight. *Journal of Fluid Mechanics*.
- Wang, Z. J. (2005). Dissecting insect flight. *Annual Review of Fluid Mechanics*, **37**, 183 – 210.
- Webb, P. W. (1971). The swimming energetics of trout. I. Thrust and power output at cruising speeds. *Journal of Experimental Biology*, **55**, 489 – 520.
- Webb, P. W. (1973a). Effects of partial caudal-fin amputation on the kinematics and metabolic rate of underyearling sockeye salmon (*oncorhynchus nerka*) at steady swimming speeds. *Journal of Experimental Biology*, **59**, 565–582.
- Webb, P. W. (1984). Form and function in fish swimming. *Scientific American*, **251**(1), 72 – 82.
- Webb, P. W. (1988). "Steady" swimming kinematics of tiger musky, an esociform accelerator, and rainbow trout, a generalist cruiser. *Journal of Experimental Biology*, **138**, 51 – 69.

Bibliography

- Weis-Fogh, T. (1972). Energetics of hovering flight in hummingbirds and in drosophila. *Journal of Experimental Biology*, **56**, 79 – 104.
- Weis-Fogh, T. (1973). Quick estimates of flight fitness in hovering animals, including novel mechanisms for lift production. *Journal of Experimental Biology*, **59**, 169 – 230.
- Westerweel, J. and Scarano, F. (2005). Universal outlier detection for PIV data. *Experiments in Fluids*, **39**, 1096 – 1100.
- Williamson, C. H. K. and Roshko, A. (1988). Vortex formation in the wake of an oscillating cylinder. *Journal of Fluids and Structures*, **2**, 355 – 381.
- Wolfgang, M. J., Anderson, J. M., Grosenbaugh, M. A., Yue, D. K., and Triantafyllou, M. S. (1999). Near-body flow dynamics in swimming fish. *Journal of Experimental Biology*, **202**, 2303 – 2327.
- Wu, J. H. and Sun, M. (2004). Unsteady aerodynamic forces of a flapping wing. *Journal of Experimental Biology*, **207**, 1137 – 1150.
- Wu, T. Y. (2001). On theoretical modeling of aquatic and aerial animal locomotion. In E. van der Giessen, T. Y. Wu, and H. Aref, editors, *Advances in Applied Mathematics*, volume 38, pages 291 – 353. Academic Press.
- Wu, T. Y.-T. (1961). Swimming of a waving plate. *Journal of Fluid Mechanics*, **10**, 321 – 344.
- Yates, G. T. (1983). Hydromechanics of body and caudal fin propulsion. In P. W. Webb and D. Weihs, editors, *Fish Biomechanics*, chapter 6, pages 177–213. Praeger Publishers.
- Young, J. and Lai, J. C. S. (2004). Oscillation frequency and amplitude effects on the wake of a plunging airfoil. *AIAA Journal*, **42**(10), 2042 – 2052.
- Zhu, Q., Wolfgang, M. J., Yue, D. K. P., and Triantafyllou, M. S. (2002). Three-dimensional flow structures and vorticity control in fish-like swimming. *Journal of Fluid Mechanics*, **468**, 1–28.

Appendix A

Summary of foil parameters, flow conditions, and results

Group	Set	$\frac{h_0}{c}$	$\theta_0(^{\circ})$	χ	$St_{0,simp}$	$St_{0,q-s}$	$St_{0,exp}$	$\frac{St}{St_h}$
I	1	0.75	0	∞	0	0.11	≈ 0.21	1.00
	2	0.50	0	∞	0	0.11	≈ 0.20	1.00
	3	0.25	0	∞	0	0.11	≈ 0.14	1.00
II	4	0.75	15	2.80	0.09	0.10	≈ 0.12	1.03
	5	0.50	15	1.87	0.09	0.11	≈ 0.20	1.07
	6	0.25	15	0.93	0.11	0.13	≈ 0.18	1.25
III	7	0.75	30	1.30	0.21	0.22	≈ 0.23	1.13
	8	0.5	30	0.87	0.23	0.25	≈ 0.26	1.26
	9	0.25	30	0.43	0.33	0.35	≈ 0.32	1.78
IV	10	0.75	45	0.75	0.41	0.42	≈ 0.45	1.29
	11	0.50	45	0.50	0.49	0.50	≈ 0.50	1.52
	12	0.25	45	0.35	0.75	0.76	≈ 0.70	2.35

Table A.1: Summary of foil kinematic parameters

St	St_h	$\alpha_{max}(^\circ)$	$\alpha_{ave}(^\circ)$	Re	$C_{l,piv}$	$C_{l,sg}$	$C_{s,sg}$	η (%)	η_F (%)	$\tilde{\Gamma}_{total,c}$	\tilde{A}_c	\tilde{M}_Γ
0.18	0.18	29.3	19.2	9375	-0.41	-0.28	2.34	-11.8	-17.1	-	-	-
0.21	0.21	33.9	22.5	7812	-0.09	-0.15	2.89	-5.2	-6.3	5.71	0.01	0.05
0.27	0.27	40.1	27.0	6250	0.34	0.21	3.41	6.2	5.9	6.27	0.24	1.51
0.36	0.36	48.3	33.5	4687	1.50	1.38	5.12	27.1	19.5	7.94	0.50	4.00
0.43	0.43	53.4	37.8	7812	2.62	3.07	6.82	44.9	27.0	9.28	0.86	8.02
0.54	0.54	59.3	43.2	6250	5.86	5.47	10.65	51.3	24.7	13.27	0.92	12.26
0.54	0.54	59.3	43.2	3125	5.09	5.18	11.02	47.0	22.6	12.09	0.82	9.86
0.71	0.71	66.0	50.0	4687	11.87	10.41	20.21	51.5	18.6	17.90	1.09	19.55

Table A.2: Experimental results for set 1

St	St_h	$\alpha_{max}(^\circ)$	$\alpha_{ave}(^\circ)$	Re	$C_{t,piv}$	$C_{t,sg}$	$C_{s,sg}$	η (%)	η_F (%)	$\tilde{\Gamma}_{total,c}$	\tilde{A}_c	\tilde{M}_Γ
0.14	0.14	24.2	15.7	7812	-0.45	-0.21	1.17	-17.7	-32.0	-	-	-
0.18	0.18	29.3	19.2	6250	-0.52	-0.15	1.74	-8.6	-12.5	4.14	0.09	0.36
0.24	0.24	36.8	24.6	4687	0.07	0.22	2.71	8.2	8.9	4.56	0.32	1.47
0.29	0.29	41.9	28.4	7812	0.47	0.68	3.38	20.2	18.2	5.65	0.47	2.64
0.36	0.36	48.3	33.5	6250	1.40	1.48	5.22	28.4	20.5	6.30	0.62	3.89
0.36	0.36	48.3	33.5	3125	1.35	1.45	5.62	25.8	18.6	5.97	0.53	3.18
0.48	0.48	56.2	40.4	4687	4.95	4.80	10.88	44.1	23.9	11.79	0.93	10.98
0.71	0.71	66.0	50.0	3125	11.02	10.79	20.82	51.8	18.7	17.25	1.09	18.82

Table A.3: Experimental results for set 2

St	St_h	$\alpha_{max}(^{\circ})$	$\alpha_{ave}(^{\circ})$	Re	$C_{t,piv}$	$C_{t,sg}$	$C_{s,sg}$	η (%)	η_F (%)	$\tilde{\Gamma}_{total,c}$	\tilde{A}_c	\tilde{M}_{Γ}
0.12	0.12	20.5	13.2	9375	-0.11	-0.05	1.03	-5.0	-10.9	2.99	-0.08	-0.23
0.12	0.12	20.5	13.2	4687	0.11	-0.07	0.77	-9.2	-19.9	-	-	-
0.14	0.14	24.2	15.7	7812	0.03	-	1.31	0.1	0.2	3.17	0.13	0.41
0.18	0.18	29.3	19.2	3125	0.27	0.28	1.77	16.1	23.2	3.64	0.24	0.86
0.18	0.18	29.3	19.2	6250	0.23	0.20	1.92	10.4	15.0	3.47	0.19	0.67
0.24	0.24	36.8	24.6	2344	0.78	0.63	3.36	18.7	20.2	4.78	0.31	1.47
0.24	0.24	36.8	24.6	4687	0.68	0.55	3.56	15.4	16.7	4.47	0.30	1.34
0.36	0.36	48.3	33.5	1562	1.19	1.75	9.07	19.3	14.0	5.85	0.55	3.21
0.36	0.36	48.3	33.5	3125	1.31	1.69	8.69	19.5	14.1	6.12	0.66	4.06
0.48	0.48	56.2	40.4	2344	4.09	3.99	16.31	24.5	13.3	10.40	0.76	7.90

Table A.4: Experimental results for set 3

St	St_h	$\alpha_{max}(^\circ)$	$\alpha_{ave}(^\circ)$	Re	$C_{l,piv}$	$C_{l,sg}$	$C_{s,sg}$	η (%)	η_F (%)	$\tilde{\Gamma}_{total,c}$	\tilde{A}_c	\tilde{M}_Γ
0.14	0.13	7.8	5.2	12500	0.31	0.06	0.40	15.7	30.4	-	-	-
0.18	0.18	14.3	9.6	9375	0.39	0.21	1.09	19.0	29.5	-	-	-
0.22	0.21	18.9	12.9	7812	0.32	0.33	1.50	21.8	26.0	-	-	-
0.25	0.24	21.8	15.0	7031	0.35	0.43	1.64	26.1	27.1	4.40	0.29	1.28
0.28	0.27	25.1	17.4	12500	0.61	0.52	1.70	30.9	28.1	4.73	0.35	1.65
0.37	0.36	33.3	23.9	9375	1.13	1.04	2.94	35.2	24.0	6.32	0.54	3.40
0.55	0.54	44.3	33.6	6250	3.22	2.93	7.03	41.7	19.0	9.40	0.83	7.84

Table A.5: Experimental results for set 4

St	St_h	$\alpha_{max}(^\circ)$	$\alpha_{ave}(^\circ)$	Re	$C_{l,piv}$	$C_{l,sg}$	$C_{s,sg}$	η (%)	η_F (%)	$\tilde{\Gamma}_{total,c}$	\tilde{A}_c	\tilde{M}_Γ
0.11	0.10	2.8	1.8	10937	-0.31	-0.10	0.07	-132.4	-334.7	3.51	-	0.01
0.15	0.14	9.2	6.1	7812	-0.21	-0.05	0.55	-8.7	-15.7	3.36	0.14	0.46
0.22	0.20	17.7	12.0	10937	0.05	0.14	0.72	18.8	23.8	3.02	0.30	0.91
0.25	0.24	21.8	15.0	9375	0.16	0.39	1.06	37.0	40.1	3.48	0.40	1.40
0.25	0.24	21.8	15.0	4687	0.11	0.39	0.94	41.7	45.2	3.89	0.43	1.66
0.30	0.29	26.9	18.8	7812	0.37	0.57	1.51	38.0	34.3	3.68	0.50	1.85
0.38	0.36	33.3	23.9	6250	0.89	0.92	2.43	37.8	27.3	4.74	0.56	2.66
0.51	0.48	41.2	30.7	4687	2.01	2.11	5.08	41.5	22.5	7.01	0.76	5.30
0.76	0.71	51.0	40.4	3125	6.05	6.13	14.31	42.9	15.5	12.82	0.93	11.94

Table A.6: Experimental results for set 5

St	St_h	$\alpha_{max}(^{\circ})$	$\alpha_{ave}(^{\circ})$	Re	$C_{t,piv}$	$C_{t,sg}$	$C_{s,sg}$	η (%)	η_F (%)	$\tilde{\Gamma}_{total,c}$	\tilde{A}_c	\tilde{M}_{Γ}
0.11	0.09	0.7	0.4	6250	-0.25	-0.09	0.15	-60.2	-173.8	5.41	-	-
0.15	0.12	5.5	3.6	9375	-0.03	0.06	0.03	-	-	2.93	0.10	0.29
0.18	0.14	9.2	6.1	7812	-0.08	0.11	0.01	-	-	2.48	0.16	0.40
0.22	0.18	14.3	9.6	6250	0.16	0.20	0.45	44.3	64.1	2.58	0.20	0.52
0.30	0.24	21.8	15.0	4687	0.46	0.35	1.29	26.9	29.2	3.33	0.33	1.10
0.44	0.36	33.3	23.9	3125	1.17	1.44	4.16	34.7	25.1	5.12	0.59	3.03
0.59	0.48	41.2	30.7	2344	2.75	2.66	8.98	29.6	16.0	8.12	0.76	6.17

Table A.7: Experimental results for set 6

St	St_h	$\alpha_{max}(^\circ)$	$\alpha_{ave}(^\circ)$	Re	$C_{t,piv}$	$C_{t,sg}$	$C_{s,sg}$	η (%)	η_F (%)	$\tilde{\Gamma}_{total,c}$	\tilde{A}_c	\tilde{M}_Γ
0.15	0.13	-7.2	-4.9	12500	-0.11	-0.14	0.08	-165.8	-319.4	-	-	-
0.20	0.18	-0.7	-0.5	9375	-0.08	-0.08	0.16	-52.3	-75.6	5.48	-	-0.01
0.24	0.21	3.9	2.8	7812	0.12	0.08	0.28	29.1	35.1	4.12	0.10	0.39
0.30	0.27	10.1	7.3	12500	0.14	0.26	0.60	43.9	42.3	3.57	0.26	0.92
0.35	0.31	13.9	10.2	10937	0.37	0.42	0.88	48.1	40.5	4.19	0.30	1.26
0.40	0.36	18.3	13.8	9375	0.60	0.71	1.43	49.8	36.0	5.06	0.58	2.91
0.60	0.54	29.3	23.5	6250	2.06	2.42	3.93	61.5	29.6	7.75	0.77	5.99

Table A.8: Experimental results for set 7

St	St_h	$\alpha_{max}(^\circ)$	$\alpha_{ave}(^\circ)$	Re	$C_{t,piv}$	$C_{t,sg}$	$C_{s,sg}$	η (%)	η_F (%)	$\tilde{\Gamma}_{total,c}$	\tilde{A}_c	\tilde{M}_Γ
0.13	0.10	-12.2	-8.3	10937	-0.31	-0.39	0.51	-77.2	-195.2	-	-	-
0.13	0.10	-12.2	-8.3	10937	-0.62	-0.40	0.53	-75.3	-190.3	-	-	-
0.18	0.14	-5.8	-4.0	7812	-0.19	-0.24	0.21	-111.5	-201.4	-	-	-
0.18	0.14	-5.8	-4.0	7812	-0.54	-0.20	0.21	-98.3	-177.6	-	-	-
0.22	0.18	-0.7	-0.5	12500	-0.05	-0.23	0.44	-53.2	-76.9	-	-	-
0.22	0.18	-0.7	-0.5	6250	0.07	-0.20	0.20	-97.9	-141.5	-	-	-
0.22	0.18	-0.7	-0.5	6250	-0.21	-0.06	0.18	-33.6	-48.5	4.64	-0.02	-0.08
0.26	0.20	2.7	1.9	10937	-0.02	-0.11	0.46	-23.5	-29.7	-	-	-
0.26	0.20	2.7	1.9	10937	0.01	0.01	0.38	3.9	4.9	3.36	0.09	0.31
0.30	0.24	6.8	4.9	9375	0.02	-0.05	0.44	-12.5	-13.6	-	-	-
0.30	0.24	6.8	4.9	9375	-0.11	0.09	0.39	22.6	24.5	3.40	0.17	0.59
0.30	0.24	6.8	4.9	4687	0.11	0.17	0.46	36.7	39.8	-	-	-
0.30	0.24	6.8	4.9	4687	0.10	0.12	0.59	19.5	21.1	3.93	0.04	0.15
0.36	0.29	11.9	8.7	7812	0.27	0.17	0.39	42.8	38.7	-	-	-
0.36	0.29	11.9	8.7	7812	-0.09	0.20	0.81	24.2	21.8	3.01	0.28	0.84
0.45	0.36	18.3	13.8	6250	0.79	0.56	1.23	45.3	32.7	-	-	-
0.45	0.36	18.3	13.8	6250	0.50	0.54	1.34	40.4	29.2	4.08	0.53	2.17
0.60	0.48	26.2	20.7	4687	1.90	1.71	2.89	59.1	32.0	-	-	-
0.60	0.48	26.2	20.7	4687	1.48	1.22	2.67	45.6	24.7	5.97	0.59	3.51
0.90	0.71	36.2	30.3	3125	4.12	3.92	6.08	64.5	23.3	-	-	-

Table A.9: Experimental results for set 8

St	St_h	$\alpha_{max}(^\circ)$	$\alpha_{ave}(^\circ)$	Re	$C_{t,piv}$	$C_{t,sg}$	$C_{s,sg}$	η (%)	η_F (%)	$\tilde{\Gamma}_{total,c}$	\tilde{A}_c	\tilde{M}_Γ
0.13	0.07	-17.4	-11.6	7812	-0.48	-0.33	0.73	-44.9	-162.2	-	-	-
0.16	0.09	-14.3	-9.6	6250	-0.34	-0.23	0.56	-40.3	-116.4	-	-	-
0.21	0.12	-9.5	-6.5	9375	-0.24	-0.05	0.36	-13.0	-28.2	-	-	-
0.25	0.14	-5.8	-4.0	7812	-0.11	-0.05	0.30	-17.8	-32.1	5.51	-0.06	-0.35
0.28	0.16	-3.5	-2.4	7031	-0.11	0.01	0.37	4.0	6.6	5.07	0.12	0.61
0.36	0.20	2.7	1.9	5469	0.09	0.20	0.58	34.2	43.2	3.80	0.18	0.68
0.51	0.29	11.9	8.7	3906	0.33	0.52	1.40	37.1	33.5	5.21	0.25	1.29

Table A.10: Experimental results for set 9

St	St_h	$\alpha_{max}(^\circ)$	$\alpha_{ave}(^\circ)$	Re	$C_{t,piv}$	$C_{t,sg}$	$C_{s,sg}$	η (%)	η_F (%)	$\tilde{\Gamma}_{total,c}$	\tilde{A}_c	\tilde{M}_Γ
0.23	0.18	-15.7	-11.6	9375	-0.84	-0.73	1.06	-68.9	-99.6	4.03	-0.26	-1.05
0.28	0.21	-11.1	-8.3	7812	-0.67	-0.64	0.65	-98.8	-119.0	3.85	-0.22	-0.85
0.34	0.27	-4.9	-3.8	12500	-0.44	-0.35	0.36	-98.2	-94.5	4.21	-0.14	-0.59
0.39	0.31	-1.1	-0.9	10937	-0.22	-0.17	0.45	-37.0	-31.2	5.16	0.03	0.13
0.46	0.36	3.3	2.7	9375	-0.01	0.02	0.64	3.0	2.2	5.99	0.28	1.65
0.55	0.43	8.5	7.0	7812	0.31	0.27	1.21	22.1	13.3	6.96	0.42	2.90
0.69	0.54	14.7	12.4	6250	1.34	0.95	2.38	39.8	19.2	7.45	0.44	3.26

Table A.11: Experimental results for set 10

St	St_h	$\alpha_{max}(^{\circ})$	$\alpha_{ave}(^{\circ})$	Re	$C_{t,piv}$	$C_{t,sg}$	$C_{s,sg}$	η (%)	η_F (%)	$\tilde{\Gamma}_{total,c}$	\tilde{A}_c	\tilde{M}_{Γ}
0.27	0.18	-15.7	-11.6	12500	-0.63	-0.41	0.81	-50.9	-73.6	6.51	-0.22	-1.45
0.40	0.26	-5.8	-4.5	8594	-0.42	-0.15	0.45	-34.4	-34.2	-	-	-
0.40	0.26	-5.8	-4.5	8594	-0.43	-0.35	0.38	-93.3	-92.7	5.13	-0.14	-0.73
0.48	0.32	-0.1	-0.1	7031	0.03	-0.03	1.33	-2.4	-2.0	5.38	0.03	0.18
0.54	0.36	3.3	2.7	6250	0.43	0.30	1.78	16.6	12.0	-	-	-
0.54	0.36	3.3	2.7	6250	0.40	0.18	1.87	9.5	6.9	5.92	0.23	1.36
0.62	0.41	7.1	5.8	5469	0.50	0.40	2.27	17.8	11.2	6.43	0.27	1.76
0.87	0.57	16.5	13.9	3906	1.60	1.35	3.51	38.5	17.4	-	-	-
0.87	0.57	16.5	13.9	3906	1.31	1.74	4.12	42.3	19.1	8.96	0.35	3.12
1.09	0.71	22.5	19.2	3125	3.12	3.31	5.60	59.1	21.4	-	-	-
1.45	0.95	29.9	25.5	2344	6.92	7.09	7.54	94.0	25.5	-	-	-

Table A.12: Experimental results for set 11

St	St_h	$\alpha_{max}(^\circ)$	$\alpha_{ave}(^\circ)$	Re	$C_{l,piv}$	$C_{l,sg}$	$C_{s,sg}$	η (%)	η_F (%)	$\tilde{\Gamma}_{total,c}$	\tilde{A}_c	\tilde{M}_Γ
0.24	0.10	-27.2	-19.4	10937	-0.11	-0.10	0.84	-11.9	-30.0	-	-	-
0.34	0.14	-20.8	-15.1	7812	-0.21	-0.07	0.80	-8.4	-15.1	-	-	-
0.56	0.24	-8.2	-6.3	4687	0.03	-0.04	0.41	-9.9	-10.8	-	-	-
0.84	0.36	3.3	2.7	3125	0.08	0.21	0.40	51.1	36.9	-	-	-
1.68	0.71	22.5	19.2	1562	1.88	1.97	2.09	94.5	34.1	-	-	-

Table A.13: Experimental results for set 12

Appendix B

Experimental Measurement of Forces

B.1 Introduction

Here we document the two methods of computing the hydrodynamic forces on a fully submerged flapping foil used in this current study. In the first method, a momentum balance around the two-dimensional velocity fields measured using PIV is performed to estimate the time-averaged sectional thrust coefficients developed by the foil. In the second method, we simply use the direct strain gauge force measurements to obtain time-averaged values of the thrust coefficient, side force coefficient, and the propulsive efficiency of the unsteady foil.

B.2 Method I : Force estimates derived from 2D velocity fields

B.2.1 Linear momentum balance

The most straightforward method for estimating the time-averaged forces on the hydrofoil is to use the linear momentum balance equations around a control volume which encompasses the hydrofoil (as shown in figure B.1).

Here, it is assumed that the velocity components $V_1(\vec{y})$, $V_2(\vec{y})$, $V_3(\vec{x})$, $V_4(\vec{x})$ are all independent of z (positive z is into of the page). The hydrofoil is assumed to be in a fixed position relative to the control volume, and since the linear momentum balance equations are only valid for a non-accelerating control volume, this analysis is only applicable for the time-averaged PIV

B.2 Method I : Force estimates derived from 2D velocity fields

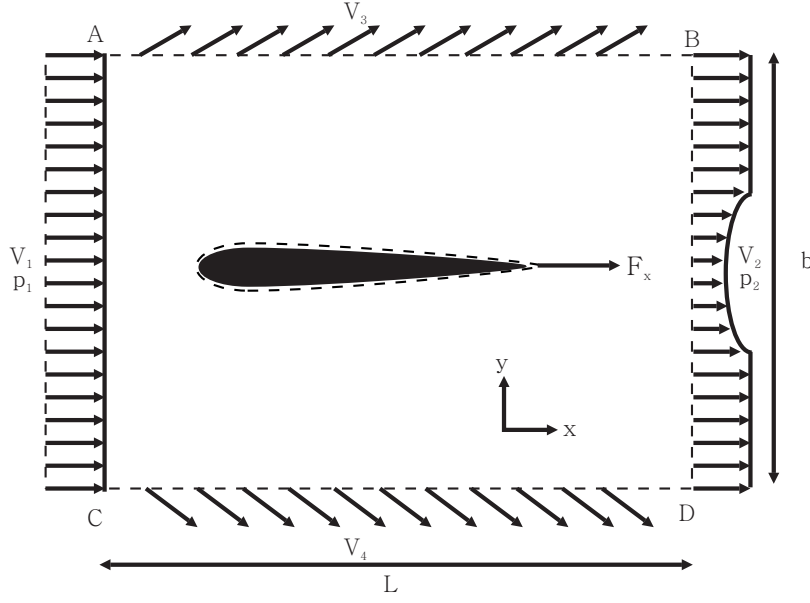


Figure B.1: Control volume around a hydrofoil

data. Therefore the result of the analysis is the estimation of the time-averaged force on the hydrofoil.

B.2.1.1 Mass balance

The mass flux term is $\dot{m} = \hat{n} \cdot \rho \vec{V} dA$, where $\vec{V} = (V_x, V_y, V_z)$ and $\hat{n} = (\hat{i}, \hat{j}, \hat{k})$ is taken as positive pointing away from the control volume. A mass balance on the control volume ABCD in figure B.1 provides:

$$\dot{m}_{CA} = -\rho w \int \vec{V}_1(y) \cdot \hat{i} dy \quad (\text{B.1})$$

$$\dot{m}_{BD} = \rho w \int \vec{V}_2(y) \cdot \hat{i} dy \quad (\text{B.2})$$

$$\dot{m}_{AB} = \rho w \int \vec{V}_3(x) \cdot \hat{j} dx \quad (\text{B.3})$$

$$\dot{m}_{DC} = -\rho w \int \vec{V}_4(x) \cdot \hat{j} dx \quad (\text{B.4})$$

where w is the depth (into the page) of the control volume.

The four mass flux terms above can be determined from the PIV data as all in-plane velocity components can be determined from the PIV velocity field. However, the flow around the foil is 3-dimensional in space, and therefore there will be mass and momentum transport out-of-plane, usually via vortex cores. This out-of-plane component cannot be measured directly using the

current PIV setup. However, if we denote the out-of-plane mass flux components as \dot{m}_{ABDC+} and \dot{m}_{ABDC-} , we can then use continuity along the entire control volume to show:

$$\dot{m}_{CA} + \dot{m}_{BD} + \dot{m}_{AB} + \dot{m}_{DC} + \dot{m}_{ABDC+} + \dot{m}_{ABDC-} = 0 \quad (\text{B.5})$$

where

$$\dot{m}_{ABDC+} = \rho \iint \vec{V}_5(x, y) \cdot \hat{k} dx dy \quad (\text{B.6})$$

$$\dot{m}_{ABDC-} = \rho \iint \vec{V}_6(x, y) \cdot \hat{k} dx dy \quad (\text{B.7})$$

where \vec{V}_5 and \vec{V}_6 are the positive (into page) and negative (out of page) out-of-plane velocity vectors, respectively.

Combining equations B.1 - B.5,

$$(\dot{m}_{ABDC+} + \dot{m}_{ABDC-}) = -\rho w \left[\int [\vec{V}_2(y) - \vec{V}_1(y)] \cdot \hat{i} dy + \int [\vec{V}_3(x) - \vec{V}_4(x)] \cdot \hat{j} dx \right] \quad (\text{B.8})$$

Equation B.8 can be used to estimate the magnitude of the mass flux of the out-of-plane component relative to the in-plane components determined from equations B.1 to B.4. It is expected that $(\dot{m}_{ABDC+} + \dot{m}_{ABDC-})$ component will be small relative to the in-plane components, as the PIV measurements are taken at the mid-span of the foil.

B.2.1.2 Momentum balance

Neglecting gravity, we can determine the force $\vec{F} = (F_x, F_y, F_z)$ on the body using the momentum equation in integral form, for a non-deforming, non-accelerating control volume (Smits, 2000):

$$\vec{F} = \int \hat{n} p dA + \frac{\partial}{\partial t} \int \rho \vec{V} dV + \int (\hat{n} \cdot \rho \vec{V}) \vec{V} dA \quad (\text{B.9})$$

At this stage, we will have to make a few simplifying assumptions. Firstly, we assume that the control volume is sufficiently large such that the streamlines representing \vec{V}_1 and \vec{V}_2 are nearly parallel, and hence $p_1 \approx p_2$ and that there is no variation in pressure along the y-axis. Secondly, we will assume that the time-averaged flow around the foil is steady, and therefore the $\frac{\partial}{\partial t}$ term is zero. Using these assumptions, equation B.9 reduces to

$$F_x = \int_{cv} (\hat{n} \cdot \rho \vec{V}) \hat{i} \cdot \vec{V} dA \quad (\text{B.10})$$

B.2 Method I : Force estimates derived from 2D velocity fields

It can be seen that the right hand term of equation B.10 is simply the momentum flux out of the control volume. The momentum fluxes at each section of the control volume ABCD is :

$$\dot{M}_{CA} = -\rho w \int \vec{V}_1^2(y) \cdot \hat{i} dy \quad (\text{B.11})$$

$$\dot{M}_{BD} = \rho w \int \vec{V}_2^2(y) \cdot \hat{i} dy \quad (\text{B.12})$$

$$\dot{M}_{AB} = \rho w \int (\vec{V}_3(x) \cdot \hat{j}) \cdot (\vec{V}_3(x) \cdot \hat{i}) dx \quad (\text{B.13})$$

$$\dot{M}_{DC} = -\rho w \int (\vec{V}_4(x) \cdot \hat{j}) \cdot (\vec{V}_4(x) \cdot \hat{i}) dx \quad (\text{B.14})$$

At this stage we still have not considered the momentum flux out of the sides of the control volume (the out-of-plane components), \dot{M}_{ABDC+} and \dot{M}_{ABDC-} . This is because there is no method to fully determine \dot{M}_{ABDC+} and \dot{M}_{ABDC-} with any degree of certainty based on a two dimensional velocity field. The fact that the out-of-plane momentum flux components are indeterminate from 2-D velocity data is clear if we write the out-of-plane terms fully:

$$\dot{M}_{ABDC+} = \rho \int \int (V_5(x,y) \cdot \hat{k}) \cdot (V_5(x,y) \cdot \hat{i}) dx dy \quad (\text{B.15})$$

$$\dot{M}_{ABDC-} = -\rho \int \int (V_6(x,y) \cdot \hat{k}) \cdot (V_6(x,y) \cdot \hat{i}) dx dy \quad (\text{B.16})$$

Although $\vec{V}_5 \cdot \hat{i}$ and $\vec{V}_6 \cdot \hat{i}$ can be determined from the PIV data, the z-components $\vec{V}_5 \cdot \hat{k}$ and $\vec{V}_6 \cdot \hat{k}$ are unknown.

To proceed, we will have to make a few simplifying assumptions. Firstly, we shall assume that the out-of-plane velocity vectors, \vec{V}_5 and \vec{V}_6 are equal but opposite, and equivalently $\vec{V}_5 \cdot \hat{k} = -\vec{V}_6 \cdot \hat{k}$ and $\vec{V}_5 \cdot \hat{i} = \vec{V}_6 \cdot \hat{i}$. This is justified as the velocity field is taken at the mid-span of the foil, that is, the plane of symmetry. Secondly, we assume that there is a representative velocity component in the x-direction, V_r , such that equations B.15 and B.16 can be written as

$$\dot{M}_{ABDC+} = \rho V_s \int \int \vec{V}_5(x,y) \cdot \hat{k} dx dy \quad (\text{B.17})$$

$$\dot{M}_{ABDC-} = -\rho V_s \int \int \vec{V}_6(x,y) \cdot \hat{k} dx dy \quad (\text{B.18})$$

If so, using equations B.6, B.7, B.8, B.17 and B.18, and using the assumptions given above, we obtain

$$\dot{M}_{ABDC+} + \dot{M}_{ABDC-} = -\rho w V_r \left[\int [\vec{V}_2(y) \cdot \hat{i} - \vec{V}_1(y) \cdot \hat{i}] dy + \int [\vec{V}_3(x) \cdot \hat{j} - \vec{V}_4(x) \cdot \hat{j}] dx \right] \quad (\text{B.19})$$

Since the x-component of force developed by the control volume can be equated to the momentum flux out of the control volume, then we can write equation B.10 as

$$F_x = \dot{M}_{AC} + \dot{M}_{BD} + \dot{M}_{AB} + \dot{M}_{CD} + \dot{M}_{ABCD+} + \dot{M}_{ABCD-} \quad (\text{B.20})$$

Combining equations B.11 ,B.14 and B.19 and setting the limits of integration (which so far has been omitted for brevity) we finally obtain the " V_r equation",

$$F_x = \rho w \left[\int_{-b/2}^{b/2} [\vec{V}_2^2(y) \cdot \hat{i} - \vec{V}_1^2(y) \cdot \hat{i}] dy + \int_{-L/2}^{L/2} [\vec{V}_3(x) \cdot \hat{j} \cdot \vec{V}_3(x) \cdot \hat{i} - \vec{V}_4(x) \cdot \hat{j} \cdot \vec{V}_4(x) \cdot \hat{i}] dx \right. \\ \left. - V_r \left[\int_{-b/2}^{b/2} [\vec{V}_2(y) \cdot \hat{i} - \vec{V}_1(y) \cdot \hat{i}] dy + \int_{-L/2}^{L/2} [\vec{V}_3(x) \cdot \hat{j} - \vec{V}_4(x) \cdot \hat{j}] dx \right] \right] \quad (\text{B.21})$$

B.2.1.3 Estimation of the V_r term

Although at first glance it may seem that equation B.21 provides an exact measure of the x-component of the force on the body given its 2-D velocity field, this is not actually the case. The weakness in the above analysis is in the V_r term, which cannot be determined directly. At every point in the velocity field, the V_r term can be thought of as the x-component of the velocity of a packet of fluid as it leaves the plane ABCD of the control volume. Globally, V_r can therefore be approximated by the average of all the x-component of velocities where packets of fluid leave the plane ABCD.

If we assume that there are no packets of fluid within the control volume that leave the control volume via the planes ABDC+ and ABDC-, then we can set $V_r = 0$, and we expect the calculated value of force to overestimate the true value of the sectional force. If we assume that all the packets of fluid leave the control volume at the free stream velocity, then we can set $V_r = U_\infty$, and we expect to underestimate the true value of the sectional force.

Alternatively, we can use the divergence at any given point as a measure of the out-of-plane motion at that point. For an incompressible fluid, we know that

$$\frac{\partial u}{\partial x} + \frac{\partial v}{\partial y} + \frac{\partial w}{\partial z} = 0 \quad (\text{B.22})$$

where u, v , and w are the x,y, and z components of the velocity, respectively. If we rewrite equation B.22 as

$$\frac{\partial V_z}{\partial z} = - \left(\frac{\partial V_x}{\partial x} + \frac{\partial V_y}{\partial y} \right)$$

B.2 Method I : Force estimates derived from 2D velocity fields

and assuming

$$V_z \propto \frac{\partial V_z}{\partial z}$$

then we can say

$$V_z \propto - \left(\frac{\partial V_x}{\partial x} + \frac{\partial V_y}{\partial y} \right) \quad (\text{B.23})$$

Equation B.23 can be used as a measure of the out-of-plane component of velocity at any given point, although it cannot give exact values of out-of-plane velocity magnitudes or direction. Nonetheless, its usefulness is twofold. Firstly, equation B.23 can be used to highlight the parts of the velocity field where the out-of-plane component is relatively high. This information may be useful in visualising the three dimensional structures behind the foil. Secondly, equation B.23 can be used to estimate the value of V_r . As V_r is interpreted as the x-component of velocity of a packet of fluid leaving the control volume at its sides, we can use the average x-component of the velocity in the areas where there is a high value of $-\left(\frac{\partial V_x}{\partial x} + \frac{\partial V_y}{\partial y}\right)$ as an estimate for V_r , that is, for every point i and j in the plane ABDC,

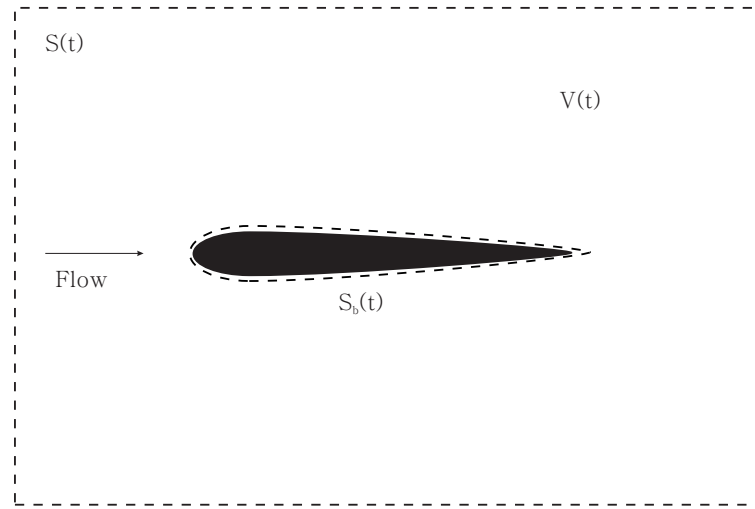
$$V_{r,est} \approx \frac{\sum V_{x,i,j} \left| \frac{\partial V_z}{\partial z} \right|_{i,j}}{\sum \left| \frac{\partial V_z}{\partial z} \right|_{i,j}} \quad (\text{B.24})$$

It has to be noted that the term $(\dot{m}_{ABDC+} + \dot{m}_{ABDC-})$ is expected to be small, therefore the third term of equation B.21 is expected to be small as well. Therefore the effect of the choice of V_r may only have a minimal impact on the value of F_x .

B.2.2 Further simplification

Equation B.21 can be further simplified if we assume that there is no out-of-plane flow, and therefore $V_r = 0$. Furthermore, if we assume that section AC is taken far enough upstream of the foil such that the flow is undisturbed by the foil, we can then assume that $\vec{V}_1 \cdot \hat{i} = U_\infty$ where U_∞ is the freestream velocity. On a similar vein, if we assume that sections AB and CD are far away from the body such that the x-component of the velocities at those sections are nearly the free-stream velocity, then $\vec{V}_3 \cdot \hat{i} = \vec{V}_4 \cdot \hat{i} = U_\infty$. With these assumptions, for a unit depth of $w = 1$, equation B.21 reduces to the "flat plate equation",

$$F_x = \rho \int_{-b/2}^{b/2} \vec{V}_2(y) \cdot \hat{i} \left(U_\infty - \vec{V}_2(y) \cdot \hat{i} \right) dy \quad (\text{B.25})$$

Figure B.2: A hydrofoil in a control volume $V(t)$

which is the commonly used formula for estimating drag on a bluff body from the measured velocity profile in its wake. Note that equation B.25 is equivalent to setting $V_r = U_\infty$ in Equation B.21.

Although the assumptions used in deriving B.25 are severe - we have assumed steady flow, 2-D flow with no pressure gradients along the control volume - it is expected that equation B.25 provides a good estimation of the time averaged thrust/drag on a unsteady foil. In fact, in similar experiments on heaving and pitching hydrofoils, Anderson (1996) reported that equation B.25, when applied to PIV data, provides comparable results to force measurements obtained via force transducers.

B.2.3 The “momentum” equation

An alternative method of calculating forces on a body given its velocity field is provided by Noca *et al.* (1999). Let's say we have a body in motion in a time dependent control volume $V(t)$ as shown in figure B.2. $V(t)$ is not infinitely large, but is externally bounded by the surface $S(t)$ and internally bounded by the body surface $S_b(t)$.

The hydrodynamic force \vec{F} acting on the foil in figure B.2 can be expressed as (Noca *et al.*, 1999):

$$\frac{\vec{F}}{\rho} = -\frac{d}{dt} \int_{V(t)} \vec{V} dV + \oint_{S(t)} \hat{n} \cdot [-p\vec{I} - (\vec{V} - \vec{V}_b)\vec{V} + \vec{T}] dS - \oint_{S_b(t)} \hat{n} \cdot (\vec{V} - \vec{V}_b) \vec{V} dS \quad (\text{B.26})$$

B.2 Method I : Force estimates derived from 2D velocity fields

where \hat{n} is the unit vector pointing out of the surface $S(t)$, \vec{V} is the flow velocity, \vec{V}_b is the body surface velocity, p is the pressure, \vec{I} is the unit tensor and \vec{T} is the viscous stress tensor for an incompressible flow, given by

$$\vec{T} = \mu(\nabla\vec{V} + \nabla\vec{V}^T)$$

where superscript \vec{V}^T is the transpose of \vec{V} .

Note the existence of the problematic pressure term in equation B.26. Fortunately, however, Noca *et al.* have derived with rigorous mathematical manipulation an alternative form of equation B.26, dubbed the "momentum equation":

$$\frac{\vec{F}}{\rho} = \frac{d}{dt} \int_{V(t)} \vec{V} dV + \int_{S(t)} \hat{n} \cdot \vec{\gamma} dS - \int_{S_b(t)} \hat{n} \cdot (\vec{V} - \vec{V}_b) \vec{V} dS \quad (\text{B.27})$$

where

$$\begin{aligned} \vec{\gamma} = & \frac{1}{2} V^2 \vec{I} + (\vec{V}_b - \vec{V}) \vec{V} - \frac{1}{N-1} \vec{V} (\vec{x} \times \vec{\omega}) + \frac{1}{N-1} \vec{\omega} (\vec{x} \times \vec{V}) \\ & - \frac{1}{N-1} \left[\left(\vec{x} \cdot \frac{\partial \vec{V}}{\partial t} \right) \vec{I} - \vec{x} \frac{\partial \vec{V}}{\partial t} \right] + \frac{1}{N-1} \left[\vec{x} \cdot (\nabla \cdot \vec{T}) \vec{I} - \vec{x} (\nabla \cdot \vec{T}) \right] + \vec{T} \end{aligned}$$

Here, $\vec{\omega}$ is the vorticity vector, \vec{x} is the spatial position vector and N is the number of spatial dimensions.

Notice that in equation B.27 the pressure term has disappeared, and therefore the force on the body can be calculated explicitly from the velocity field around the body and its derivatives. Equation B.27 is also exact in the sense that the only assumption used in its derivation is the assumption that the flow is incompressible - the "momentum equation" above provides an instantaneous force vector (rather than a force component), and is valid for a unsteady, moving body in a viscous fluid in a flow containing pressure gradients, unlike equations B.21 and B.25. However, the "momentum equation" is only valid for regions where the velocity field can be measured, that is, equation B.27 can only provide forces on a 2-D body given a 2-D field - it cannot predict the forces on a 3-D body only given a 2-D velocity field. In fact, it is impossible to calculate the three dimensional forces on a 3-D body only given its 2-D velocity field.

Caution has to be shown when using equation B.27 with discrete data, as under certain conditions, the results of the equation may be susceptible to noise. This is due to the $(\vec{x} \times \vec{\omega})$ and $(\vec{x} \times \vec{V})$ terms, which essentially amplifies terms which are positioned far away from the origin.

Nevertheless, for well resolved data with a good signal to noise ratio (with large force coefficients, for example), Noca *et al.* find that the "momentum equation" is a good estimator of the actual force on the body. This is further echoed in a separate study by Tan *et al.* (2005).

B.2.3.1 Simplification of the “momentum equation”

If we are only interested in the time-averaged forces on the hydrofoil, equation B.27 can be simplified by saying that $\frac{\partial}{\partial t} = 0$. Furthermore, since there is no flow through the solid boundary of the foil, the third term on the right hand side of equation B.27 is also zero. Therefore, for the time averaged case, and setting $N = 2$ for a 2-D flow, we can say that

$$\vec{F} = \rho \int_S \hat{n} \cdot \vec{\gamma}_{ave} dS \quad (\text{B.28})$$

where

$$\begin{aligned} \vec{\gamma}_{ave} = & \frac{1}{2} V^2 \vec{I} - \vec{V} \vec{V} - \vec{V} (\vec{x} \times \vec{\omega}) + \vec{\omega} (\vec{x} \times \vec{V}) \\ & + \left[\vec{x} \cdot (\nabla \cdot \vec{T}) \vec{I} - \vec{x} (\nabla \cdot \vec{T}) \right] + \vec{T} \end{aligned}$$

as the time average value of \vec{V}_b equals to zero.

One of the benefits of using the time averaged data is in the removal of the time dependent $\frac{\partial}{\partial t}$ terms, which, in the current PIV setup, is highly under-resolved due to the limitations in the laser pulsing frequency (fixed at 10Hz). If we expand $\vec{\gamma}_{ave}$, and recalling that $\vec{x} = (x, y, z)$, $\vec{\omega} = (\omega_x, \omega_y, \omega_z)$ and $\vec{V} = (V_x, V_y, V_z)$, we obtain

$$\vec{\gamma}_{ave} = \begin{bmatrix} \chi_1 & \chi_2 \\ \chi_3 & \chi_4 \end{bmatrix} \quad (\text{B.29})$$

B.2 Method I : Force estimates derived from 2D velocity fields

where

$$\begin{aligned}
 \chi_1 &= \frac{1}{2} \sqrt{V_x^2 + V_y^2} - V_x^2 - yV_x\omega_z + \mu \left[2y \frac{\partial^2 V_y}{\partial y^2} + y \frac{\partial^2 V_x}{\partial x \partial y} + y \frac{\partial^2 V_y}{\partial x^2} + 2 \frac{\partial V_x}{\partial x} \right] \\
 \chi_2 &= -V_x V_y + xV_x\omega_z - \mu \left[x \frac{\partial^2 V_x}{\partial x \partial y} + x \frac{\partial^2 V_y}{\partial x^2} + 2x \frac{\partial^2 V_y}{\partial y^2} - \frac{\partial V_x}{\partial y} - \frac{\partial V_y}{\partial x} \right] \\
 \chi_3 &= -V_x V_y - yV_y\omega_z - \mu \left[2y \frac{\partial^2 V_x}{\partial x^2} + y \frac{\partial^2 V_x}{\partial y^2} + y \frac{\partial^2 V_y}{\partial y \partial x} - \frac{\partial V_x}{\partial y} - \frac{\partial V_y}{\partial x} \right] \\
 \chi_4 &= \frac{1}{2} \sqrt{V_x^2 + V_y^2} - V_y^2 + xV_y\omega_z + \mu \left[2x \frac{\partial^2 V_x}{\partial x^2} + x \frac{\partial^2 V_x}{\partial y^2} + x \frac{\partial^2 V_y}{\partial y \partial x} + 2 \frac{\partial V_y}{\partial y} \right]
 \end{aligned}$$

All the terms in equation B.29 can be obtained directly or indirectly from the PIV velocity field and the properties of the fluid.

B.2.4 Vortex added mass method

Dabiri (2005) derived a method to estimate forces on a body immersed in fluid solely based on wake velocity measurements. This method is based on the concept that the forces developed on the body can be estimated from the forces used to generate the vorticity field, and therefore the vortical structures, in the wake. The forces used to generate these vortical structures can, in turn, be estimated from the "added mass" of these vortical structures. This method is particularly applicable to estimating forces on swimming and flying animals or animal-like bodies, due to the fact that swimming and flying animals produce clear vortical structures in their wakes.

This method starts with the relationship between the forces on a body to generate vorticity, and its vorticity field, developed by Saffman (1992) for an inviscid, incompressible flow:

$$\vec{F} = \rho \left[\frac{\partial}{\partial t} \int_{\mathbb{R}} \vec{x} \times \vec{\omega} d\forall + \frac{\partial}{\partial t} \int_{\mathbb{R}} \vec{\phi} \hat{n} dS \right] \quad (\text{B.30})$$

where \mathbb{R} is the region of fluid containing all the vorticity generated by the body. Note that there is no pressure term in equation B.30, however, the velocity potential term, $\vec{\phi}$ is indirectly related to the pressure.

The key to the analysis is the assumption that all the vorticity in the wake is arranged into thin, closed vortex loops, each with an area A and circulation Γ . With this assumption, equation B.30 is reduced to:

$$\vec{F} \approx \rho \frac{d}{dt} (A\Gamma + \bar{c}_{ii} A A_w \vec{V}_{vw}) \quad (\text{B.31})$$

where \bar{c}_{ii} is the two-dimensional approximation to the added mass coefficient of the vortical structures, A_w is the wake vortex width and \vec{V}_{vw} is the wake vortex velocity (see Dabiri (2005) for more details).

The problem with using equation B.31 is the difficulty in determining the boundaries of the vortical structures. A proper boundary to the vortical structures is required to accurately determine A , A_w and \bar{c}_{ii} . Furthermore, equation B.31 relies on data that is well-resolved in the time domain, and is also difficult to implement for a wake with either multiple vortical structures, or no clearly defined vortical structures.

B.2.5 Test cases

Due to the difficulty in implementing the vortex added mass method, only the calculations based on the linear momentum balance (section B.2.1) and the "momentum" equation (section B.2.3) will be used to estimate the forces on the unsteady hydrofoil. Forces are then converted to non-dimensional thrust coefficients, C_t , based on equation

$$C_{t,i} = \frac{F_{t,i}}{1/2\rho U_\infty^2 c s} \quad (\text{B.32})$$

where c is for foil chord length, s is the foil span (set to $s = 1$), and subscripts $i = 1, 2, 3, 4$ denote the values obtained using the "flat plate equation" (equation B.25), " V_r equation", setting $V_r = 0$ (equation B.21), " V_r equation", setting $V_r = V_{r,est}$ (equations B.21 and B.24) and "Momentum equation" (equation B.28) respectively. It is expected that $C_{t,1}$ and $C_{t,2}$ underestimate and overestimate the true value of the sectional lift coefficient respectively.

The four equations above are numerically integrated along the boundary of the control volume using the trapezoidal method. All spatial derivatives are estimated using finite difference techniques (centre-differences).

Selected velocity fields for cases $\frac{h_0}{c} = 0.5$ and $\theta_0 = 30^\circ$ are shown in figure B.3. The flow is from left to right. The position of the foil shown denotes the average location of the foil. Due to the shadow of the foil, the whole region of the flow cannot be illuminated all the time - the vectors in the area of the flow which is shadowed by the foil on at least one instantaneous image sample are disabled and are considered invalid for any analysis.

The shadowed region consisting of invalid vectors poses two problems. Firstly, the estimation of V_r requires a computation across the whole velocity field, and therefore any "holes" in the data will give rise to an inaccurate estimation of V_r . As there is no direct way to obtain the data

B.2 Method I : Force estimates derived from 2D velocity fields

on the shadowed side of the foil (other than to setup the PIV experiment to illuminate both sides of the foil simultaneously), the shadowed vectors are simply not used in the computation of V_r .

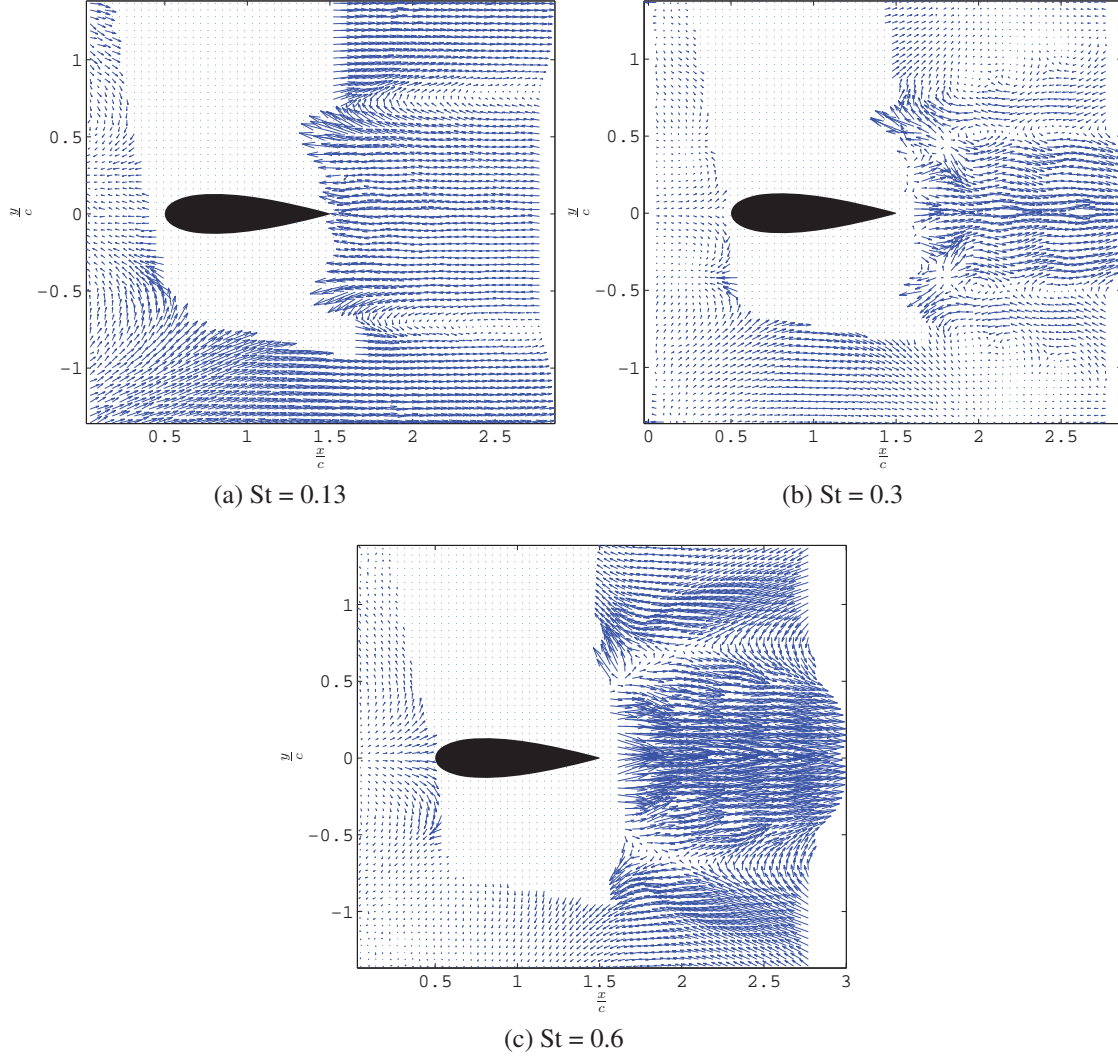


Figure B.3: Time averaged velocity fields relative to the foil at various St , for selected test cases where $\frac{h_0}{c} = 0.5$ and $\theta_0 = 30^\circ$. Flow is from left to right. Note that the vectors in the shadow of the foil are disabled

Secondly, the force estimation equations B.21 and B.28 requires a line integral (in two dimensions) along the perimeter of the control volume - this line integral will, at some stage, be required to cross the shadowed region where valid data is unavailable. Therefore, to sidestep this issue, the disabled velocity data of $\vec{V}_3(x) \cdot \hat{j}$ is replaced with the equal but opposite values of $\vec{V}_4(x) \cdot \hat{j}$ along the opposite side of the control volume. Inevitably, this assumes that the flow is symmetrical along the line $\frac{y}{c} = 0$, which is not strictly true, however, it provides a reasonable approximation for the purposes of calculating time-averaged forces on the foil.

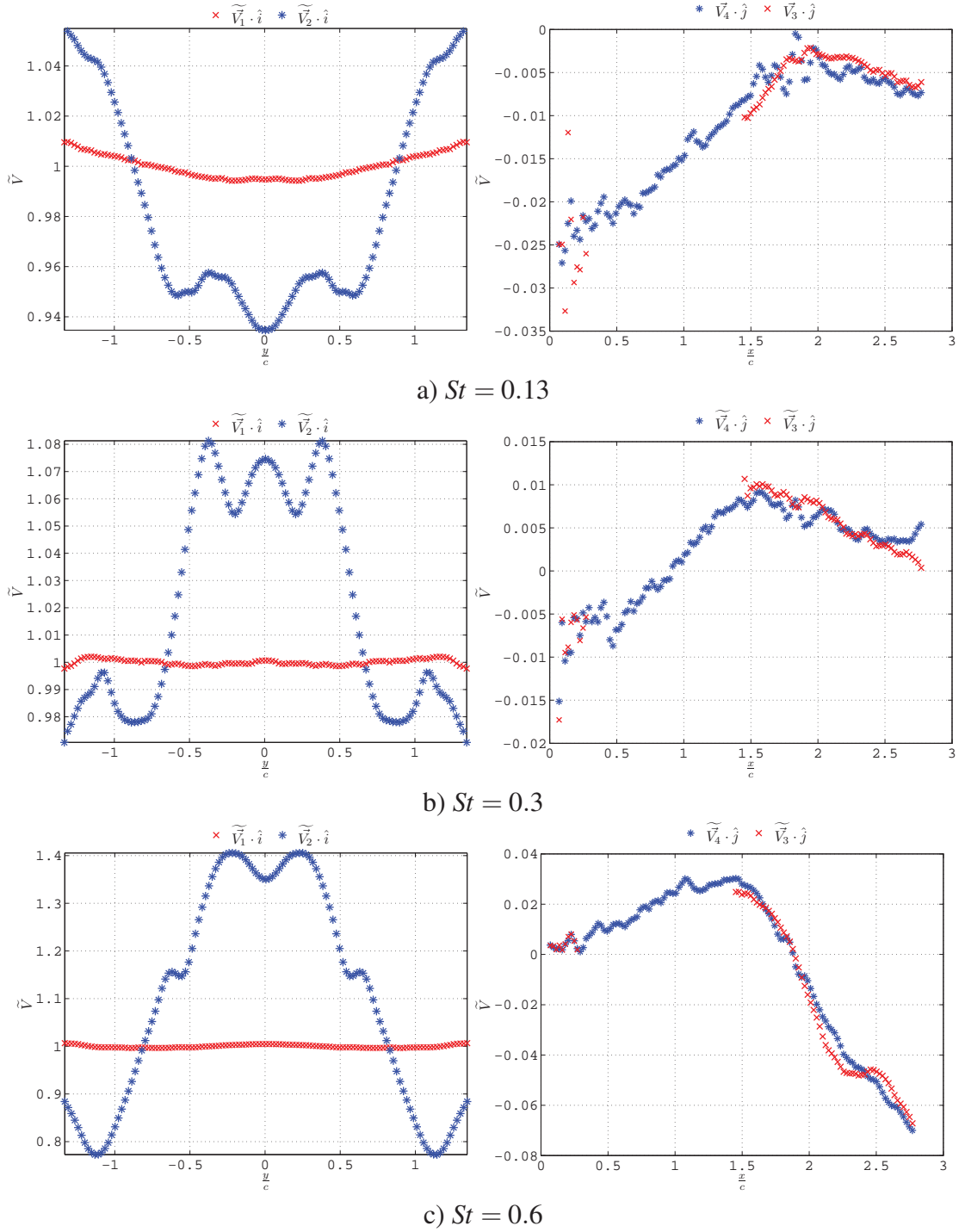


Figure B.4: Velocity profiles along the control volume of the foil for selected test cases in figure B.3. For definitions of V_1 , V_2 , V_3 and V_4 , see figure B.1

Figure B.4 displays the velocity profiles of the three test cases shown in figure B.3, at the “entry” and “exit” of the control volume, that is, at $\frac{x}{c} \approx 0$ and $\frac{x}{c} \approx 2.8$, and along the sides of the control volume ($\frac{y}{c} \approx -1.4$ and $\frac{y}{c} \approx 1.4$). The non-dimensional velocities \tilde{V} are obtained by normalising

B.2 Method I : Force estimates derived from 2D velocity fields

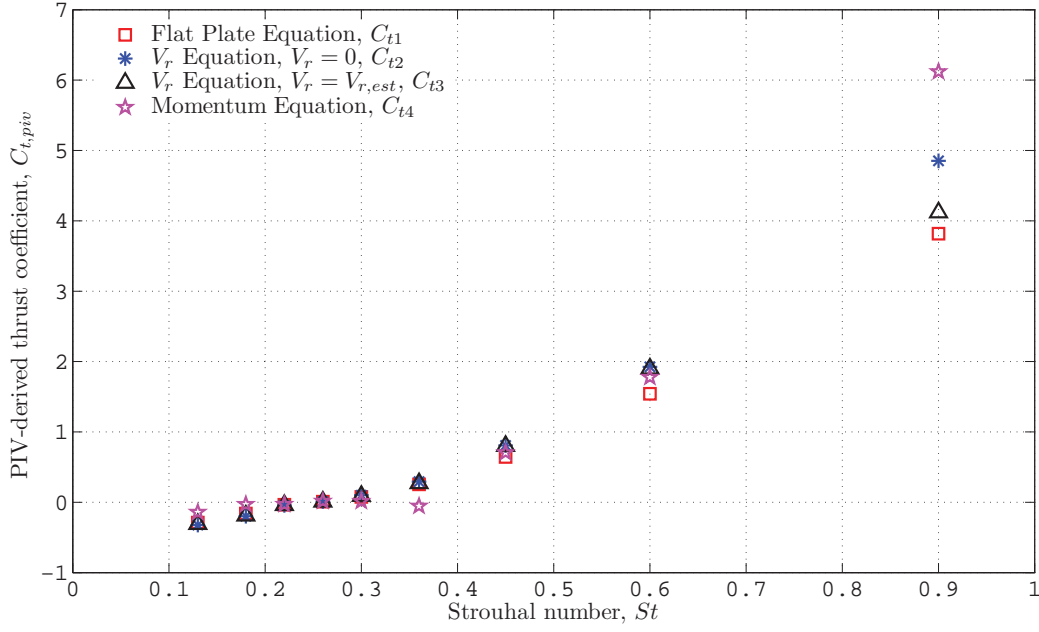


Figure B.5: Time averaged thrust coefficient, C_t calculated using various methods vs Strouhal number, St , for selected test cases.

the velocities with the free-stream velocity,

$$\tilde{V} = \frac{V}{U_\infty} \quad (\text{B.33})$$

It is clear from the velocity profiles that the flow entering the control volume upstream of the foil is not exactly uniform, but is slightly affected by the presence of the unsteady foil. However, this upstream effect of the foil on the flow is minimal. Of particular importance is the fact that the flow seems to be very symmetrical along the line $\frac{y}{c} = 0$; this is noticeable for all velocity components $\tilde{V}_1 \cdot \hat{i}$, $\tilde{V}_2 \cdot \hat{i}$, $\tilde{V}_3 \cdot \hat{j}$, and $\tilde{V}_4 \cdot \hat{j}$. This supports the assumption that the motion of the foil is symmetrical.

Furthermore, it is also clear that the centreline velocity in the wake downstream of the foil increases as the Strouhal number increases, implying an increase in thrust as St increases, as predicted by the author's previous work (Lau *et al.*, 2004) and the Q-S model. This trend is more evident if we plot the thrust coefficients, C_{t1} , C_{t2} , C_{t3} and C_{t4} against St , for a slightly larger range of cases (see figure B.5).

Figure B.5 shows clearly that as St increases, the thrust coefficient increases as well. This observation is independent of the method used to estimate the force coefficient. However, the main purpose of this current study is the accuracy of the force calculation method; figure B.5 shows that the first three methods, the "flat plate equation", the " V_r equation" setting $V_r = 0$,

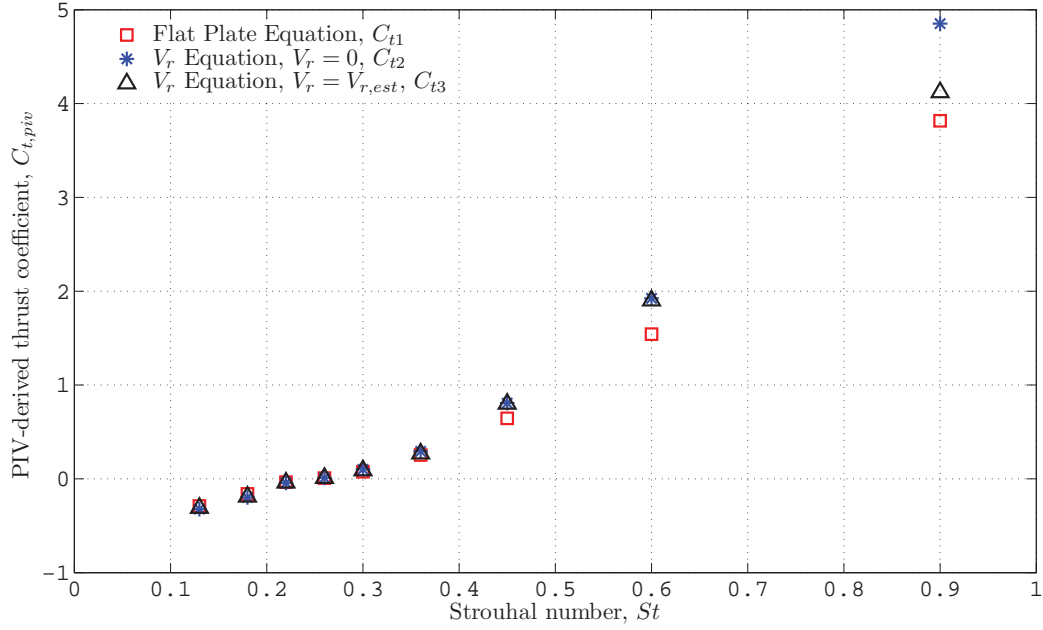


Figure B.6: Time averaged thrust coefficient, C_t calculated using the " V_r equation" and the "flat plate" equation

and the " V_r equation" setting $V_r = V_{r,est}$ provide thrust coefficients which are quite consistent with one another. However, the thrust coefficients estimated using the "momentum equation" shows some inconsistency. At this stage the reason for the poor performance of the "momentum equation" remains unclear, however, we postulate that the momentum equation is highly sensitive to random noise fluctuations in the velocity field. The noise in the velocity is amplified by the $(\vec{x} \times \vec{\omega})$ and $(\vec{x} \times \vec{u})$ terms in equation B.28, where the origin of the term \vec{x} is theoretically arbitrary, however, using real discretised data, the origin of \vec{x} has some effect on the thrust coefficients calculated. Furthermore, the noise in the data is also amplified by the fact that the velocity derivative terms, such as $\vec{\omega}$ and the second order derivative terms such as $\frac{\partial^2 u}{\partial x^2}$ can only be estimated using numerical techniques (such as finite-difference techniques), which inherently act as random and/or bias noise amplifiers (for a more detailed discussion on the noise transmission characteristics of finite-difference techniques, please refer to appendix C).

If we plot the thrust coefficient data without using values obtained from the "momentum equation", the graph looks more consistent (see figure B.6). The difference between the values of C_{t1} , C_{t2} and C_{t3} are relatively small - suggesting that these three methods are robust and fairly accurate. Also note that the values of C_{t3} always lie in between the values of C_{t1} and C_{t2} ; as predicted, the values of C_{t1} and C_{t2} provide under- and over-estimations of the true thrust coefficient values respectively, and therefore they can be thought of as the upper and lower limits to the true value of the time-averaged sectional thrust coefficient of the foil.

B.3 Force measurements from strain gauges

Figure B.6 shows that for low values of St , there is an approximate linear relationship between the time averaged thrust coefficient, and the Strouhal number. Above $St \approx 0.5$, the slope gradually increases, suggesting a stronger exponential component (consistent with numerical Q-S model results, discussed in chapter 3), although there are far too few data points to make any conclusive statements at this stage.

These results show reasonable agreement with thrust measurements of unsteady foils performed by Anderson *et al.* (1998), who, at similar heave and pitch amplitudes, obtained a value of $C_t = 1.86$ at $St = 0.55$, while we obtain a value of $C_{t3} = 1.9$ at $St = 0.6$.

In summary, both the “flat plate” and “ V_r ” equations are consistent not only with each other, but also with selected data obtained from published literature. Therefore, for the purposes of this thesis, the “ V_r equation”, whereby $V_r = V_{r,est}$ is selected as the method of choice for estimating time-averaged forces based on 2-D PIV data.

B.3 Force measurements from strain gauges

In chapter 2, we discussed the experimental method used to obtain the instantaneous thrust $F_{t,sg}(t)$, side force $F_{s,sg}(t)$, and moment $M_{sg}(t)$, developed by the unsteady foil. These values can be used to obtain the time-averaged thrust and side force coefficients, $C_{t,sg}$ and $C_{s,sg}$ respectively, using the equations

$$C_{t,sg} = \frac{\frac{1}{T} \int_0^T F_{t,sg}(t) dt}{\frac{1}{2} \rho U_\infty^2 c s} \quad (B.34)$$

$$C_{s,sg} = \frac{\frac{1}{T} \int_0^T |F_{s,sg}(t)| dt}{\frac{1}{2} \rho U_\infty^2 c s} \quad (B.35)$$

Meanwhile, the productivity is defined as

$$\eta = \frac{C_{t,sg}}{C_{s,sg}} \times 100\% \quad (B.36)$$

while the experimentally measured propulsive efficiency is defined as

$$\eta_F = \frac{U_\infty \int_0^T F_{t,sg}(t) dt}{\int_0^T |F_{s,sg}(t) \cdot h'(t)| dt + \int_0^T |M_{sg}(t) \cdot \theta'(t)| dt} \times 100\% \quad (B.37)$$

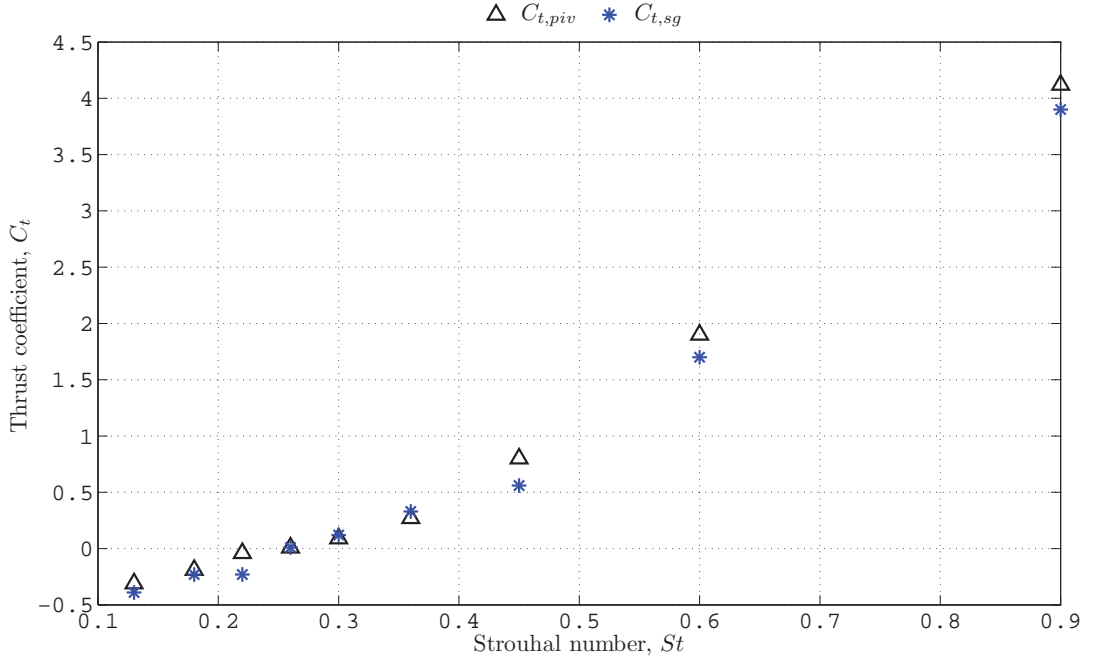


Figure B.7: Comparison of $C_{t,piv}$ and $C_{t,sg}$ at $\frac{h_0}{c} = 0.5$ and $\theta_0 = 30^\circ$

where $h'(t)$ is the instantaneous heave velocity and $\theta'(t)$ is the instantaneous angular velocity of the foil.

B.4 Errors in experimental force and efficiency data

Assuming the basis of the momentum analysis and the corresponding equation relating the force on the foil to the velocity integral around an arbitrary control volume is sound, then it is likely that the thrust coefficients obtained from the PIV velocity field (denoted $C_{t,piv}$) are accurate, due to the fact that the velocity integral is not sensitive to the random noise in the velocity field. However, the effect of the assumptions of the momentum analysis in section B.2 on the final thrust measurement is unknown.

The random errors in the digitally filtered time-averaged values of $C_{t,sg}$ and $C_{s,sg}$ are also expected to be very small, due to the fact that the typical voltage data sample is long ($\approx 120,000$ data points).

Fortunately, we can also compare the thrust coefficient obtained using the PIV velocity data $C_{t,piv}$, and the thrust coefficient based on the strain gauge results, $C_{t,sg}$, as shown in figure B.7. The results show a good agreement between the thrust coefficient results, suggesting that the

B.5 Chapter summary

thrust measurements are likely to be accurate. This also implies that the side force measurements are also consistent. This is due to the fact that both the thrust and side force measurements are linked, since they are both obtained using the same two force components (i.e., foil chord-wise and normal force components - see chapter 2).

The experimental results of efficiency, on the other hand, has fairly significant errors. This is due to the fact that the pitching moments of the foil, measured using strain gauges, has a much larger inertial component relative to the hydrodynamic component. The moments generated when the foil was placed in air are only approximately 5% smaller than the moments generated by the foil when it was fully submerged in water. This implies that the hydrodynamic moments on the foil are small, approximately 20 times smaller than the inertial moments. This small hydrodynamic moment signal therefore has a significant noise component, which manifests itself as large errors in the evaluation of propulsive efficiency η_F . This error is particularly evident when the angles of attack of the foil are small ($St \approx St_0$), when the total hydrodynamic forces on the foil are small anyway.

B.5 Chapter summary

In this chapter, the methods of retrieving time-averaged hydrodynamic force measurements were discussed in detail. The time averaged thrust coefficient is obtained using two different methods, firstly, by integrating the PIV velocity field around the foil, and secondly, by direct strain gauge measurements. The strain gauge measurements also provide the time-averaged side forces and propulsive efficiencies developed by the foil.

To estimate the forces derived from the PIV velocity field around a body fully immersed in a flow, three different equations were developed based on existing mathematical analyses. The three methods developed, namely the " V_r equation" (setting $V_r = 0$ or $V_r = V_{r,est}$), the "flat plate equation" and the "momentum equation", were applied to PIV data gathered around an unsteady foil. An alternate method, called the "vortex added mass" method, was also briefly discussed, however, due to the difficulty in implementing this method to PIV data, this method was not considered any further.

All methods, in its current incarnations, can only provide an estimation of the time-averaged sectional thrust coefficient values, due to the nature of the PIV velocity fields in which they are applied to.

The thrust coefficient computed using the V_r , flat plate, and the momentum equations were tabulated and plotted for ten selected flow cases with varying Strouhal numbers. From the results,

it can be gathered that the V_r and flat plate equations perform relatively well; they provide consistent and comparable results. However, the "momentum equation" seems to perform poorly. The reason for this is currently unknown.

The " V_r equation", whereby the value of V_r is fixed at $V_r = 0$, provides an upper limit to the true value of the thrust coefficient, whereas the "flat plate" equation (which is equivalent to setting $V_r = U_\infty$ in the " V_r equation") provides a lower limit to the true value of the measured thrust coefficient. On the other hand, by setting $V_r = V_{r,est}$, where $V_{r,est}$ is approximated from mean values of the divergence-weighted velocity vector field, we can obtain an approximate compromise between the upper and lower limits of C_t . From the test cases, the C_t values obtained using $V_r = V_r$ show good consistency, and therefore the " V_r equation", whereby V_r is set to $V_{r,est}$, will be used as the basis for all thrust coefficient measurements from PIV data from this point forward.

The post-processing and analysis of strain gauge measurement is fairly straightforward; the instantaneous thrust, side force, and moments on the foil are simply time-averaged across the entire data sample, consisting of approximately 120,000 data points.

The thrust and side force results are estimated to be very accurate, due to the fact that a large number of data points is used in the strain gauge measurements, and that the time-averaged PIV velocity field data has very low random noise values. The thrust coefficients based on the PIV measurements and the strain gauge measurements are also comparable, further indicating that the force results are accurate. Nonetheless, the experimentally-derived efficiency values have relatively large errors, due to the fact that the hydrodynamic moments on the foil are very small compared to the inertial moments on the foil and the experimental random noise values. Therefore, the experimentally-evaluated efficiency results should be used with caution, particularly when $St \approx St_0$, where the hydrodynamic forces are estimated to be the smallest.

Appendix C

Estimating Circulation based on Discrete Velocity Data

C.1 Introduction

Experiments using particle image velocimetry (PIV) provide a wealth of data in the velocity plane. However, in many cases, it is necessary to measure vorticity, and subsequently, the circulation of vortical structures in a particular field of interest. Here, we discuss the methods used to estimate circulation based on a number of different vorticity estimation schemes, each with inherent benefits and drawbacks. We also illustrate the effect of experimental noise and data resolution on the circulation estimate, and finally recommend a particular vorticity estimation scheme for specific use in the unsteady foil experiments discussed in this thesis.

C.2 Estimation of circulation

The circulation is mathematically defined as

$$\Gamma_{vel} = \oint_p \vec{V} \cdot d\vec{l} \quad (C.1)$$

$$\Gamma_{vor} = \int_S \vec{\omega} \cdot d\vec{S} \quad (C.2)$$

where $\vec{\omega}$ is the vorticity, Γ_{vel} is the circulation based on the velocity integral, Γ_{vor} is the circulation based on the vorticity integral, p is the integration path that encloses the integration region S , and $d\vec{l}$ is the unit vector along integration path p . To measure the circulation of a vortical

structure of interest, the path p is chosen such that it encompasses that particular vortex. However, in reality, the boundary of any experimentally measured vortical structure is difficult to determine accurately. Thus, we propose using an iso-vortical contour of value ω_T as an estimate of the boundary of a vortex, and therefore providing a clearly defined path and region of integration. This method has already been described in Hassan *et al.* (2007).

To illustrate the method of estimation circulation, we shall use an example of a PIV-derived vorticity field in the wake of an oscillating foil, shown in Figure C.1. Note that these vorticity fields were derived from the PIV velocity fields using a particular vorticity estimation scheme (the circ-5 scheme), the details of which will be discussed in more in the following sections.

From the wake vorticity contours shown in figure C.1a, we may determine that there are three vortical structures of interest, denoted as γ_1 , γ_2 and γ_3 . To determine the paths of integration of these three vortical structures, p_1 , p_2 , and p_3 respectively, the user is required to define a starting location for each of these vortices. For the experiments presented in this thesis, this process is done manually by specifying a location that is contained within each vortical structure, shown in figure C.1a as X. The region of integration, S , is then the area within the iso-vortical contour ω_T that also contains point X. The path of integration is then simply the perimeter of S , shown in figure C.1b.

A key effect of this methodology is that both Γ_{vel} and Γ_{vor} are dependent on ω_T and thus the vorticity (Γ_{vor} doubly so since it is an integral of the vorticity field), and hence the circulation estimate is dependent on the method of estimating vorticity. These vorticity estimation schemes will be discussed below.

C.3 Vorticity estimation schemes

C.3.1 Definition of vorticity

The first step is to define vorticity $\vec{\omega} = (\omega_x, \omega_y, \omega_z)$, for a continuous velocity field $\vec{V} = (V_x, V_y, V_z)$, as the curl of the velocity vector:

$$\vec{\omega} = \vec{\nabla} \times \vec{V} \quad (C.3)$$

The velocity field obtained from PIV experiments is only limited to two dimensions, therefore we can only obtain the out-of-plane vorticity component,

$$\omega_z = \frac{\partial V_y}{\partial x} - \frac{\partial V_x}{\partial y} \quad (C.4)$$

C.3 Vorticity estimation schemes

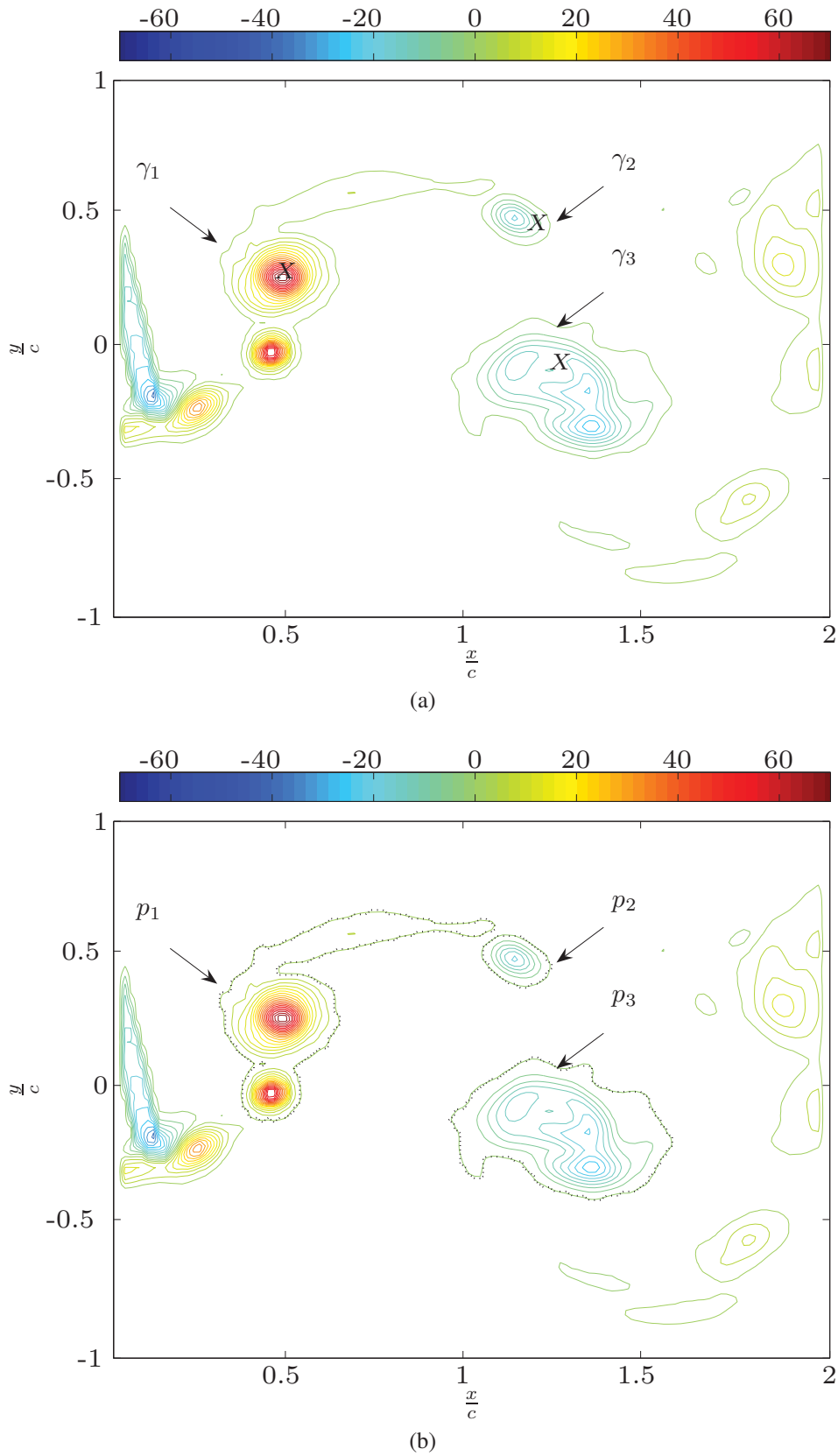


Figure C.1: Example of region of integration for the flapping foil experiments. Flow is from left to right. Vorticity contours are in units $\frac{1}{s}$

Scheme Name	Implementation
Centre Difference	$\left(\frac{df}{dx}\right)_i \approx \frac{f_{i+1} - f_{i-1}}{2\Delta}$
Poly-4	$\left(\frac{df}{dx}\right)_i \approx \frac{-f_{i+2} + 8f_{i+1} - 8f_{i-1} + f_{i-2}}{12\Delta}$
Least Squares	$\left(\frac{df}{dx}\right)_i \approx \frac{2f_{i+2} + f_{i+1} - f_{i-1} - 2f_{i-2}}{10\Delta}$
Richardson-6	$\left(\frac{df}{dx}\right)_i \approx \frac{1/8f_{i+4} - 5f_{i+2} + 32f_{i+1} - 32f_{i-1} + 5f_{i-2} - 1/8f_{i-4}}{45\Delta}$

Table C.1: Commonly used finite difference techniques (Raffel *et al.*, 1998)

Scheme Name	a	b	α
Compact-4	1.5	0	0.25
Compact-6	14/9	1/9	1/3

Table C.2: Coefficients for compact schemes

Equation C.4 forms the basis of the majority of the schemes used to determine the out-of-plane vorticity - the vorticity is simply calculated using estimates of the velocity differential terms in equation C.4. This will be further discussed below.

C.3.2 Finite difference techniques

The most straightforward technique to obtain the velocity differential terms on the right hand side of equation C.4 for discrete velocity data in a rectangular grid of spacing Δ is to use finite-difference techniques. Some commonly used techniques are shown in Table C.1 (Fouras and Soria, 1998; Raffel *et al.*, 1998).

These finite difference techniques are then applied in turn to obtain $\frac{\partial V_y}{\partial x}$ and $\frac{\partial V_x}{\partial y}$ at each point in the velocity field of interest.

C.3.3 Iterative techniques

Etebari and Vlachos (2005) has also listed alternative methods for obtaining velocity derivatives using iterative schemes. Two of these schemes, called the compact-4 and compact-6 schemes,

C.3 Vorticity estimation schemes

can be used to obtain velocity derivatives by solving the equation:

$$\left(\frac{df}{dx}\right)_i \approx b \frac{f_{i+2} - f_{i-2}}{4\Delta} + a \frac{f_{i+1} - f_{i-1}}{2\Delta} - \alpha \left[\left(\frac{df}{dx}\right)_{i+1} + \left(\frac{df}{dx}\right)_{i-1} \right] \quad (\text{C.5})$$

where the coefficients a , b and α are given in table C.2.

A third scheme is also proposed by Etebari and Vlachos, which is a combination of the compact-4 scheme and the Richardson-6 scheme (with modified coefficients), dubbed the compact-richardson-4 hybrid scheme, or simply, the hybrid-CR4 scheme. In the hybrid-CR4 scheme, the velocity derivative can be written as

$$\left(\frac{\partial f}{\partial x}\right)_i \approx \frac{1}{1239} \sum_{k=1,2,4} A_k \left(\frac{\partial f}{\partial x}\right)_{i,k-grid} \quad (\text{C.6})$$

where $A_1 = 272$, $A_2 = 1036$, $A_3 = -69$ and $\left(\frac{\partial f}{\partial x}\right)_{i,k-grid}$ is the derivative obtained using the compact-4 scheme for a grid spacing of k .

As with the finite difference techniques, the velocity derivatives obtained for $\frac{\partial V_y}{\partial x}$ and $\frac{\partial V_x}{\partial y}$ are then replaced into equation C.4 to obtain the vorticity field.

C.3.4 Circulation-method

The circulation-method of calculating the out-of-plane vorticity from the velocity field varies from the methods discussed above, in the sense that it does not use the velocity derivatives to calculate vorticity. The circulation-method estimates vorticity directly using the relationship between the circulation, Γ around a closed curve l encompassing a surface S , and the vorticity within S , following the equation:

$$\Gamma = \oint_l \vec{V} \cdot d\vec{l} = \int_S \vec{\omega} \cdot d\vec{S} \quad (\text{C.7})$$

As the surface S approaches zero, say, around a point i, j , then

$$\omega_{i,j} \approx \frac{1}{S} \oint \vec{V} \cdot d\vec{l} \quad (\text{C.8})$$

For discrete data on a regular grid with spacing Δ , the path l can be taken along the 8 neighbours (a kernel size of 3 x 3) of any point i, j . This is called the circ-3 scheme, and is written explicitly as

$$(\omega_z)_{i,j} \approx \frac{\Gamma_{i,j}}{4\Delta^2} \quad (\text{C.9})$$

where

$$\begin{aligned}
 \Gamma_{i,j} = & \frac{1}{2}\Delta(V_{x,i-1,j-1} + 2V_{x,i,j-1} + V_{x,i+1,j-1}) \\
 & + \frac{1}{2}\Delta(V_{y,i+1,j-1} + 2V_{y,i+1,j} + V_{y,i+1,j+1}) \\
 & - \frac{1}{2}\Delta(V_{x,i+1,j+1} + 2V_{x,i,j+1} + V_{x,i-1,j+1}) \\
 & - \frac{1}{2}\Delta(V_{y,i-1,j+1} + 2V_{y,i-1,j} + V_{y,i-1,j-1})
 \end{aligned} \tag{C.10}$$

Sometimes it is useful to make the surface S slightly larger, encompassing the neighbouring 24 vectors for example (a kernel size of 5 x 5), especially for oversampled data. This is called the circ-5 scheme, written explicitly as

$$(\omega_z)_{i,j} \approx \frac{\Gamma_{i,j}}{16\Delta^2} \tag{C.11}$$

where

$$\begin{aligned}
 \Gamma_{i,j} = & \frac{1}{2}\Delta(V_{x,i-2,j-2} + 2V_{x,i-1,j-2} + 2V_{x,i,j-2} + 2V_{x,i+1,j-2} + V_{x,i+2,j-2}) \\
 & + \frac{1}{2}\Delta(V_{y,i+2,j-2} + 2V_{y,i+2,j-1} + 2V_{y,i+2,j} + 2V_{y,i+2,j+1} + V_{y,i+2,j+2}) \\
 & - \frac{1}{2}\Delta(V_{x,i+2,j+2} + 2V_{x,i+1,j+2} + 2V_{x,i,j+2} + 2V_{x,i-1,j+2} + V_{x,i-2,j+2}) \\
 & - \frac{1}{2}\Delta(V_{y,i-2,j+2} + 2V_{y,i-2,j+1} + 2V_{y,i-2,j} + 2V_{y,i-2,j-1} + V_{y,i-2,j-2})
 \end{aligned} \tag{C.12}$$

C.4 Performance of vorticity calculation schemes

The performance of any vorticity calculation scheme is rated based on how well the output from each individual scheme compares with the “true” values of vorticity. The performance of each scheme is defined by two independent parameters, the bias error on the vorticity ω_{bias} and the random error transmission λ_0 . The bias error is defined as the consistent underestimating or overestimating of vorticity by a particular vorticity calculation scheme, usually most pronounced at the location of peak vorticity. The random error transmission is the ratio of how much noise in the velocity field is transmitted to the vorticity field,

$$\lambda_0 = \frac{\epsilon_\omega}{\epsilon_u} L \tag{C.13}$$

C.4 Performance of vorticity calculation schemes

where ε_u is the random noise in the velocity field, ε_ω is the random noise in the vorticity field, and L is an appropriate length scale.

These two errors usually have opposing requirements in a vorticity scheme; a vorticity calculation scheme usually either has low bias error, or low random noise transmission, but not both (Etebari and Vlachos, 2005). Therefore, depending on the requirements of the user and the quality of the velocity data used, one may choose to use differing vorticity calculation schemes for different applications.

C.4.1 Analytic values of random error transmission

The effect of the vorticity estimation scheme on the random error transmission can be shown analytically.

If we write

$$\lambda_0 = K \frac{1}{(\Delta/L)} \quad (\text{C.14})$$

we can determine the constant K for each scheme based on the coefficients and implementation of each scheme. For example, for the central-difference scheme,

$$\begin{aligned} \omega_z &= \frac{\partial V_y}{\partial x} - \frac{\partial V_x}{\partial y} \\ \omega_{z,CD} &= \frac{V_{y,i+1,j} - V_{y,i-1,j}}{2\Delta} - \frac{V_{x,i,j+1} - V_{x,i,j-1}}{2\Delta} \end{aligned} \quad (\text{C.15})$$

Assuming the uncertainty in V_y and the uncertainty in V_x are both equal to σ_u , then the variance in the sample $\omega_{z,CD}$ is equal to the sum of variances of each of the terms on the right hand side of equation C.15, leading to

$$\begin{aligned} \sigma_{w,CD}^2 &= \frac{\sigma_u^2 + \sigma_u^2}{4\Delta^2} + \frac{\sigma_u^2 + \sigma_u^2}{4\Delta^2} \\ &= \frac{\sigma_u^2}{\Delta^2} \\ \sigma_{w,CD} &= \frac{\sigma_u}{\Delta} \end{aligned} \quad (\text{C.16})$$

Using equation C.13, and using the standard deviation σ as a measure of the uncertainty ε , we obtain

$$\begin{aligned} \lambda_{0,CD} &= \frac{1}{(\Delta/L)} \\ \therefore K_{CD} &= 1 \end{aligned} \quad (\text{C.17})$$

Scheme	K
Centre Difference	1
Poly-4	1.3437
Least Squares	0.4472
Richardson-6	1.4395
Circulation-3	0.6123
Circulation-5	0.2339
Compact-4	1.5
Compact-6	1.556
Hybrid Compact-Richardson-4	0.7085

Table C.3: Random noise transmission coefficients (Etebari and Vlachos, 2005)

This process is then repeated for each of the vorticity schemes. The values for K for all vorticity schemes are shown in table C.3 (Etebari and Vlachos, 2005).

Combining equations C.13 and C.14, we can explicitly determine the random error in vorticity based on the resolution, vorticity estimation scheme used, and the random noise in velocity,

$$\epsilon_{\omega} = \frac{K_{scheme} \cdot \epsilon_u}{\Delta} \quad (C.18)$$

From these results it can be seen that for a fixed, normalised data resolution of $\frac{\Delta}{L}$, and fixed random noise in velocity, ϵ_u , the scheme which will give the lowest random noise in vorticity is the circ-5 scheme, while the scheme which will most amplify the random noise is the compact-6 scheme.

C.5 Description of numerical experiment

The purpose of this experiment is to determine the most appropriate vorticity estimation scheme for any given experimental velocity field data of a specific resolution, $\frac{\Delta}{L}$ and random noise content, ϵ_u . To achieve this, we perform a numerical experiment on the Oseen vortex, which conveniently has both an analytically defined velocity and vorticity field (in polar co-ordinates),

C.5 Description of numerical experiment

given by

$$V_\theta(r) = \frac{\Gamma_0}{2\pi r} \left[1 - e^{-r^2/(2L^2)} \right] \quad (\text{C.19})$$

$$V_r(r) = 0 \quad (\text{C.20})$$

$$\omega_z(r) = \frac{\Gamma}{2\pi L^2} e^{-r^2/(2L^2)} \quad (\text{C.21})$$

where r is the distance from the Oseen vortex core, L is the characteristic length of the Oseen vortex (corresponding to one standard deviation of the vorticity contained within the Oseen vortex), and Γ_0 is the circulation of the Oseen vortex. Throughout this report, the circulation of the Oseen vortex is set to $\Gamma_0 = 1$ unit.

The Oseen vortex is generated numerically onto a grid of spacing Δ , resulting in velocity and vorticity data with resolution $\frac{\Delta}{L}$. Figure C.2 shows an example of the velocity field of a noiseless analytic Oseen vortex with a resolution of $\frac{\Delta}{L} = 0.46154$. Note that the vector field is generated for an Oseen vortex with a size of $\pm 6L$, whereas the region or field of interest (shaded white) is limited to $\pm 4L$. This is to ensure that the region of interest is sufficiently far away from the boundaries, where the vorticity estimation schemes are not applied due to the lack of velocity data points. Also note that the velocity at the centre of the vortex core, i.e., at $r = 0$, is set to $V_\theta(0) = 0$ to avoid the mathematical singularity at that point.

To simulate experimental data, random noise is artificially added to the analytic velocity field with a random normal distribution, such that the standard deviation is $\epsilon_u \cdot V_{max}$, where V_{max} is the maximum velocity magnitude in the discretised velocity field.

The magnitude of noise added to the velocity field is varied from $0 \leq \epsilon_u \leq 0.1$, while the resolution of the numerical data is varied from $0.16 \leq \frac{\Delta}{L} \leq 0.50$. For each noise and resolution value, the vorticity field, $\omega_{measured}$ is estimated for each and every vorticity estimation scheme. The circulation is also estimated using both the velocity and vorticity integrals, Γ_{vel} and Γ_{vor} respectively, for each of the nine vorticity estimation schemes. This process is repeated 10,000 times. For every vorticity estimation scheme, random noise in velocity ϵ_u , and data resolution $\frac{\Delta}{L}$, three important parameters can be obtained:

1. The random noise in the estimated vorticity field, ϵ_ω , which is simply the standard deviation of the vorticity within all 10,000 samples
2. The bias error in the circulation estimate, $\frac{\Gamma}{\Gamma_0}$, where Γ is the average of the circulation estimate across all 10,000 samples
3. The random error in circulation, $\frac{\sigma_\Gamma}{\Gamma_0}$, where σ_Γ is the standard deviation in the circulation estimates across all 10,000 samples

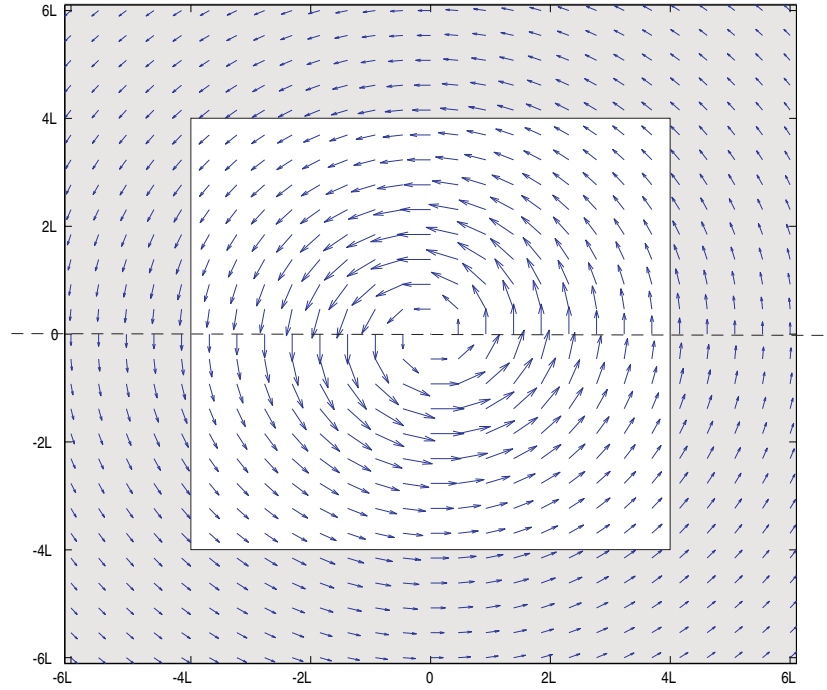


Figure C.2: Velocity field of an analytic Oseen vortex for $\frac{\Lambda}{L} = 0.46154$

Note that using equation C.18, the measured random noise in vorticity ϵ_ω can be used to numerically estimate the values of K_{scheme} . For all schemes presented here, the analytically derived and numerically estimated values of K were accurate to within 3 significant figures, thereby confirming the values in table C.3.

C.6 Vorticity bias error

For the special case where $\epsilon_u = 0$, we can also quantify the bias error for each vorticity estimation scheme, as a function of $\frac{\Lambda}{L}$. The quantifying parameter is the normalised bias error at the centre of the analytic vortex core, $\widetilde{\omega}_{bias}$, which coincides with the location of the peak vorticity,

$$\widetilde{\omega}_{bias} = \frac{\omega_{measured}(0) - \omega_{analytic}(0)}{\omega_{analytic}(0)} \times 100\% \quad (C.22)$$

where $\omega_{measured}$ is the numerically estimated vorticity while $\omega_{analytic}$ is the analytic Oseen vorticity field.

C.6 Vorticity bias error

	$\widetilde{\omega}_{bias} (\%)$			
Scheme	$\frac{\Delta}{L} = 0.6$	$\frac{\Delta}{L} = 0.46154$	$\frac{\Delta}{L} = 0.333$	$\frac{\Delta}{L} = 0.24$
Centre Difference	-8.483	-5.141	-2.727	-1.426
Poly-4	-1.739	-0.664	-0.192	-0.053
Least Squares	-24.669	-15.887	-8.811	-4.721
Richardson-6	-0.797	-0.213	-0.037	-0.006
Circ-3	-12.252	-7.537	-4.041	-2.126
Circ-5	-35.963	-24.052	-13.743	-7.49
Compact-4	-0.451	-0.144	-0.037	-0.01
Compact-6	-0.084	-0.015	-0.002	0
Hybrid-CR-4	-4.935	-0.749	0.132	0.06

Table C.4: Summary of normalised bias errors at Oseen vortex core, $\widetilde{\omega}_{bias}$ for various vorticity schemes

The results are summarised in table C.4 for four discrete resolution values. It is clear that the least squares, circ-3 and circ-5 schemes underestimate the peak vorticity most severely. The centre difference and hybrid-CR4 schemes have a moderate performance, whereas the poly-4, richardson-6, compact-4 and compact-6 schemes have very low bias errors, on the order of 1% or less of the peak vorticity, at the worst resolution. Most notably, the compact-6 scheme has the lowest bias error of all the schemes, with a bias error of less than 0.1% at the worst resolution. However, this is not surprising, as the coefficients for the compact-6 scheme were chosen to minimise the bias error (Etebari and Vlachos, 2005).

Based on tables C.3 and C.4, it is evident that the vorticity estimation schemes that produce lower vorticity bias errors amplify random noise in the velocity field, and vice versa. The correct choice of scheme for the direct estimation of vorticity then depends strongly on the user requirements; in flow conditions which have large velocity fluctuations (e.g. highly turbulent flow), one may be inclined to choose a scheme with a low random noise transmission, such as the circ-5 scheme. On the other hand, if the experimental velocity measurements have low random velocity errors (e.g. phase-averaged data with large number of samples), then the user may lean towards choosing a scheme with lower bias error, such as the compact-6 scheme.

Alternatively, a user may choose a scheme with neither large bias errors or large random error transmission ratios, such as the centre-difference scheme. At this stage it should be noted that the hybrid-CR4 scheme is the only scheme tested that achieves a simultaneous reduction in both the bias error and the random error transmission, relative to the CD scheme, confirming the findings by (Etebari and Vlachos, 2005).

C.7 Errors in circulation

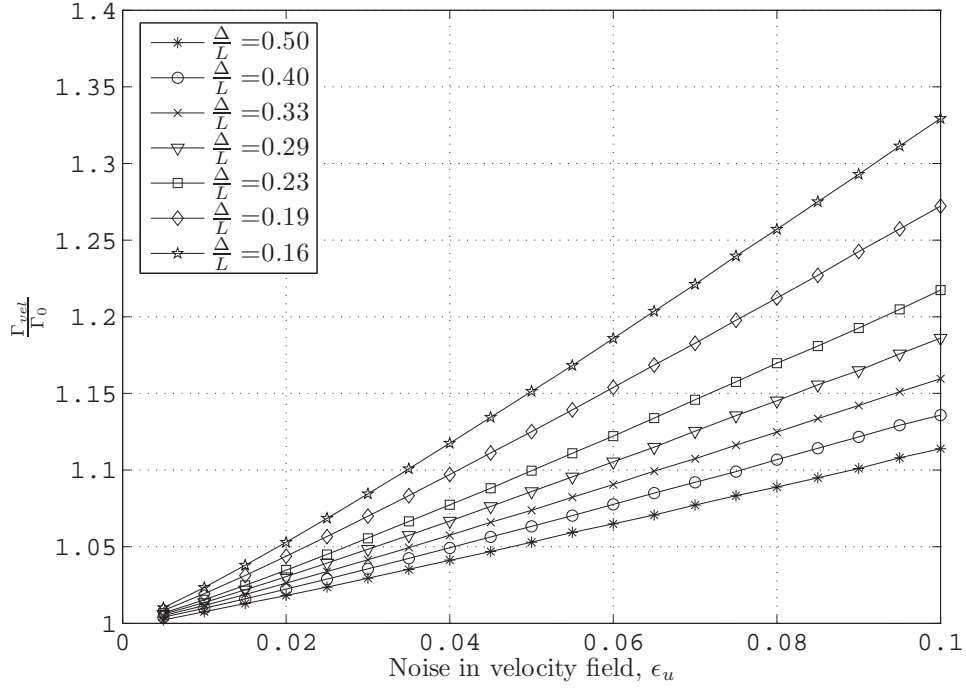
The random and bias errors in circulation, $\frac{\Gamma}{\Gamma_0}$ and $\frac{\sigma_\Gamma}{\Gamma_0}$ respectively are both dependent on the noise content in the velocity field ϵ_u , the resolution of the velocity data $\frac{\Delta}{L}$, and the type of vorticity estimation scheme used. We illustrate the effect of the former two parameters on the circulation estimate based on a single scheme, the centre-difference scheme. This is shown in figures C.3 and C.4. Note that the qualitative trends of these results are also representative of all other vorticity estimation schemes.

From these numerical results it is evident that both the random and bias errors in circulation are both approximately linearly related to ϵ_u . Thus, from a practical perspective, it is paramount that the experimentally measured velocity field contain as low a random noise content as possible. The results also indicate that the circulation bias errors are more susceptible to variations in the data resolution, $\frac{\Delta}{L}$. Surprisingly, higher resolution data (i.e. low values of $\frac{\Delta}{L}$) leads to larger bias errors in the circulation estimate. This is due to the fact that, in its current implementation, the path of integration will contain more potentially noisy velocity vectors when the data resolution is higher. The random error in circulation, $\frac{\sigma_\Gamma}{\Gamma_0}$, however, appears to be fairly insensitive to the data resolution.

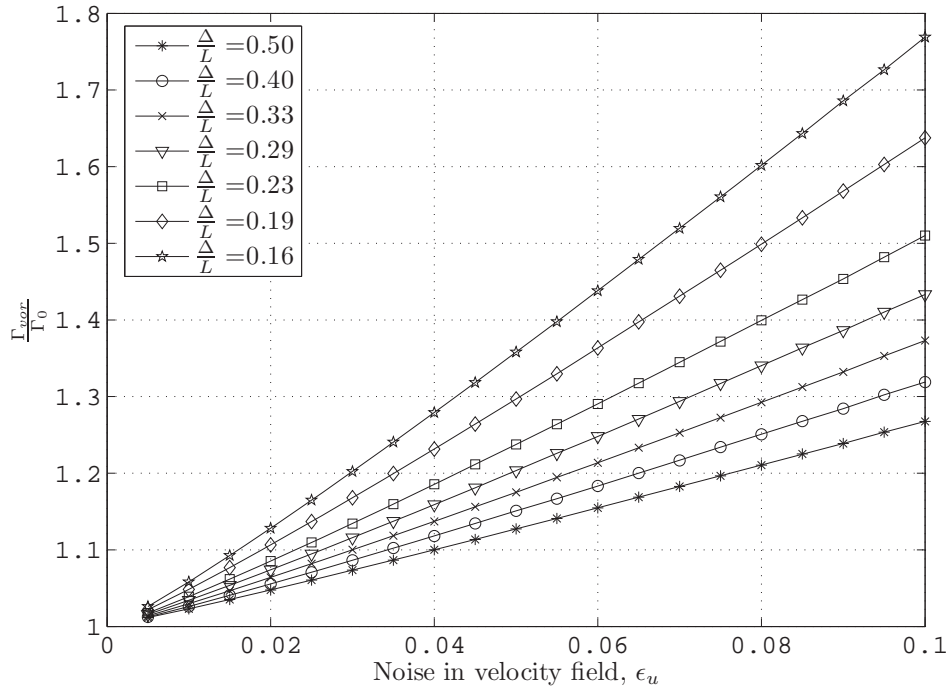
From figures C.3a and C.3b, it can be seen that the circulation bias errors produced by the velocity integral, Γ_{vel} are generally lower than those of the vorticity integral, Γ_{vor} . This is probably due to the fact that Γ_{vor} uses vorticity values in its computation, which in itself is a derived quantity and is thus doubly susceptible to random noise.

The effect of the choice of Γ_{vel} or Γ_{vor} on $\frac{\sigma_\Gamma}{\Gamma_0}$, for the centre-difference scheme, is negligible (see figures C.4a and C.4b). However, this is not typical for all vorticity estimation schemes; it is unique to the CD scheme due to the fact that the value of K for the centre-difference scheme is $K_{CD} = 1$. For schemes with $K < 1$, the random error in circulation using the velocity integral, relative to the vorticity integral, will be $\frac{\sigma_{\Gamma,vel}}{\sigma_{\Gamma,vor}} > 1$, and vice versa.

C.7 Errors in circulation

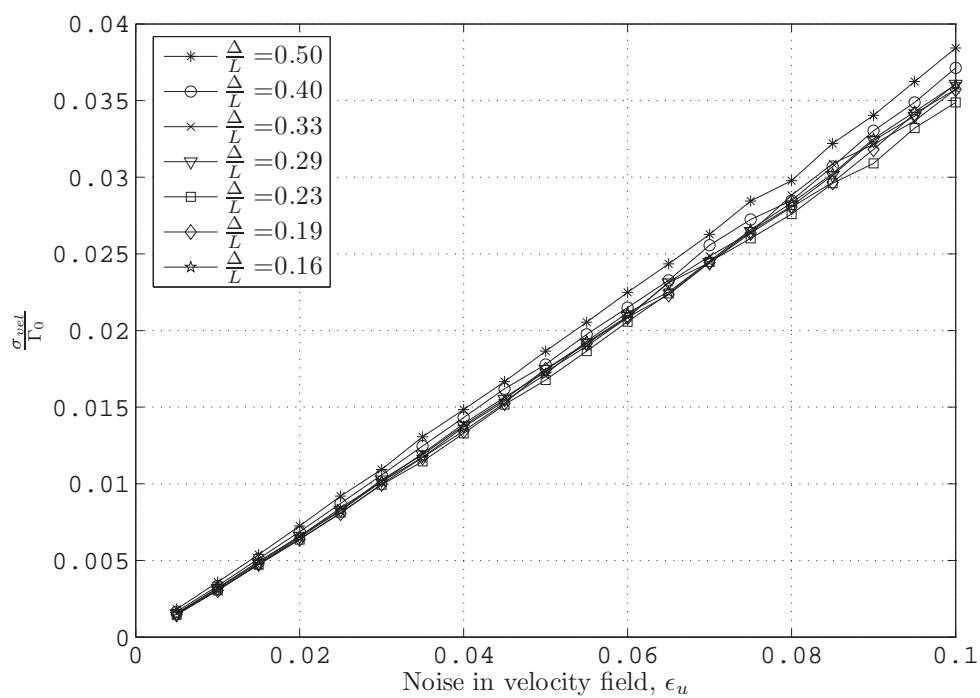


(a)

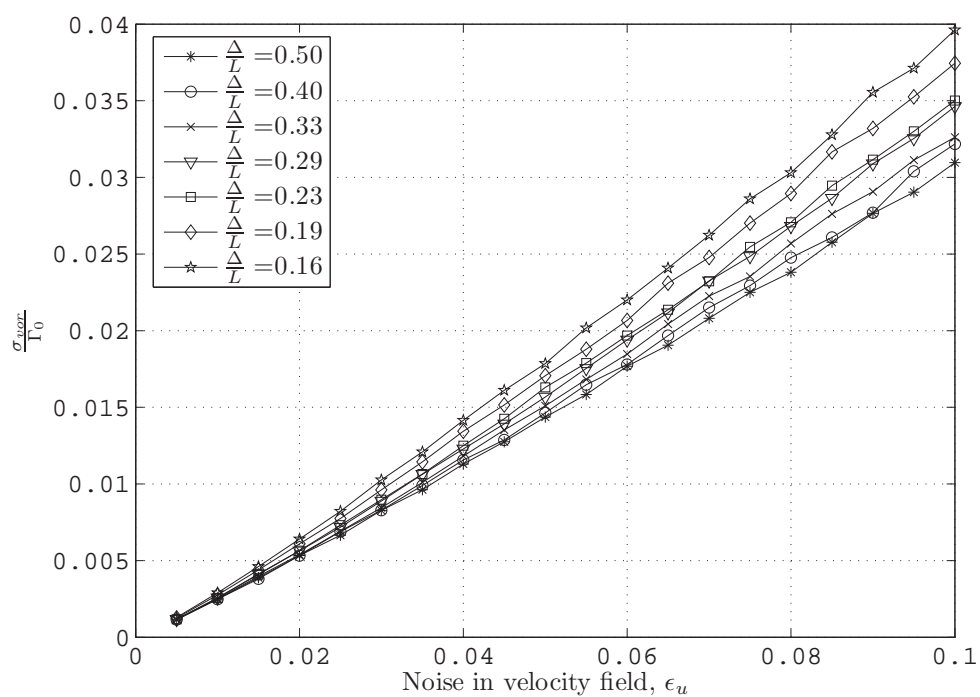


(b)

Figure C.3: Effect of $\frac{\Delta}{L}$ and ϵ_u on the circulation bias error for the centre-difference scheme



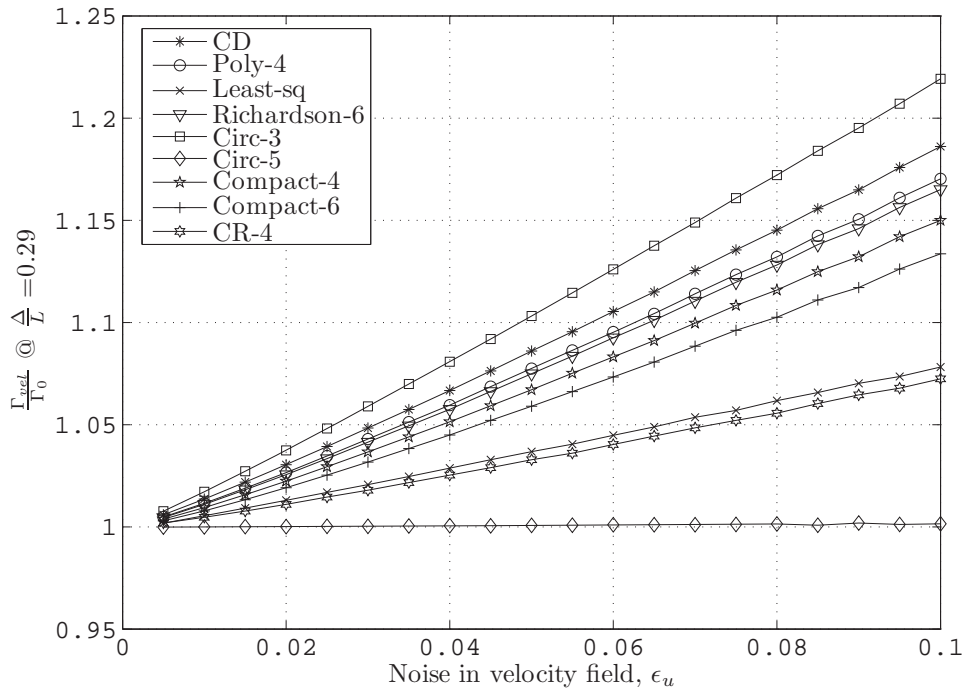
(a)



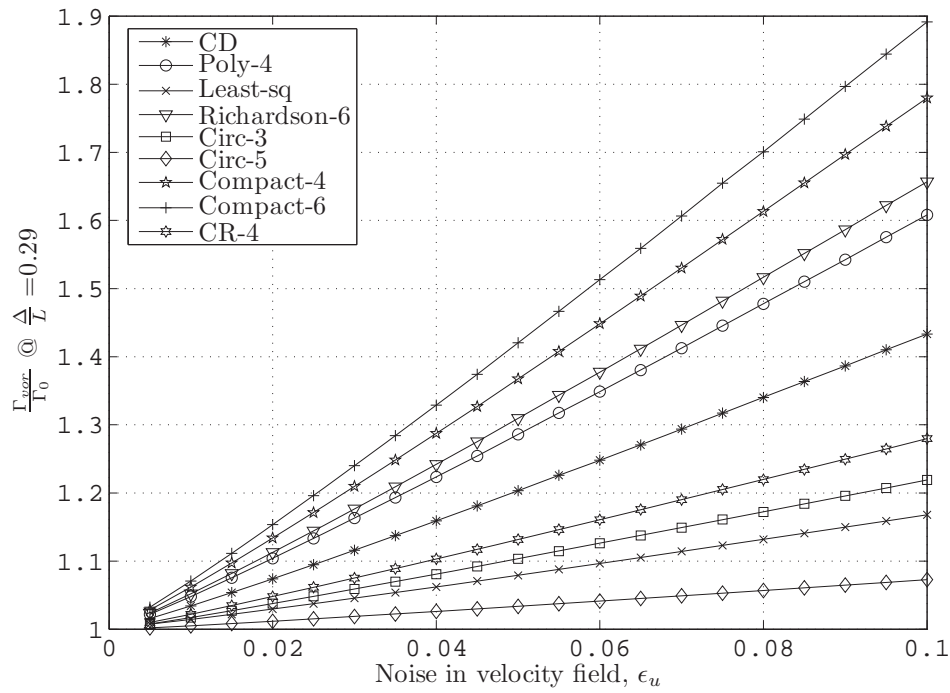
(b)

Figure C.4: Effect of $\frac{\Delta}{L}$ and ϵ_u on the random error in circulation for the centre-difference scheme

C.7 Errors in circulation



(a)



(b)

Figure C.5: Effect of vorticity estimation schemes and ϵ_u on the circulation bias error at a fixed $\frac{\Delta}{L} = 0.29$

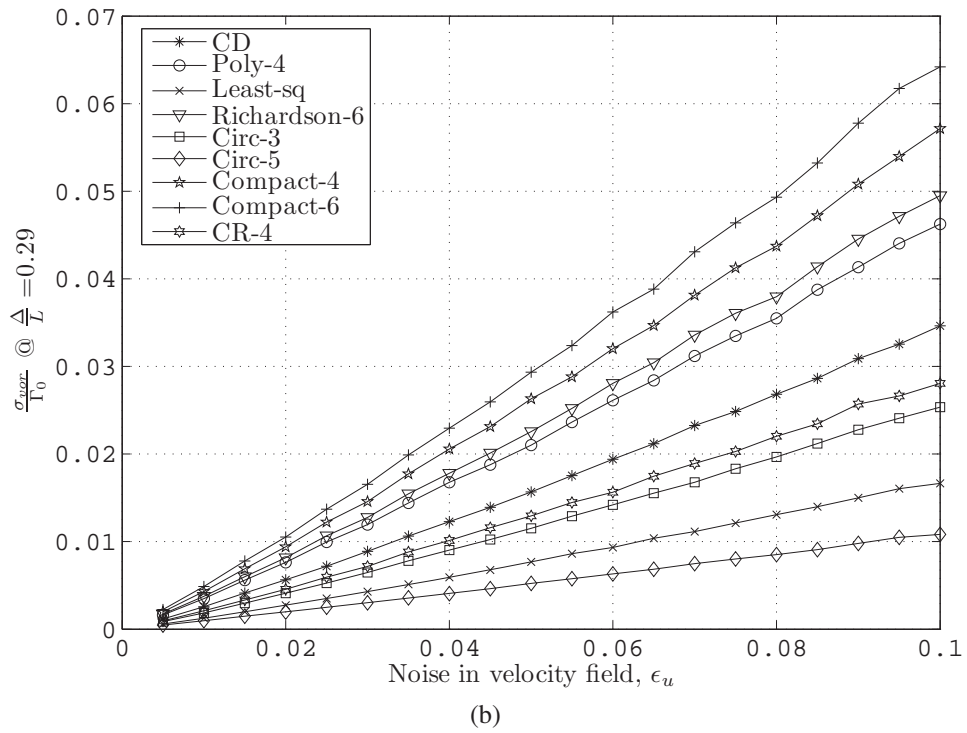
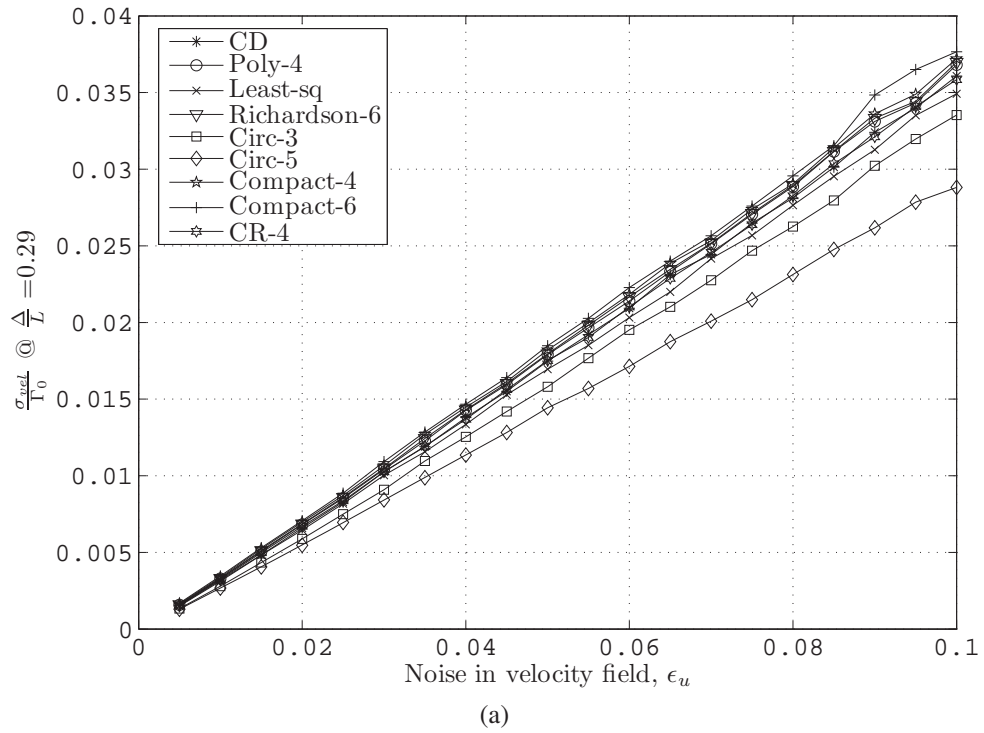


Figure C.6: Effect of vorticity estimation schemes and ϵ_u on the random error in circulation at a fixed $\frac{\Delta}{L} = 0.29$

C.7 Errors in circulation

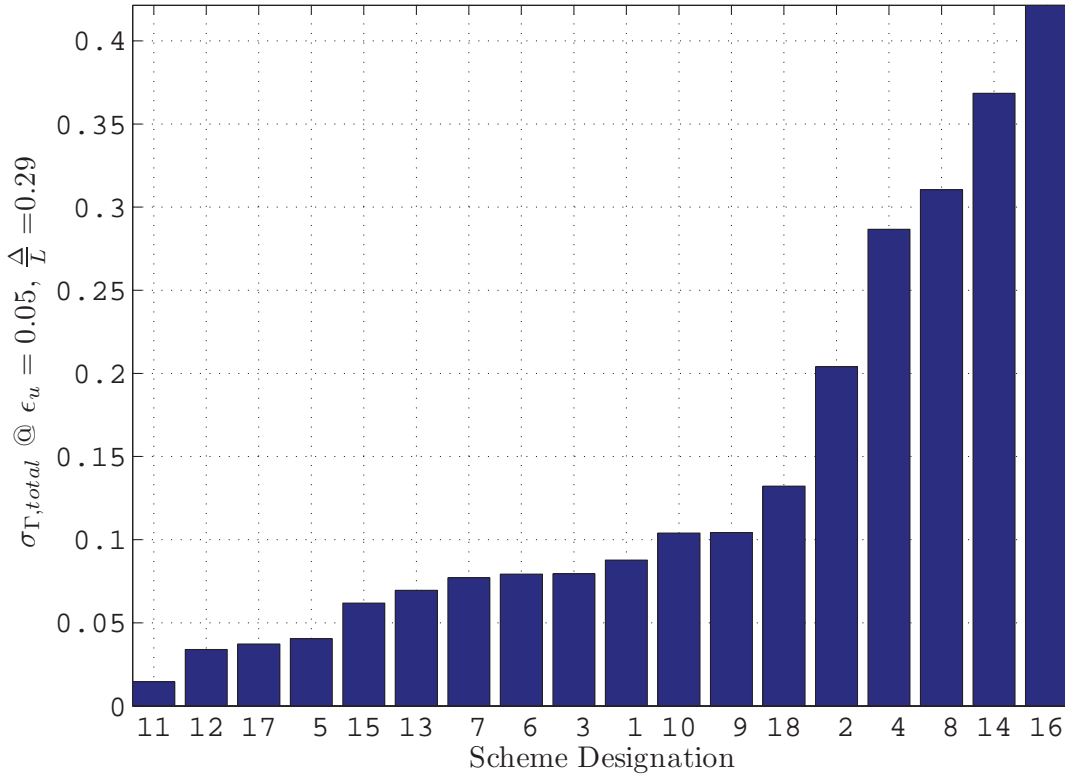


Figure C.7: Total errors in the circulation estimate for all tested schemes at $\epsilon_u = 0.05$ and $\frac{\Delta}{L} = 0.29$. For list of scheme designations, please refer to table C.5

Figures C.5 and C.6 illustrate the differences in the circulation estimate based on each vorticity estimation scheme for both Γ_{vel} and Γ_{vor} at a fixed resolution of $\frac{\Delta}{L} = 0.29$, which is representative of all other tested values of $\frac{\Delta}{L}$. The scheme which clearly displays the best performance is the circ-5 scheme. The circ-5 scheme consistently produces the lowest bias and random errors in the circulation, regardless of ϵ_u . Furthermore, in general it can be seen that the velocity integral produces less bias error than the vorticity integral, that is, $\frac{\Gamma_{vel}}{\Gamma_{vor}} \lesssim 1$ for all schemes, however, the ratio $\frac{\sigma_{\Gamma, vel}}{\sigma_{\Gamma, vor}}$ is dependent on the scheme used, as previously explained.

To obtain a measure of the **total** error in the circulation estimate, we sum the contributions of both the bias and random errors in circulation,

$$\sigma_{\Gamma, total} = \sqrt{\left[\frac{\Gamma}{\Gamma_0} - 1\right]^2 + \left[\frac{\sigma_{\Gamma}}{\Gamma_0}\right]^2} \quad (C.23)$$

We can then use the total error as a single measure of the relative strengths of each vorticity estimation scheme. As an example, for a typical unsteady foil experiment presented in this thesis, we estimate that $\frac{\Delta}{L} \approx 0.29$ and $\epsilon_u \approx 0.05$ (see chapter 2). At these values, the total errors range from $0.015 \lesssim \sigma_{\Gamma, total} \lesssim 0.421$, depending on the scheme used (see figure C.7).

Scheme	Scheme Designation	Γ_{vel} or Γ_{vor}	Ranking (1 = lowest value)				
			$\widetilde{\omega}_{bias}$	λ_0	$\frac{\Gamma}{\Gamma_0}$	σ_Γ	$\sigma_{\Gamma,total}$
CD	1	Γ_{vel}	7	5	10	9	10
	2	Γ_{vor}			14	6	14
Poly-4	3	Γ_{vel}	4	6	8	11	9
	4	Γ_{vor}			15	15	15
Least-squares	5	Γ_{vel}	8	2	4	8	4
	6	Γ_{vor}			9	2	8
Richardson-6	7	Γ_{vel}	3	7	7	12	7
	8	Γ_{vor}			16	16	16
Circ-3	9	Γ_{vel}	7	3	11	7	11
	10	Γ_{vor}			12	3	11
Circ-5	11	Γ_{vel}	9	1	1	5	1
	12	Γ_{vor}			2	1	2
Compact-4	13	Γ_{vel}	2	8	6	13	6
	14	Γ_{vor}			17	17	17
Compact-6	15	Γ_{vel}	1	9	5	14	5
	16	Γ_{vor}			18	18	18
Hybrid-CR4	17	Γ_{vel}	5	4	3	10	3
	18	Γ_{vor}			13	4	13

Table C.5: Summary of the performance of each vorticity estimation scheme

The scheme which produces the lowest $\sigma_{\Gamma,total}$ is, not surprisingly, the circ-5 scheme, while the compact-6 scheme tends to perform poorly, due to its high random error transmission ratio.

C.8 Conclusions and recommendations

Based on a numerical simulation of the analytic Oseen vortex, nine different schemes were used to estimate vorticity, and subsequently circulation, from discrete velocity data with varying random noise values, ϵ_u , and spatial resolution $\frac{\Delta}{L}$. The performance of these schemes are quantified in terms of the bias error in vorticity, $\widetilde{\omega}_{bias}$, the random error transmission ratio (from velocity to vorticity), λ_0 , the bias error in circulation, $\frac{\Gamma}{\Gamma_0}$ and the random error in circulation, $\frac{\sigma_\Gamma}{\Gamma}$.

The results of this simulation illustrates the effect of ϵ_u and $\frac{\Delta}{L}$ on these four quantities. For all vorticity estimation schemes, an increase in the data resolution (i.e. decrease in $\frac{\Delta}{L}$) increases

C.8 Conclusions and recommendations

λ_0 while decreases $\widetilde{\omega}_{bias}$, while an increase in ϵ_u increases the random noise in the vorticity linearly (see equation C.18). ϵ_u has no effect on the vorticity bias error.

The random and bias errors in circulation, $\frac{\sigma_\Gamma}{\Gamma}$ and $\frac{\Gamma}{\Gamma_0}$ respectively also show an approximate linear relationship with ϵ_u within the range $0 \leq \epsilon_u \leq 0.1$. An decrease in $\frac{\Delta}{L}$ produces larger circulation bias errors, however, the resolution has negligible effect on the random noise in circulation.

However, the primary motivation of these simulations is to determine the most appropriate vorticity estimation scheme to use for any particular application. Each scheme is ranked based on its performance in reducing the four non-dimensional error parameters, λ_0 , $\widetilde{\omega}_{bias}$, $\frac{\sigma_\Gamma}{\Gamma}$ and $\frac{\Gamma}{\Gamma_0}$. The summary of this ranking system is shown in table C.5.

Generally, relative to the centre-difference scheme, each scheme is designed either to reduce either $\widetilde{\omega}_{bias}$ or λ_0 , but not both. The only exception to this is the hybrid-CR4 scheme, which achieves modest reductions in both $\widetilde{\omega}_{bias}$ or λ_0 relative to the CD scheme.

The most suitable choice of scheme to estimate vorticity depends on the individual application. In cases where the experimental velocity field contains large random errors, ϵ_u , or for flow cases where the bias error in vorticity is not as important as the random error, a scheme with a low value of λ_0 , such as the circ-5 scheme, should be chosen. On the other hand, for flow cases where the random noise in the velocity field is relatively small, or for flow cases where the bias error in vorticity is important, then a scheme with a low value of $\widetilde{\omega}_{bias}$, such as the compact-6 scheme, should be used. If a balance of both low λ_0 and $\widetilde{\omega}_{bias}$ is required, we recommend the hybrid-CR4 scheme.

In terms of evaluating circulation, the best performing vorticity estimation scheme is the circ-5 scheme. The circ-5 scheme, used either in conjunction with the velocity or vorticity integrals, Γ_{vel} or Γ_{vor} respectively, show low values of both the random $\frac{\sigma_\Gamma}{\Gamma}$, and bias errors in circulation, $\frac{\Gamma}{\Gamma_0}$. This remains true for all values of random velocity noise magnitudes ϵ_u and data resolution $\frac{\Delta}{L}$. Additionally, in general, the velocity integrals, Γ_{vel} , produce lower circulation bias errors than the vorticity integrals, Γ_{vor} , while Γ_{vor} produces lower random errors in circulation than Γ_{vel} only for schemes with $K < 1$. This is manifested in the fact that the total errors in circulation, $\sigma_{\Gamma,total}$ are typically lower for Γ_{vel} than Γ_{vor} , and it is thus recommended that Γ_{vel} be used instead of Γ_{vor} for the estimation of circulation.

In conclusion, for the specific unsteady hydrofoil experiment presented in this thesis, and based on the total error in circulation, $\sigma_{\Gamma,total}$, we recommend the use of the circ-5 method (velocity integral) for evaluating circulation.